IMPERIAL COLLEGE LONDON

STUDIES INTO THE VIBRO-ENHANCEMENT OF PENETRANT INSPECTION AND THE ULTRASONIC INSPECTION OF DIFFUSION BONDS

by

Katherine Anne Milne

A thesis submitted to Imperial College London for the degree of

Engineering Doctorate

Research Centre in Non-destructive Evaluation

Department of Mechanical Engineering

Imperial College London

London SW7 2AZ

March 2010

I confirm that the work reported in this thesis and submitted for the degree of Engineering Doctorate is original and my own. The work of other authors has been appropriately referenced.

Katherine Milne

Preface

The four years of my Engineering Doctorate were divided between two projects: vibro-enhanced fluorescent penetrant inspection and ultrasonic non-destructive evaluation of titanium diffusion bonds. The project was originally entitled 'Vibro-Enhanced Non-destructive Evaluation'. Prompted by work previously carried out at Imperial College and Bath University into two vibration-based techniques - vibro-acoustic modulation and thermosonics - the aim was to look at vibration as a means of enhancing non-destructive evaluation techniques that are conventionally used to detect fatigue cracks in aeroengine components. The premise was that the reliability of conventional methods was limited by the width of the fatigue crack and that vibration could be used to actively open the crack, thereby improving reliability. A literature review of conventional non-destructive evaluation techniques indicated that the reliability of both fluorescent penetrant inspection and ultrasonics was related to crack width, although the relationship between crack width and reliability is different for the two techniques (see Part I, Section 5.1. of this thesis).

The project plan was to concentrate upon the effect of crack width on the reliability of fluorescent penetrant inspection and the potential of vibration as a means of actively enhancing the penetrant inspection for the first two years. The relationship between crack width and ultrasonic response and the potential of vibro-enhancement would be pursued in the final two years, once a suitable application had been identified and the requisite equipment had been purchased.

Vibro-acoustic modulation is an example of a nonlinear ultrasonic inspection. During the literature review into nonlinear ultrasonic inspection for the detection of fatigue cracks, I was also exposed to literature on the nonlinear ultrasonic inspection of bonded interfaces, such as diffusion bonds, inertia welds and adhesive joints. As the work on fluorescent penetrant inspection was coming to an end, the Rolls-Royce plc Technology Acquisition team for Non-destructive Evaluation identified a pressing need to develop an improved ultrasonic inspection for titanium to titanium diffusion bonds. Nonlinear ultrasonic inspections of bonded interfaces have been reported by several authors in the academic literature. However, it was clear that a nonlinear solution would require considerable resource and a working solution could not realistically be achieved in the timescales requested. Also, several options for improving the conventional ultrasonic inspection through signal processing methods were identified. The research that had been carried out on the ultrasonic inspection of diffusion bonds between pieces of highly textured forged Ti-6Al-4V was limited and therefore there were areas where the basic understanding of the problem could be improved. This project had clearly defined requirements, a strong industrial pull and a dedicated funding stream. For these reasons, it was decided to focus on this project during the final two years of my Engineering Doctorate programme.

Acknowledgements

I would like to give my sincerest thanks to Prof. Peter Cawley for his excellent academic supervision over the past four years. I am very grateful to both my industrial supervisors David Wright and Anthony Dunhill, for providing ideas, backing and moral support. The members of the Rolls-Royce plc Non-destructive Evaluation team have kept me smiling and helped me out in countless ways. I would like to thank them all, but especially Stephen Press without whose mentorship I would have been lost on many an occasion.

For both of the projects pursued during the course of this doctorate, I received considerable support from a variety of sources. TJ Wire Erosion Ltd. and TiSiCs helped with sample production. For the project on Vibro-Enhanced Fluorescent Penetrant Inspection (Part I of this thesis) I would like to thank the Rolls-Royce plc Mechanical Test department, particularly Roger Smith and Phil Minion, and the Rolls-Royce plc Experimental Vibration department. Professor Glen McHale at Nottingham Trent University gave me invaluable guidance in the field of wetting. Marco Morbidini of the Non-destructive Testing group at Imperial College was a teacher and a friend.

For the project on the ultrasonic inspection of titanium diffusion bonds (Part II of this thesis), I am profoundly indebted to Prof. Peter B. Nagy of the University of Cincinnati for his time and insight. I would like to thank members of the Rolls-Royce plc Materials team, including Adrian Walker, Dave Rugg, Richard Whittaker, Gareth Friend and, in particular, Steve Twigg and Phillip Doorbar for their expertise and support. Thanks are also due to

Andrew Palfreyman, Sebastian Davies and Lee Webster at Intertek Ltd. and Steve Sharples of the University of Nottingham.

I would like to thank Rolls-Royce plc and the Research Centre in Non-destructive Evaluation (RCNDE) for funding this EngD and for giving me an opportunity to be part of such an amazing scheme. Thanks are due to Nina Hancock for dealing with every problem and to Prof. Chris Scruby for being there for us. Finally I would like to thank my friends and family, who I love very much, especially Ian Edmonds, who gave me a home in Derby, and Paul Hill, who made me happy, kept me sane and cooked my dinner.

Contents

PART I

VIBRO-ENHANCED FLUORESCENT PENETRANT INSPECTION

1. Introduction

Fluorescent liquid penetrant is used to inspect the vast majority of critical aeroengine components at some point during their lives. The reliability of the method is affected by a number of factors, including the type of liquid penetrant that is used, human factors and the nature of the defect. It is widely recognized that liquid penetrant is less sensitive to tight fatigue cracks.

One of the factors affecting the safe life of aeroengine components is the defect size that can reliably be detected using non-destructive testing techniques. For surface breaking fatigue cracks, it is now standard to express technique reliability in terms of crack length. The first aim of this project is to demonstrate the effect of crack width on the length of the fatigue crack that can be reliably detected.

Fatigue is the main failure mechanism for aeroengine components and is often also the life-limiting factor. Improving the reliability of penetrant inspection for the detection of fatigue cracks could allow us to increase the life of the components or the time between inspection intervals, which would have clear cost-benefits for an aeroengine manufacturer such as Rolls-Royce plc. The second aim of this project was to investigate the possibility of improving the probability of detecting tight cracks by actively opening the crack during inspection. Vibration was investigated as it is an efficient way of inducing strains in a component and because there may be some effect due to the dynamic loading. The aims of the project were to:

1. Find what magnitude of cross-crack strain is required to significantly increase the probability of detection.

2. Understand how these strains relate to the crack mouth opening.
3. Determine at what point in the penetrant process the strain has to be applied.
4. Vibrate the samples at different levels of dynamic strain during processing to investigate the potential of vibro-enhancement.

Section 2 explains the industrial motivation and context for this project. The fluorescent penetrant process, its uses, advantages and limitations are briefly described. Metal fatigue is then discussed, including how the inspection reliability at manufacture and after the component enters service affects the calculated safe fatigue life of the component. Finally the way in which reliability is determined for aerospace inspections is described.

Section 3 is a literature review. It reviews research on how load history and residual stresses affect the width of fatigue cracks. Secondly it reviews the penetrant process, including basic wetting theory, the mechanism by which liquids fill (wetting) and empty (de-wetting) entrapments and the effect of crack morphology on the penetrant process. The use of vibration for actively promoting fluid flow and the wetting and dewetting of entrapments is also reviewed.

Section 4 describes how a series of cracked samples were generated by cyclic loading, including the requirements for the sample geometry and crack morphology and the method of generating and detecting the cracks. Section 5 reviews methods for measuring crack width and then describes the method that was finally adopted. The reliability of the penetrant process is highly dependent upon the skill of the inspector. In order to simplify the study, it was decided to

use a method for automatically detecting penetrant indications. Section 6 briefly reviews options for an automatic detection of fluorescent penetrant indications and then describes the chosen method.

Section 7 investigates the effect of crack width on the reliability of the fluorescent penetrant process. Cracked samples were progressively loaded, causing the crack mouth to open during the penetrant process. The cross-crack strain required to achieve an improvement in the reliability of the penetrant process was determined. The points during the penetrant process at which the crack mouth had to be actively opened in order to obtain this improvement were also investigated.

Section 8 looks into one potential method for enhancing the fluorescent penetrant process by using vibration to actively open the crack during processing. The strains that are required for the vibro-enhanced fluorescent penetrant inspection to work are compared to the threshold strain for crack propagation.

Finally, the findings of Part I of this thesis are summarised in Section 9, along with suggestions for future work.

2. Project Context

2.1. Fluorescent Penetrant Inspection of Aeroengine Components

The majority of aerospace gas turbine inspections are carried out using one of five non-destructive testing methods: penetrant, magnetic particle, eddy current, ultrasound and X-ray. These methods have been referred to as 'the Big Five'. Visual inspection is not counted even though it is universally used and an integral part of penetrant and magnetic particle inspection. Variations of these methods are used to detect defects at manufacture, such as inclusions or porosity, or in-service defects, such as cracking and wear.

Penetrant inspection is the most established of these inspection methods for aeroengine components. In the aerospace division of Rolls-Royce plc penetrant is now used to inspect over 90% percent of components between manufacture and the end of their serviceable lives. The penetrant process is simple: a paint is applied to the surface of the component and is left to 'penetrate' into surface breaking features; after a period of time the paint is washed off the surface; any paint remaining in surface-breaking features should then bleed back onto the surface, forming a visible 'indication'. Normally a developer is applied to the component, to encourage the penetrant to bleed and to increase the brightness of the indication. Penetrant testing can only be used to detect surface-breaking defects. The method is used to detect manufacturing defects, such as laps, cold shuts, seams, surface porosity and thermal cracking, and defects generated in-service, particularly fatigue cracks.

The basic components of a penetrant system are the liquid penetrant itself and a remover. The penetrant may be a brightly coloured liquid, for inspection under white light, or a fluorescent liquid, for inspection in a darkroom under ultraviolet (UV) light. The remover may be water, an emulsifier - like a detergent - or a solvent. Only fluorescent liquid penetrants are used on aerospace components by Rolls-Royce plc. The penetrant systems are categorised by the type of remover that they use and by their sensitivity to surface breaking defects. Rolls-Royce plc assumes that, using the highest sensitivity penetrant system, an 'engineering crack' (a semi-elliptical crack 0.030" (0.76mm) long by 0.015" (0.38mm) deep) will reliably be detected, assuming that the component surface is clean and the surface roughness meets specification. Rough surfaces will hold more penetrant than smooth surfaces during washing. After the excess penetrant has been removed, the penetrant trapped by the surface roughness will bleed back causing a 'background', which will mask indications from defects (see Figure 1). Less sensitive penetrants are therefore used on rough surfaces, as they can be removed more easily. However, they are also less likely to penetrate into defects and so the sensitivity of the inspection is lower.

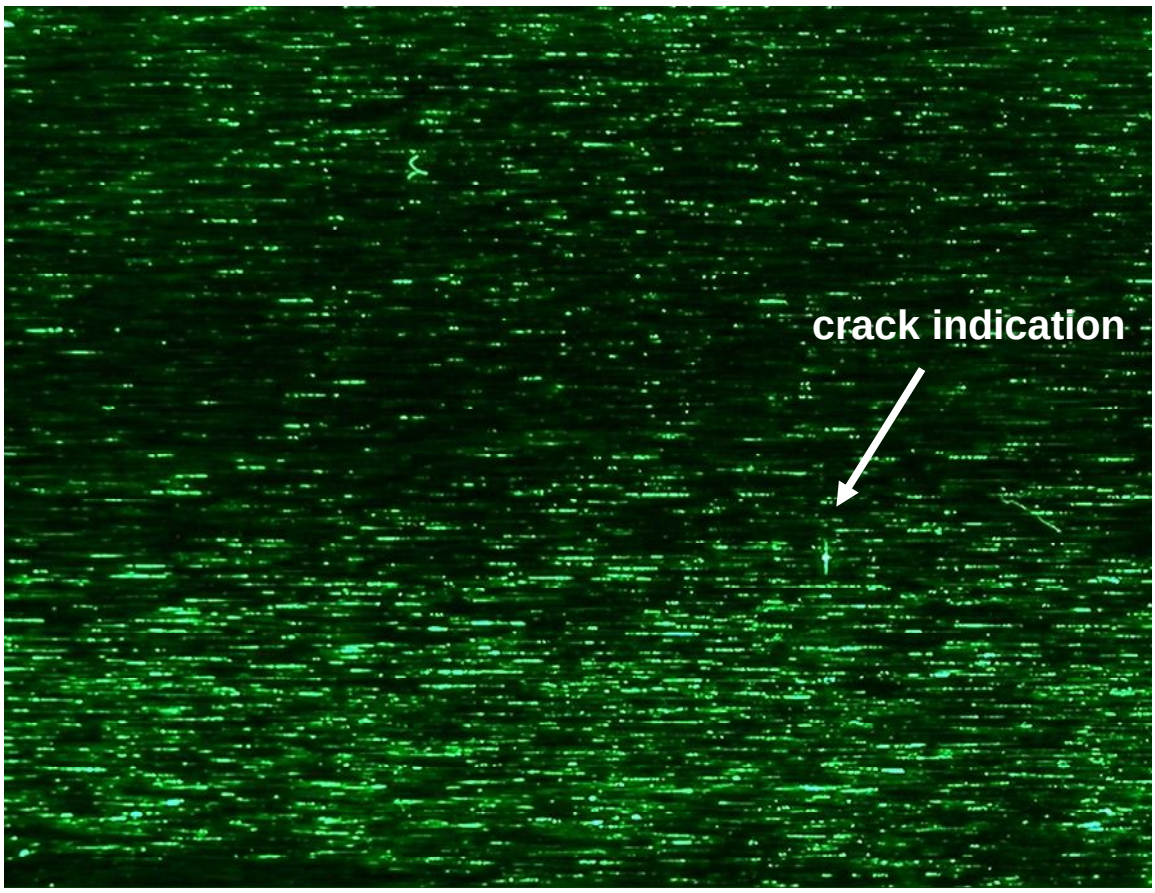

Figure 1. Rough, cracked sample processed with fluorescent penetrant. The sample was generated for this project and contained a crack 0.84mm long ($a_{tip\text{-}to\text{-}tip}$). Image taken with sample under ultraviolet light. There is a large amount of fluorescence or 'background' due to penetrant trapped by surface roughness. The crack indication is difficult to distinguish from the background.

Penetrant inspection has many advantages. Large, complex components can be processed. The process is quick, simple and relatively cheap and is sensitive to a wide variety of defects. The main disadvantage is its dependence on human skill during processing and visual inspection. The reliability of the inspection is highly dependent upon the experience and skill of the inspectors and whether they are tired, complacent etc. However, human inspectors are also particularly adept at detecting defects, at differentiating between indications due to defects and due to the geometry of the component and at differentiating between different types of defect [1, 2].

2.2. Metal Fatigue

Metal fatigue has been estimated to result in approximately 90% of all metallic failures [3]. Fatigue cracks are generated by cyclic loading of components. An engine component will experience a combination of different loads that vary with time. Design engineers define two types of cycle to simplify their models: engine loading due to the take-off-cruise-landing cycle, which is referred to in the aerospace industry as 'low cycle fatigue', and vibration loading, which is referred to as 'high cycle fatigue'. If the cyclic loading exceeds some threshold value then a crack will eventually initiate and propagate in the material. If the crack is not detected in time then the component will fail, which could lead to engine failure.

The fatigue performance of a metal is characterised by four parameters:

1. the fatigue limit or stress below which a crack will never initiate;
2. the number of cycles to crack initiation;
3. the rate of crack propagation;
4. the threshold stress that will cause a crack of a given length to propagate.

These parameters are normally measured on standardised samples at a number of different cyclic loads. Engineers take account of the material's fatigue performance in the design of component geometry. They also use the material data to calculate the life of the component – the number of engine cycles or on-wing hours that the component will last without cracking.

2.3. Inspection at Manufacture and Calculation of Component Life

The life of metallic aeroengine components is dictated by their fatigue performance. Design engineers must balance the need to make lightweight engine components, which will improve the specific fuel consumption (fuel consumed per unit thrust), against components that will last. In general, rotating components limit the life of the engine, as they experience much higher stresses than static components. The life of components dictates the intervals between engine shop visits and overhauls.

Lifing methodologies can be separated into two broad categories:

1. The manufacturing process is well controlled and components are assumed to be free of defects. The life is based upon material test data [4].
2. The defects generated during manufacturing may be detected by inspection. Then the life is calculated assuming an initial defect size, which correlates to the defect size that can be reliably detected. This is termed damage tolerance lifing [5].

In the first scenario, the components are assumed to be initially free of any defects. If the fatigue limit of the material is exceeded, a fatigue crack will initiate eventually. However, if the material properties are well controlled, the material should behave in a statistically predictable way. Mechanical testing is carried out to determine the fatigue performance of the material. Multiple tests are carried out to determine the variability in the material behaviour. The data from these tests is used in models to predict the probable life of the component. The calculated lives are validated by rig tests of the full component. The quality of each batch of material and of the manufacturing

process is assured by a raft of measures, including cut-ups, mechanical tests and non-destructive testing techniques, such as X-ray and ultrasonics. Inspection is used to detect gross manufacturing defects, such as inclusions, but is not used as a basis for lifing calculations.

Some manufacturing processes cannot be so well controlled and the component may contain defects that can be detected using conventional inspection techniques. In this case, the size of defect that can be reliably found using the chosen NDT technique is determined. This is the threshold detectable defect size, a_0. The life of the component is calculated as the number of cycles for a fatigue crack to propagate from the initial flaw size, a_0, to the critical size, a_c, which would result in failure of the component [5]. The Paris-Erdogan equation is widely used to relate the stress range, $\Delta\sigma$, to the crack growth rate da/dN [3]:

$$\frac{da}{dN} = C\left(Y\Delta\sigma\sqrt{\pi a}\right)^m \tag{2.1}$$

C and m depend upon the material, environment, residual stresses and cyclic load, Y is a geometrical factor, a is the crack length and N is the number of cycles. The increase in crack length with cycles for the same stress range according to Equation 2.1 is plotted for three different initial flaw sizes, a_0, in Figure 2. By improving the inspection technique, a_0 is reduced and so the life of the component can be increased. The interval between in-service inspections is also determined by the threshold detectable defect size (see Section 2.4).

Some lifing methodologies also incorporate the probability of the component receiving damage during manufacture and assembly e.g. scratches during lifting [6, 7]. Inspections will probably not be in place that will detect all of

these defects. Inspections can be introduced or the life can be based upon a probabilistic calculation of the size, distribution and type of defects.

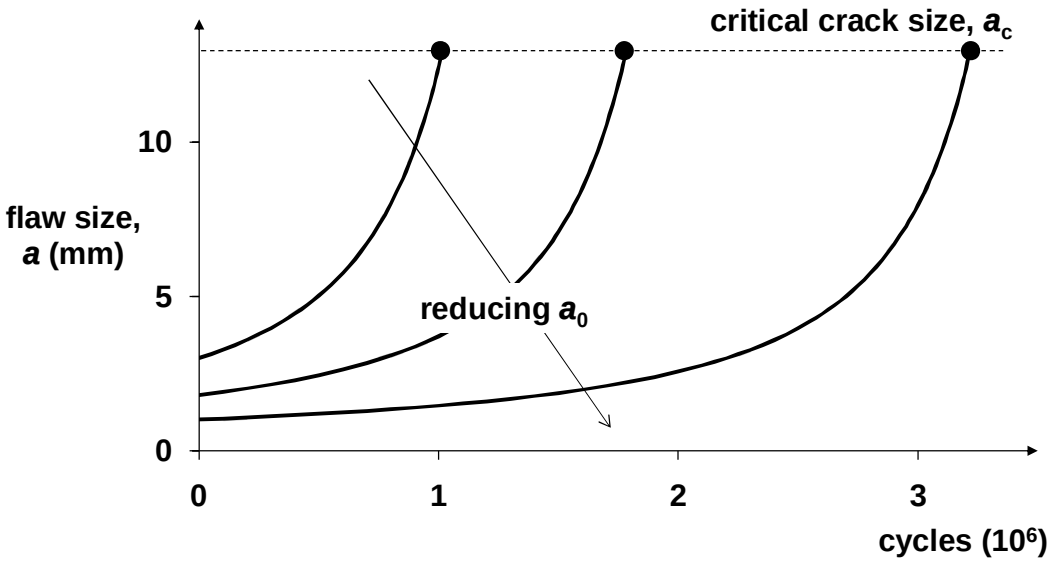

Figure 2. Schematic showing flaw size, a, against time or number of cycles. As the detectable defect size, a_0, is decreased, the time for the flaw to grow to the critical flaw size, a_c, is increased i.e. the life of the component increases. Calculated using the Paris-Erdogan law (Equation 2.1) for $\Delta\sigma$=100MPa, C=0.11x10^{-11}, m=3.85, Y=1.12. After [5].

2.4. In-service Inspection

If a defect is detected well within the predicted life of a component, this indicates that either that the materials data or lifing calculations were incorrect, that the material properties did not meet specification or that a defect was introduced during manufacture, assembly or a routine service that was not detected by inspection. When a defect is detected, a failure investigation is carried out and in some cases the component is re-designed or a new inspection is introduced, either during overhaul or on-wing, to check the integrity of the component. The number of cycles between in-service inspections must be less than the number of cycles for a fatigue crack

to propagate from the threshold detectable defect size, a_0, to the critical size for failure, a_c (see Figure 2).

An alternative lifing methodology is 'retirement for cause' [8, 9]. Regular inspections are carried out during the life of the component. Once a defect is detected, the safe residual life is calculated and the component is replaced onto the engine until the residual life has elapsed. For 'retirement for cause' to work, the inspection must be reliable and provide full coverage of areas that could initiate a defect. It must also allow the size of the defect to be estimated. Ultimately, if inspection can detect sufficiently small defects and reliability can be demonstrated, this strategy would become more attractive to Original Engine Manufacturers (OEMs).

2.5. Probability of Detection

The threshold defect size detectable with NDT, a_0, is based on a probabilistic determination of the reliability of the NDT process, called the probability of detection (POD). The POD is a function of the inspection process variables, including the nature of the defect, component geometry, human factors etc. These considerations are described in a U.S. Department of Defense Military Handbook on 'Non-destructive Evaluation System Reliability Assessment' [10].

A penetrant inspection is a hit/miss inspection i.e. either a defect is detected (a hit) or it is not (a miss). The results of a penetrant reliability assessment are illustrated in Figure 3.

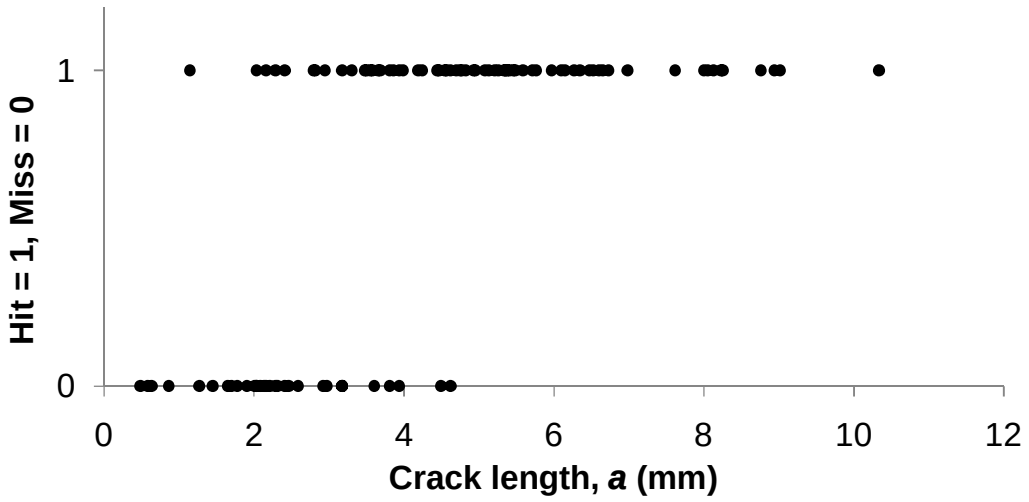

Figure 3. Hit/miss results of a penetrant reliability study on a suite of samples carried out for this project. If the defect is found then it is a 'hit' and given a result of 1. If the defect is not found then it is a 'miss' and given a result of 0.

POD can be calculated by simply dividing the number of defects detected by the total number of defective samples inspected. A POD of 1 indicates that all defects were found all of the time. In a full reliability study the probability of false positives (PFP) or false calls is also calculated as the number of times that a defect is detected divided by the total number of defect-free samples inspected [10].

To determine at what defect size the POD begins to decrease below 1, the results can be plotted as a histogram. For surface-breaking fatigue cracks the most important dimension for the life of the component is the length of the crack. Cracks would therefore be grouped by length and the POD calculated for each group, as shown in Figure 4.

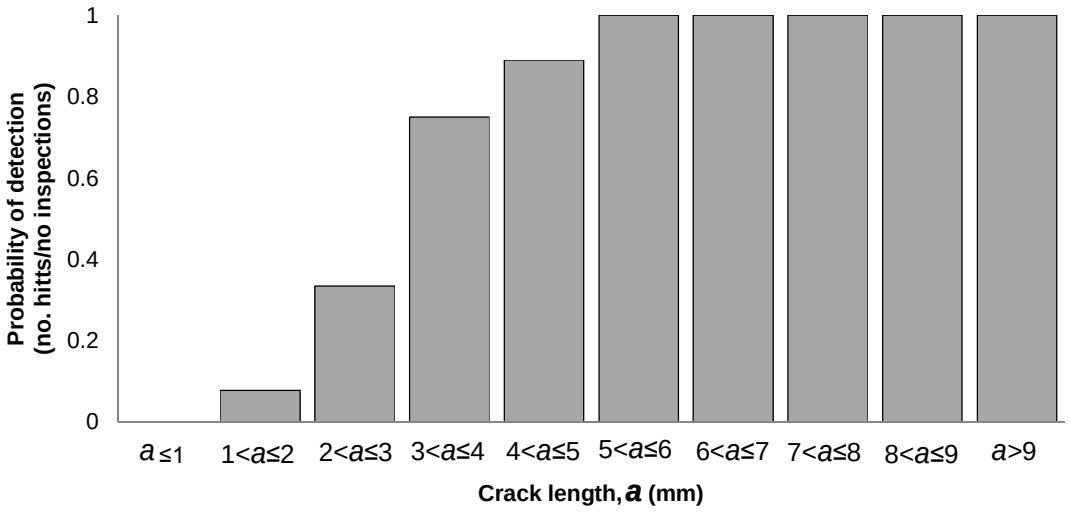

Figure 4.Histogram plot of results shown in Figure 3, showing probability of detecting cracks in a given length range.

To directly compare the capability of different techniques and for lifing calculations, it is convenient to use a single crack length. It is also important to quantify the confidence with which this reliability of detection can be achieved. Therefore, POD is now expressed in terms of a crack length, $a_{90/95}$, which will be detected 90% of the time with 95% confidence. To obtain this number a continuous function, which relates probability of detection to crack length, must be fitted to the binary hit/miss data. The methodology for binary response and regression analysis is explained in detail in the Department of Defense Military handbook on the assessment of the POD (or reliability) of a system [10] and also in a paper by Cook et al [11]. The method is summarised here.

A convenient 'link' function is adopted that is bounded between 0 and 1 and that has an S-shape. The Department of Defense handbook [10] identifies four suitable functions. The logisitic or 'logit' model was used for this project:

$$\mathrm{POD}(X) = \frac{\mathrm{e}^{(\beta_0+\beta_1 X)}}{1+\mathrm{e}^{(\beta_0+\beta_1 \mathrm{X})}} \quad (2.2)$$

where β_0 and β_1 are constants. X can be the crack length, *a*, or log of the crack length, log(*a*). The form is selected which gives the best fit to the data. In this project log(*a*) was used. Therefore:

$$\mathrm{POD}(a) = \frac{\mathrm{e}^{[\beta_0+\beta_1 \log(a)]}}{1+\mathrm{e}^{[\beta_0+\beta_1 \log(a)]}} \quad (2.3)$$

The values of β_0 and β_1 that give the best fit to the data must be determined. An ordinary least squares regression is not suitable for binary data as it assumes that the variance does not change with the mean value of POD(*a*) and that response varies about the mean value of POD(*a*) with a normal distribution. This is not the case for an inspection with a hit/miss response. If the probability of an outcome Y_i is POD(a_i), then the variance in *Yi* is a function of POD(a_i):

$$\mathrm{Var}(Y_i) = \mathrm{POD}(a_i)[1 - \mathrm{POD}(a_i)] \quad (2.4)$$

To find the values of β_0 and β_1 that give the best fit to the data, the maximum likelihood method is used instead. The probability that the outcome Y_i of an inspection of crack a_i is 1 (a hit) is POD(a_i). The probability that the outcome Y_i is 0 (a miss) is 1-POD(a_i). For binary data the likelihood, *L*, of the function fitting the data is the multiple of these probabilities summed for each inspection:

$$L\big((\beta_0, \beta_1); Data\big) = \prod_{i=1}^{n} \mathrm{POD}(a_i)^{Y_i}[1 - \mathrm{POD}(a_i)]^{1-Y_i} \quad (2.5)$$

The parameters of the logistic function β_0 and β_1 are varied iteratively to find the maximum value of *L*:

$$L\big((\beta_0, \beta_1); Data\big) = \prod_{i=1}^{n} \left(\frac{\mathrm{e}^{[\beta_0+\beta_1 \log(a)]}}{1+\mathrm{e}^{[\beta_0+\beta_1 \log(a)]}}\right)^{Y_i} \left(\frac{1}{1+\mathrm{e}^{[\beta_0+\beta_1 \log(a)]}}\right)^{1-Y_i} \quad (2.6)$$

The natural log of Equation 2.5 is taken to simplify the calculation. β_0 and β_1 are varied iteratively to maximise the log of the likelihood, ln(L). These values of β_0 and β_1 describe the 50% confidence bound (see Figure 5).

The likelihood ratio statistic, Λ, is used to determine the position of the lower (95%) and upper (5%) confidence bounds, shown in Figure 5. The model that gave the maximum likelihood of fit to the data, POD(a, β_0, β_1) can be termed θ_0. The likelihood, L_A, that an alternative model, θ_A, with slightly different values of β_0 and β_1 fits the data can also be calculated. The likelihood ratio statistic, Λ, is the ratio of the two likelihoods:

$$\Lambda = \frac{L_A}{L_0} \tag{2.7}$$

The statistic -2ln(Λ) is used to test the null hypothesis, that the models θ_0 and θ_A both describe the same data [12]. The test statistic has a χ^2 distribution with 2 degrees of freedom. The probability of rejecting the null hypothesis when it is true (Type I error) is the significance of the test. The upper (5%) and lower (95%) confidence bound are both found by evaluating the test statistic at a significance of 0.05 (5% likelihood of rejecting the null hypothesis). For a χ^2 distribution with 2 degrees of freedom, a significance of 0.05 is indicated when $-2\ln(\Lambda) = 5.99$. To find the lower (95%) confidence bound:

1. Select a value of probability of detection, POD e.g. 0.9.
2. Vary β_0 and β_1 so that the crack length, a, for the selected POD is minimised and the test statistic, $-2\ln(\Lambda) = 5.99$.
3. Repeat for a range of values of POD to construct the curve POD(a).

To find the upper confidence bound, the same procedure is followed but β_0 and β_1 are found to maximise the crack length, a.

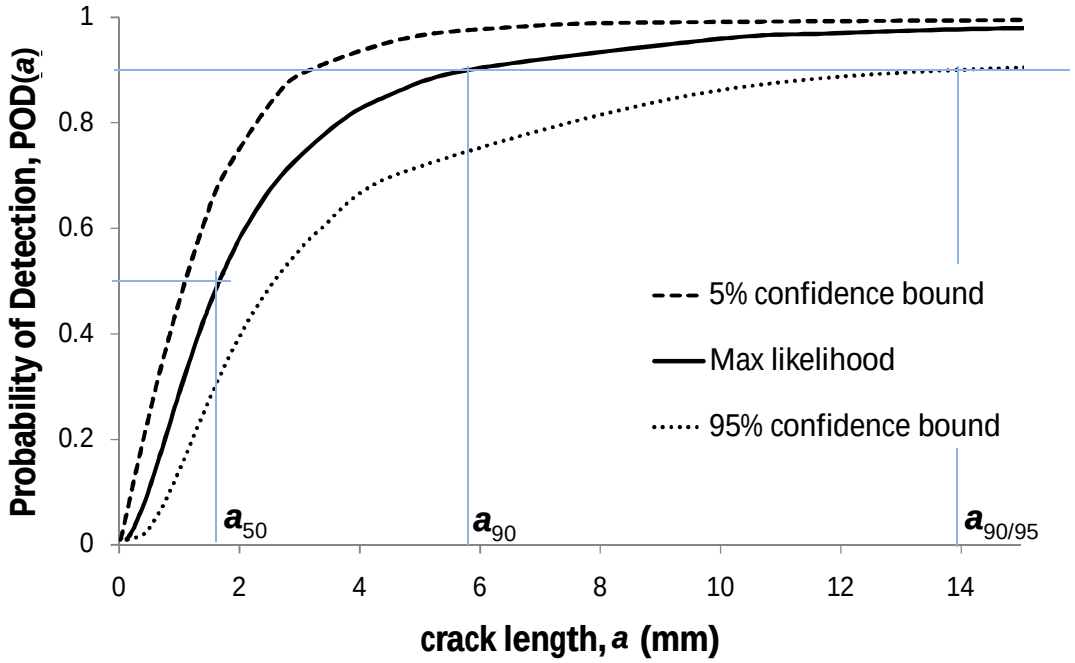

Figure 5. Probability of detection curves calculated by fitting a logistic function to the binary data using the maximum likelihood method, as specified in [10]. a_{50} is the crack length that will be detected 50% of the time, a_{90} is the crack length that will be detected 90% of the time, $a_{90/95}$ is the crack length that will be detected 90% of the time with 95% confidence.

2.6. Crack Width and Reliability of Penetrant Inspection

Currently, probability of detection, POD, is always plotted against the crack length, *a*, for surface breaking defects. This became the convention because crack length is the preferred dimension for lifing calculations. However, other defect dimensions may affect the reliability of an inspection system. The initial aim of this project was to investigate to what extent the crack width affects the reliability of the fluorescent penetrant process used by Rolls-Royce plc.

The reliability of a penetrant process is assessed by inspecting a family of specimens containing surface breaking fatigue cracks. Longer cracks are, in

general, more open than short cracks. However, cracks of the same length may have different crack widths due to the presence of residual stresses from machining or the load history (see Section 3.1). Understanding the effect of crack width on reliability will help us to understand whether the current approach can be used to draw conclusions for all fatigue cracks. If the reliability of a penetrant process is dependent upon crack width, then opening the crack, either statically or using vibration, could be used to improve the sensitivity of the process.

3. Crack Width and Fluorescent Penetrant Inspection

The initial aim of this project was to investigate whether the width of surface-breaking fatigue cracks affects the reliability of the fluorescent penetrant process. The second aim was to look at whether the reliability of the fluorescent penetrant process could be improved by opening the cracks during processing, by applying either a static or dynamic load and causing the crack width to change.

The first section in this literature review (Section 3.1) discusses the factors affecting the width of a fatigue crack and how the width changes upon the application of load. Section 3.2 outlines the penetrant process and then reviews the factors affecting the filling of a crack by a liquid and subsequent bleedout. In particular, it will look at how crack morphology affects the reliability of the penetrant process. The final section (Section 3.3) reviews work on improving penetration of entrapments by applying either a static or a dynamic load.

3.1. Crack Width

If the reliability of the fluorescent penetrant process is dependent upon fatigue crack width, or the gap between the crack faces, then it is necessary to understand what affects crack mouth opening for surface breaking cracks. For this project, which will look at how the inspection reliability can be improved by loading the sample and so changing the crack opening, we would also like to know how a crack behaves under applied load.

The crack mouth opening at zero load and how the crack behaves upon the application of load are both determined by:

1. the load history;
2. the residual stresses introduced into the material by manufacturing or repair processes.

3.1.1 The effect of load history on crack width

When load is applied across a crack, the stress field at the tip is concentrated. The intensity of the stress concentration depends upon the loading configuration, the crack geometry and the half-length, *a*, of the crack.

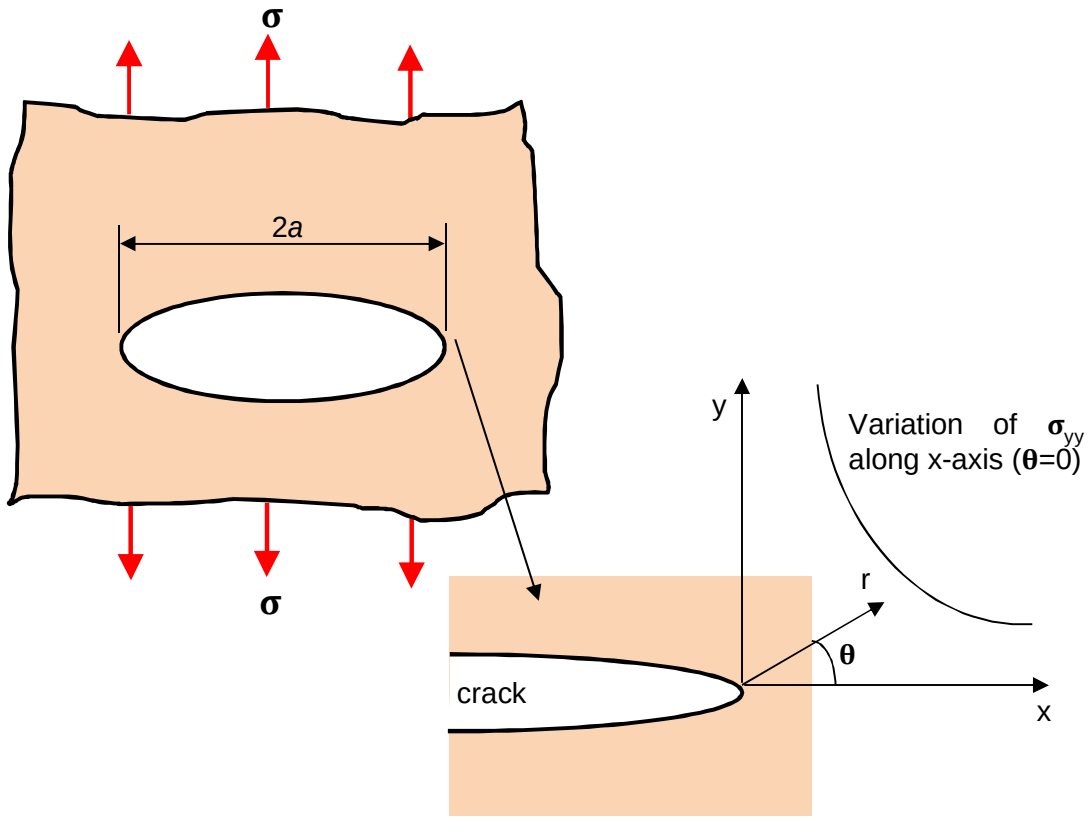

Figure 6. Stress distribution at crack tip in an infinite plate. After Benham et al [4].

From linear elastic theory, for a through-crack of half-length, *a*, in an infinite plate (Figure 6), with stress σ applied orthogonal to the crack plane (Mode I loading), the stress intensity factor, K_I is:

$$K_I = \sigma\sqrt{\pi a} \tag{3.1}$$

The stress in the direction orthogonal to the crack plane will vary as:

$$\sigma_{yy} = \frac{K_I}{\sqrt{2\pi r}} \tag{3.2}$$

where r is the distance from the crack tip. This equation predicts that, at very small distances from the crack tip, $\sigma_{yy} \rightarrow \infty$. In reality, above a certain stress the material will yield and no more stress will be supported. When this happens, the stress must be redistributed to satisfy equilibrium. Assuming an elastic perfectly-plastic material, the size of the yielded region or plasticised zone, r_p, can be calculated from [5, 13]:

$$r_p = \frac{1}{\pi}\left(\frac{K_I}{\sigma_{YS}}\right)^2 \tag{3.3}$$

where σ_{YS} is the tensile yield stress.

K_I varies proportionally with the applied stress: as the applied stress is increased, the size of the plasticised zone increases. The shape of the plastic zone depends upon the geometry and the mode of loading. If the applied stress is then reduced by some amount $\Delta\sigma$ to a tensile stress σ-$\Delta\sigma$, reverse plastic flow occurs, assuming that crack tip blunting is negligible. The size of the area that experiences reverse plastic flow, r_c, will depend upon $\Delta\sigma$. The stress within this region will be the yield stress in compression. Therefore the size of r_c can be derived by replacing K_I by ΔK_I and σ_{YS} by $2\sigma_{YS}$:

$$r_c = \frac{1}{\pi}\left(\frac{\Delta K_I}{2\sigma_{YS}}\right)^2 \tag{3.4}$$

For $\Delta\sigma$=0 (the applied stress is totally removed), the size of r_c will be one quarter that of the area originally yielded in tension, r_p. The compressive

stress around the crack tip, caused by cyclic loading, holds the crack tip closed and is termed plasticity-induced crack closure. The residual stress at the crack tip must be balanced by tensile stresses away from the crack tip. As the crack propagates, the stress intensity at the crack tip increases and the size of the plastic zone at each successive cycle increases. An envelope of plasticised material is left in the wake of the crack tip.

Elber [14] first observed the phenomenon of plasticity-induced closure and postulated that it decreased the effective stress-intensity range at the crack tip. The stress intensity range, ΔK, is defined as:

$$\Delta K = K_{max} - K_{min} \tag{3.5}$$

The *effective* stress intensity range, ΔK_{eff}, is:

$$\Delta K_{eff} = K_{max} - K_{op} \tag{3.6}$$

where K_{op} is the stress intensity factor above which the crack is fully open.

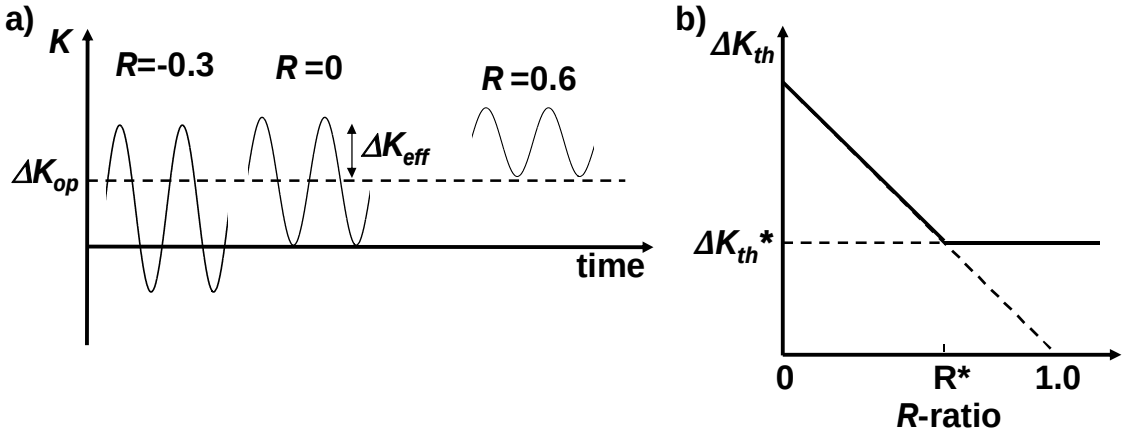

Figure 7.a) Shows effect of crack closure on effective stress intensity range ΔK for different R-ratios. Below the crack opening stress intensity, K_{op}, the crack is closed and so will not propagate. b) Shows variation in threshold stress-intensity range ΔK_{th} with R-ratio. After Anderson [3].

Cyclic loads are often expressed in terms of the ratio of minimum to maximum stress or *R*-ratio:

$$R - \text{ratio} = \frac{\sigma_{min}}{\sigma_{max}} \tag{3.7}$$

Figure 7a illustrates the effect of plasticity-induced crack closure on the effective stress intensity range for different *R*-ratios. Figure 7b shows the variation of the threshold stress-intensity range for crack propagation, ΔK_{th}, with *R*-ratio. At high *R*-ratios the crack never closes. The effective stress-intensity range ΔK_{eff} is equal to the applied stress-intensity range, ΔK. The threshold stress-intensity range K_{th} will then be equal to the intrinsic fatigue threshold of the material, ΔK_{th^*}. Below a certain *R*-ratio, *R**, crack closure will occur for part of the cycle. From Figure 7 it can be seen that, for increasing *R*-ratios, lower stress intensity ranges are required before the threshold for crack propagation is exceeded.

Other mechanisms for crack closure have also been identified. Roughness, oxidation or the presence of viscous fluids in the crack can prevent the faces mating perfectly and effectively wedge it open. The obstructions can carry load and so the compliance is similar to that of the undamaged material. A positive external load has to be applied to overcome the wedging effect. A more detailed explanation of crack closure mechanisms is given by Anderson [5] and Suresh [13]. The overall result is the same for both plasticity-induced closure and wedging mechanisms; the threshold stress-intensity range, ΔK_{th}, or the minimum stress intensity range at which crack propagation will occur, is increased.

The literature mainly focuses on crack-tip closure, as this affects the crack propagation rates, but does not discuss how the load history can affect the

rest of the crack, away from the crack-tip. This, rather than the state of the crack-tip, is expected to impact on the reliability of a penetrant process. However, the above discussion does make it clear that the crack morphology will be affected by the load history, including the loading mode, the *R*-ratio, the stress-intensity range and how these vary with time.

3.1.2 The effect of residual stresses on crack width

Residual stresses can be introduced into components either as a by-product of a machining process, in the case of quenching and welding, or intentionally, in the case of shot peening. Shot peening improves the fatigue performance of components in a number of ways [15, 16]:

1. peening strain hardens the surface, which increases the yield strength;
2. surface finish is improved, meaning fewer crack initiation points;
3. compressive residual stresses are introduced into the first few hundred microns of material under the surface.

The compressive stress at the surface is thought to mitigate crack initiation and propagation, as the compressive stress has to be overcome by an external tensile stress before fatigue occurs. Research has shown that thermal effects, static loading, cyclic loading and crack extension can relieve residual stresses [16] and so affect the rate of crack propagation in the material. The mechanisms for the relaxation of residual stresses are not fully understood.

For components that are shot-peened after the crack has initiated, the compressive residual stresses introduced have been shown to clamp the crack tip and retard crack propagation, thereby extending the component life

[15]. At zero load, cracks in a shot-peened component may be tighter than cracks generated with the same load history in a 'neutral' surface e.g. one with negligible compressive stresses [17].

3.2. Factors Affecting the Sensitivity of the Penetrant Process

This section outlines the steps of the penetrant process (Section 3.2.1), particularly that used by Rolls-Royce plc for the inspection of critical rotating components. It then outlines basic wetting theory (Section 3.2.2) and discusses factors affecting the penetration of liquid into a flaw (Section 3.2.3) and subsequent bleedout of the liquid (Section 3.2.4), concentrating on crack morphology and crack width in particular. Section 3.2.5 will review vibration as a method for actively encouraging liquids to enter and exit from surface-breaking cracks.

3.2.1 The penetrant process

There are numerous permutations of the fluorescent penetrant inspection process but according to Lovejoy [18] there are six basic steps:

1. Precleaning and drying of the surface in preparation for inspection.
2. Application of the penetrant to the surface.
3. Removal of excess penetrant by washing and/or emulsification.
4. Application of developer.
5. Inspection of the surface.
6. Post-cleaning to remove process residues.

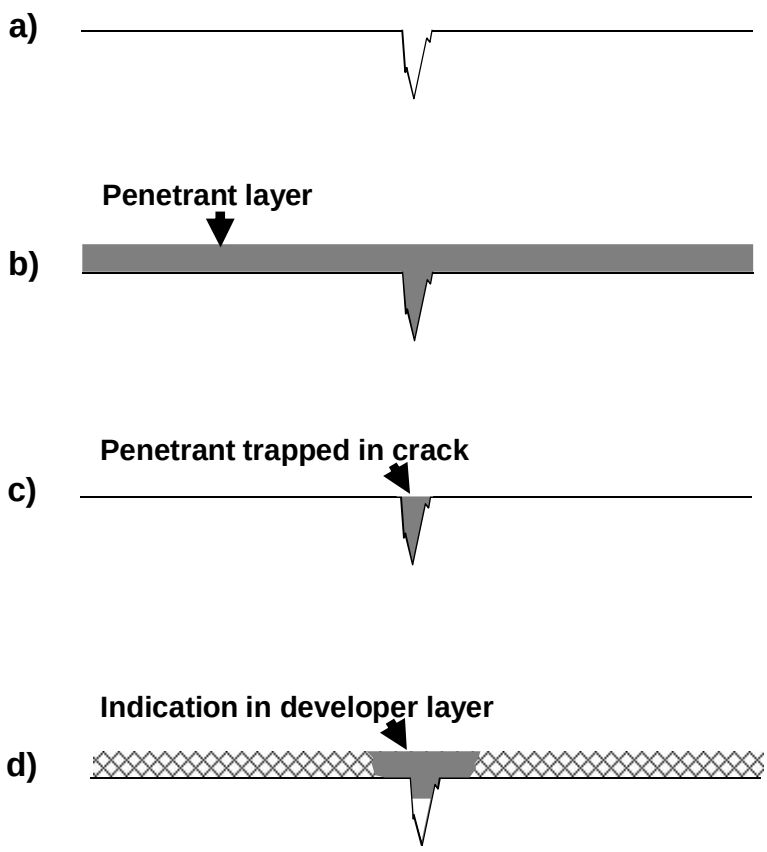

Figure 8. Basic steps in the penetrant inspection: a) clean empty crack b) after penetrant application c) after removal of surface excess penetrant d) indication ready for inspection. After Lovejoy [18].

The process is illustrated in Figure 8. The component is first cleaned in order to remove any foreign material that could prevent the liquid penetrant entering discontinuities. Newly manufactured components may be chemically etched to remove material that has been smeared across discontinuities during machining. Engine-run components may have coatings stripped using a mechanical or chemical strip. Liquid penetrant is applied to the surface of the component by spraying, immersion or using a brush and is left to 'dwell' for a period of time.

Rolls-Royce plc use fluorescent penetrants exclusively. Post-emulsifiable penetrants are the most commonly used for critical rotating components, as they are considered to be the most sensitive. A water spray is used to remove

the excess penetrant from the surface. The penetrant is oil-based and hydrophobic, so the action of the spray is purely mechanical. The component is then dipped into or sprayed with a hydrophilic emulsifier, which removes more excess penetrant by a detergent action. The component is washed again with water to remove the emulsion, oven-dried and then inspected. For the process to reveal material defects such as cracks and pores, it is critical that the liquid penetrates into discontinuities during dwell.

Spontaneous bleedout of liquid penetrant from a crack has been observed in the course of this project. Below a certain film thickness and concentration of penetrant, however, fluorescence will not be observed [19]. Cracks with a larger volume are more likely to contain sufficient penetrant to ensure that the threshold of fluorescence is exceeded when the penetrant bleeds back out into the layer of developer. Vaerman [20] created a POD curve for penetrant inspection independent of human factors by automatically detecting the flaws with a laser to excite the fluorescence and a photo detector. He showed that POD increased with crack depth as well as crack length.

Developers are used almost universally. They consist of white particles which may or may not be suspended in a carrier fluid. They act in a number of ways:

1. The liquid penetrant coats the developer particles, increasing the effective film thickness and therefore the brightness of the indication [21].

2. If a solvent based penetrant is used, then the solvent actively draws penetrant out of the crack. Solvent based developers cause penetrant indications to spread more than dry powder developers [22].
3. For coloured liquid penetrants, which are used for inspection under white light, the white developer also acts as a contrasting background to make the defects more visible. Colour penetrants are not used by Rolls-Royce plc.

Dry powder developers are popular because they can be applied easily in a storm chamber. Developers where powder is suspended in a solvent carrier fluid are sprayed onto the surface of the component. The solvent flows across the surface carrying the suspended powder and then evaporates, leaving the powder behind. A developer was not used in the penetrant process adopted for this project; it is difficult to ensure even coverage of the surface and the white developer particles fluoresce under ultraviolet light, making the automatic detection of penetrant indications more difficult.

There are clearly a large number of variables in the liquid penetrant process. The aim of this project was to investigate the effect of crack width specifically.

3.2.2 Basic wetting theory

First the theory for a droplet or film lying in equilibrium on a flat, rough or chemically heterogeneous surface will be explained. Then wetting theory will be applied to liquid penetrant to understand the effects of the physical

properties of the penetrant, the surface condition and the geometry of the defect upon wetting.

Assuming that no contaminants are present during the period that the liquid penetrant is left on the surface (dwell), the system contains three phases: the solid, the liquid penetrant and air. The boundary where two phases come into contact is called a surface. Unlike the molecules in the bulk of the material, the forces on the molecules at the surface are unbalanced [21]. These molecules exist in a higher energy state. The forces between molecules within the same phase are called cohesional forces while those between two separate phases are called adhesional forces. If the adhesional forces between two phases are equal to or greater than the cohesional forces then the two phases are miscible. If the cohesional forces are greater than the adhesional forces then an interface will exist with a surface energy per unit area, γ. A fluid will reduce the free energy by reducing its surface area. This is why droplets tend to assume a spherical shape.

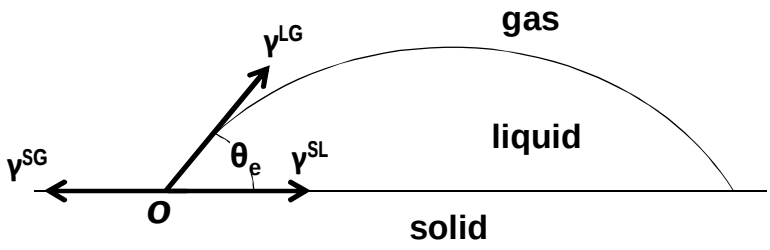

Figure 9. Contact angle, θ_e, at liquid (L) - solid (S) -gas (G) interface where γ is the surface tension [23].

The concepts of surface tension and surface energy were developed during the 19th century [24]. Young derived an equation for the static contact angle, θ_e, of a liquid in equilibrium on an ideal flat solid surface (Figure 9) by assuming that each surface was in a state of biaxial tension. Balancing forces

at the point of contact, O, between the solid-gas (SG), solid-liquid (SL) and liquid-gas (LG) interfaces gives:

$$\gamma^{SG} = \gamma^{SL} + \gamma^{LG} \cos\theta_e \tag{3.8}$$

where γ^{ij} are the interfacial tensions per unit length and $\cos\theta_e$ is called the wetting coefficient. γ^{ij} can also be taken as surface energy per unit area.

Young's assumption - that surfaces exist in a state of tension – appears reasonable. It explains well-known phenomena, such as the ability of an insect or pin to float on water. However, until Gibb's work on the thermodynamics of surfaces, it had no firm theoretical basis. Gibb demonstrated that a surface tension must exist due to the excess free energy of the system. The geometry of the meniscus and therefore the contact angles at a solid-liquid-gas interface in equilibrium will be such that the free energy in the system is minimised.

Roura and Fort have used a thermodynamic approach to derive Young's equation for a small control volume around the line of contact between a solid, liquid and gaseous phase [25]. They show that Young's equation is obeyed locally for all geometries and that the effect of gravity on the equilibrium contact angle is negligible compared to the effect of surface tension.

The equilibrium contact angle, θ_e, is therefore a measure of a liquid's affinity for the solid surface. If the wetting coefficient $\cos\theta_e = -1$ then the liquid to solid tension is large; a drop placed on the surface would not wet it but would remain separated by a thin film of vapour. If $-1 < \cos\theta_e < 0$ then the solid is said to be tending towards non-wetting. If $0 < \cos\theta_e < 1$ then the

solid is said to be tending towards wetting. If $\cos\theta_e=1$ then the system is not in equilibrium. Instead, a film will form on a flat surface (Figure 10).

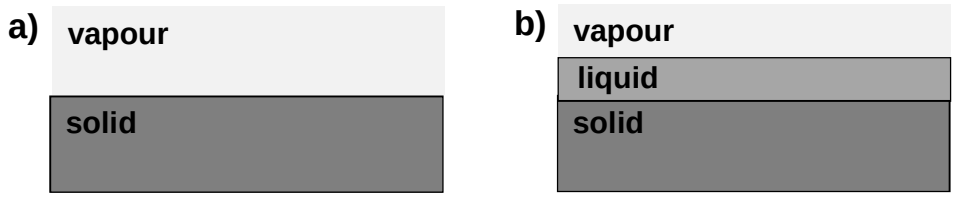

Figure 10. a) Two-phase system containing solid and vapour. b) Three-phase system containing solid, liquid and vapour. The liquid has formed into a thin film on the surface i.e. the spreading power S (Equation 3.9) is greater than zero.

The spreading power S of the film is defined as:

$$S = \gamma^{SG} - (\gamma^{SL} + \gamma^{LG}) \geq 0 \tag{3.9}$$

For a given liquid and solid, a low equilibrium contact angle, θ_e, suggests that the liquid will seek to cover the solid and enter discontinuities to minimise the surface energy of a system. The driving force is the pressure difference across the liquid-gas interface, the action of which is best illustrated by studying penetration of liquid from a reservoir into a capillary.

Penetration into a capillary (Figure 11) is initiated by the formation of a curved meniscus. To minimise the energy in the system, the meniscus will make the angle θ (Equation 3.8) with the walls of the capillary. In the absence of external force fields the meniscus will be perfectly spherical. The curvature results in an interfacial pressure: the pressure at 1 in Figure 11 will be lower than the pressure at 2 and therefore also lower than the pressure at 3. The bulk of the fluid is not in equilibrium and it is this that drives liquid into the capillary until the pressure difference is balanced by an external force (gravity for a vertical capillary). The ASNT NDT handbook therefore calls the interfacial pressure difference the capillary pressure [21]. The pressure

difference across the interface is related to its curvature according to the Young-Laplace equation [26]:

$$\Delta P = \gamma^{LG}\left(\frac{1}{R_1} + \frac{1}{R_2}\right) \tag{3.10}$$

where R_1 and R_2 are the two principal radii of curvature. The principal directions are both perpendicular to the surface tangent plane at that point and are also perpendicular to one another. Marmur [26] states that capillary penetration may also be arrested if the liquid meets an edge, as shown in Figure 11.d. The curvature is flattened, reducing the interfacial pressure.

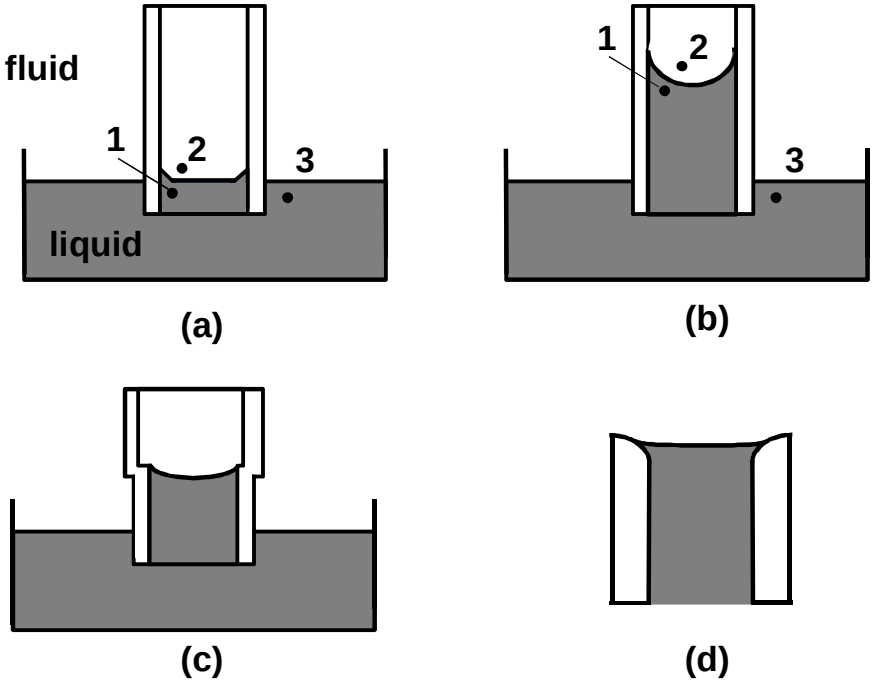

Figure 11. Stages in capillary rise: a) the formation of a meniscus; b) rise to the equilibrium height; c) rise up to an edge; d) magnified view of the edge showing the diminished curvature of the meniscus. After Marmur [26].

The capillary length, κ^{-1} (m), is defined as:

$$\kappa^{-1} = \sqrt{\frac{\gamma^{LG}}{\rho g}} \tag{3.11}$$

where ρ is the density (kg/m^3) and g is the acceleration due to gravity (9.81m/s^2). For systems less than κ^{-1} in size, surface tension dominates over gravity. The capillary length of water is 2.7mm, given that the surface tension is 0.0728N/m.

While the contact angle at a microscopic level must satisfy Young's equation, at a macroscopic level spreading depends upon surface roughness and surface heterogeneity (or local variations in surface chemistry). Two theoretical models are commonly used to explain the effect of surface roughness on wetting behaviour. Wenzel [27] modelled a liquid droplet sitting on a solid surface. He assumed that the liquid is in contact with the solid surface at all points beneath the droplet. For this case the apparent contact angle θ is given by:

$$\cos\theta = r\cos\theta_e \tag{3.12}$$

where θ_e is the contact angle of the liquid with a perfectly smooth solid surface as calculated from Young's equation (Equation 3.8) and r is the roughness factor, which is defined as the actual surface area divided by the area obtained from a planar projection of the surface. Wenzel's equation implies that roughness will magnify the wetting behaviour of a liquid on a given solid; 'a contact angle of more than 90º is increased by roughening the surface, and one of less than 90º is lessened by roughening the surface' [28]. The Wenzel case also predicts that rough surfaces can be invaded by liquids with non-zero Young's law contact angles i.e. from Wenzel's equation, the surface will be invaded when $\theta_e < \cos^{-1}(1/r)$.

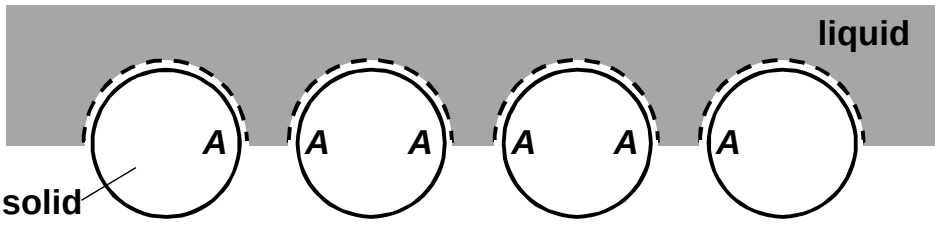

Figure 12. Water on cylinders. Assuming zero hydrostatic pressure, the water will infiltrate the cylinders, coming to rest in position AA determined by the smooth surface-water contact angle θe and the surface geometry. After Cassie and Baxter [29].

The Cassie-Baxter model [29] assumes that the liquid bridges the peaks of the surface, as shown in Figure 12. For this case the apparent contact angle θ is given by:

$$\cos\theta = \varphi_s \cos\theta_e - (1 - \varphi_s) \tag{3.13}$$

where φ_S is the fraction of the solid surface that remains dry. In effect the resultant angle is a weighted average of the contact angle of the liquid on the smooth solid θ_e and the contact angle of the droplet with air (180º as the water tends to form a spherical droplet).

According to Young's equation (Equation 3.8) the contact angle depends upon the surface energy, which varies between materials. For instance, oxides generally have higher surface energies than their base metals [21]. This implies that the contact angle will be lower or that, for a film, the spreading power will be higher on an oxide than on the base metal. For surfaces that are chemically heterogeneous (they have microscopic patches with different chemistries), the apparent contact angle θ will be intermediate between those predicted by Young's equation for each of the patches.

For a surface that is smooth but heterogeneous on a microscopic scale the change in surface energy ΔE caused by extending a droplet of water to cover the solid surface by an area *dA* is:

$$\Delta E = ({\gamma_1}^{SL} - {\gamma_1}^{SG}) f dA + ({\gamma_2}^{SL} - {\gamma_2}^{SG})(1 - f) dA + \gamma^{LG} \cos\theta \, dA \quad (3.14)$$

where γ_1^{ij} are the solid-liquid, solid-gas and liquid-gas surface tensions for material 1, γ_2^{ij} are the solid-liquid, solid-gas and liquid-gas surface tensions for material 2 and f is the fraction of the surface made up of material 1. Substituting Young's equation, the apparent contact angle is:

$$\cos\theta = f \cos\theta_1 + (1 - f) \cos\theta_2 \quad (3.15)$$

If material 2 is air then θ_2 is 180º and the equation reduces to the Cassie-Baxter equation for incomplete penetration of a liquid onto a rough solid surface [28, 30]. Schwartz and Garoff [31] have shown that the apparent contact angle is a strong function of the arrangement or the two solid materials as well as of the coverage fraction, *f*.

The observed contact angle of a liquid on a homogeneous flat surface will display hysteresis [26]. If liquid is added to a drop its contact angle will increase until the contact line starts to advance. The maximum contact angle achieved is called the advancing contact angle. If liquid is removed from the droplet its contact angle will decrease until the contact line starts to recede. The minimum contact angle achieved is called the receding contact angle. Hysteresis is thought to be caused by surface roughness or chemical heterogeneity.

Bico et al [32] manufactured surfaces with a controlled profile (Figure 13) in order to investigate the effects of roughness on the wetting properties of the surface. They dipped the sample into a reservoir of liquid and measured the

height *z* that the liquid rises up the sample. They compared their results to a theoretical model, which combines the Wenzel and Cassie-Baxter approaches. Bico et al assume that the liquid invades the structure but does not wet the tops of the pillars (hemi-wicking). If, as shown in Figure 14, a small quantity of the surface *dz* is wet with liquid of height *z* then, neglecting gravity, the change in interfacial energies is given by:

$$\Delta E = (\gamma^{SL} - \gamma^{SG})(r - \varphi_s)dz + (1 - \varphi_s)\gamma^{LG}dz \qquad (3.16)$$

The first term is the energy required to wet a dry solid. The second term is the energy required to create the liquid-vapour interface associated with the propagation of a film along the surface.

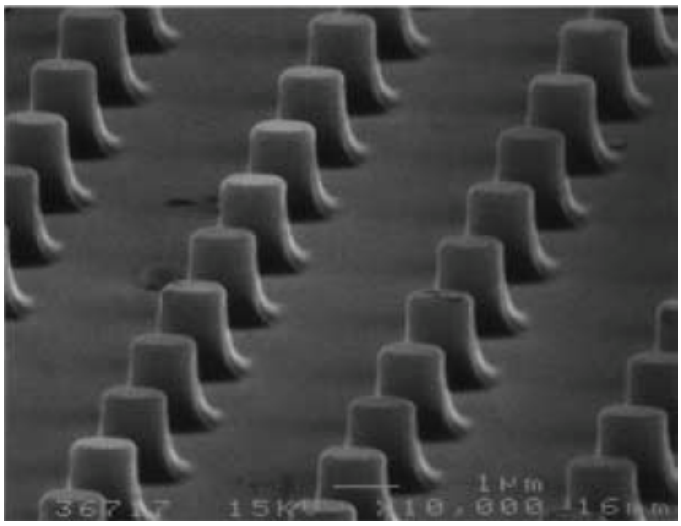

Figure 13. Image of surface under SEM. Surface parameters were estimated from the image: the roughness factor, r=1.3 and the fraction of the solid that remains dry, ϕ_s =5%. After Bico et al [11].

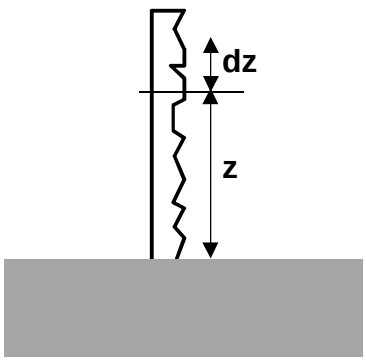

Figure 14. Rough surface in contact with a reservoir showing small displacement of the liquid across the solid surface. After Bico et al [11].

For the film to propagate *dE* must be negative. Substituting Young's equation (Equation 3.8) gives a critical contact angle above which wetting will not occur:

$$\cos\theta_c = \frac{1-\varphi_s}{r-\varphi_s} \tag{3.17}$$

which is a modification of Wenzel's critical angle for invasion of a rough surface.

From scanning electron microscope (SEM) images, Bico et al estimated the values of r and φ_S for their manufactured surface. They partially immersed the sample in reservoirs of different liquids and observed the liquid to solid contact angle at which imbibition occurred. The predicted angle was 40° and the observed threshold was between 30° and 35°. They argue that the experimental results are lower than the thermodynamically predicted results as r and φ_S are an average across the entire surface. The liquid cannot 'know' that another line of spikes lies ahead of it. For this geometry a meniscus is able to flow around the spikes, which conditions flow over the spikes. For extension of the film to occur they state that the contact angle must be greater than $\theta_{min}=\delta/d=27°$, where δ is the height of a spike and d is the distance between two spikes. For $\theta_{min}<\theta<\theta_c$ a metastable state occurs where the liquid contact line is pinned and follows the rows of spikes, adopting a square shape as shown in Figure 15.

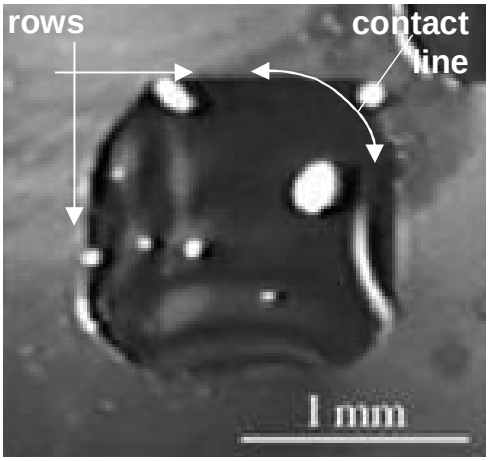

Figure 15. Metastable drop of ethyl malonate (θ=32°) on the structured surface shown in Figure 13. The contact line follows the direction of the rows of micron-scale columns. After Bico et al [32]

The metastable state is a local energy minimum. The contact line cannot move to find the minimum global energy because it would first have to overcome local energy barriers, as illustrated in Figure 16 for a chemically heterogeneous surface. External energy would have to be input to overcome these energy barriers.

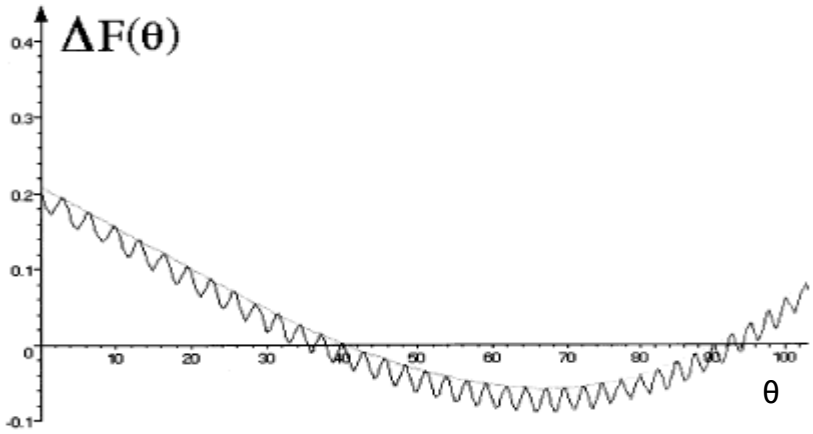

Figure 16. Shows change in surface energy ΔF required to reach a given contact angle θ for an ideally smooth surface with a periodic pattern of chemical heterogeneity. Each local minima coincides with a metastable state. After Della Volpe et al [33].

3.2.3 Factors affecting penetration of a liquid into a surface-breaking crack

The factors discussed here are the properties of the liquid penetrant, including contact angle, specific gravity and viscosity, and also temperature, surface contamination, surface roughness and the morphology of the flaw.

The contact angle of a liquid penetrant depends upon the chemistry and roughness of the material it is in contact with, as described in Section 3.2.2. Penetrants are formulated to give near zero contact angles for most metals [21]. Surface-active agents (surfactants) such as fatty acids are substances that preferentially dissolve in and concentrate themselves at interfaces and particularly at the contact line. They act to lower the surface tension (and therefore the contact angle) and they encourage spreading [21]. Surfactants are intentionally added to liquid penetrants to improve their sensitivity. For films that are thin compared to the capillary length, the effect of surface tension will dominate over gravity (see Section 3.2.2). The specific gravity of liquid penetrants therefore has negligible effect upon its ability to penetrate defects [25, 34]. For low contact angle penetrants, surface roughness should encourage spreading (Equations 3.12 and 3.13), so long as contact line pinning does not occur.

Viscosity does not directly affect the static contact angle although it does affect the dynamic contact angle and therefore the rate at which the liquid will fill a defect [34]. The dynamic contact angle is the apparent contact angle of the liquid as it moves over a solid surface with velocity, v (m/s). It depends upon the surface tension and the dynamic viscosity μ (Ns/m^2) and is related to the capillary number Ca [26]:

$$Ca = \frac{\mu v}{\gamma^{LG}} \tag{3.18}$$

The capillary number is the ratio of the typical speed *v* to the characteristic speed *v'*. The characteristic speed is given by the surface tension divided by the viscosity, i.e. $v'=\gamma^{LG}/\mu$. The characteristic timescale is κ^{-1}/v' where κ^{-1} is the capillary length.

For out of equilibrium spreading, the driving force per unit length of contact line, *F*, is:

$$F = \gamma^{LG}(\cos\theta_e - \cos\theta) \tag{3.19}$$

where θ_e is the Young's Law contact angle and θ is the dynamic contact angle. The liquid penetrant manufacturer, Sherwin Incorporated, claim that the sensitivity of penetrant to small tight cracks can be significantly improved by applying penetrant to hot components (above 70°C) [35, 36]. They suggest that heat may improve the process by lowering the viscosity of the liquid, so causing it to 'flow or migrate more vigorously', and by displacing surface contaminants.

A volatile liquid may invade a surface more quickly. Evaporation can cause internal circulation of molecules within a fluid. A common example is the formation of coffee rings, where the solute is transported to the pinned contact line [37]. If a drop of liquid is placed on a surface, evaporation will occur all along the liquid-gas interface. Two pure modes of evaporation have been identified – constant contact angle and constant contact area [37, 38]. Mixtures of the two modes can also occur. In the constant contact area mode, the contact line is pinned and so cannot move. The droplet maintains its radius as evaporation occurs by allowing internal flow from the centre of

the droplet towards the contact line. The vertical height of the droplet decreases. Coffee rings are caused by this mechanism,

The effect of surface contamination will depend upon the chemistry of the contaminant. As oxides have a higher surface energy [21] than their base metals, assuming that they do not physically block the flaw opening, then they will encourage spreading and penetration. Contamination of the liquid penetrant with either water or with dust particles tends to increase the contact angle between the solid surface and the penetrant, as both water and dust have higher surface energies than the penetrant itself.

The equations for a liquid in equilibrium indicate that, depending upon the surface chemistry and topology a liquid with contact angle, θ, may prefer to bridge a gap in the material rather than penetrate into it.

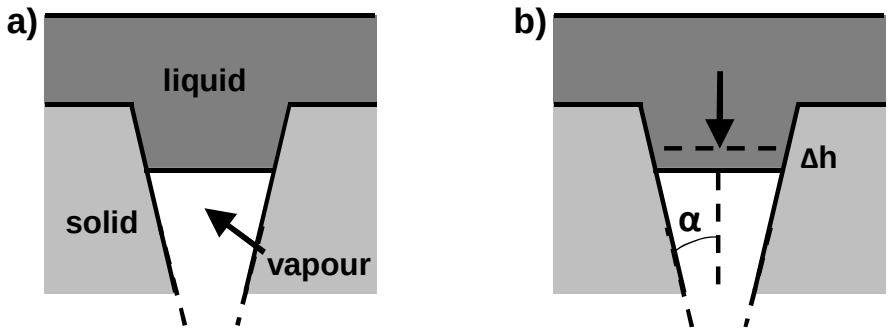

Figure 17. Penetration of liquid into simple wedge with angle α.

The critical contact angle for the liquid to penetrate into some simple surface geometries can be derived. To fill a wedge with perfectly smooth walls as shown in Figure 17:

$$\Delta E = 2(\gamma^{SL} - \gamma^{SG})\frac{\Delta h}{\cos\alpha} - 2\gamma^{LG}\Delta h \tan\alpha \qquad (3.20)$$

Penetration is favoured when ΔE<0:

$$0 > \frac{\gamma^{SL}-\gamma^{SG}}{\gamma^{LG}}\frac{1}{\cos\alpha} - \tan\alpha \quad (3.21)$$

$$0 > \frac{\gamma^{SL}-\gamma^{SG}}{\gamma^{LG}} - \sin\alpha \quad (3.22)$$

Substituting Young's equation (Equation 3.8), penetration will occur when the contact angle, θ, is less than a critical value, $\theta_{critical}$:

$$\cos\theta_{critical} = \sin\alpha \quad (3.23)$$

If the walls are parallel (α=0°), a wedge will fill for any contact angle below 90°. Cracks have near parallel faces and the crack width (separation between the crack faces) is much smaller than the depth. This model is two-dimensional. Real surface features, such as surface-breaking cracks, are three-dimensional. Real surface features do not have perfectly smooth faces, so the critical angle for penetration will vary along the depth. Roughness may lower the effective contact angle of the liquid and so encourage spreading and penetration into the defect. Alternatively the contact line could become pinned at some local feature, impeding penetration of the liquid into the feature.

Gas trapped in defects may resist the entry of liquid into a crack. The ASNT NDT Handbook [21] derives an equation for the smallest crack width that will be infiltrated by liquid penetrant. The derivation assumes that a film of penetrant on the surface traps air inside a crack, as shown in Figure 18. As penetrant enters the crack the trapped gas becomes compressed. When the capillary pressure is balanced by the pressure of the trapped gas, no more penetrant is able to enter.

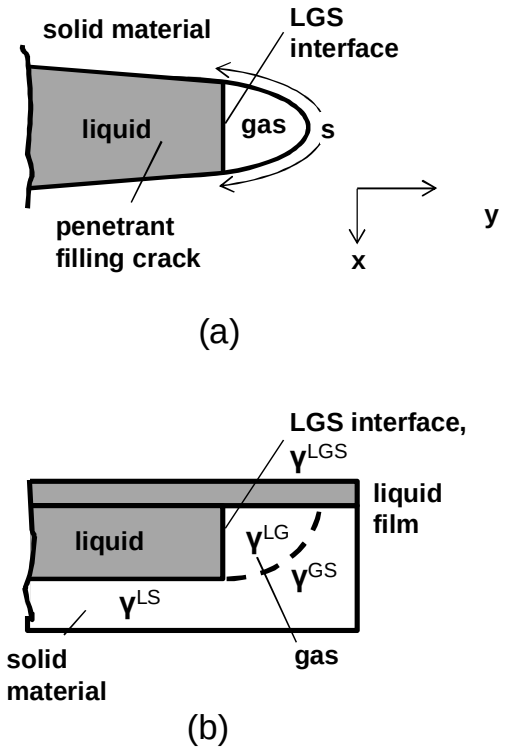

Figure 18. Penetrant within crack during formation of entrapment a) top view b) side view. Eventually the pressure of the air trapped in the crack tip balances the capillary pressure. LGS stands for liquid-gas-solid. After ASNT NDT Handbook [21].

The final position, *y*, of the liquid at the solid-liquid-gas interface occurs when the energy change for a surface element *ds* moving *dy* is zero:

$$2(\gamma^{SG} - \gamma^{SL})ds - 2(P - P_0)xdy = 0 \qquad (3.24)$$

where *s* is the perimeter of the solid-liquid-gas interface within the crack, *P* is the final pressure of the gas in the crack tip per unit depth, P_0 is the initial gas pressure (atmospheric), *x* is the width of the interface per unit depth, *y* is the position of the interface along the crack length, *ds*/*dy* is the rate of change of perimeter areas with the motion of the interface along *y*, γ^{SG} is surface energy of the solid-gas interface, γ^{SL} is surface energy of the solid-liquid interface.

The change in gas pressure is equal to the capillary pressure, P_c:

$$P_C = P - P_o \tag{3.25}$$

Assuming that the sides of the crack are perfectly smooth then substituting Young's equation:

$$(\gamma^{LG} \cos\theta) ds = P_c x dy \tag{3.26}$$

The critical crack opening is then:

$$x_c = \{(\gamma^{LG} \cos\theta)/P_c\}(ds/dy) \tag{3.27}$$

By substituting ds/dy =3 (value for a spherical pore), γ_L =0.1N/m , θ=0° and P_c=10^5 N/m^2 (atmospheric pressure) the ASNT handbook calculated a limiting pore diameter of 3μm.

Only Clark et al [6] have explicitly studied the effect of crack closure on the reliability of a liquid penetrant process. They progressively increased the compressive load across a crack during processing, causing the crack faces to come closer together, and compared the length of the developed penetrant indication to the actual length of the crack. They found that the sizing reliability decreased with an increasing compressive load until the crack could no longer be detected using the selected penetrant process.

Conflicting opinions exist about whether the crack size affects the rate at which penetrant is drawn into the crack and therefore the POD for a specific dwell time. Prokhorenko and Migun [39] suggest that the rate is dependent upon numerous factors including the distance between the flaw walls. Deutsch [40] derives the following equation for fill time of an elliptical void:

$$\text{Fill time} = \frac{2l^2\mu}{\gamma^{LG}\cos\theta}\frac{a^2+b^2}{(a+b)ab} \tag{3.28}$$

where l is the defect depth, μ is the dynamic viscosity, γ^{LG} is the liquid-gas surface tension, θ is the contact angle and a and b are the flaw width and

length respectively. Substituting the liquid penetrant properties: μ=0.008232Ns/m^2 [41], γ^{LG}=0.1N/m [21], θ=0° [21]; and the crack dimensions: a=1µm, b=2mm, l=1mm, gives a fill time of 0.165s. Increasing the crack width decreases the fill time. Typically the penetrant is left to dwell on the component surface for between 10 and 60 minutes. The industry perception is that both the background and defect indications become brighter as dwell time is increased. The ASNT Handbook [21] states that even relatively tight cracks fill practically immediately.

The liquid penetrant will enter surface features other than the defect. The penetrant will bleed back out onto the surface of the component, reducing the contrast between any defect indications and this 'background'. If the surface holds a lot of penetrant then this background could entirely mask a defect indication. Rough surfaces typically hold more penetrant than smooth ones and so the background is brighter. To minimise this problem, penetrants with higher contact angles are used that are less likely to penetrate the surface features. The background is reduced but so is the sensitivity of the penetrant to defects. Inspectors must trade-off between contrast and sensitivity when deciding what liquid penetrant to use.

In summary, the literature reviewed indicates that some surface contaminants can lower the contact angle and so promote spreading and penetration of surface features. However, if a fatigue crack is full of solid contaminants then no liquid will be able to enter. If a fatigue crack is full of liquid contaminants then these would have to be displaced by the liquid penetrant, which will depend upon the chemistry of the two liquids. For this

project it is therefore important to use defects that are known to be free of contaminants and that can be cleaned between successive inspections.

The two-dimensional wedge model indicates that liquids with low contact angles are likely to penetrate surface features with near-vertical walls. The model presented in the ASNT NDT handbook [21], where trapped air resists the penetration of liquid into the crack, suggests that there is a minimum crack width below which no liquid will enter. Neither model accounts for the roughness of the surface or of the crack faces. Wetting theory indicates that, in general, surface roughness can promote spreading. However, in some cases contact line pinning will occur, which will impede spreading and penetration of the defect. An external force is required to overcome local metastable states.

3.2.4 Factors affecting bleedout of liquid from a surface-breaking crack

The equilibrium equations for a two-dimensional wedge (Equation 3.23) suggest that liquid with low contact angles will enter and remain in a surface breaking feature. However, spontaneous bleedout, where the liquid flows from the surface feature onto the surface after penetrant processing, is commonly observed. Spontaneous bleedout is also referred to as self-development, as an indication forms without the use of a powder or solvent-based developer. The ANST handbook [21] and the literature on penetrant processing do not discuss the mechanisms for self-development in any detail. The ASNT handbook instead focuses on the ‘efficiency’ of a penetrant entrapment or the amount of liquid which, having entered the crack during

dwell, remains during water washing and emulsification to bleed back out onto the surface.

The penetrant process for high sensitivity post-emulsifiable penetrants is complex. After leaving the penetrant to dwell for a period of time, the surface film is actively removed by scrubbing the surface with water. An emulsifier is then applied to the surface, which will further remove penetrant by a detergent process. Components are then dried, using an air gun to remove most of the liquid from the surface and then by heating in an oven at up to 70°C for one hour. Using this process, spontaneous bleedout has been observed on the cracked samples used in this study. The application of a solvent developer caused further bleedout and an increased brightness of the indications. Spontaneous bleedout could be caused by one or a combination of these steps: by chemical gradients introduced by the miscible emulsifiers, by the scrubbing action of the water spray, by the pressure fluctuations caused by the air gun or by evaporation of the penetrant carrier fluid during drying. These effects have not been modelled or investigated rigorously.

Substantial research into the effects of chemical and thermal gradients on droplet mobility [42] has been carried out in the field of microfluidics (laboratories on a chip or chip manufacturing processes). A sufficiently high chemical gradient will cause droplets to move uphill [43]. Thermal gradients have two effects [44, 45]. The droplet will want to move towards the area of lower surface energy (the cold region). However, due to the temperature dependence of surface tension, Marangoni flows will also be induced within the droplet, which will drive it in a particular direction. Due to the combination of these two effects, motion has been observed both from hot

to cold surfaces and vice versa [44]. Motion of a droplet on a surface is a far simpler system than that of penetrant inspection, which has multiple process steps and various chemicals.

To summarise Sections 2.3.3 and 2.3.4, liquid may not infiltrate the crack if:

- the crack faces are in contact or if there is some surface contaminant blocking penetration;
- some dimension of the crack does not exceed the threshold for wetting (similar to the minimum radius for penetration of liquid into a capillary);
- air trapped in the crack resists penetration;
- contact line pinning occurs;
- the dwell time of the penetrant on the surface is insufficient, although the literature indicates that this last is highly unlikely.

Penetrant that has entered the crack may be depleted during washing and emulsification. Spontaneous bleedout is known to occur for some defects but the factors affecting spontaneous bleedout are not well understood. The crack may not be detected if the indication is small compared to background indications or if the film thickness is so low that the dimensional threshold for fluorescence is not exceeded. The evidence suggests that cracks with larger volumes are more likely to develop visible indications but if they are wide and shallow they will also be susceptible to overwashing.

3.2.5 Vibration to enhance wetting and dewetting

The second aim of this project was to investigate vibration as a means of enhancing the reliability of fluorescent penetrant inspection. The original premise of the project was that, by actively opening the crack, the volume of penetrant entering would be greater and therefore the probability of developing a detectable indication would increase. In the field of wetting, vibration is used to overcome contact line pinning. When the contact line is 'pinned' the solid-liquid-vapour interface remains fixed even if, for example, the droplet lies on a slope, thereby inhibiting flow (Section 3.2.2). Examples of where vibration has been used to enhance fluid mobility and specifically wetting and dewetting of entrapments are described here.

In Section 3.2.2 contact angle hysteresis was described, whereby the contact line becomes pinned due to local changes in surface roughness or chemistry. Several researchers have used vibration to overcome hysteresis on rough and chemically heterogeneous surfaces and thereby obtain a value for the contact angle predicted by Young's equilibrium equation (Equation 3.8). The vibration provides the energy required to overcome the energy barriers, allowing the liquid to probe all possible contact angles. Two methods have been adopted. The first is to place a droplet on a sample and then vibrate the sample either vertically or horizontally by coupling it to a loudspeaker membrane. The contact angle can be measured directly (using optical methods [46]) or indirectly (by measuring the drop diameter and weight and then calculating the contact angle [47]). The second method is to use a Wilhelmy balance. The height that a liquid rises up a sample from a reservoir is measured and so the contact angle is found. Either the sample [48] or the reservoir (liquid in a beaker) can be vibrated [33]. Most authors use a

continuous excitation but Decker and Garoff [48] imparted a train of pulses to the sample and observed the evolution of the contact angle. The frequencies used have varied from 30 to 800Hz.

If the vibrational energy used is large enough then the liquid contact line will move forward and backward on the surface [49, 50]. If the applied inertial force is asymmetric [43, 51] or there is a surface energy gradient then mobility of a droplet can be induced. Roughness gradients [52] or ratchet topologies are also used but combined with an external actuation [53, 54] to overcome energy barriers inherent in a rough surface. External actuation can increase droplet velocity. The actuation may be vibration [51-53, 55, 56], but electrostatic attraction [53, 54, 57-59] and a pressure differential [57] have also been used.

Figure 19. Simulated first four modes of vibration of a water droplet. After Dong et al [51].

Much of the work on the vibration of droplets on hydrophobic or gradient surfaces has shown that the amplitude of droplet oscillation or the droplet velocity depends upon the frequency as well as the amplitude of vibration [49-51, 56] i.e. there is some resonance effect. The resonant frequency of a droplet will vary with its mass and radius. A droplet has many modes of vibration (Figure 19). Excitation of one mode may result in motion in one direction, while excitation of another mode could cause the droplet to move in the opposite direction [51].

Extensive work, reviewed by Hamida and Babadaglia [60], has also been carried out on the subject of mechanical excitation to encourage drainage of porous oil reservoirs. Various researchers had shown an increase in oil yield. Various modes of excitation were used with a frequency range 40Hz to 5.5MHz. Unfortunately, the mechanisms and their interactions are not yet fully understood: 'squeezing', perturbation of local pressures, reduced surface tension density and viscosity as a result of liquid heating by ultrasonic radiation and nonlinear effects, such as cavitation, were listed by Hamida and Babadaglia, amongst others.

Recognising that a certain capillary pressure is required before liquid will enter into very narrow capillaries, Nakanishi et al [61] applied an external pressure to encourage penetration of molten aluminium into alumina capillaries 0.8mm in diameter. This did give improved penetration but the aluminium did not spread along the full length of the capillary. They found that complete penetration could be achieved if an ultrasonic horn was used instead. They used a frequency of 20.5kHz and power of 500kW/m^2. This indicates that it could be possible to make penetrant enter even narrower cracks by sending an ultrasonic wave through the liquid.

In summary, vibration of the sample may encourage bleed out by actively squeezing penetrant out of the crack during the compressive part of the cycle. Vibration of the wetted surface may enhance the wetting behaviour of the penetrant, by changing the surface energy at the liquid-solid interface (or contact line). Penetration of liquids into defects could also be improved by sending sonic or ultrasonic waves through the liquid.

For this project, it was decided to excite the sample, rather than the liquid, causing the crack to open and close in a clapping mode. The dynamic cross-crack strains could then be directly related to the crack width and volume.

4. Crack Propagation

4.1. Sample and Fixture Design

In the assessment of the reliability of a real non-destructive evaluation technique [10], the samples and target defects should be representative of the actual component and real defects. Geometry, material, part processing, surface condition and the characteristics of the target defect must all be taken into account. This project was interested in the effect of crack width on the reliability of the fluorescent penetrant inspection (FPI) and so all other variables were kept constant where possible. The following considerations were made in selecting the sample geometry and the method for generating the defects:

- **Real fatigue cracks vs. notches.** Spark eroded notches are commonly used for the validation of ultrasonic and eddy current NDE methods. Notches are difficult to generate with widths less than ~10µm. Fatigue cracks with widths as low as ~0.5µm were observed during the course of this project. Notches are not expected to open and close in the same way as real fatigue cracks upon the application and removal of load. For these reasons it was decided to generate samples containing real fatigue cracks.
- **Fatigue crack aspect ratio**. Fatigue cracks can have almost any aspect ratio, depending upon the stress distribution in the component during crack propagation. Shallow and deep cracks will behave differently under applied load. In this project, the aim was to keep a constant length-to-depth aspect ratio of 2:1.
- **Surface finish**. Rougher surfaces retain more penetrant, making it more difficult to separate the 'background' from indications due to

defects. The highest sensitivity penetrant is only used on components in their final machined state, when the surface roughness is better than 1.6µm Ra. Machining processes can introduce residual stresses that can be relieved by cyclic loading and propagation of a crack in the surface. All samples should have the same ground surface finish of 1.6µm Ra.

- **Neutral surface.** This implies that the surface is clean and has not been machined after generating the fatigue crack. There were concerns that machining would cause metal to be smeared across the crack, which would prevent the liquid penetrant entering.
- **Part geometry.** The samples should be easy to load either statically or dynamically, so causing the fatigue crack to open or close.
- **Automatic detection**. The intention was to image the sample and then use image processing to detect real crack indications. The aim was to produce a crack on a flat surface away from corners, so that it could be imaged easily.

Two options were considered for generating fatigue cracks: loading on a tensile test rig or thermal cycling, using a method patented by TrueFlaw. The thermal method has the advantage that cracks can be produced in almost any geometry. However, the method is expensive and the cracks produced are wide compared to fatigue cracks.

Figure 20. Photograph of rectangular bar sample (130x7x21mm), showing the hemispherical dimple in the rear face. Cracks were generated on the face opposite the hemispherical dimple by cyclically loading the samples in 3-pt bend on a resonance fatigue rig.

The samples selected were rectangular cross-sectioned bars cut from a sintered nickel alloy disk (Udimet 720Li) with a hemispherical dimple machined in the back face (Figure 20). The material properties are proprietary to Rolls-Royce plc. A technical drawing is included in Appendix A. Long thin bars (130x7x21mm) were chosen as they can be loaded easily, causing a crack to open, both statically and dynamically. By clamping the bar at one end and by exciting at the clamp at the natural frequency, the bar can be caused to resonate, generating high strains with relatively little energy input.

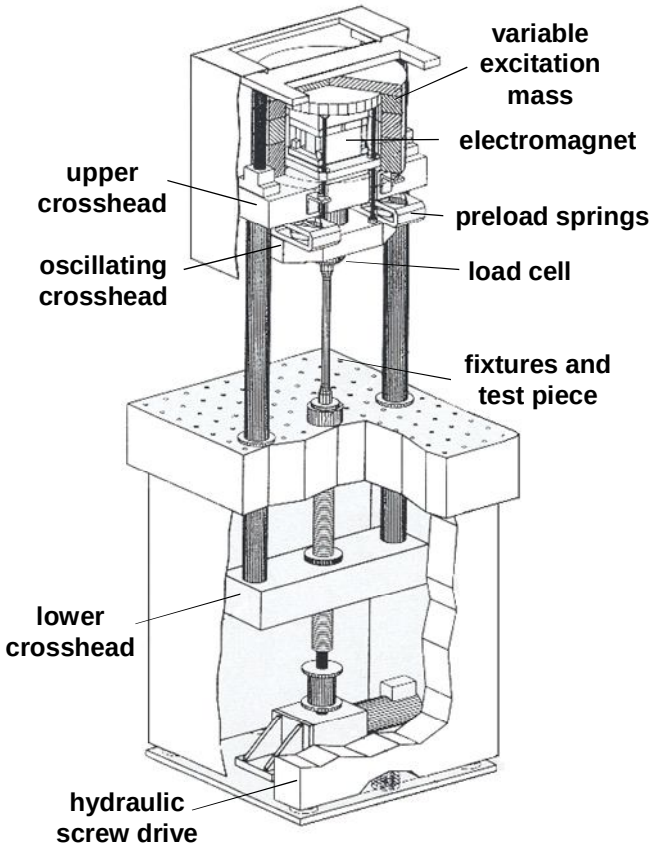

Figure 21. Schematic of Amsler Vibrophore showing hydraulic screw drive for application of the static load and electromagnet and springs for application of the dynamic load. After Amsler [62].

Cracks were generated by cyclically loading the bars in three-point bend on an Amsler Vibrophore [62] - a resonance rig for high frequency (~100Hz)

cyclic loading is shown in Figure 21. A static load is applied by an hydraulic screw drive. The dynamic load is generated by an electrodynamic shaker and transmitted to the sample through the fixtures. The frequency of excitation can be tuned to find the resonant frequency of the system. The applied dynamic and static load applied to the fixtures is monitored by a load cell.

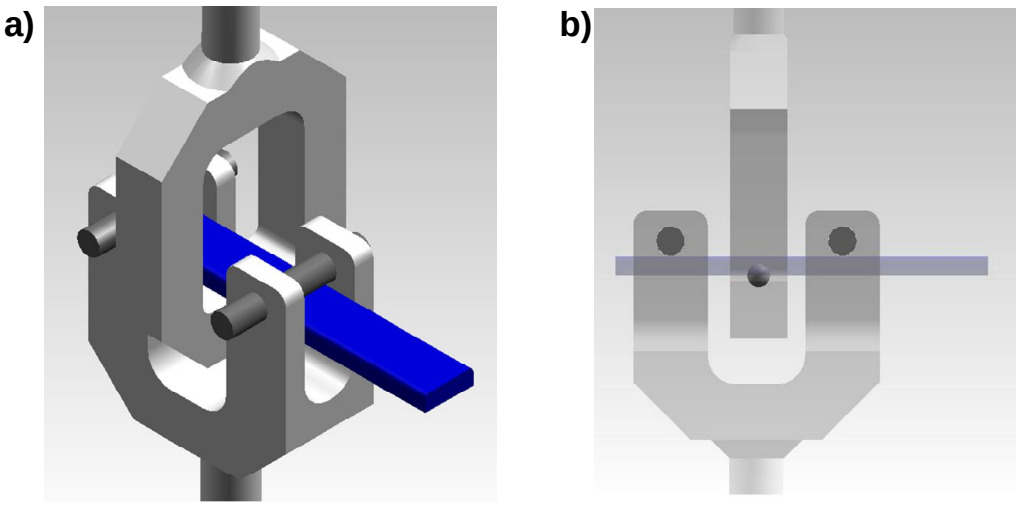

Figure 22. Fixtures used in the Amsler Vibrophore resonance machine for crack propagation a) isometric view b) side view with fixtures rendered semi-transparent to show three-point bend supports.

During cyclic loading, the sample is supported by two roller supports and a 6mm ∅ ball bearing, which locates into the 8mm ∅ hemispherical dimple in the large flat face of the sample (Figure 22). Technical drawings for the fixtures are included in Appendix B.

A static finite element analysis was carried out in ABAQUS [63] in order to determine the stress distribution during cyclic loading. First a plane rectangular-ended bar was modelled. The bar was simply supported in three positions. The results of the model were validated using bending theory and agreed well. The hemispherical dimple was then incorporated into the model geometry. The roller supports were simulated by simple supports along two

lines of nodes. The ball bearing loading was simulated by applying a pressure equivalent to a total force of 1N to a small area in the apex of the hemispherical dimple. Contact forces between the rollers or ball bearing and the sample were not modelled. The results are shown in Figure 23. The three-point bend configuration ensures that the bending stress (or component of stress along the axis of the bar, S33) is highest at the central support. The dimple produces a stress concentration causing cracks to initiate on the opposite flat surface, rather than on a corner. Cracks were expected to initiate in the high stress region on the flat face opposite the hemispherical dimple and propagate across the bar (perpendicular to the longitudinal axis).

Alternative sample geometries were considered, such as a spot weld or notch that would act as a starter feature for a fatigue crack; however, only the hemispherical dimple allows a fatigue crack to be generated in an as-machined face, without any subsequent machining to remove the starter feature.

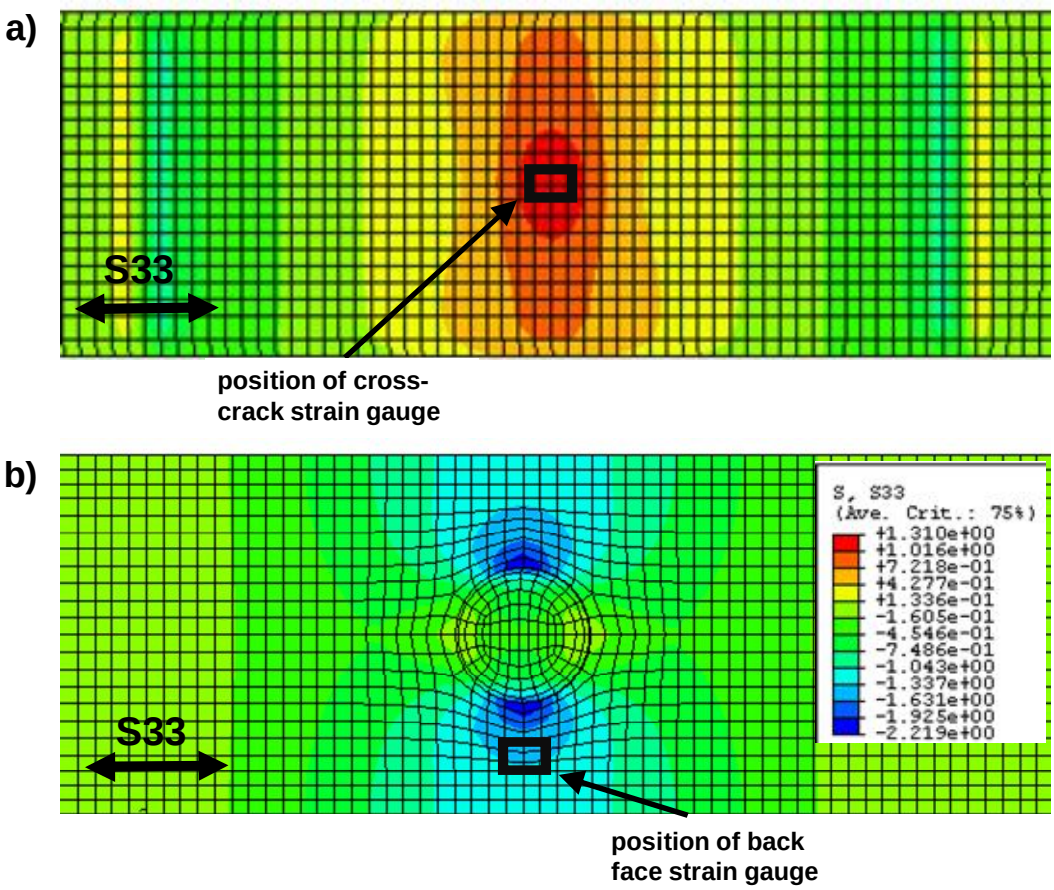

Figure 23. Results of static finite element analysis carried out in ABAQUS [63] for sample geometry loaded in three-point bending, showing the stress component in the direction parallel with the longitudinal axis of the bar, S33. Roller supports were simulated by constraining the positive vertical displacement. The load from the ball bearing was simulated by applying a pressure to a small area in the apex of the hemispherical dimple. The total applied load was equal to 1N. a) the top and b) bottom of the sample. Foil strain gauges were fixed to a sample during cyclic loading in the two positions indicated here: in the highest stress position on the front face (cross-crack), which corresponds to the position of crack initiation, and next to the hemispherical dimple on the back face.

4.2. Crack Propagation and Detection

A static or mean load of 5kN was applied. Foil strain gauges with a 2mm gauge length and 350Ω gauge resistance were fixed to the sample on the large flat face opposite the hemispherical dimple and on the back face next to the hemispherical dimple, in the positions shown in Figure 23. $\varepsilon_{min.}/\varepsilon_{max}$

measured by both of the strain gauges was 0.92. Assuming that the stress-strain relationship is linear, then $\varepsilon_{min.}/\varepsilon_{max}$ is directly proportional to the stress *R*-ratio (Equation 3.7).

The samples were initially cycled for 10^5 cycles. Then, every 2000 cycles, the cyclic load was interrupted and the samples were inspected to detect cracks. The disadvantage of this sample design is that, without a starter feature, the time to crack initiation is highly variable and, without an online method of monitoring for initiation, catching the crack when it is still short is difficult. Furthermore, multiple cracks can initiate in these samples. The number of initiation sites can be limited by fatiguing the specimen for a very high number of cycles at a low mean stress. However, in this high endurance regime, the variability in time to crack initiation becomes even greater.

Cracks were expected to initiate in the high stress region on the flat face opposite the hemispherical dimple and propagate across the bar (perpendicular to the longitudinal axis). Several methods for detecting short cracks in this position were investigated including acetate and rubber replica, penetrant, eddy current and in situ microscopy. A combination of visual inspection and surface acoustic waves proved to be the most effective method for finding short cracks. If the light incident upon the metal surface is at the right angle then even small cracks in a sample covered in scratches are apparent. With the sample still loaded statically, a 10MHz 0.25" Ø ultrasonic surface wave probe was placed on the longer end of the sample. When load is applied, sound passes into the roller as well as along the bar. The supposed path of the surface waves from the probe to the crack is shown in Figure 24, along with the ultrasonic A-scan. Each peak in the A-

scan corresponds to one rotation of the surface waves around the roller. The roller circumference is almost identical to the distance between point of contact of the roller with the sample and the crack (30mm). Any response from the crack therefore increases the amplitude of the third peak in the A-scan. This response can be damped by pressing on the surface of the bar between the roller and the crack. If a crack is present, a decrease in the amplitude of the third peak is observed. Using this method a crack 0.36mm long was found.

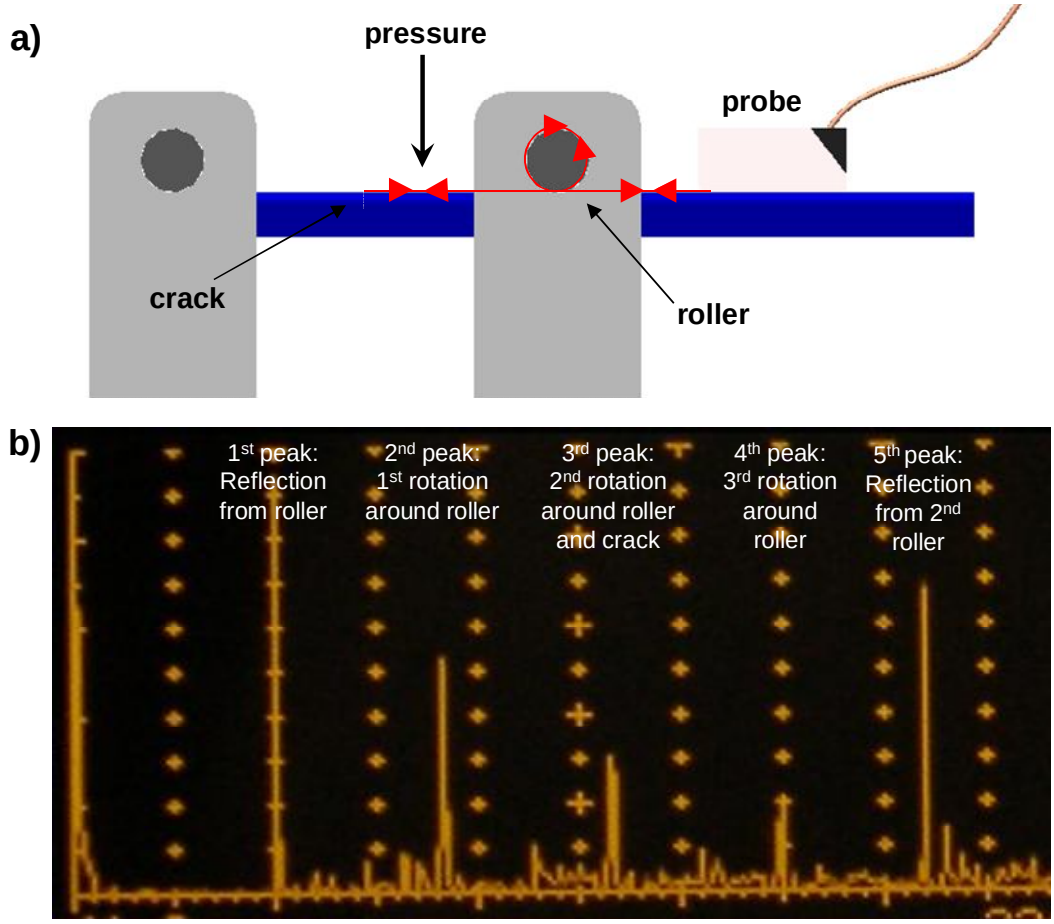

Figure 24. a) To detect cracks, cyclic loading was paused at intervals and the sample was inspected using a 10MHz 0.25" ø surface wave probe. The supposed path of ultrasound between the probe and the crack is shown by the red arrows. b) For an uncracked sample, the peaks in the ultrasonic A-scan correspond to the reflection from the point of contact between the first roller and the sample or sound that has travelled around the first roller and returned to the probe. The fifth peak is the reflection from the point of contact between the second roller and the sample. By coincidence cracks initiate so that the reflected signal corresponds with the 3rd peak. When a crack is present, the amplitude of the 3rd peak can be changed by applying pressure over the position of the crack, which damps the reflection from the crack.

4.3. Characterisation of Cracks: Length and Aspect Ratio

The conventional way of expressing the reliability of a penetrant process is to calculate the threshold detectable crack length $a_{90/95}$ that can be detected 90% of the time with 95% confidence (see Section 2.6). To determine $a_{90/95}$, a curve linking probability of detection to crack length, *a*, must be generated. Samples containing fatigue cracks of a range of lengths are required. The length range should cover the transition from low to high probability of detection. According to the current issue of the U.S Department of Defense Military Handbook [10] on the assessment of the reliability of NDE systems, in the 1980s "consensus was that target sizes should be uniformly distributed on a log scale covering the expected range of increase of the POD(*a*) function". Now the handbook recommends that more realistic curves and tighter confidence bands are obtained if the crack lengths are distributed equally over the expected range of increase of the POD(*a*) function. The handbook also recommends that more samples are concentrated at the expected value $a_{90/95}$ and that a minimum of 60 cracked samples are generated.

Generating 60 cracked samples was unrealistic within the timescales of this project. The aim of the project was to investigate the effect of a single variable – the crack width - on the reliability of the penetrant process. The method used was to open the crack mouth by incrementally increasing the applied load and to process and inspect the samples at each load increment. Therefore a baseline (zero load) $a_{90/95}$ would be established. The $a_{90/95}$ at each load increment could then be compared to the baseline value. It was decided to aim for around 10 cracked samples, covering the length range of interest. The target crack length range was driven by two criteria:

1. To generate cracks around the detection threshold of the highest sensitivity fluorescent penetrant process used in the aerospace industry;
2. To generate cracks that the automatic detection method did not always find.

The automatic detection method always detected cracks longer than 5mm. Cracks shorter than ~1mm were frequently missed. The default design criteria used by Rolls-Royce plc is that an NDT processes will achieve a reliable inspection on an engineering crack, which is 0.030" (0.76mm) long by 0.015" (0.38mm) deep. In other words, Rolls-Royce plc requires that its highest sensitivity penetrant process will achieve an $a_{90/95}$ of 0.76mm.

In total, fourteen cracks were generated. One sample contained multiple cracks. Another sample was damaged and so could not be used. The remaining twelve samples were used in the reliability studies. The crack lengths were measured by imaging the samples under calibrated binocular microscopes at 200X magnification. This magnification allowed the crack tip to be resolved. The binocular stage was moved incrementally along the length of the crack and a series of overlapping images were taken. These images were then stitched together as shown in Figure 25, to allow the total crack length to be measured. Two lengths were measured (Figure 25): the shortest distance between the crack tips, $a_{tip\text{-}to\text{-}tip}$, and the full length of the crack surfaces, following the shape of the crack, a. The twelve samples contained cracks with lengths $a_{tip\text{-}to\text{-}tip}$ in the range of 0.36mm to 16mm, with five of the cracks shorter than 1mm in length. A list of the crack lengths and sample serial numbers is included in Table 1.

Table 1. Crack lengths for twelve samples used in penetrant reliability studies.

	Sample serial number	Crack length, *a* (mm)	Crack length, $a_{tip\text{-}to\text{-}tip}$ (mm)
1	VE013	0.37	0.36
2	VE014	0.51	0.50
3	VE017	0.57	0.51
4	VE012	0.72	0.68
5	VE005	0.93	0.84
6	VE018	1.26	1.17
7	VE016	3.19	3.04
8	VE003	4.89	4.57
9	VE004	5.01	4.64
10	VE009	7.46	7.00
11	VE008	8.50	7.87
12	VE002	16.76	16.04

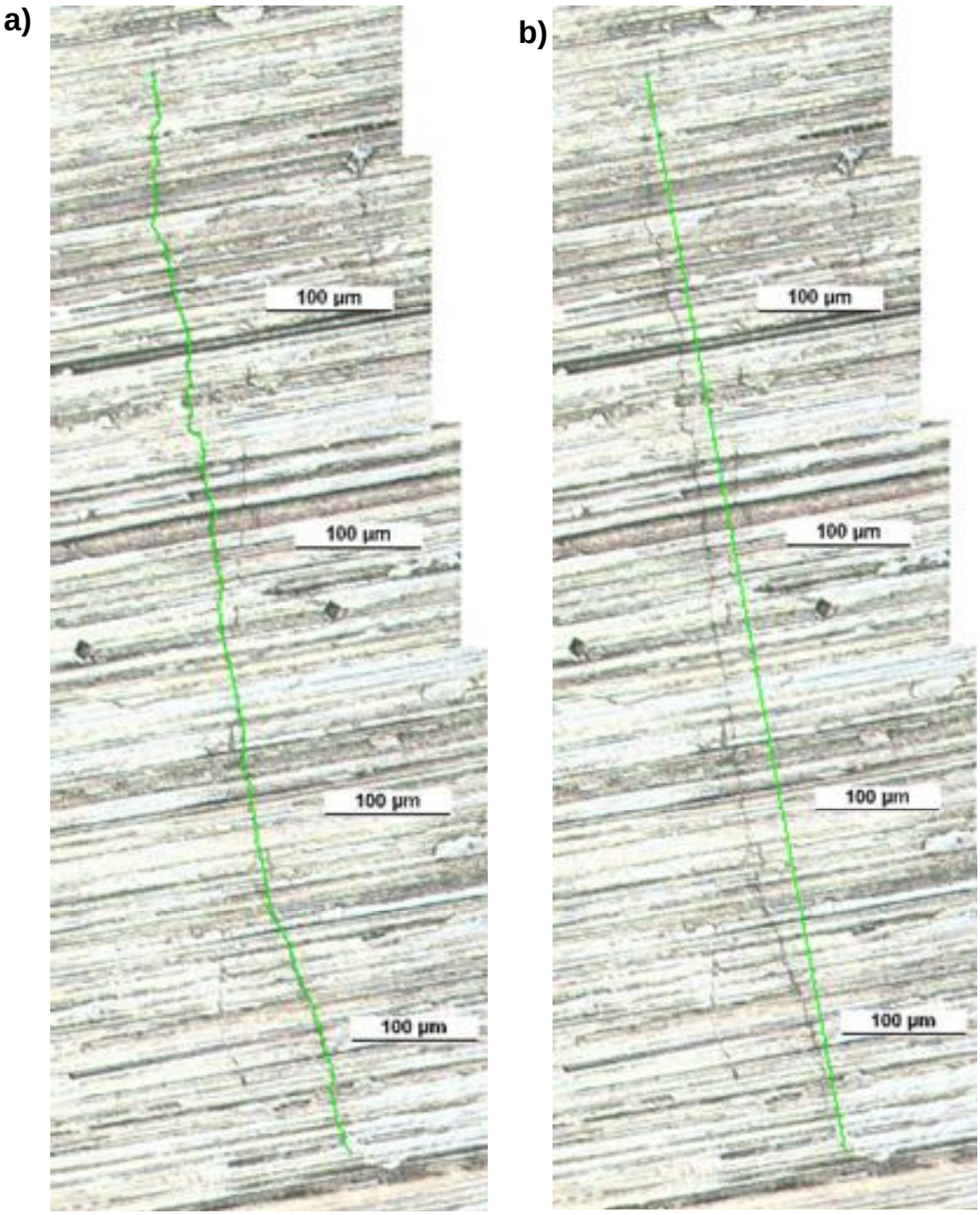

Figure 25. A series of images were taken under a binocular microscope at 200X magnification. These were then stitched together so that the total crack length could be measured. The measurement was made in two different ways. a) following crack shape, *a*. b) the shortest distance between the crack tips, $a_{tip\text{-}to\text{-}tip}$.

The damaged sample, which contained a crack $a_{tip\text{-}to\text{-}tip}$=1.44mm, was broken open to reveal the fracture surface shown in Figure 26a. It has a length: depth aspect ratio of 2:1. After the penetrant testing, a longer crack ($a_{tip\text{-}to\text{-}tip}$=7.87mm) was also broken open. The fracture surface is shown in Figure

26b. This crack has extended further laterally and has an aspect ratio of ~ 3:1.

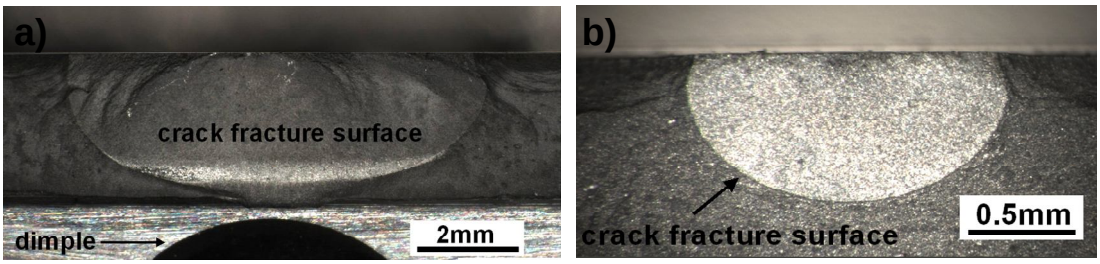

Figure 26. Fracture surfaces of a) a 1.44mm long crack in damaged sample b) a 7.87mm long crack.

5. Measurement of Crack Mouth Width with Applied Load

Penetrant reliability is probably dependent upon both the width of the crack and upon the total crack volume (see Section 3.2). The aim was to monitor how the crack width changed upon the application of load. Ideally, the width at all points along the depth and length of the crack would be measured. However, this was not feasible within the cost constraints of this project. The adopted method measured the change in width of the crack mouth at the surface with the application of load.

This section briefly reviews possible methods for the measurement of crack width and volume (Section 5.1). The adopted method is then described with results for seven of the twelve cracks (Section 5.2).

5.1. Methods for the Measurement of Crack Width

Twelve samples containing surface-breaking fatigue cracks were generated for this project (Section 4.3). The width of these fatigue cracks at the surface (the crack mouth) was initially determined by measuring the distance between the crack edges under a scanning electron microscope (SEM). The crack openings were between 400nm and 2μm. Upon loading this increased to as much as 20μm. The adopted technique must therefore have a resolution of at least 1μm.

Most of the experimental measurement of crack closure has been carried out in the field of fracture mechanics [5]. The main aim for researchers in this field is to measure the applied stress at which the crack tip is fully open, as

this is related to the threshold stress for crack propagation (Section 3.1). Stoychev and Kujawski [64] carried out a comprehensive literature review on measurement methods. They grouped experimental techniques into direct and indirect methods.

Direct methods include optical measurements [65-69], interferometry [70, 71], full-field strain measurements [72, 73] and radiography [74]. Interferometry techniques have the highest resolution but the set-up is tricky and often a laser light source is needed. A major limitation of most of the direct techniques is that the through-thickness crack closure of thumbnail cracks cannot be observed for opaque materials. Only radiography has the potential to achieve this and the resolution is not normally sufficient. Khor et al [74] carried out tomography using a synchrotron X-ray and claimed a voxel resolution of 0.7μm. However, in order to achieve this, the samples had to be 1mm^2 in cross-section.

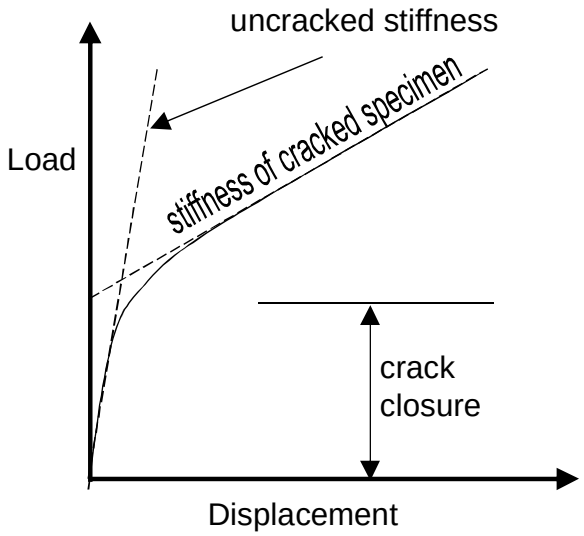

Figure 27. Load vs. displacement curve for a crack, which has a residual compressive stress holding the crack tip closed at zero load. The crack opening load can be determined by finding the point where the gradient of the curve changes. After Anderson [5].

Indirect methods include caustics, compliance measurements and non-destructive techniques, such as ultrasonics. Only the out-of-plane displacement can be measured with caustics [75]. The method can be used to directly measure the stress intensity at the crack tip but not the crack opening. Compliance methods measure displacement or strain as a function of applied load. If the crack is held closed by residual compressive stresses, load can be transmitted across the crack faces. The stiffness is then that of an undamaged specimen. If the crack is fully open then the stiffness will be lower. The crack opening load can therefore be identified from the change in gradient of the load-displacement graph (see Figure 27). The various compliance methods are illustrated in Figure 28. The crack width can be measured with crack mouth clip gauges [65, 70, 72, 76-80], push gauges parallel to the crack planes [81] or strain gauges during either static [65, 70, 72, 80, 82] or dynamic [83, 84] loading. The strain gauges can be positioned near the crack tip (called near-tip strain gauges) or on an uncracked face (back face strain gauge) [14, 85-87].

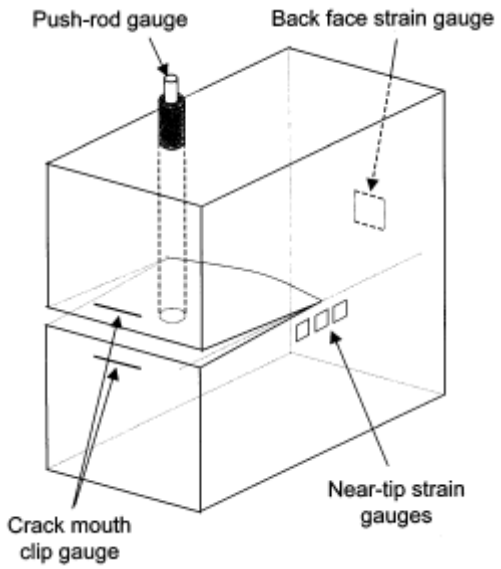

Figure 28. Mechanical compliance measurement methods. After Yigeng Xu et al [20].

The effect of crack closure on the sensitivity of ultrasonic techniques is two-fold. For a closed or partially closed crack the proportion of the incident ultrasonic wave that is reflected is reduced due to the transmission of energy across the contacting faces. A closed crack can be almost transparent to an ultrasonic beam [88, 89]. However, the crack also causes a non-linear stress-strain response. This can cause the generation of upper harmonics of an incident acoustic wave [90]. Furthermore, if the cracked specimen is simultaneously subjected to two different frequencies (e.g. a low frequency vibration and an ultrasonic wave), then the non-linearity will cause the high frequency wave to be modulated in amplitude and/or phase by the low frequency or 'pump' wave [91]. While ultrasonic techniques are clearly sensitive to crack closure, they are not a direct measurement. The linear methods (reflected or transmitted amplitude of the ultrasonic wave) may be misleading if, for example, there is some contaminant in the crack i.e. an acoustically open crack may not be the same as a mechanically open crack [92]. Once the crack is fully closed or fully open, no further information can be gained from ultrasonic methods.

With the resources available to this project, the most practical methods of measuring the crack closure are the compliance methods and direct observation. They are simple and have no related health and safety implications. Compliance techniques have the advantage that they give some information on the average closure load for the whole crack rather than just the closure at the surface. Back face and crack-tip strain gauges (Figure 29) were used to measure the compliance of a sample containing a 4.57mm long crack. However, the non-linearity in the load vs. displacement curve was not measurable, suggesting that the compliance of the bar was not significantly

affected by the presence of this relatively long crack. An optical method for measuring the variation of the crack closure with applied load was adopted. The method only gives information about the crack mouth opening at the surface and the resolution is limited, as will be discussed in the following section.

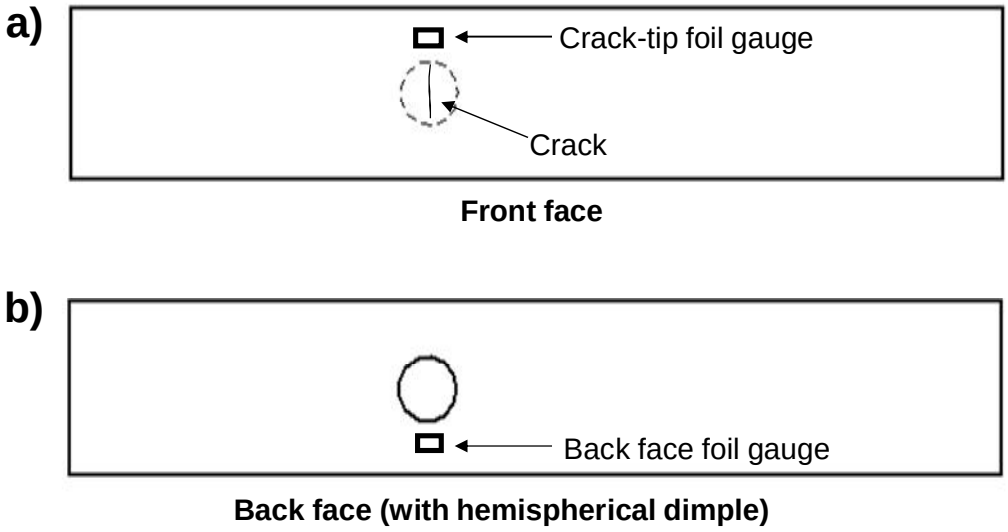

Figure 29. Schematic of sample with hemispherical dimple showing the typical position and orientation of a surface breaking crack and the positioning of back-face foil gauge and crack-tip foil gauge, which were used to measure the compliance of the cracked sample.

5.2. Adopted Method for the Measurement of Crack Width

An optical method for measuring the variation of the crack mouth opening with applied load was adopted. To provide marker points on the specimen, the distance between which could be measured accurately, indents were made either side of the crack between 75μm and 100μm apart and halfway along its length using a Vickers hardness indenter. A second set of indents was made in line with these, but distant from the crack, 5mm from the edge of the sample. A Vickers hardness indenter makes indents with diamonds the shape of a square-based pyramid, the apex of which has a nominal angle of 136°. The diagonal of the indents in the samples was around ~20μm. The indent positioning is illustrated in Figure 30.

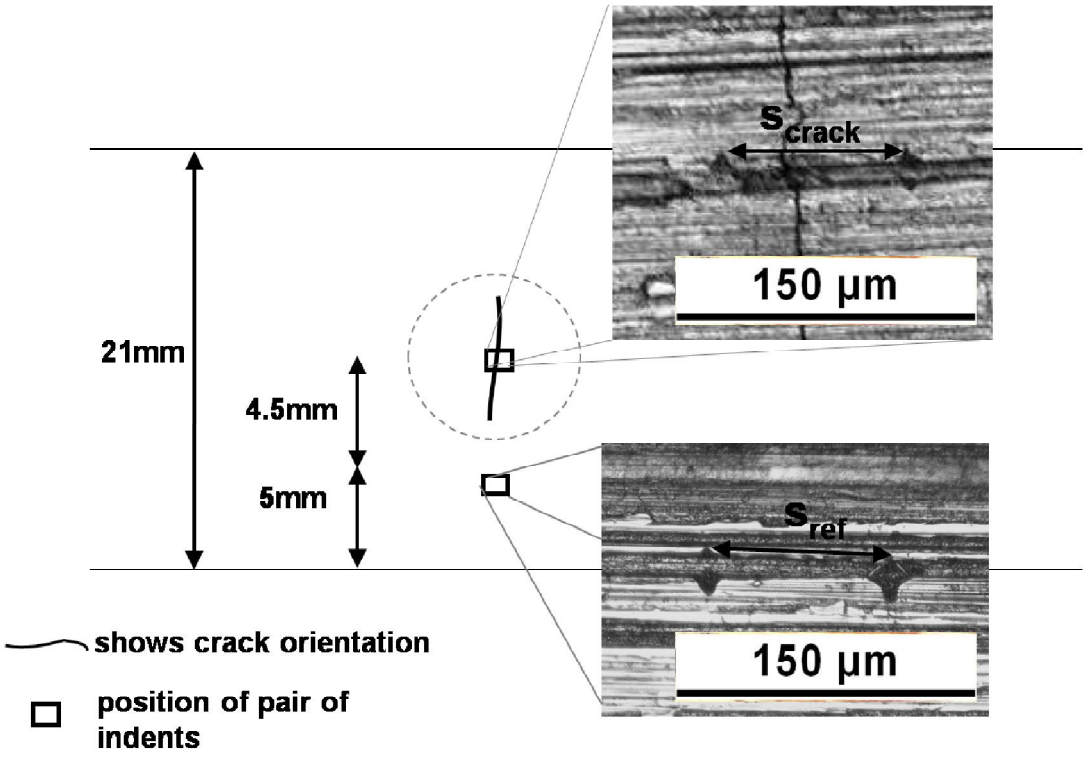

Figure 30. Schematic showing positioning of Vickers indents for crack mouth opening measurement on front face of samples (opposite hemispherical dimple). One pair was made either side of the crack midway along its length. The other pair was made distant from the crack. The indent spacing was 75-100μm.

A miniature 3-point bend rig (see Figure 31a) was built that allowed a static load to be applied while the sample was viewed under a scanning electron microscope (SEM) at up to 750X magnification. First the separation of the two indent pairs, s_{crack} and s_{ref}, was measured at zero load. Then the applied load was increased incrementally and the change in indent separation, Δs_{crack} and Δs_{ref}, was measured on a calibrated digital image using callipers.

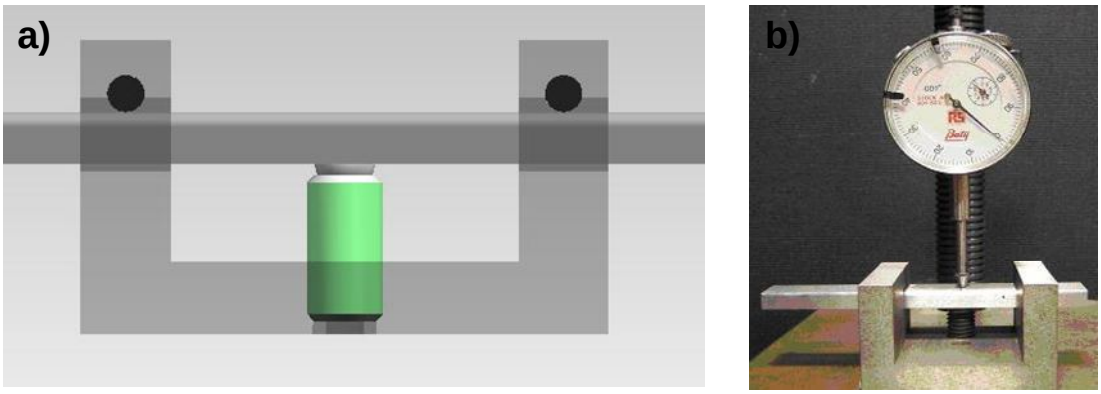

Figure 31. a) Illustration of miniature three-point bend rig rendered semi-transparent to show three-point bend supports: two roller supports above the sample and a ball bearing under the sample to provide the point loading. b) Measurement of maximum vertical displacement on mini-rig using dial gauge.

The right hand corner of the diagonal indent was used as a reference point. Two potential sources of error were identified in the measurement of crack mouth opening. The corner of the indent was selected manually each time and so the measured separation was not consistent. Also, the rig had to be removed from the SEM vacuum chamber between measurements in order to increase the applied load. This meant that the position of the sample in the chamber could vary slightly between load increments and affect the perspective in the digital image. To quantify these errors, the distance between the right hand corner of each indent pair (over the crack and distant from the crack) was measured five times on the same image and the mean value calculated. The maximum standard deviation for any measurement on

the same image was 1.1μm. The maximum standard deviation between subsequent measurements of the separation of the reference indents on any sample was 0.78μm.

Even in an uncracked sample, the indent pairs would move apart upon the application of a load due to elastic strain of the bar. On an uncracked sample Δs_{crack} and Δs_{ref} were both less than the reading error of the technique. Therefore any significant increase in indent separation, Δs_{crack}, was assumed to be due to crack mouth opening.

Foil gauges could not be placed over the crack during crack mouth opening measurement or penetrant testing to allow the direct measurement of strain. The alternatives were to either measure the strain in a position on the back face of the sample or to measure the maximum vertical displacement of the sample with a dial gauge. As crack mouth opening measurements were carried out in a vacuum chamber and as the samples were penetrant tested many times, it was more practical to measure the vertical displacement with a dial gauge. On an uncracked sample, the maximum vertical displacement, the back face strain and the strain in the position where all the cracks had initiated, ε, were measured as the load was increased incrementally. Measurement of maximum displacement with a dial gauge is shown in Figure 31b. The positions of the foil gauges on the back face of the sample and in the position where all the cracks had initiated – or cross-crack position - are shown in Figure 23. The measured values of strain and displacement for a given applied load were verified using a static finite element model in ABAQUS [63]. The model was validated using beam theory for a simple rectangular cross-section bar.

Figure 32a shows the variation of indent separation, Δs_{crack}, or crack mouth opening with the equivalent strain, ε, in an uncracked sample across the position at which a crack would initiate. As a first approximation of rate of change of crack mouth opening with strain ($\delta s_{crack}/\delta\varepsilon$), a linear least squares fit was carried out for the data for each crack. The gradients of the fitted line for each crack are plotted against their crack length in Figure 32b. The results for seven samples are shown: five 'short' cracks, which were either never or rarely detected during the baseline penetrant experiments, and two longer cracks, which were always detected. There was not enough time available on the scanning electron microscope to carry out these measurements for all twelve of the samples. The crack mouth opened more for longer cracks for a given applied load, as would be expected given that a larger crack will decrease the stiffness of the sample more. It is therefore expected that smaller cracks will require higher strains to obtain the same improvement in the POD for the penetrant process. The increase in crack opening for the shortest crack ($a_{tip\text{-}to\text{-}tip}$ = 0.36mm) is 0.65μm, which is less than the largest standard deviation in the measured separation (1.1μm).

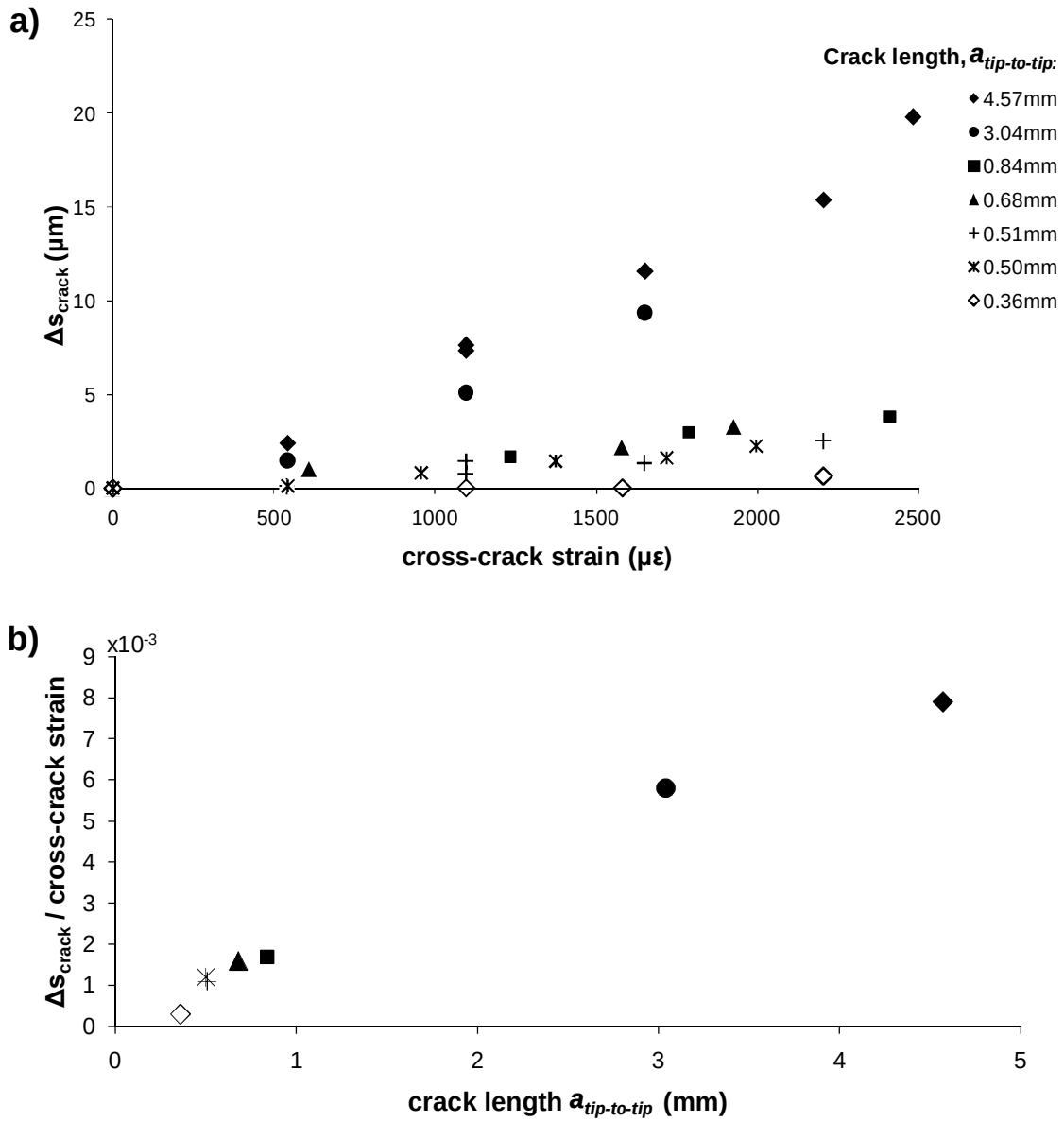

Figure 32. a) Separation of indents, Δs_{crack}, vs. equivalent cross-crack strain in an uncracked sample, ε, for seven of the cracked samples b) gradient (Δs_{crack}/ ε) of linear least squares fit for each set of data in (a).

6. Automatic Detection

The fluorescent penetrant process has a large number of variables, including dwell time, emulsification time, cleaning, heat and light, as outlined in Section 2.1 and discussed in more detail in Section 3.2. The reliability of penetrant inspection is heavily dependent upon the human inspector. An inspector may become less vigilant over time, either due to fatigue or complacency [2], and so miss defects. With experience, an inspector may become more skilled at spotting defects or less likely to make a false call [93]. In the determination of the threshold crack length $a_{90/95}$ that can be reliably detected by an NDT process, the dependence on human inspectors can be accounted for to some extent by asking a large number of qualified inspectors to inspect a large number of good and defective samples.

Designing an experiment that is fair and properly takes account of human inspection to find $a_{90/95}$ is problematic for reasons including:

1. Inspectors at one plant may be more reliable than inspectors at another, depending upon the level of training and experience and upon the plant culture.
2. If inspectors think that they are being tested, then they may perform better than on a normal day.
3. If the experiment uses samples where all the cracks are at the same position and orientation, then inspectors become familiar with the samples, increasing the probability of detecting an indication.

This project investigates the effect of crack width on the reliability of inspection. Two different approaches could be adopted: a full study could be

carried out with a large number of human inspectors or human inspectors could be eliminated altogether and replaced with an automatic detection method. The first approach would allow a more direct comparison with what could be expected in a real-life inspection. It would also reveal whether the variability introduced by human inspectors outweighs any improvement in reliability caused by increasing the crack width. The second approach would allow the two variables – crack width and the effect of human inspectors – to be separated.

For this study the number of inspectors and cracked samples available was limited, making a full reliability study unfeasible. Therefore, it was decided to adopt a method for automatically detecting fluorescent penetrant indications. This section briefly reviews alternatives for automatically detecting fluorescent penetrant indications due to cracks (Section 6.1). The adopted method is described in Section 6.2.

6.1. Methods for Automatic Detection of Fluorescent Penetrant Indications

Three different methods for automatic detection of fluorescent penetrant indications from fatigue cracks were identified:

1. Brightness measurement with a spotmeter.
2. Laser scanning and/or pattern recognition.
3. Imaging with a digital camera and pattern recognition.

Spotmeters measure the average brightness over a spot. A spotmeter was used by Iowa State University [94] in their studies on fluorescent penetrant

for the US Air Force. It was assumed that a brighter indication is more likely to be detected by an inspector. As a spotmeter integrates over an area, if the spot size is kept constant then a long crack will have a higher brightness than a short one. Once the crack length is longer than the spot, then there may be no increase in the measured brightness, although it could be argued that the probability of detecting the indication has increased. Detectability is not necessarily well correlated with brightness [95].

In laser scanning penetrant inspection [96], a focussed violet laser beam is scanned across the surface, exciting the liquid penetrant trapped in flaws locally. Spot sizes as small as 0.025mm can be achieved. A single element photodetector, confocal with the laser beam, detects light emitted by the penetrant at each point in the scan. The digital image generated contains information on the brightness and the shape of indications. Image thresholding can be used to remove any pixels below a specified brightness. Algorithms can eliminate indications based upon their size, shape or orientation. Image analysis therefore works in a way analogous to the human eye – discriminating between background penetrant and the actual crack – to give either a ‘hit’ or ‘miss’ result.

The third option is to image an area with a digital camera. Again image analysis is used to decide if an indication for a fatigue crack is present or not. This method was selected because it is inexpensive and gives a hit/miss result, analogous to that from a human inspector in a real penetrant process. Image analysis software is readily available.

6.2. Adopted Method for Automatic Detection

After penetrant processing, the cracked samples were illuminated in a darkroom with an ultraviolet mercury vapor lamp and imaged with a digital camera. The relative position of the sample, UV light and digital camera was identical each time. The intensity of the UV light at the sample surface was measured with a Spectroline DIX UV light meter and adjusted to 2000μW/cm² before each exposure. The exposure time was fixed. The camera was fitted with coloured filters, which eliminate the UV light reflected from the surface of the sample back to the camera aperture and allowed only the green light from the indications to pass. The camera was manually focused on a sheet of fine-printed text before each exposure and calibrated from a photograph of a steel rule lying on the sample, taken under white light, immediately after the first photograph.

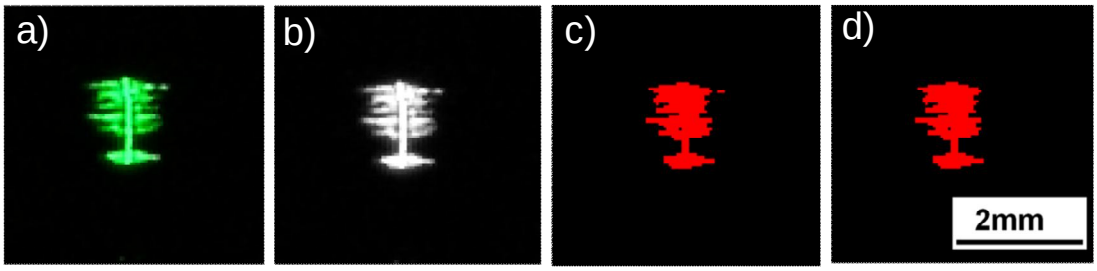

Figure 33. Automatic detection algorithm for cracks longer than ~0.8mm a) original image b) green plane extracted – each pixel has a brightness value between 0 and 256 c) thresholded so that all pixels with a brightness value < 130 are set to 0, while all pixels with a brightness value ≥ 130 are set to 1 d) image filtered to remove particles smaller than 0.012mm². The remaining particles are assumed to be crack indications.

The detection algorithms were built in NI Vision Builder [97] image-processing software. They were adapted by trial and error so that they eliminated any background indications entirely but left as many of the actual

crack indications as possible. Two algorithms were used in conjunction. On the samples generated for this study, cracks longer than ~0.8mm tended to have a greater amount of bleed out, which spread laterally along the grinding marks on the sample surface. For these cracks the steps shown in Figure 33 were used: the green plane of the image was extracted, the images were thresholded at a brightness of 130 (of 256 digital brightness levels) and then 'particles' less than 0.012mm^2 were removed. The combination of threshold brightness and particle area were chosen to remove all background indications from the images. A particle is a group of connected pixels, which touch either along an edge or corner to corner. They can also be called 'clusters'. The remaining particles were assumed to be crack indications.

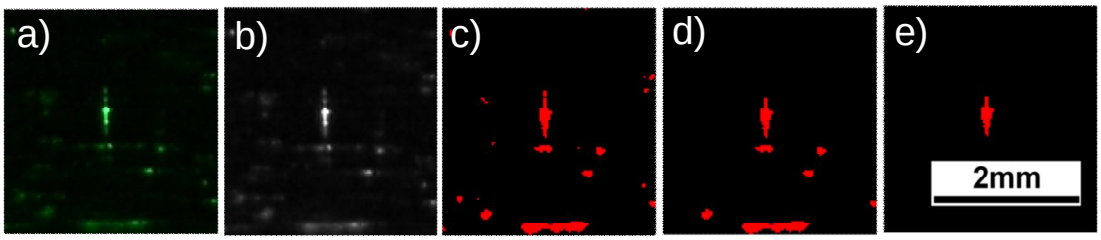

Figure 34. Automatic detection algorithm for cracks shorter than ~0.8mm a) original image b) green plane extracted – each pixel has a brightness value between 0 and 256 c) thresholded so that all pixels with a brightness value < 40 are set to 0, while all pixels with a brightness value ≥ 40 are set to 1 d) image filtered to remove particles smaller than 0.01mm^2 e) particles with maximum Feret diameter oriented more than 15º off vertical removed; the remaining particles are assumed to be crack indications.

Cracks shorter than ~0.8mm had linear penetrant indications; there was little bleed out and the cracks could only be differentiated from the background by their orientation (most of the background was due to penetrant trapped in grinding marks which conveniently always ran perpendicular to the cracks). A lower threshold was chosen as, at the previous threshold of 130, indications from some of the short cracks were filtered out. For these samples the steps shown in Figure 34: after extracting the green plane of the image, the image

was thresholded at 40, particles less than 0.01mm^2 were removed and then particles with a non-vertical maximum Feret diameter (oriented more than 15º off vertical) were removed. A Feret diameter is a line perpendicular to a pair of parallel lines that just enclose the particle, with a length equal to the distance between those lines. The remaining particles were assumed to be crack indications.

The algorithms effectively act like a human inspector, on a hit/miss basis. The long crack algorithm mostly only finds longer indications (from cracks >~0.8mm), which are large and bright. The short crack algorithm will probably *not* find these longer cracks; their indications are removed as there is substantial lateral bleed out and the longest Feret diameter is often not vertical. If the crack indication is found by either of the algorithms then it is a 'hit'.

Over the five baseline runs, the algorithms did not always give the same result for a given sample. The manual penetrant process is inherently variable, resulting in changes in the size, shape and brightness of the crack indication and affecting whether the indication is detected by the algorithms. The algorithms are conservative and will miss very faint indications; the 0.68mm long crack ($a_{tip\text{-}to\text{-}tip}$) nearly always developed a faint indication that could be observed on close visual inspection but that was not always found by the algorithms. Cracks longer than $a_{tip\text{-}to\text{-}tip}$=4.6mm were always detected during the baseline tests. These algorithms are not sophisticated enough to be applied in actual component inspection; however, they work well enough to allow an objective study to be carried out on the effect of crack mouth opening on the sensitivity of the penetrant process.

7. Static Tests

7.1. Baseline Tests

The twelve cracked samples were penetrant tested on a manual penetrant line at least 5 times each to find the threshold crack length detectable ($a_{90/95}$) for this process. Ultra-high sensitivity post-emulsifiable fluorescent penetrant (Aerospace Materials Specification AMS-2644-1 penetrant type 1D4 [98]) was applied with a brush to the cracked face and left to dwell for 20 minutes. The excess penetrant was removed by water washing. The samples were then immersed in a bath of emuslifier for 4 minutes, water-washed again, dried with an air gun and left for 10 minutes before inspecting. This emulsification time was chosen to reduce the brightness and number of background indications, making it easier to build a working automatic detection algorithm.

The probability of detecting the crack in each sample could be calculated by dividing the number of times the crack was detected by the algorithm (number of hits) by the number of inspections (number of runs). This is plotted against crack length in Figure 35. To determine $a_{90/95}$ the curve fitting procedures described in Section 2.5 must be adopted. The software mh1823 was developed for the production of POD curves, to the specification in the Department of Defense Military Handbook on the reliability assessment of non-destructive evaluation systems [10]. Using this software, the baseline $a_{90/95}$ for this family of cracked samples was determined to be 12.24mm $a_{tip-to-tip}$. This is high compared to the 0.76mm $a_{90/95}$ quoted by Rolls-Royce plc for inspection without automatic detection using this sensitivity of penetrant.

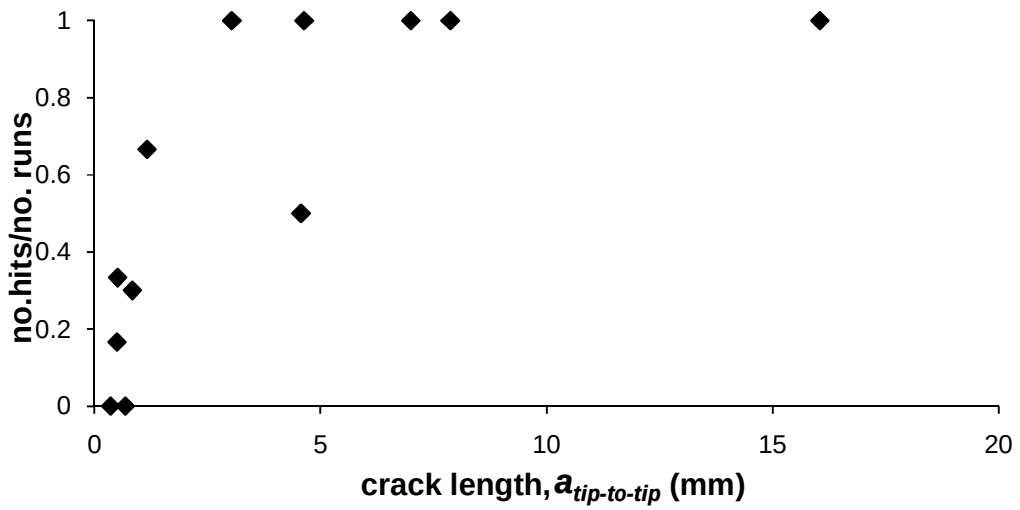

Figure 35. Probability of detection data (number of 'hits'/ number of runs) for each crack at zero load.

$a_{90/95}$ could be high for a number of reasons. Firstly, the confidence bands become tighter as the number of samples is increased. Only twelve samples were processed for this study. More samples would be required to produce a statistically significant result. Sample sets of >60 have been recommended for penetrant reliability studies [10]. Secondly, the detection algorithms will miss some indications i.e. they are conservative. In particular, the algorithm only detected a crack of length $a_{\text{tip-to-tip}}$=4.57mm 50% of the time. Finally, these cracks are considered to be unusually tight compared to most in-service cracks. This is possible as these cracks were generated under conditions different from those in an aeroengine. The samples were loaded unimodally in three-point bend. In-service cracks are often propagated under mixed loading modes. These samples were produced by cycling at a low peak stress (41% of 0.2% strain proof stress at room temperature) for upwards of 100k cycles in order to avoid multiple crack initiation sites. Engine stresses may be higher and superimpose a low frequency, high stress range cycle (engine take-off and landing cycle) on a high frequency, low stress range cycle (vibration loading). In-service cracks are also exposed to

the engine environment. Tight cracks are often attributed to residual stresses, which can either be present due to machining processes or can accumulate during cyclic loading and crack propagation.

Cleaning the samples thoroughly between runs was critical to avoid penetrant that had entered the crack in a previous test reappearing. During the initial tests it was found that, if the crack was not cleaned, further bleed out could be caused simply by applying a tensile load across the crack, causing the crack mouth to open, and then removing it, causing the crack mouth to return to its previous position. It appeared that opening the crack allowed the liquid to redistribute. As the load is removed and the crack faces come back together, liquid is 'squeezed' onto the surface. The cracks were cleaned by applying an equivalent cross-crack strain of 1000με and then a drop of acetone on the surface. As the acetone evaporates, the penetrant diffuses into the acetone and is carried towards the contact line. The load is then removed, reapplied and the process repeated until no more indications appear.

A blank sample containing only Vickers indents was also penetrant inspected. No indications were detected, either by the algorithms or upon visual inspection under a binocular microscope. The indents are small and shallow. Therefore, while penetrant will remain in grinding marks and cracks, it is washed out of the indents.

The five samples containing cracks shorter than 1mm (Table 1) were also visually inspected under a binocular microscope after processing with very short emulsification times (5s) and very long dwell times (8hrs) to check that

the sensitivity could not be dramatically improved just by changing the process parameters. Except for the 0.68mm long crack ($a_{tip\text{-}to\text{-}tip}$), which nearly always developed a faint indication that could be observed on close visual inspection in both the baseline tests and these tests, no indications were observed.

7.2. Penetrant Tests on Static Rig

The samples were statically loaded on the miniature three-point bend rig at different points during the process. The maximum vertical displacement of the sample was measured with a dial gauge (see Section 5.2) and correlated to the equivalent strain in the cross-crack position of an uncracked sample. The load was only applied for 15s during a total dwell time of 2 minutes. Such short dwell and loading times were used to keep similarity between the tests with static and dynamic loading (vibration). It would be impractical to dynamically load samples for the 20-minute period used in the baseline tests. It is thought that longer dwell times will not result in more liquid penetrating the defect; spontaneous flow occurs in the order of a few seconds (see Section 3.2). Instead, it is thought that any observed increase in indication brightness or background is due to the concentration of the fluorescent penetrant particles as the carrier fluid evaporates with time [21]. Each crack was tested a minimum of three times at each strain level.

First, a tensile load was applied for the entire process. The penetrant was applied with a brush and left to dwell for 2 minutes. Then, with the sample still on the miniature three-point bend rig, the sample was water-washed, immersed in emulsifier, water-washed again and then air dried, following the

same process used for the baseline penetrant tests. It was found that, if a tensile load was applied for the entire process, a faint indication would appear. If the load was then removed after processing, more liquid penetrant would be forced out of the crack, increasing the size and brightness of the indication (Figure 36). For a given load the increase in POD was higher for longer cracks, which agrees with the observed crack mouth openings.

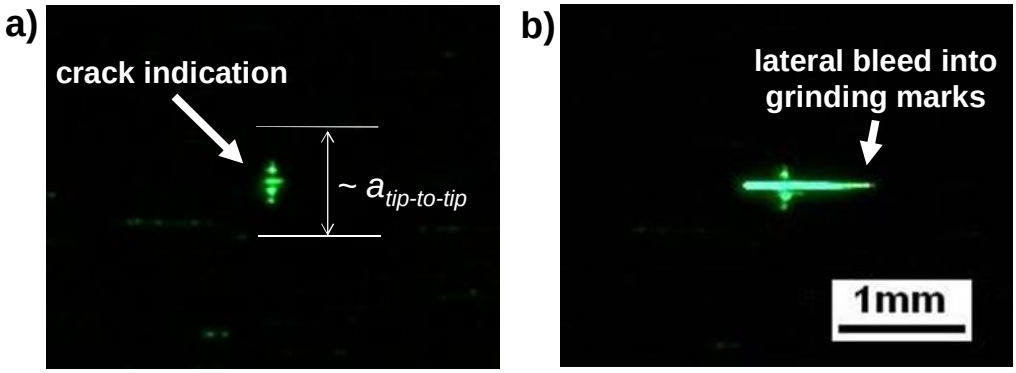

Figure 36. Sample containing crack $a_{tip\text{-}to\text{-}tip}$=0.84mm processed with an equivalent cross-crack strain of ~710με applied for the entire process. a) The indication with the load still applied post-processing. The penetrant has only bled out from the centre of the crack. b) The indication after the load has been removed. More penetrant has been 'squeezed' out of the crack and has spread laterally along the grinding marks on the sample surface.

It would not be practical to dynamically load the samples during the entire penetrant process. Therefore static tests were then carried out loading just at specific points during the penetrant process. Tests were carried out with load applied:

1. Just during dwell. The penetrant was applied with a brush. The load was applied for 15s and then the sample was removed from the three-point bend rig. Two minutes after it was brushed on, the penetrant was washed off and the sample was then processed as per the baseline method.

2. Just after processing. The sample was processed as normal. After the ten-minute bleed out time, the sample was photographed. Then the sample was loaded for 15s in the three-point bend rig, after which a second photograph of the sample was taken.
3. Loading both during dwell and after processing.

It was found that the crack mouth had to be open both during penetrant dwell and after processing (Method 3) to allow bleed out from the short tight cracks. No improvement in sensitivity was observed for Method 1 or Method 2. The number of hits by the automatic detection algorithms divided by the number of runs for each crack at four different cross-crack strains, ε, processed using Method 3 are plotted in Figure 37.

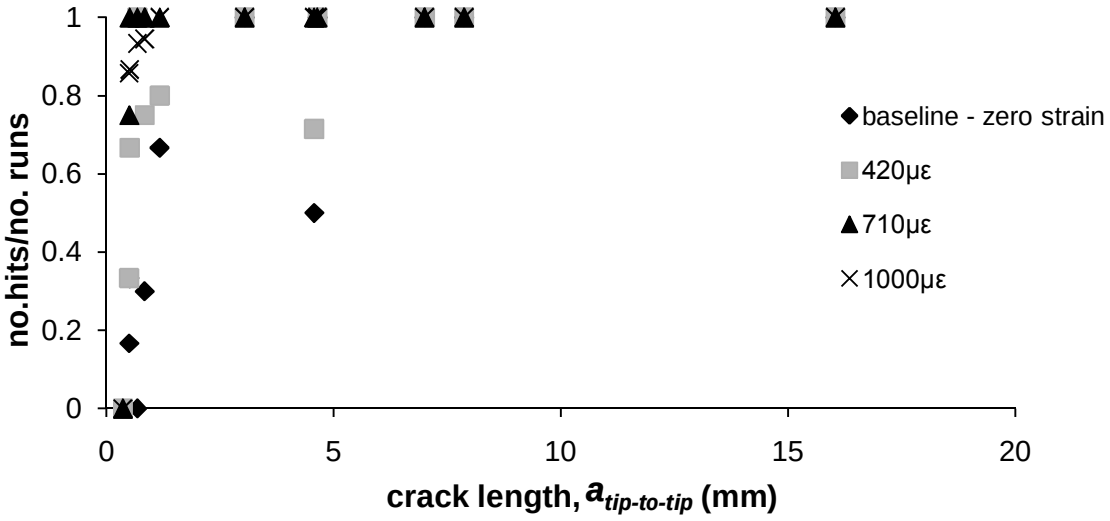

Figure 37. Probability of detection data (number of 'hits'/ number of runs) for each crack when loaded during dwell and after penetrant processing to different equivalent cross-crack strain, ε, levels.

For cross-crack strains of 0με and 420με the number of hits divided by the number or runs does not increase monotonically with crack length, $a_{tip\text{-}to\text{-}tip}$. Each crack length corresponds to only one cracked sample (see Table 1). In

particular, the automatic detection algorithm missed the 4.57mm long crack 50% of the time in the baseline study (0με) and 68% of the time at 420με. The number of hits divided by the number of runs is seen to increase with applied load for all but the shortest crack ($a_{tip\text{-}to\text{-}tip}$=0.36mm).

Figure 38 shows the generated POD curves for the 50% confidence band. With increasing cross-crack strain the curve migrates to the left i.e. there is a greater probability of finding small cracks. The 710με curve has a vertical transition because the minimum number of repeat tests - 3 per crack - was carried out and all but the shortest crack was found in every case. More tests were carried out at 1000με and a more realistic curve was obtained.

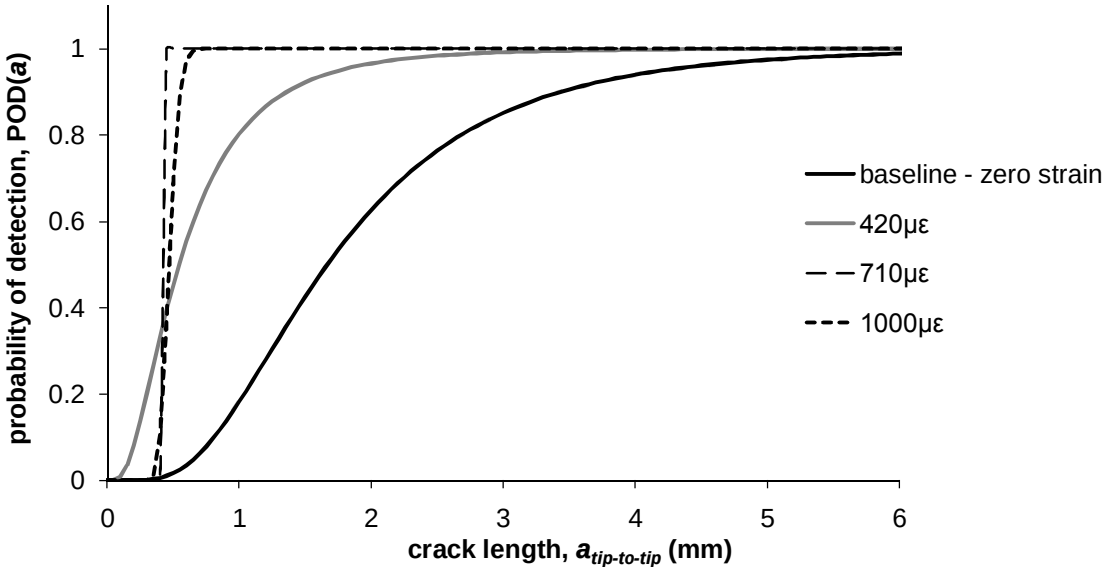

Figure 38. Probability of detection curves (50% confidence band) calculated by mh1823 POD software (developed for MIL-HDBK-1823 [10]) for set of cracked samples when loaded during dwell and after penetrant processing to different equivalent cross-crack strain, ε, levels. The line for 710με has such a steep gradient because the data set is small.

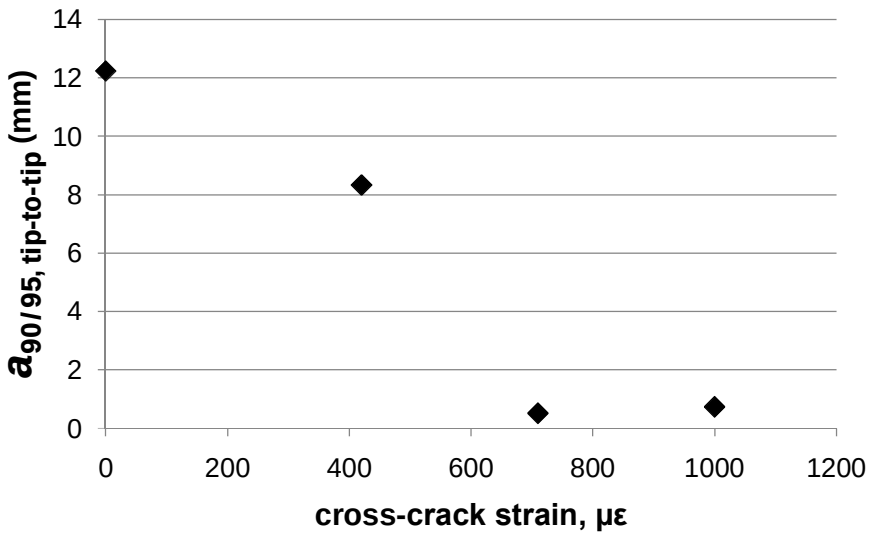

Figure 39. Crack length, measured by the shortest length between crack tips, that will be reliably detected 90% of the time with 95% confidence, $a_{90/95}$, against cross-crack strain applied during penetrant processing.

Increasing the cross-crack strain increases the crack mouth opening, as was shown in Section 5.2, and so increases the crack volume. With increasing crack width, the liquid penetrant can enter shorter cracks and so $a_{90/95}$ decreases with applied cross-crack strain. This is shown in Figure 39 where $a_{90/95}$, as calculated by the mh1823 POD software, decreases with the cross-crack strain applied during penetrant processing. There was no measureable increase in crack mouth opening for the smallest crack ($a_{tip\text{-}to\text{-}tip}$=0.36mm). This crack was not detected at any level of cross-crack strain. As already discussed, it is thought that these cracks are tighter than in-service cracks. The observed improvement in $a_{90/95}$ in this study is probably greater than it would be if a population of real fatigue cracks in aeroengine components were tested.

At the highest levels of cross-crack strain (≥710με), $a_{90/95}$ for the automatic detection process falls within Rolls-Royce plc's quoted inspection reliability

($a_{90/95}$=0.76mm) for high sensitivity fluorescent penetrant inspection with human inspectors. The large variation in $a_{90/95}$ with cross-crack strain underlines the effect of crack width on the penetrant process. It suggests that, while representing an inspection system's reliability as a function of crack length is desirable as a basis for the calculation of component life and inspection intervals, the morphology of the target defects can have a large effect on the calculated value of $a_{90/95}$. Generating a representative family of defects can be very difficult.

8. Vibro-Enhanced Penetrant

Vibration was investigated as a method for improving the probability of detecting short tight cracks during the liquid penetrant process. It was thought that vibration may encourage bleed-out by actively squeezing penetrant out of the crack during the compressive part of the cycle. Also, by changing the surface energy at the liquid-solid interface, vibration energy may enhance the wetting behaviour of the penetrant.

The literature review found that a range of frequencies and modes of vibration have been used to promote filling and emptying of entrapments, although research has concentrated on rough surfaces, pores and capillaries rather than fatigue cracks (Section 3.2). Fatigue cracks can be opened and the crack volume increased by applying a tensile load orthogonal to the plane of the crack. The relationship between applied cross-crack strain and crack mouth opening was determined in Section 5.2. The static tests (Section 7.2) demonstrated that the reliability of the penetrant process expressed in terms of $a_{90/95}$ is dependent upon crack mouth opening. Therefore the simplest approach for 'vibro-enhancement' was to vibrate the samples in a bending mode, generating stress orthogonal to the crack plane and thereby causing the faces of the fatigue crack to clap. The dynamic strains can then be directly compared to the static strains applied during crack mouth opening measurements. The sample geometry (long thin bars) had been chosen (Section 4.1) so that they could be clamped at one end and vibrated at resonance in a bending mode.

The potential applications of vibro-enhanced penetrant are linked to the mode and amplitude of excitation that is required. For example, inducing high amplitude strains in large aeroengine discs could be problematic. However, inducing strains in compressor or turbine blades, particularly the blade aerofoil, is much easier. It can be achieved by clamping the blade root and then exciting the clamp or by coupling an actuator directly to the aerofoil. Section 8.1 describes the vibration rig adopted to excite the cracked samples in this project. Section 8.2 describes the results of some vibro-enhanced penetrant experiments.

8.1 Vibration Rig

The aim was to achieve alternating cross-crack strains, $\varepsilon_{0\rightarrow pk}$, that were comparable to those in the static tests e.g. up to 1000$\mu\varepsilon$. A PZT exciter was used, shown in Figure 40. The exciter is made by bolting two PZT discs between cylinders of steel. The discs are separated from the steel cylinders and one another by copper plates. The PZT exciter is a half-wave resonator; the first resonant frequency, *f*, is determined by the material and the length of the exciter, *l*, by:

$$f = \frac{c}{2l} \tag{8.1}$$

where c is the acoustic velocity of a compressive wave in the exciter material. A hole was drilled through the samples so that they could be bolted directly to the PZT exciter. The resonant frequencies of the PZT exciter were found using an impedance analyser. The first two electrical anti-resonances, which correspond to the first two mechanical resonances, were at 14.5kHz and 27.3kHz. At the resonant frequencies the impedance was purely resistive and had a value of 267Ω. Off-resonance (at 19kHz) the impedance was 3.14kΩ.

The exciter was driven by a sinusoidal input signal, amplified by an Inter-M PA-935 acoustic amplifier, which has a power output of 35W and an output impedance of 285Ω. A Walsall transformer with core type EI78/27.5 was used to impedance match the amplifier to the exciter at the driving frequency, thereby maximising the power in.

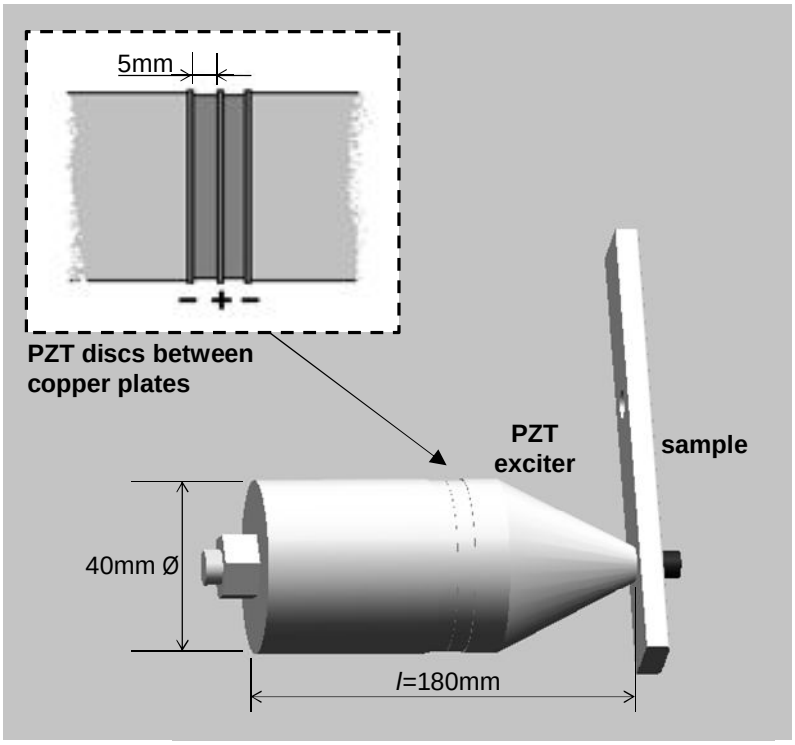

Figure 40. PZT exciter or half-wave resonator used to excite the cracked samples 180mm long x 40mm Ø. The sample is bolted to the end of the exciter. The detail shows how voltage is applied across the PZT discs via copper plates. The PZT discs are 5mm thick.

A modal analysis was used to predict the natural frequencies and mode shapes of the sample. The nodes were fully fixed over a circular region to simulate bolting the sample. The finite element model was validated by calculating the natural frequencies and mode shapes analytically for transverse vibration of a fixed-free beam with a rectangular cross-section. Table 2 lists the first four natural bending frequencies calculated by the FE model and by the analytical solution for the sample fixed 30mm away from

one end (50mm from the hemispherical dimple). The predicted mode shapes are shown in Figure 41.

Table 2. Natural frequencies for blank sample with hemispherical dimple calculated by FE modal analysis in ABAQUS [63] with the bar fully fixed 30mm from the end (see Figure 41) and the analytical solution for transverse vibration of fixed-free 100mm beam with rectangular cross-section. Experimentally measured frequency of resonance for sample bolted to PZT exciter 30mm from end.

Finite element (Hz)	Analytical solution (Hz)	Experimental (Hz)
574	597	-
3476	3742	3530
9700	10477	9380
17942	20531	17452

Only the resonant frequencies for the bending modes for the long end of the sample are listed in Table 2. The FE model also found other modes (e.g. torsional) some of which would generate strain at the back-face position. However, the bending modes will be preferentially excited by these rigs and will cause clapping of the crack faces, as the dominant stress component is perpendicular to the crack, along the axis of the bar.

To experimentally measure the strain, foil strain gauges with a 2mm gauge length and 350Ω gauge resistance were fixed to an uncracked sample in the cross-crack and back face positions (Figure 23). A dynamic strain gauge amplifier and oscilloscope were used to monitor the amplitude of the dynamic strain during vibration. The strain, ε, is related to the measured voltage by:

$$\varepsilon = \frac{V'}{V \times GF \times gain} \tag{8.2}$$

where V' is the measured voltage, V is the voltage across the strain gauge and GF is the gauge factor. The PZT exciter was driven by an Inter-M PA-935 acoustic amplifier, the output of which was not grounded. A common ground was connected between the PZT exciter and the strain gauge amplifier to avoid interference.

With the sample bolted to the PZT exciter in the same position (30mm from one end), the frequency of the excitation signal was swept between 0 and 30kHz. The back face strain was monitored. The frequency of the first three resonances was noted and compared to those predicted by the FE model. The first resonance observed was at 3.35kHz, which is similar to the natural frequency of the second bending mode of the bar predicted by FE (Table 2). The highest dynamic strains in the back face position were achieved at a frequency of around 17kHz, which corresponds approximately with the frequency for the fourth bending mode. The crack lies on an antinode for this mode shape, as shown in Figure 41. The bar was excited at around 17kHz for all subsequent vibro-enhanced penetrant tests. The frequency was adjusted to control the dynamic strain.

The measured value of dynamic strain was verified using the FE model and a laser vibrometer. An uncracked sample was excited in its fourth bending mode. The laser was used to measure the velocity of the sample in the crack position. The frequency was known from both the excitation signal and from the time trace of the measured velocity. Therefore, the amplitude of the displacement could be found. The strain was simultaneously measured with a foil gauge on the back face of the sample. The measured ratio of back face

strain to maximum displacement was compared to the ratio predicted by the modal analysis.

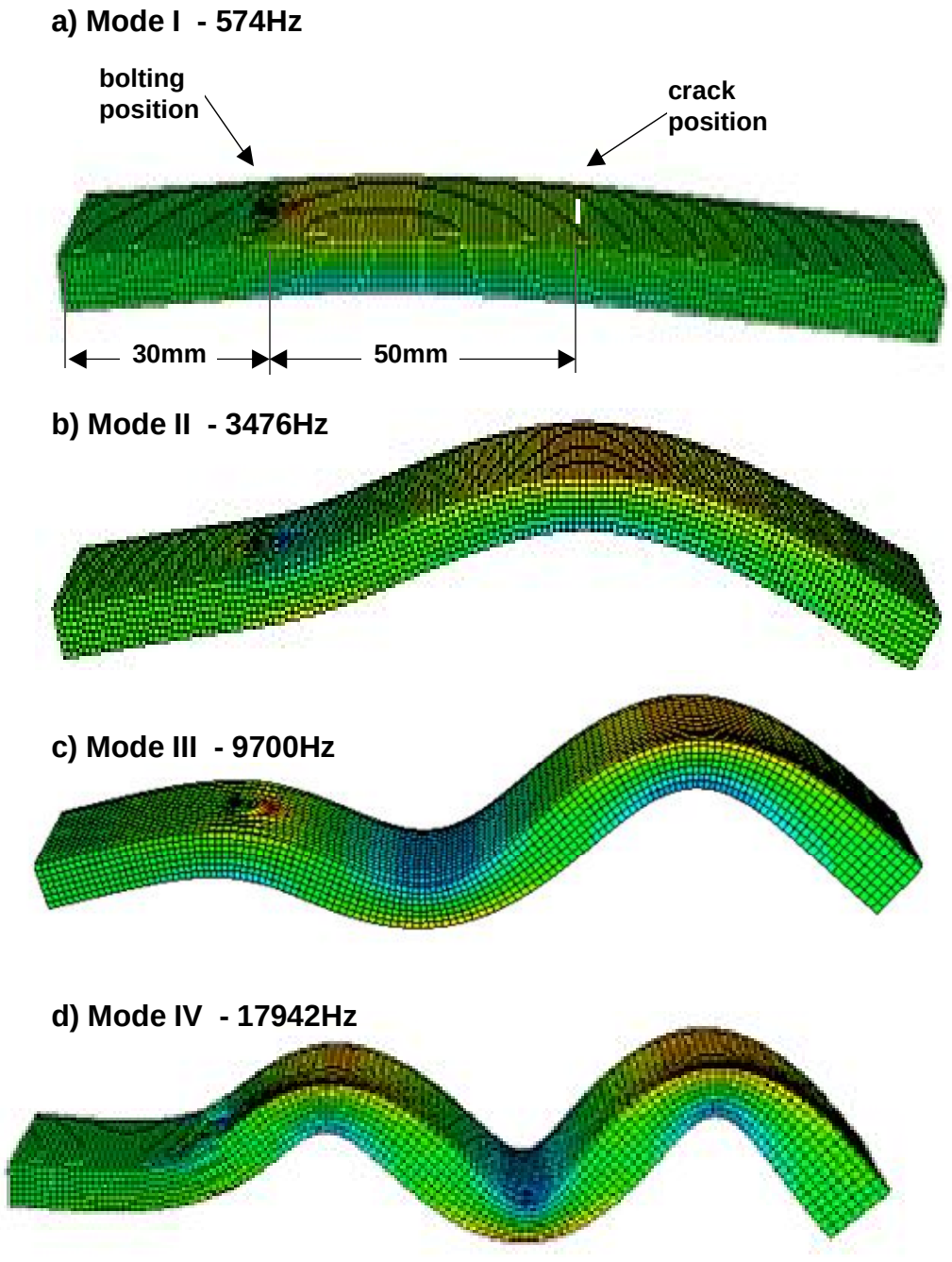

Figure 41. Mode shapes for rectangular-ended sample with hemispherical dimple 'bolted' to exciter 30mm from the end. Finite element modal analysis in ABAQUS software [63].

8.2 Penetrant Tests on Vibration Rig

The second aim of this project was to investigate whether vibration could increase the reliability of the fluorescent penetrant process. A vibration rig was selected (Section 8.1) that allowed the samples to be vibrated in a bending mode with an antinode at the crack position, thereby efficiently generating high cross-crack strains. The static penetrant tests (Section 7.2), where the cracks had been loaded statically causing the mouth to open during processing, showed that an improvement in reliability was achieved only when the load was applied both during dwell, allowing the penetrant to enter the cracks, and during bleed out, allowing the penetrant to exit.

To investigate the potential of vibration as a means of increasing the reliability of the fluorescent penetrant process, the five shortest cracks were tested at dynamic strain amplitudes $\varepsilon_{0\rightarrow pk}$ from 100με to 700με with 100με increments. These five cracks had lengths in the range where the greatest improvement in process reliability could be obtained. The dynamic strain level was controlled manually and was viewed on an oscilloscope, the required strain amplitude being set with a cursor. The amplifier gain was varied and the excitation frequency tuned until the dynamic strain amplitude reached the cursor level. The sample was vibrated at this strain amplitude for 15s. The maximum strain achieved was limited by the foil gauges; at high strain amplitudes the gauges tended to break after a few seconds of vibration.

Before increasing the level of applied dynamic strain, the crack lengths were measured to check that no propagation had occurred. The longest crack that was inspected using vibration as part of a process was $a_{tip\text{-}to\text{-}tip}$=0.84mm. The

cracks were vibrated up to $\varepsilon_{0\rightarrow pk}$ of 700μstrain and no crack propagation was observed.

First the possibility of vibration aiding bleed out by 'squeezing' the penetrant out of the crack was investigated. Penetrant was brushed onto the samples and then a static load was applied for 15s during dwell, such that the equivalent cross-crack strain, ε, was 1000μstrain. The static tests showed that this level of strain applied during dwell should allow the penetrant to enter all but the shortest crack. The penetrant was left to dwell for a total of 2 minutes. Then the samples were processed as per the baseline method. After processing, the samples were vibrated at resonance for 15s at a given $\varepsilon_{0\rightarrow pk}$. At $\varepsilon_{0\rightarrow pk}$ > 500μstrain bleed-out was observed repeatedly for two of the cracks, with length $a_{tip\text{-}to\text{-}tip}$ = 0.84mm and 0.68mm (Figure 42). No improvement was observed for any of the other samples.

The tests on the static rig had demonstrated that a load must be applied both during dwell and after processing to improve the POD. Next, the possibility that vibration could be used to aid penetration of liquid into the crack was investigated. The penetrant was applied with a brush and the samples were vibrated at resonance for 15s. The penetrant was left to dwell for a total of 2 minutes. The samples were then processed as per the baseline method and an image was taken. After processing the samples were vibrated for 15s at the same load as that used during dwell and photographed. The dynamic strain was increased incrementally, until $\varepsilon_{0\rightarrow pk}$ = 710 μstrain. No bleed out was observed either when the samples were vibrated post-processing or when the cracks were subsequently statically

loaded and unloaded (Figure 43). It was concluded that no penetrant was entering the shorter cracks.

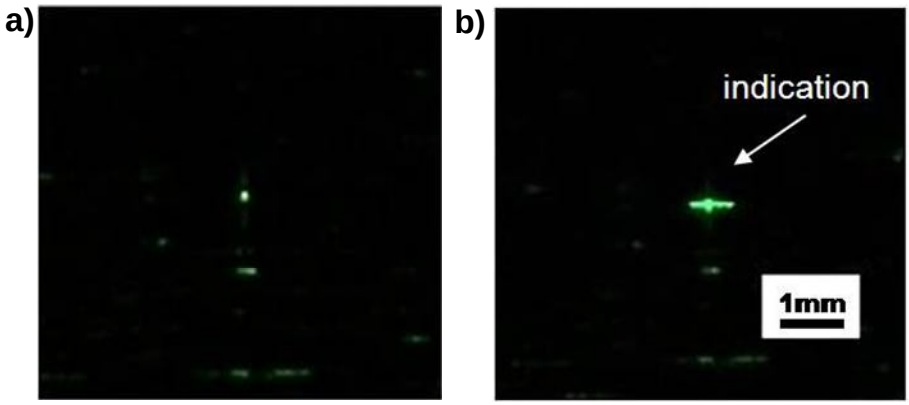

Figure 42. Sample with crack length $a_{tip\text{-}to\text{-}tip}$ = 0.68mm processed with a static equivalent cross-crack strain of ~1000με applied during dwell and a dynamic equivalent cross-crack strain of $\varepsilon_{0\rightarrow pk}$ = 570με applied for 15s ten minutes after penetrant removal a) shows the crack position ten minutes after penetrant removal. The indication is very faint; b) shows the indication which has developed during vibration.

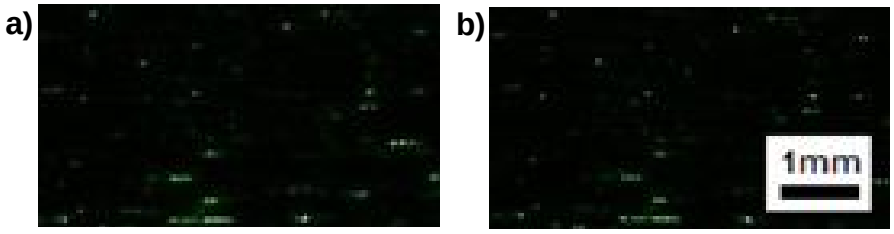

Figure 43. Sample with crack length $a_{tip\text{-}to\text{-}tip}$ = 0.68mm. The sample has been loaded with a dynamic equivalent cross-crack strain of $\varepsilon_{0\rightarrow pk}$ = 710με applied for 15s during dwell and also for 15s ten minutes after penetrant removal a) shows the crack position ten minutes after penetrant removal; b) image after vibration - no indication has developed.

It is not known whether this is just a frequency effect (the crack is not open for long enough to allow the penetrant to flow in) or whether the penetrant is being actively squeezed out immediately after it enters. During the purely tensile loading cycle on the miniature three-point bend rig this 'pumping' effect was observed (see Figure 36, Section 7.2); during vibration there is also a compressive part of the cycle.

This type of dynamic loading (clapping of the crack faces) therefore does encourage bleed out. However, although no crack propagation was observed at any point during the vibration tests, the cross-crack strain required to cause bleed out approached the fatigue threshold of the material. This method would therefore not be acceptable to aid the development of indications. The amplitude of the cross-crack strain is also the same as the static strains that had to be applied to cause bleed out for the same short cracks.

Only one type of loading was investigated in the course of this study, which caused the crack faces to open and close in a clapping action. The reviewed literature indicates that other mechanisms could promote filling or bleedout of entrapments. Different modes of mechanical excitation, either of the sample or of the liquid penetrant, may therefore be more efficient at encouraging bleed out without approaching crack propagation thresholds. Unfortunately, initial ad hoc trials did not support this hypothesis and the project was discontinued before it could be tested systematically.

9. Conclusions

9.1. Review of Part I of Thesis

The aims of this project were to demonstrate that the crack width affects the reliability of fluorescent penetrant inspection and to investigate vibration as a means of actively enhancing the reliability of the penetrant process.

To do this a family of samples containing single semi-elliptical surface breaking cracks in a flat as-machined surface was required. A method was developed to generate these cracked samples (Section 4) by cyclically loading rectangular bar-shaped samples in 3-point bending and inspecting the samples in-situ periodically with an ultrasonic surface wave technique. Using this method, 12 samples containing single fatigue cracks between 0.36mm and 16mm in length were generated.

An optical method was developed to measure the change in crack mouth-opening of a fatigue crack midway along its length with applied cross-crack load. The crack mouth opening was observed to increase with applied load. For a given applied load, the increase in crack mouth opening was greater for long cracks. This is to be expected since the longer cracks would cause a more significant reduction in the stiffness of the rectangular bars.

In order to remove the bias introduced by human inspectors in a penetrant process due to, for example, knowledge of the samples, a method for automatically detecting fluorescent penetrant indications from fatigue cracks was developed. The surface of the cracked samples was imaged under ultraviolet light using a digital camera after penetrant processing. An image

processing algorithm was used to separate indications from fatigue cracks from indications due to background e.g. surface roughness or foreign material on the surface of the sample. The automatic detection mimics the behaviour of a human inspector, giving a binary response i.e a 'hit' if an indication is detected or a 'miss' if it is not. Binary regression methods can therefore be used to determine the reliability of the inspection (Section 2.5). From the binary regression a crack size, $a_{90/95}$, that could be detected 90% of the time with 95% confidence, which can be used as the basis for damage tolerance lifing calculations.

The success of the image processing algorithm depended partly on the fact that the cracks were normal to the grinding direction of the material. The crack indications could therefore be separated from the majority of the background indications by their orientation. This may not be the case in machined components; therefore it is unlikely that this automatic detection algorithm could be used in anger. The automatic detection algorithm is also conservative, not detecting some short faint indications that could be seen by eye. Using this method, the baseline reliability of the penetrant process, expressed in terms of the crack length, $a_{90/95}$, that could be detected 90% of the time with 95% confidence, was found to be 12.24mm. This is significantly longer than the Rolls-Royce plc requirement for high sensitivity inspection – 0.76mm. However, the algorithm did allow us to carry out an experiment that was independent of the human inspector for this project.

The cracked samples were then processed with a bending load applied across the crack causing it to open during various stages in the penetrant process. The cracked samples were processed and inspected at least three

times each. It was found that short cracks had to be opened both during dwell, allowing the liquid penetrant to enter the crack, and after processing, to allow the liquid penetrant to exit the crack and an indication to develop. Four loads were tested. These were related to an equivalent strain in an uncracked sample in the crack position, ε, and orthogonal to the crack plane: baseline (0με), 420με, 710με and 1000με. $a_{90/95}$ decreased with ε up to 710με, where it appeared to reach a lower limit. $a_{90/95}$ at ε=1000μ was 0.73mm, within the Rolls-Royce plc requirement for high sensitivity liquid penetrant inspection.

The reliability of the penetrant process, $a_{90/95}$, is therefore closely linked to the crack mouth opening and so the crack width. The width of fatigue cracks depends on the load history and also upon the residual stress field in which the crack resides. The simplistic approach of stating a crack length $a_{90/95}$ that will be reliably detected may lead to an incorrect calculation of the component life. However, it is necessary to keep this finding in context. A large number of factors affect the reliability of the penetrant process, including the bias introduced by the human inspector. This factor has been eliminated in this piece of work and may far outweigh the effect of variations in crack width.

Finally, the vibro-enhancement of the fluorescent penetrant process was investigated. Penetrant was allowed to enter the cracks, by statically loading the samples during dwell. After processing, the samples were bolted to a PZT exciter and a bending mode of the samples was excited, which caused the crack faces to clap, opening and closing cyclically. It was found that at alternating cross-crack strains, $\varepsilon_{0\rightarrow pk} \geq 500\mu$strain, bleedout was encouraged,

such that two of the short cracks that were not always detected by the automatic detection algorithm during the baseline tests were always detected. Unfortunately, even to cause bleed out once penetrant had already entered into the crack, cross-crack strains in the order of the fatigue threshold were required. This dynamic strain was also similar to the static strain that had been required for bleed out to occur (ε =710μstrain), so there is no significant advantage to be gained from dynamically loading the samples. For these reasons, the technique does not show potential for practical application. The possibility that the same mode of vibration could be used to aid penetration of liquid into the crack was also investigated. No improvement in sensitivity was observed.

9.2. Brief Summary of Main Contributions

The main contributions of Part I of this thesis can be summarised as follows:

- a method of generating thumbnail cracks in an as-machined surface and a complementary method of detecting cracks in-situ on the fatigue rig were developed. Fatigue cracks as short as 0.36mm in length were generated using this method;
- the reliability of the penetrant process, expressed in terms of the crack length that will be detected 90% of the time with 95% confidence, $a_{90/95}$, has been shown to be closely linked to the crack mouth opening and therefore the crack width;
- it has been demonstrated that the reliability of processing can be improved by applying a tensile load across the crack, however this requires prior knowledge of the likely crack position and orientation;

- vibration that causes a crack to open and close cyclically in a clapping action can cause penetrant to exit from a crack however, it will also prevents it from entering. The strains required to cause bleed out are of the same order of magnitude as the threshold for crack propagation and so vibro-enhancement of penetrant inspection using this frequency and mode of excitation would not be practical.

These results have been presented at an international NDT conference and published as proceedings [99]. A paper has been published by the refereed journal, Insight [100].

9.3. Future Work

The automatic detection algorithms developed for this project are unlikely to be applicable to the inspection of actual components. However, automatic detection of penetrant indications has significant advantages over a human inspector. An algorithm would not be affected by factors such as tiredness and boredom and so could be considered more reliable. The reduction in manpower could also result in a reduction in costs.

It may be possible to use automatic detection algorithms as part of a fluorescent penetrant inspection now where the geometry is constant and where the crack size that must be detected is in the order of millimetres. For example, automatic detection could be used alongside remote penetrant testing for applications in the nuclear industry. The algorithms used in this project were simple; they measured the brightness of the indications and one feature (the orientation of the Feret diameter) of the clusters of pixels. More sophisticated algorithms may allow shorter cracks to be detected reliably.

Only one type of vibration testing has been investigated for this project. It is possible that vibrating the sample or transmitting acoustic waves through the liquid penetrant, could improve the reliability of the penetrant process by overcoming contact line pinning. *Ad hoc* experiments were carried out as part of this project but showed no improvement. They were not reported in detail here as the parameters were not well controlled. It would be worth investigating alternative methods of vibration. Alternative forms of actuation, such as heat, may also improve the reliability. A better scientific understanding of the factors affecting filling of flaws and particularly of bleedout would contribute to a more directed approach.

This project has highlighted a general lack of understanding of the factors that affect the sensitivity of the liquid penetrant process. It is recommended that more research is undertaken to understand the physical processes discussed in Section 3.2 that drive the filling and, in particular, the emptying of surface-breaking defects with liquid. The results of such work would drive the development of new liquid penetrants or the enhancement of the penetrant process by, for example, the introduction of vibration or heat at different stages. This is expected to eventually result in a more reliable inspection method.

It is also strongly recommended that the use of automatic detection as part of the penetrant process is pursued. Automatic detection could be applied in industry for very simple component geometries now. Alternative image processing methods, such as edge detection and cluster analysis, should be considered for a next generation algorithm with an improved detection rate.

Appendix A – Technical Drawing of U720Li Blanks

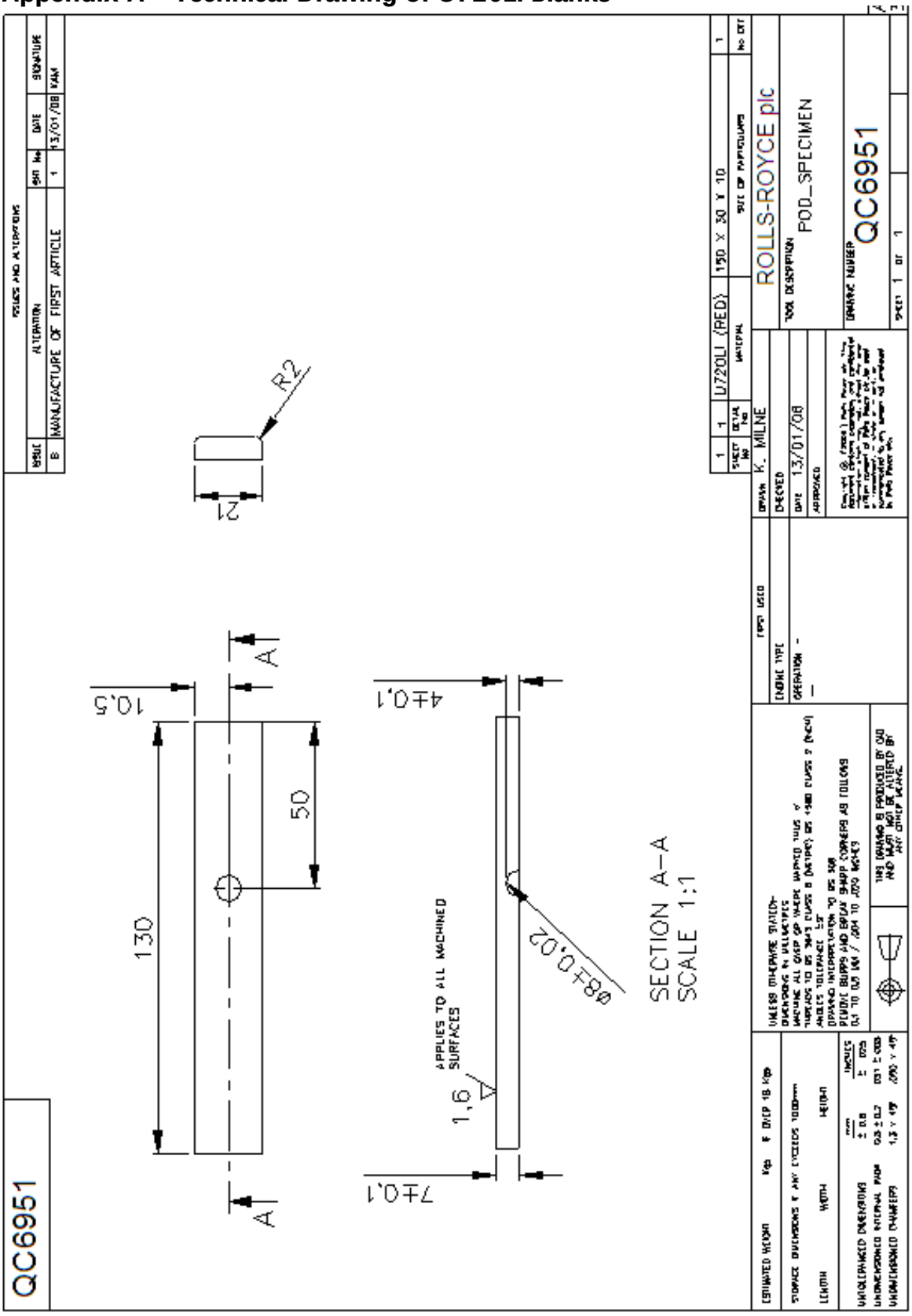

Appendix B – Technical Drawings of Fixtures for Crack Propagation

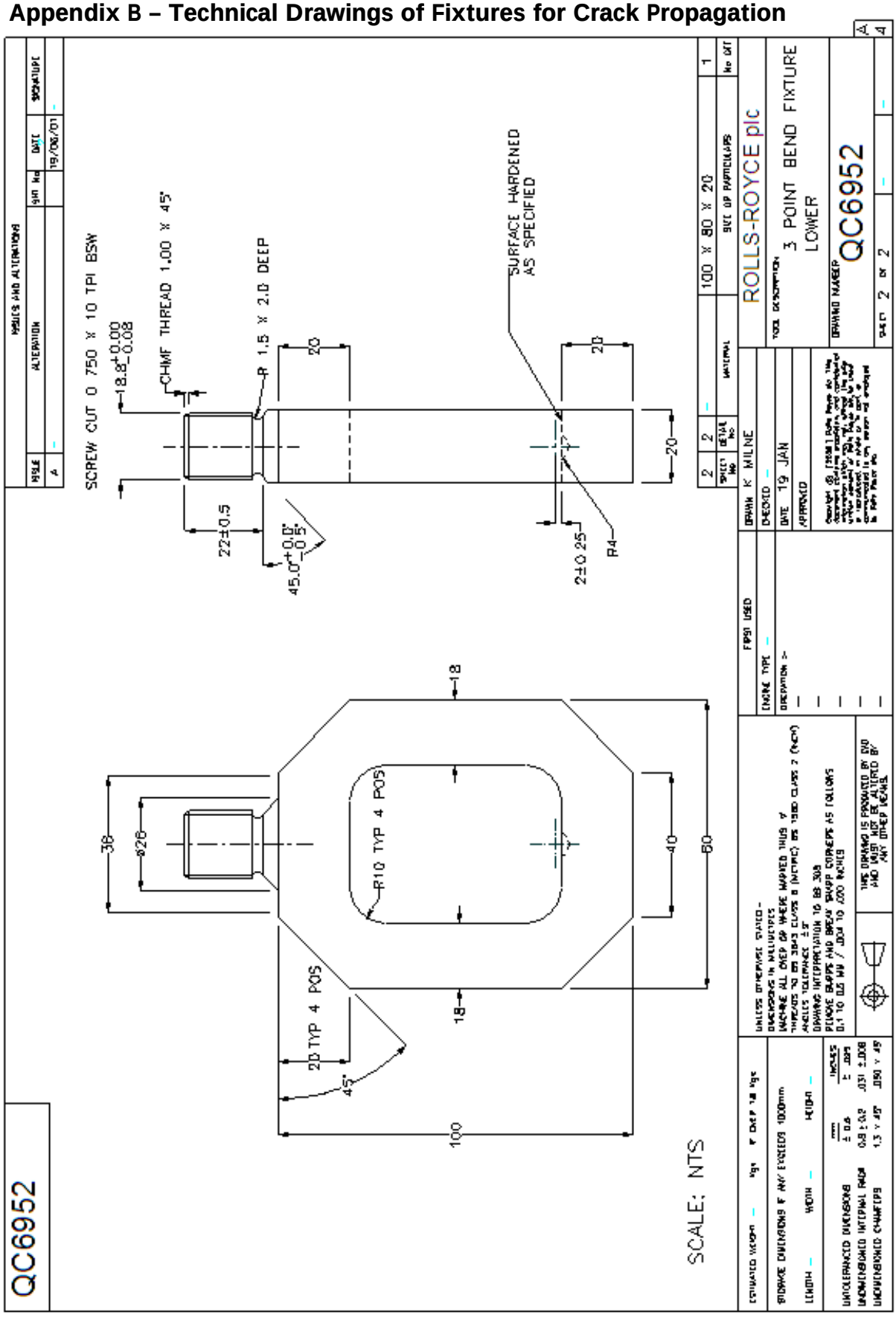

Job No. 2

QC6952

ISSUES AND ALTERATIONS				
ISSUE	ALTERATION	SPN No.	DATE	SIGNATURE
A	–	1	19/01/98	–

SCREW CUT Ø 750 X 1.0 TPI BSW

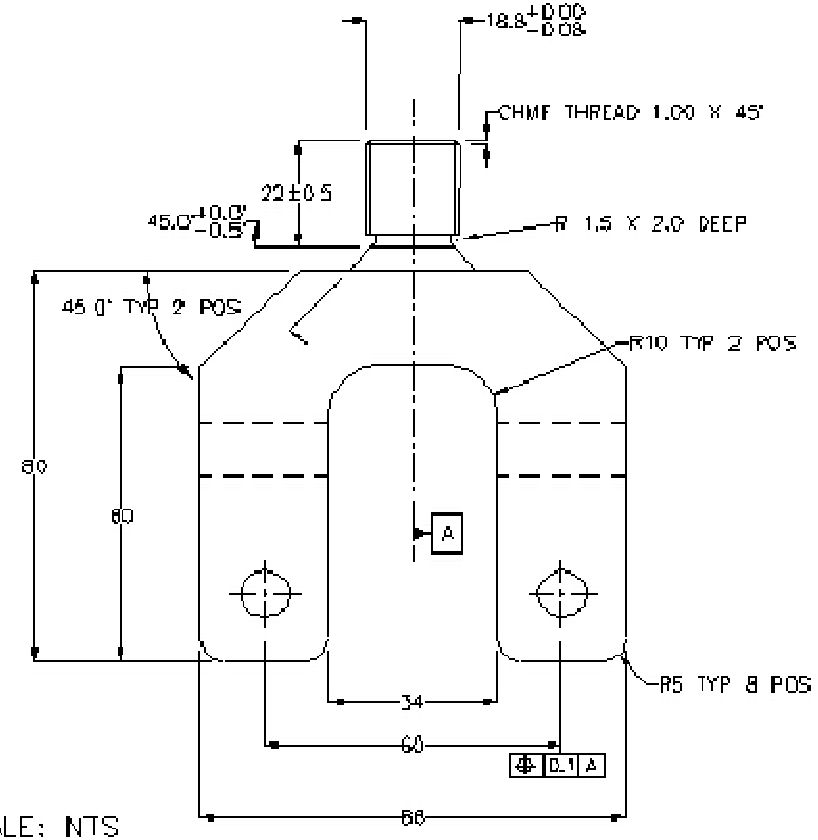

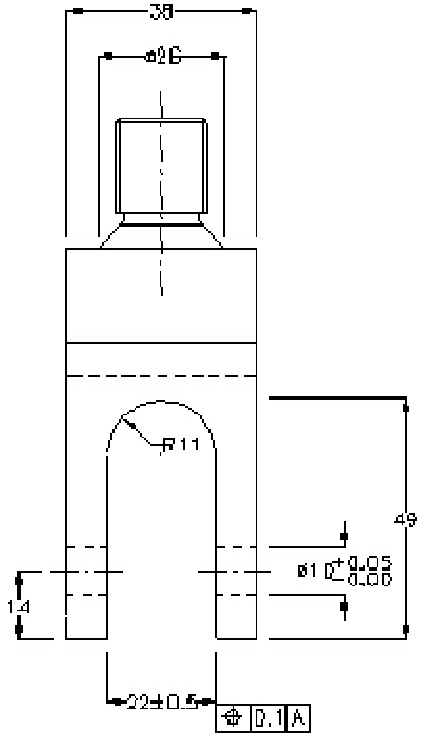

SCALE: NTS

QTY REQ'D	QTY MADE	MATERIAL	SIZE OF PARTICULARS	No. OFF
1	1	–	110 X 90 X 20	1

ESTIMATED WEIGHT – kgs @ 0.00 kg/m³

STORAGE DIMENSIONS IF ANY CYCLICS 1500mm

LENGTH – WIDTH – HEIGHT –

	mm	Inches
UNTOLERANCED DIMENSIONS	± 0.8	± .005
UNDIMENSIONED INTERNAL RADII	0.8 ± 0.2	.031 ± .008
UNDIMENSIONED CHAMFERS	1.0 x 45°	.040 x 45°

UNLESS OTHERWISE STATED–
DIMENSIONS IN MILLIMETRES
MACHINE ALL EDGE OF SHEET MARKED THUS √
THREADS TO BS 3643 CLASS 6 (METRIC) BS 7580 CLASS 2 (INCH)
ANGLES TOLERANCE ± 1°
DRAWING INCORPORATION TO BS 308
REMOVE BURRS AND BREAK SHARP CORNERS AS FOLLOWS
0.1 TO 0.5 mm / .004 TO .020 INCHES

THIS DRAWING IS PRODUCED BY ROLLS-ROYCE plc AND MUST NOT BE ALTERED BY ANY OTHER MEANS

FIRST USED	
ENGINE TYPE –	
OPERATION No.	
–	
–	
–	
–	
–	

DRAWN K MILNE	
CHECKED	
DATE 19 JAN	
APPROVED	

ROLLS-ROYCE plc

TOOL DESCRIPTION
3 POINT BEND FIXTURE
UPPER

DRAWING NUMBER
QC6952

SHEET 1 OF 2 | – | –

A4

Job No. –

Appendix C - List of Figures

Appendix D - List of Tables

REFERENCES

1. Larson, B., Study of the factors affecting the sensitivity of liquid penetrant inspections: review of literature published from 1970 to 1998, DOT/FAA/AR-01/95, US Department of Transportation Federal Aviation Administration, 2002.
2. Drury, C.G., Human factors - good practices in fluorescent penetrant inspection, Human Factors in Aviation Maintenance - Phase Nine, Federal Aviation Authority, 1999.
3. Callister, W.D., *Fundamentals of Material Science and Engineering,* 5th ed, John Wiley & Sons, 2001.
4. Benham, P., Crawford, R.J., Armstrong, C.G., *Mechanics of Engineering Materials,* 2nd ed, Longman, 1996.
5. Anderson, T.L., *Fracture Mechanics - Fundamentals and Applications,* 2nd ed, Taylor & Francis Group, 2005.
6. Claudio, R.A., Fatigue behaviour and structural integrity of scratch damaged shot peened surfaces at elevated temperatures, PhD, University of Portsmouth, 2005.
7. Claudio, R.A., Burgess, A., Branco, C.M., Byrne, J., Failure analysis of scratch damaged shot peened simulated components at high temperature, *Engineering Failure Analysis*, **16**(4), 1208-1220, 2009.
8. Powell, B.E., Duggan, T.V., Predicting the onset of high cycle fatigue damage: an engineering application for long crack fatigue threshold data, *International Journal of Fatigue*, **8**(4), 187-194, 1986.
9. Annis, C.G., VanWanderham, M.C., Harris, J.A., Sims, D.L., Gas turbine engine disc retirement-for-cause: an application of fracture mechanics and NDE, *Journal of Engineering for Power*, **103**, 198-200, 1981.
10. Non-destructive evaluation system reliability assessment, MIL-HDBK-1823, US Department of Defense, 2007.
11. Cook, D., Dixon, P., Duckworth, W.M., Kaiser, M.S., Koehler, K., Meeker, W.Q., Stephenson, W.R., *Binary Response and Logistic Regression Analysis*, in *Beyond Traditional Statistical Methods*, 2001.
12. Leone, J., *Statistics and experimental design in engineering and the physical sciences,* 2nd ed, Probability and Mathematical Statistics, Vol. 1, Wiley, 1977.
13. Suresh, S., *Fatigue of materials*, Cambridge University Press, 1991.
14. Elber, W., Fatigue crack closure under cyclic tension, *Engineering Fracture Mechanics*, **2**, 37-45, 1970.
15. Farrahi, G.H., Majzoobi, G.H., Hosseinzadeh, F., Harati, S.M., Experimental evaluation of the effect of residual stress field on crack growth behaviour in C(T) specimen, *Engineering Fracture Mechanics*, **73**, 1772-1782, 2006.

16. McClung, R.C., A literature survey on the stability and significance of residual stresses during fatigue, *Fatigue Fract Engng Mater Struct*, **30**, 173-205, 2006.
17. Press, S., *Private Communication*, K. Milne, Editor, Rolls-Royce plc, 2006.
18. Lovejoy, D., *Penetrant testing - a practical guide*, Chapman and Hall, 1991.
19. Alburger, J.R., Dimensional transition effects in visible colour and fluorescent dye liquids. In *23rd Annual Conference of the Instrument Society of America*, **8**, pages 29-41, 1969.
20. Vaerman, J., Fluorescent penetrant inspection; automatic method for sensitivity qualification. In *11th World Conference on NDT*, **3**, pages 1920-1927, 1985.
21. ASNT, *Non-destructive testing handbook - liquid penetrant tests*, Vol. 2, American Society for Metals, 1982.
22. Brasche, L., Lopez, R., Eisenmann, D., Wright, A., McReynolds, J., Developer Studies. In *ASNT Fall Conference*, Charleston, South Carolina, 2008.
23. de Gennes, P.-G., Brochard-Wyart, F., Quere, D., *Capillarity and wetting phenomena*, Springer, New York, 2004.
24. Rowlinson, J.S., Widom, B., *Molecular theory of capillarity*, Dover Publications, Mineola, N.Y., 2002.
25. Roura, P., Fort, J., Local thermodynamic derivation of Young's equation, *Journal of colloid and interface science*, **272**, 420-429, 2004.
26. Marmur, A., Penetration and displacement in capillary systems, in *Modern approaches to wettability - theory and applications*, Edited by M.E. Schrader, Loeb, G.I., Plenum Press, 1992.
27. Wenzel, R.N., Resistance of solid surfaces to wetting by water, *Industrial and engineering chemistry*, **28**(2), 988-994, 1936.
28. Cassie, A.B.D., Contact angles, *Discuss. Faraday Soc.*, **3**, 11-16, 1948.
29. Cassie, A.B.D., Baxter, S., Wettability of porous surfaces, *Transactions of the Faraday Society*, **40**, 546-551, 1944.
30. McHale, G., Newton, M.I., Frenkel's method and the dynamic wetting of heterogeneous planar surfaces, *Colloids and surfaces*, 193-201, 2002.
31. Schwartz, L.W., Garoff, S., Contact angle hysteresis on heterogeneous surfaces, *Langmuir*, **2**, 219-230, 1985.
32. Bico, J., Tordeux, C., Quere, D., Rough wetting, *Europhysics letters*, **55**(2), 214-220, 2001.
33. Della Volpe, C., Maniglio, D., Morra, M., Siboni, S., The determination of a 'stable-equilibrium' contact angle on heterogeneous and rough surfaces, *Colloids and surfaces*, **206**, 47-67, 2002.
34. Larson, B., Study of the factors affecting the sensitivity of liquid penetrant inspections: review of literature published from 1970 to 1998.,

DOT/FAA/AR-01/95, Centre for Aviation Systems Reliability, Iowa State University, 2002.

35. Sherwin, A.G., Holden, W.O., Heat assisted penetrant inspection. In *American Society of Non-destructive Testing*, San Diego, California, 1979.
36. Sherwin, A.G., Goff, R., Back to basics: heat assisted fluorescent penetrant testing revisited, *Materials Evaluation*, **58**(6), 720-725, 2000.
37. Deegan, R.D., Bakajin, O., Dupont, T.F., Huber, G., Nagel, S.R., Witten, T.A., Capillary flow as the cause of ring stains from dried liquid drops, *Nature*, **389**, 827-829, 1997.
38. Erbil, H.Y., McHale, G., Newton, M.I., Drop evaporation on solid surfaces: constant contact angle mode, *Langmuir*, **18**, 2636-2641, 2002.
39. Prokhorenko, P.P., Migun, N.P., *Introduction to capillary testing theory*, Nauka Teknika Publishing House, 1988.
40. Deutsch, S.A., Preliminary study of the fluid mechanics of liquid penetrant testing, *Journal of Research of the National Bureau of Standards*, **84**, 287-291, 1979.
41. Chemetall, *Britemore 668A Level 4 post-emulsifiable fluorescent dye penetrant - technical datasheet*, 2009.
42. Brochard, F., Motions of droplets on solid surfaces induced by chemical or thermal gradients, *Langmuir*, **5**, 432-438, 1988.
43. Chaudhury, M.K., Whitesides, G.M., How to make water run uphill, *Science*, **256**(5063), 1539-1541, 1992.
44. Brzoska, J.B., Brochard-Wyart, F., Rondelez, F., Motions of droplets on hydrophobic model surfaces induced by thermal gradients, *Langmuir*, **9**, 2220-2224, 1993.
45. Kataoka, D.E., Troian, S.M., Patterning liquid flow on the microscopic scale, *Nature*, **402**, 794-797, 1999.
46. Smith, T., Lindberg, G., Effect of acoustic energy on contact angle measurements, *Journal of colloid and interface science*, **66**(2), 363-366, 1978.
47. Meiron, T.S., Marmur, A., Sam Saguy, I., Contact angle measurement on rough surfaces, *Journal of colloid and interface science*, **274**, 637-644, 2004.
48. Decker, E.L., Garoff, S.,, Using vibrational noise to probe energy barriers producing contact angle hysteresis, *Langmuir*, **12**, 2100-2110, 1996.
49. Celestini, F., Kofman, R., Vibration of submillimeter-size supported droplets., *Physical review. E, Statistical, nonlinear, and soft matter physics*, **73**(4), 041602, 2006.
50. Noblin, X., Buguin, A., Brochard-Wyart, F., Vibrated sessile drops: transition between pinned and mobile contact line oscillations, *The European Physical Journal E*, **14**, 395-404, 2004.

51. Dong, L., Chaudhury, A., Chaudhury, M.K., Lateral vibration of a water drop and its motion on a vibrating surface, *The European Physical Journal E*, **21**, 231-242, 2006.
52. Shashtry, A., Case, M.J., Bohringer, K.F., Directing Droplets Using Microstructured Surfaces, *Langmuir*, **22**(14), 6161-6167, 2006.
53. Buguin, A., Talini, L., Silberzan, P., Ratchet-like topological structures for the control of microdrops, *Applied Physics A: Materials Science & Processing*, **75**, 207-212, 2002.
54. Sandre, O., Gorre-Talini,L., Ajdari,A., Prost,J., Silberzan,P., Moving droplets on asymmetrically structured surfaces., *Physical review. E, Statistical physics, plasmas, fluids, and related interdisciplinary topics*, **60**(3), 2964-72, 1999.
55. Daniel, S., Chaudhury, M.K., Rectified motion of liquid drops on gradient surfaces induced by vibration, *Langmuir*, **18**(9), 3404-3407, 2002.
56. Daniel, S., Sircar, S., Gliem, J., Chaudhury, M.K., Ratcheting Motion of Liquid Drops on Gradient Surfaces, *Langmuir*, **20**(10), 4085-4092, 2004.
57. Burns, M.A., Johnson, B.N., Brahmasandra, S.N., Handique, K., Webster, J.R., Krishnan, M., Sammarco, T.S., Man, P.M., Jones, D., Heldsinger, D., Mastrangelo, C.H., Burke, D.T., An integrated nanoliter DNA analysis device, *Science*, **282**(5388), 484-487, 1998.
58. Pollack, M.G., Shenderov, A.D., Fair, R.B., Electrowetting-based actuation of droplets for integrated microfluidics, *Lab on a chip*, **2**(96-101), 2002.
59. Washizu, M., Electrostatic actuation of liquid droplets for micro-reactor applications. In *IEE Industry Applications Society Annual Meeting*, New Orleans, Louisiana, pages 1867-1873, 1997.
60. Hamida, T., Babadagli, T., Immiscible displacement of oil by water in consolidated porous media due to capillary imbibitions under ultrasonic waves', *J. Acoust. Soc Am.*, **133**(3), 1539-1555, 2007.
61. Nakanishi, H., Tsunekawa, Y., Okumiya, M., Mohri, N., Ultrasound-assisted pressureless infiltration of molten aluminium into alumina capillaries, *Journal of materials science letters*, **12**, 1313-1315, 1993.
62. *Roell Amsler Operation Manual*
63. *ABAQUS CAE Users' Manual, Version 6.4*, 2004.
64. Stoychev, S., Kujawski, D., Methods for crack opening load and crack tip shielding determination: a review, *Fatigue Fract Engng Mater Struct*, **26**, 1053-1067, 2003.
65. Allison, J.E., Ku, R.C., Pompetzki, M.A., A comparison of measurement methods and numerical procedures for the experimental characterization of fatigue crack closure. In *Mechanics of fatigue crack closure*, Philadelphia, ASTM, pages 171-185, 1988.
66. Davidson, D.L., Nagy, A., A low-frequency cyclic-loading stage for the SEM, *J. Phys. E: Sci. Instrum.*, **11**, 207-210, 1978.

67. Jia Zhen Zhang, J.Z.Z., Zhao Xin Meng, Direct high resolution in situ SEM observations of very small fatigue crack growth in the ultra-fine grain aluminium alloy IN 9052, *Scripta Materialia*, **50**, 825-828, 2004.
68. McClung, R.C., Sehitoglu, H., Closure behaviour of small cracks under high strain fatigue histories. In *Mechanics of fatigue crack closure*, Philadelphia, ASTM, pages 279-299, 1988.
69. Rodel, J., Kelly, J.F., Lawn, B.W., In situ measurements of bridged crack interfaces in the scanning electron microscope, *J. Am. Ceram. Soc.*, **73**(11), 3313-3318, 1990.
70. Ray, S.K., Grandt, F., Comparison of methods for measuring fatigue crack closure in a thick specimen. In *Mechanics of fatigue crack closure*, Philadelphia, ASTM, pages 197-213, 1988.
71. Lee, J.J., Sharpe, W.N.,Jr., Closure measurements of short fatigue cracks. In *Mechanics of fatigue crack closure*, Philadelphia, ASTM, pages 270-278, 1988.
72. Riddell, W.T., Piascik, R.S., Sutton, M.A., Zhao, W., McNeill, S.R., Helm, J.D., Determining fatigue crack opening loads from near-crack-tip displacement measurements. In *Advances in fatigue crack closure measurement and analysis*, West Conshohocken, PA, ASTM, **2**, pages 157-174, 1999.
73. Sutton, M.A., Wei Zhao, McNeill, S.R., Helm, J.D., Piascik, R.S., Riddell, W.T., Local crack closure measurements: development of a measurement system using computer vision and a far-field microscope. In *Advances in fatigue crack closure measurement and analysis*, West Conshohocken, PA, ASTM, **2**, pages 145-156, 1999.
74. Khor, K.H., Buffiere, J-Y., Ludwig, W., Toda, H., Ubhi, H.S., Gregson, P.J., Sinclair, I., In situ high resolution synchrotron x-ray tomography of fatigue crack closure mechanisms, *J. Am. Ceram. Soc.*, **16**, 3511-3515, 2004.
75. Wallhead, I.R., Edwards, L., A study of crack closure using the optical method of caustics and consequences for the use of ΔK_{eff} as a fatigue crack driving force, *Engineering Fracture Mechanics*, **22**(6), 997-1011, 1998.
76. Sheth, J.K., Gerberich, W.W., The effect of test frequency and geometric asperities on crack closure mechanisms. In *The mechanics of fatigue crack closure*, Philadelphia, ASTM, pages 112-120, 1988.
77. Foroughi, R., Radon, J.C., Crack closure behaviour of surface cracks under pure bending. In *Mechanics of fatigue crack closure*, Philadelphia, ASTM, pages 260-269, 1988.
78. Carman, C.D., Turner, C.C., Hillberry, B.M., A method for determining crack opening load from load-displacement data. In *Mechanics of fatigue crack closure*, Philadelphia, ASTM, 1986.
79. Dawicke, D.S., Newman, J.C., Grandt, A.F., Through-the-thickness fatigue crack closure behaviour in an aluminium alloy, 102590, NASA, 1990.

80. Doker, H., Bachmann, V., Determination of crack opening load by use of threshold behaviour. In *Mechanics of Fatigue Crack Closure*, Philadelphia, ASTM, pages 247-259, 1988.
81. Fleck, N.A., Smith, R.A., Crack closure - is it just a surface phenonmenon?, *International Journal of Fatigue*, **4**(3), 157-160, 1982.
82. Ritchie, R.O., Yu, W., Holm, D.K., Blom, A.F., Development of fatigue crack closure with the extension of long and short cracks in aluminium alloys 2124: a comparison of experimental and numerical results, *Mechanics of Fatigue Crack Closure*, 300-316, 1988.
83. Sarma, V.S., Jaeger, G., Koethe, A., On the comparison of crack closure evaluation using dynamic and static compliance methods, *International Journal of Fatigue*, **23**, 741-745, 2001.
84. Duffour, P., Morbidini, M., Cawley, P., A study of the vibro-acoustic modulation technique for the detection of cracks in metals, *Journal of Acoustical Society of America*, **119**(3), 1463-1475, 2006.
85. Krasovskii, A.Y., Pinkyak, I.S., A method for measuring current values of the crack-tip opening displacement under cyclic loading, *Strength of Materials*, **34**(4), 322-33, 2002.
86. Ohta, A., Kosuge, M., Sasaki, E., Change of fatigue crack closure level with gauge location along crack line, *International Journal of Fracture*, **15**, 53-57, 1979.
87. Carman, C.D., Turner, C.C., Hillberry, B.M., A method for determining crack opening load from load-displacement data. In *Mechanics of fatigue crack closure*, Philadelphia, ASTM, 1988.
88. Clark, R., Dover, W.D., Bond, L.J., The effect of crack closure on the reliability of NDT predictions of crack size, *NDT International*, **20**, 269-275, 1987.
89. Salam Akanda, M.A., Saka, M., Relationship between closure stress of small fatigue cracks and ultrasonic response, *Journal of Nondestructive Evaluation*, **23**, 37-47, 2004.
90. Buck, O., Morris, W.L., Richardson, J.M., Acoustic harmonic generation at unbonded interfaces and fatigue cracks, *Appl Physics Letters*, **33**, 371-373, 1978.
91. Donskoy, D., Sutin, A., Ekimov, A., Nonlinear acoustic interaction on contact interfaces and its use for non-destructive testing, *NDT&E International*, **34**, 231-238, 2001.
92. Schijve, J., Fatigue crack closure: observations and technical significance. In *Mechanics of fatigue crack closure*, Philadelphia, pages 5-34, 1988.
93. Kauppinen, P., Sillanpaa, J., Reliability of surface inspection methods. In *12th World Conference on NDT*, **2**, pages 1723-1728, 1989.
94. Brasche, L., Clements, L., Orvilliers, A., Griffiths, K., Lopez, R., Engineering studies of cleaning and drying processes in preparation of fluorescent

penetrant inspection, DOT/FAA/AR-03/73, US Department of Transportation Federal Aviation Administration, 2004.
95. Available from: www.statisticalengineering.com
96. Available from: www.laser-ndt.com/penetrant.html
97. *Vision Builder for Automated Inspection v2.6*, National Instruments.
98. QPL-AMS-2644-4 Qualified products list, SAE Material Specification AMS2644 - Inspection Material, Penetrant, 2004.
99. Milne, K., Cawley, P., Dunhill, A., Wright, D.C., Vibro-Enhanced Fluorescent Penetrant Inspection (FPI). In *Review of Progress of Quantitative Nondestructive Evaluation*, Colorado, **27A**, pages 1583-1590, 2007.
100. Milne, K., Cawley, P., Dunhill, A., Wright, D.C., Vibro-Enhanced Fluorescent Penetrant Inspection, *Insight*, **51**(7), 373-383, 2009.

PART II

ULTRASONIC INSPECTION OF TITANIUM DIFFUSION BONDS

1. Introduction

Diffusion bonds offer several advantages over alternative welding methods, including the ability to produce near-net shapes and achieve almost parent metal strength. However, voids remnant from the joining process can be tens of microns in diameter, making them difficult to detect with conventional pulse-echo immersion inspection at any significant metal depth. In titanium the inspection is particularly challenging; the anisotropic microstructure is highly scattering and the diffusion bond itself forms an interface between regions of preferred crystallographic orientation (macrozones), which can act as a weak spatially coherent reflector. The microstructure and texture of Ti-6Al-4V can change substantially within a single forging due to the degree of work that the material has experienced.

Diffusion bond defects can be significantly shorter than the acoustic wavelength and the macrozone size. However, they may also be distributed in the plane of the diffusion bond. This EngD project investigated various ultrasonic inspection methods for detecting voids distributed on the diffusion bond between pieces of forged Ti-6Al-4V. The aims of the project were to:

1. Generate a suite of Ti-6Al-4V samples containing good and partial diffusion bonds and a variety of microstructures, typical of forged titanium.
2. Investigate the factors limiting the sensitivity of the conventional ultrasonic pulse-echo immersion inspection, including backscatter from the bulk material and the weak spatially coherent reflection from the interface.

3. Determine a method for differentiating between the component of the reflected signal due to backscattered noise – both from the parent metal and from the interface – and distributed voiding.

Section 2 explains the industrial motivation and context for this project. The diffusion bonding process and diffusion bond defects are described. The conventional method for inspecting titanium aeroengine forgings is outlined.

Section 3 is a literature review. Ti-6Al-4V is one of the most common titanium alloys and was used to generate the diffusion bonded samples for this project. Its microstructure is described and the concept of microtexture – the preferential alignment of grains over millimetre scales – is introduced. The effect of microtexture on the ultrasonic inspection of titanium and titanium diffusion bonds is discussed. Finally, the various methods available for the inspection of diffusion bonds are reviewed.

In Section 4, the manufacture of good and partially bonded Ti-6Al-4V samples is described. These samples are inspected using a conventional pulse-echo immersion method and then sectioned and metallurgically examined to determine the quality of the diffusion bond. In Section 5, various ultrasonic methods are investigated for the discrimination of well bonded and partially bonded samples. In particular, a method for determining the phase of the ultrasonic wave reflected from the bond is introduced and used to calculate a ‘complex reflection coefficient’, which combines both phase and magnitude. Finally, the application of the symmetric reflection technique, where a reflection coefficient is calculated for ultrasonic inspection from both sides of the diffusion bond, to the Ti-

6Al-4V diffusion bonded samples is described. The findings of Part II of this thesis are summarised in Section 6, along with suggestions for future work.

2. Project Context

2.1. Titanium Diffusion Bonds in Aeroengine Components

Diffusion bonding can generate joins with almost parent metal strength in near net shapes [1]. The joining method is extensively used by Rolls-Royce plc in the manufacture of wide chord fan blades and is now also an integral part of the manufacturing process for titanium metal matrix composite (TiMMC) compressor discs [2]. Images of an aeroengine fan with wide chord fan blades and a TiMMC compressor disc are shown in Figure 1a and Figure 1b respectively.

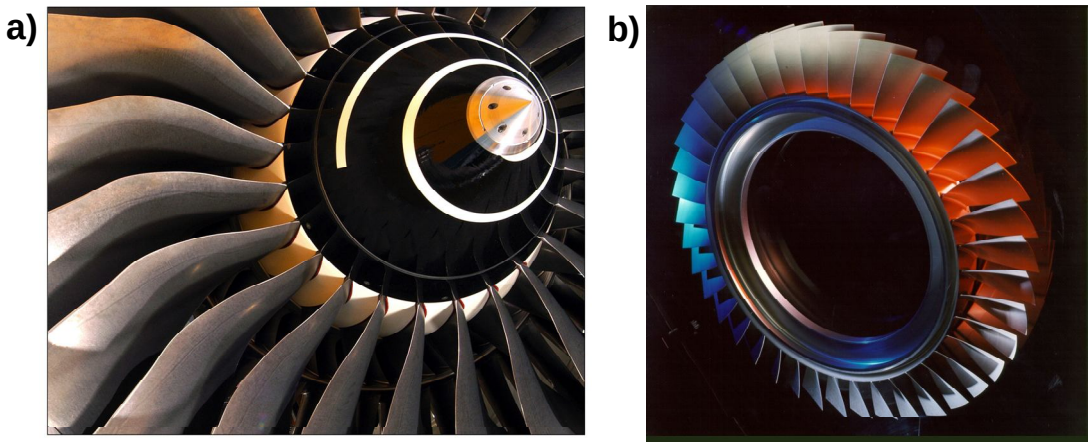

Figure 1. a) Wide chord fan blades in a Rolls-Royce plc civil engine. b) Titanium metal matrix composite bladed compressor disc (blisk). The metal matrix core reinforces the web of the blisk, affording significant weight reductions. Photographs courtesy of Rolls-Royce plc.

Cost and safety drive the requirement for a more sensitive diffusion bond ultrasonic inspection. Wide chord fan blades and compressor discs are high cost components to manufacture. Each successive manufacturing process adds value. Discs are normally machined to a simple cross-section with flat surfaces (called rectilinear) to facilitate ultrasonic inspection at an early stage in the manufacturing process. At the rectilinear stage, metal paths up to

100mm are likely. For some titanium forgings at depths of 100mm, the root mean square backscattered noise amplitude for a 5MHz ultrasonic inspection as per the Rolls-Royce plc standard [3] can be as high as -8dB compared to the reflection from a 0.050" (1.27mm) diameter flat-bottomed hole at the same depth in stainless steel [4]. -8dB corresponds to a flat-bottomed hole diameter of 0.032" (0.81mm). Diffusion bond defects are generally much smaller than these diameters (see Section 2.2). It would therefore be useful to improve sensitivity to defects at greater metal paths.

The initial aims were to:

1. Determine the sensitivity of conventional ultrasonic inspection to partial voiding.
2. Investigate potential methods for improving the sensitivity of ultrasonic inspection to partial voiding.

During the inspection of diffusion bonded components prior to the start of this project, low amplitude spatially coherent reflections had been observed from the diffusion bond. These were attributed to the aligned boundary between two pieces of titanium with slightly different texture. The presence of this reflection may further reduce the achievable defect signal to backscattered noise ratio. It was decided to investigate the effect of texture at the bond line on the ultrasonic response and, if necessary, to investigate methods for differentiating between reflections due to texture and those due to voiding. This developed into the primary aim of the EngD project.

2.2. Diffusion Bond Defects

Diffusion bonds are formed by pressing two clean and relatively smooth surfaces together at temperatures well below the melting point of the parent material. Gas is evacuated from between the two surfaces to be joined.

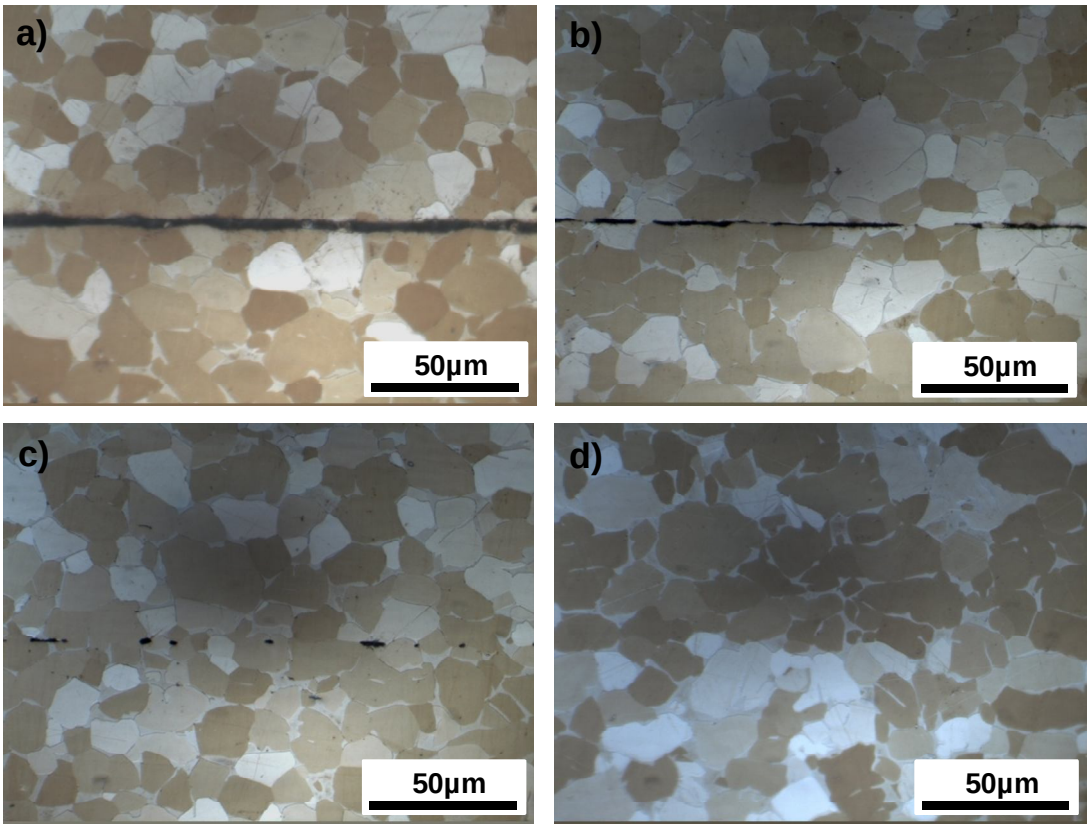

Figure 2. Images of bond line in sample HUCK01 generated at Rolls-Royce plc for this project (see Section 0): a) total lack of bond b) poor bond c) isolated pores d) good bond. The sample is cross-rolled Ti-6Al-4V.

Figure 2 shows a Ti-6Al-4V sample that was manufactured for this project using hot isostatic press conditions selected specifically to generate bond line defects (Section 0). The images are indicative of the different stages of diffusion bonding. Initially the surfaces are unbonded (Figure 2a). As the surfaces are pressed together, asperities will come into contact and plastically deform, closing the space between the two surfaces, as shown in

Figure 2b. Diffusion will occur across the contacting asperities leaving isolated voids (Figure 2c). Creep deformation and vacancy diffusion [5, 6] will result in the voids filling completely over time. Ojard *et al* [5] stated that interfacial contact occurs in two stages: first long wavelength surface asperities are eliminated by creep, then the remaining voids due to short wavelength asperities are collapsed by creep or filled by surface diffusion. Interfacial diffusion can only take place once interfacial contact has been achieved.

As the diffusion process progresses, the voids shrink and compress. In the final stages of diffusion bonding, grain growth occurs across the bond line. Eventually the bond line will disappear altogether and the strength will be equal to that of the parent material [5, 7]. Figure 2d shows an example of a well-bonded diffusion bond line. Grain growth has occurred across the interface.

Diffusion bond defects can be caused by contamination or incorrect bonding parameters (time, temperature and pressure). Contamination [8-10] includes surface oxidation or foreign bodies due to poor cleanliness. The defects may be isolated inclusions and/or a dispersed layer of contaminant. The layers may be very thin (<1 micron) and the surfaces may be in intimate contact along the entire bond line [10].

Large pores may form if gas becomes trapped between the bonded surfaces. This can occur if the vacuum has failed or if the surface areas are large and do not favour evacuation [11]. If only partial bonding has occurred then small dispersed voids of the order of the surface roughness will be present [10, 12,

13]. Figure 3 shows the variation of eight mechanical properties, including tensile and fatigue strength, with the percentage bonded area. The fatigue strength is significantly more affected by the presence of microvoids at the bond line. This is probably because, while the reduction of the load bearing area is small, the voids act as crack initiation sites.

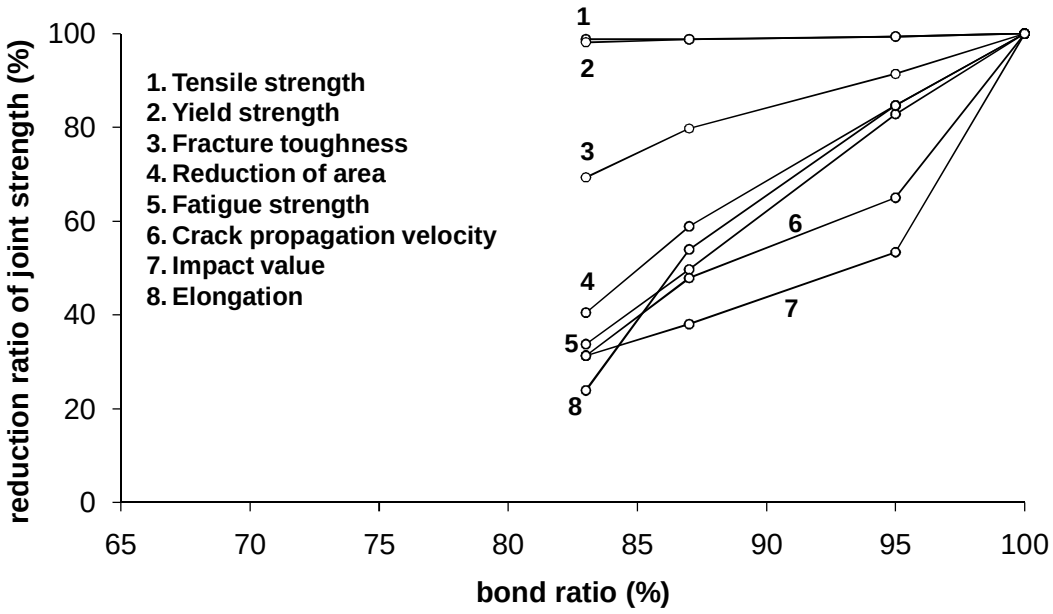

Figure 3. Variation in eight mechanical properties with the bond ratio (percentage of the bond where diffusion has occurred). After Ohsumi *et al* [1].

Once the surfaces come into intimate contact via plastic deformation, diffusion across the bond line can begin. If the process is arrested and the component is removed from the pressure chamber, regions of incomplete diffusion can remain. Incomplete diffusion results in a diminished bond strength. The atoms from one material have not diffused sufficiently far into the other material [5]. The interdiffusion distance is a function of temperature, time and pressure. Nieters *et al* [6] observed that early in the diffusion process there were two distinct textures either side of the bond line. After time, grains grow across the bond line and become randomly

oriented. Figure 4 shows the relationship between the interdiffusion distance [5], measured optically, and the ultimate tensile strength for copper to nickel diffusion bonds.

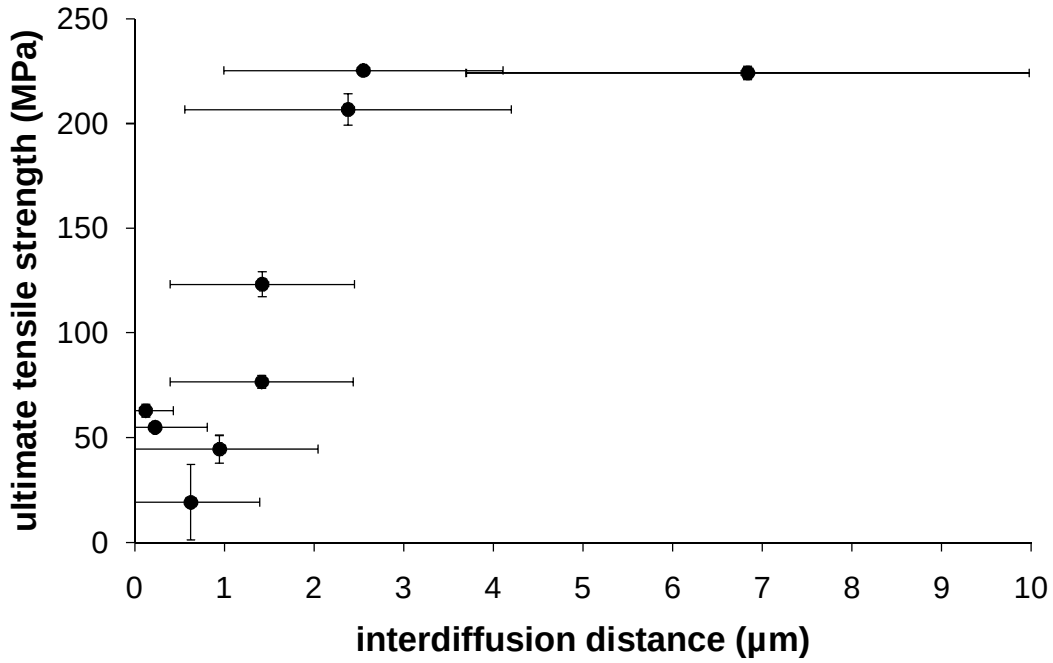

Figure 4. Relationship between ultimate tensile strength and the interdiffusion distance in Cu-Ni specimens. After Ojard *et al* [5].

With extended diffusion times recrystallisation [14] or precipitation of unwanted phases at the bond line [15] can occur. Precipitation does not occur in Ti-6Al-4V. Figure 5 shows the diffusion bond line of one of the Ti-6Al-4V samples generated for this project. Fine grains appear to have nucleated at the interface. This could be the result of surface diffusion filling the voids. This was the only example of fine grains that was observed.

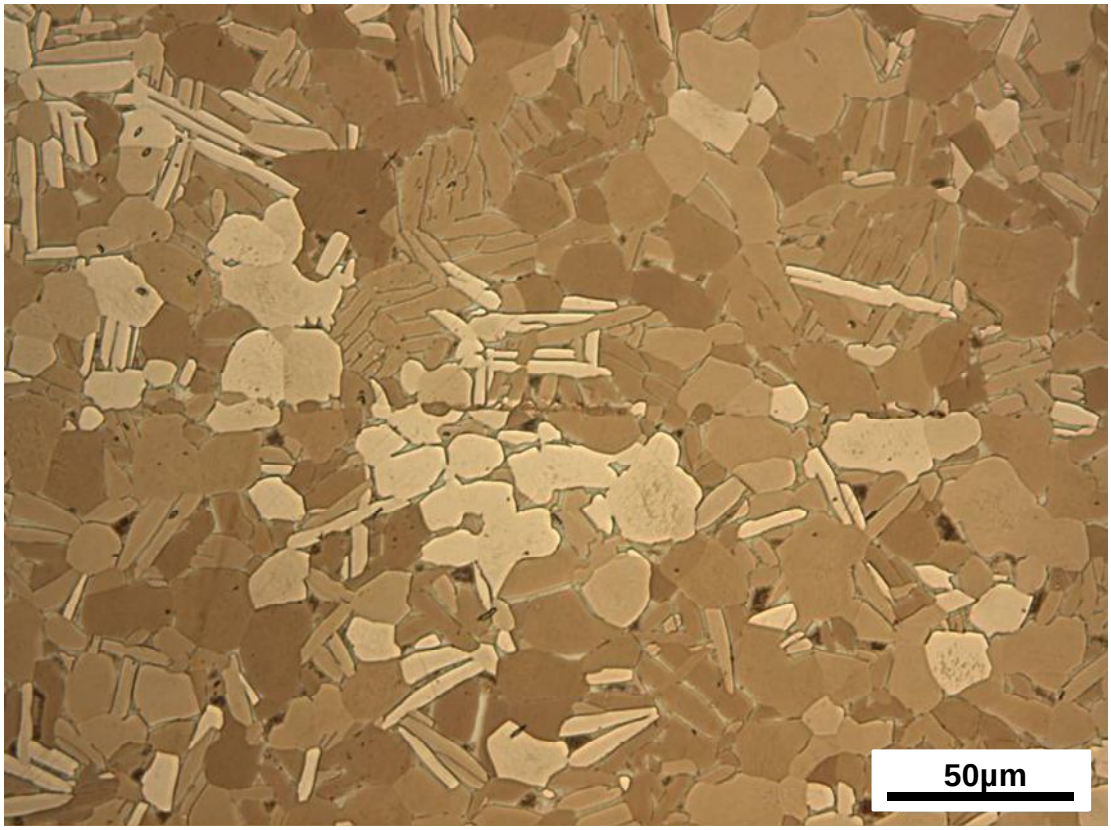

Figure 5. Fine grains at the bond line of a Ti-6Al-4V sample generated for this project (Sample # 11 – see Section 0). The sample has been heavily etched. The dark regions between grains are fine platelets of secondary alpha (see Section 3.1.1).

2.3. Conventional Ultrasonic Inspection Method for Titanium Forgings

The aim of this project is to improve the sensitivity of ultrasonic inspection of Ti-Ti diffusion bonds between forged pieces of Ti-6Al-4V. Titanium forgings are inspected using a pulse-echo ultrasonic immersion technique as per the company standard RPS705 [3].

In RPS705 the amplitude of the reflected ultrasound is measured. If the amplitude exceeds a threshold then the component is rejected. Three scans

with longitudinal bulk waves are carried out: one normal to the surface (0°), one incident at 5° in water and one incident at -5° in water.

RPS705 inspections are carried out with a probe with a nominal frequency between 4-6MHz. At these frequencies, a 0.025" flat-bottomed hole can normally be differentiated from the material noise at depths up to 4", even for Ti-6Al-4V, which has high levels of backscattered grain noise (see Section 3.1.2).

The first step in an RPS705 calibration is to set the water path – the distance between the transducer and the component surface. The amplitude reflected from a 2.5mm diameter steel ball is measured against water path. The transducer is moved to maximise the amplitude of the reflection from the steel ball. A working range is then found by moving the transducer away from and towards the steel ball until the signal amplitude decreases by 6dB in each direction. The inspection must be set up so that the water path from the transducer face to the component is in this working range.

With the water path set, the amplitude of the reflection from a 0.050" (1.27mm) flat-bottomed hole in a series of steel calibration blocks is measured. The blocks contain flat-bottomed holes at depths between 0.1" and 4". Due to attenuation and focussing the amplitude of the reflected signal will vary with the depth of the flat-bottomed hole. The measured amplitude is adjusted by -3dB to compensate for the difference in acoustic impedance between titanium and steel. The flat-bottomed hole depth for which the amplitude of the reflected signal is highest is assumed to be the focal depth. A distance amplitude correction (DAC) curve is created which

brings the amplitude of the signal reflected by the 0.050" flat-bottomed hole to the same screen height across the entire calibrated range. The shape of the DAC curve depends upon the water path, probe size, focal length and frequency. The distance amplitude curve does not improve the signal to noise ratio. It is used as a means of comparing and rejecting defects over a range of metal paths. Without distance amplitude correction, for a homogeneous polycrystalline metal, the grain noise is typically highest at the focal depth [16]. With distance amplitude correction the noise is lowest at the focal zone but the signal to noise ratio is not changed (see Figure 6).

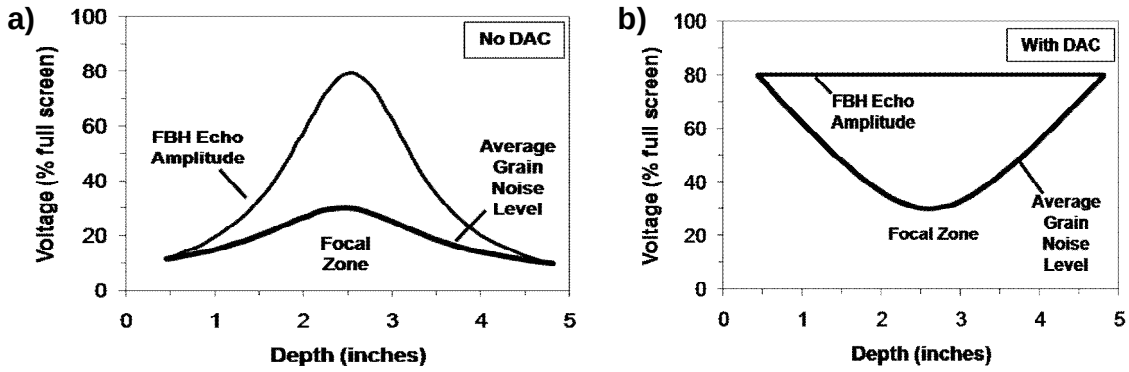

Figure 6. Typical dependence of backscattered material noise on depth in a pulse-echo inspection of a polycrystalline metal with a focussed probe: a) no distance amplitude correction (DAC), b) with distance amplitude correction (DAC). After Margetan *et al* [16].

Finally, the scan pitch is set. It is assumed that the beam diameter is smallest at the focal depth. The calibration block for which the flat-bottomed hole depth is closest to the focal depth is used. With the transducer normal to the surface and at the chosen water path, the transducer is centred over the flat-bottomed hole, so that the reflected amplitude is maximised. The transducer is translated first to the right and then to the left until the reflected amplitude decreases by 6dB. The beam diameter is taken as the separation of

these two points. The scan pitch is taken as half the beam diameter to ensure complete coverage at all depths.

The spatial resolution of the ultrasonic inspection is limited by the beam diameter. The diameter varies with depth due to beam spread and focussing. Spherically focused immersion transducers can achieve a smaller focal spot than planar transducers. The beam diameter at the focal plane can be calculated from the diffraction or Airy disc limit, D_L (mm) [17]:

$$D_L = \frac{1.22\lambda F}{2r} \tag{2.1}$$

where λ is the wavelength (m), F is the focal length (m) and r is the radius of the aperture (m). For instance, for a 5MHz spherically focused transducer with a 10mm aperture radius and a 75mm focal distance in water, the diffraction limit is 1.32mm. This is similar to the diameter of the flat-bottomed holes used for calibration. If the diameter of the beam at the focal depth is smaller than the flat-bottomed hole then the 6dB-drop method described will simply measure the diameter of the hole. It is then necessary to use a smaller diameter flat-bottomed hole.

3. Ultrasonic Inspection of Titanium and Titanium Diffusion Bonds

The aims of this project were to investigate methods for improving the sensitivity of ultrasonic inspection to diffusion bond defects and to separate between good diffusion bonds with texture mismatch at the bond line and partial bonds, where voids are distributed over a region of the bond line. The first section in this literature review (Section 3.1) will discuss the microstructure and microtexture of Ti-6Al-4V and its implications for ultrasonic inspection. In Section 3.2, the microtexture at a Ti-6Al-4V diffusion bond and its effect on the incident ultrasound will be described. It will be concluded that two regions with different preferred crystallographic orientation ('macrozones') either side of the bond line can result in a reflection, analogous to the reflection at an ideal interface between two dissimilar materials. Next diffusion bond defects will be classified in terms of ultrasonics. This is important to understand which techniques are applicable to which type of defect. Finally, linear and nonlinear ultrasonic methods for the inspection of diffusion bonds between both similar and dissimilar materials will be reviewed.

3.1. Ultrasonic Inspection of Titanium Alloys

3.1.1. Microstructure and microtexture of Ti-6Al-4V

Titanium has two constituent phases [18]: an hexagonal close packed (HCP) phase, α, and a body centred cubic (BCC) phase, β. The α is stable at room temperature and will transform to β at the β-transus temperature (882°C for pure titanium). In alloys, α and β can co-exist over a range of temperatures.

In Ti-6Al-4V, the alloying elements aluminium (Al) and vanadium (V) act to stabilise the α and β phases respectively. Their relative proportions and the microstructure can be controlled by heat treatment and deformation.

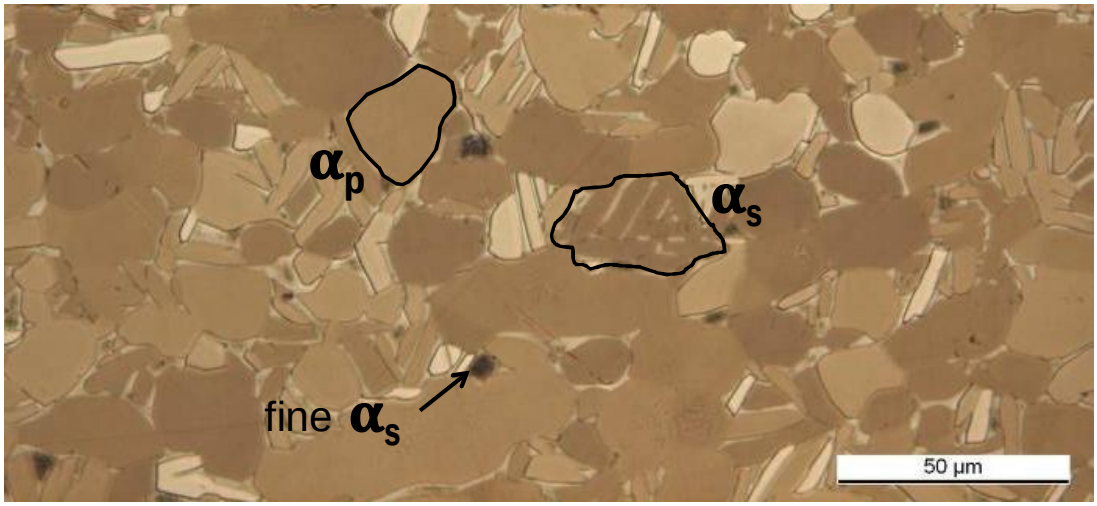

Figure 7. Micrograph of polished Ti-6Al-4V sample (sample #10) cut from a forged Rolls-Royce plc aeroengine disc, taken for this project using binocular microscope at 1000x magnification. Image shows primary alpha grains, α_p, and secondary alpha colonies, α_s. Retained β is present as thin films between the α_s platelets. In some places the retained β can undergo a martensitic type transformation to fine α_s.

The Ti-6Al-4V samples that have been used in the course of this project have a duplex microstructure. The processing route to obtain such a microstructure is as follows [19]:

1. Homogenisation above the β-transus temperature. Upon cooling to room temperature large β grains (>500µm) transform into fine α lamellae.
2. Deformation (or work) in the α-β phase field to generate dislocations, which encourage recrystallisation in Stage 3. Deformation introduces texture into the material. The degree of texture depends upon the amount of work and the type e.g. rolling, forging etc.
3. Recrystallisation near the β-transus temperature. Equiaxed primary α_p grains grow at 'triple-points' between β grains. The volume

fraction of α_p is determined by the recrystallisation temperature while the size of the α_p grains depends upon the width of the α lamellae after Stage 1. During cooling from the recrystallisation temperature, the β transforms into colonies of secondary α_s platelets. Their thickness is affected by the cooling rate. β is retained in thin films between the α_s. Deformation and recrystallisation can be repeated several times to refine the grain size [20].

4. Age hardening. This can include the precipitation of $TiAl_3$ particles and/or the transformation of retained β phase into fine secondary α_s.

Figure 7 shows the microstructure of a Ti-6Al-4V sample cut from a forged disc with equiaxed α_p grains, α_s colonies and fine α_s.

Historically the aim has been to produce an homogeneous α_p/α_s microstructure [20]. Processes were designed to control the volume content of equiaxed α_p grains, the size of the α_s colonies and the width of the α_s platelets. These parameters have been linked to mechanical properties [19]. More recently it has been realised that these optically homogeneous microstructures can have a preferred crystallographic orientation over much larger regions. This 'microtexture' can significantly affect the mechanical performance under some loading regimes [21]. Domains in which the majority of the main axes of the HCP crystals are aligned within a few degrees are termed 'macrozones' [22-24].

The mechanisms by which macrozones form are not fully understood. During β-α transformation, Burger's relationship [18] states that, for a given crystallographic orientation of the parent BCC grain, twelve possible HCP orientations or *variants* can occur with equal probability. However, in a

macrozone certain variants appear with much higher frequency than others [25]. The size and shape of these macrozones has been related back to deformation of the billet [24], before recrystallisation. Some thermo-mechanical processes e.g. hot rolling can encourage the formation of macrozones [22] that are millimetres in size.

At room temperature a large proportion of duplex Ti-6Al-4V is in the hexagonal close packed α phase. One of the Ti-6Al-4V diffusion bonded samples generated for this project (Sample #2 – see Section 4) was scanned using electron backscattered diffraction (EBSD). EBSD allows the phase of the microstructure at each point to be determined. Figure 8 is a phase map showing the occurrence of α and β titanium for a typical region of microstructure away from the diffusion bond line. This sample contains less than 4% of the body centred cubic β phase.

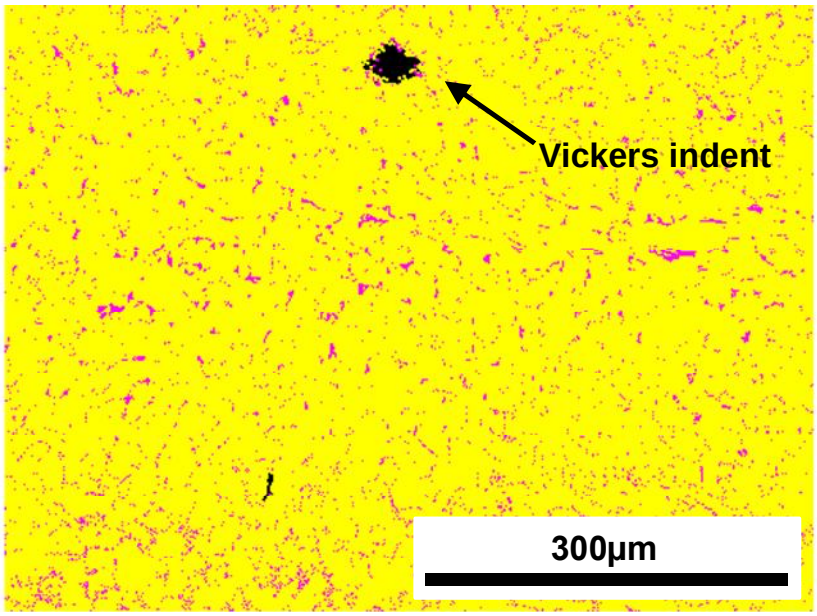

Figure 8. Metallurgical phase map of Ti-6Al-4V sample (sample #2), generated using electron backscatter diffraction (EBSD) at ITS Testing Ltd for Rolls-Royce plc. EBSD pixel size = 1.743µm. Yellow indicates hexagonal close packed α-phase (95.5% of scanned area). Pink indicates body centred cubic β (3.9% of scanned area). Black indicates that the phase could not be determined (0.6% of scanned area). Typical grain diameters were 10-100µm.

The HCP structure is highly anisotropic. The Young's Modulus, E, of a single titanium HCP crystal varies from 145GPa for loading along the main axis, orthogonal to the basal plane, to 100GPa parallel to the basal plane (see Figure 9) [18].

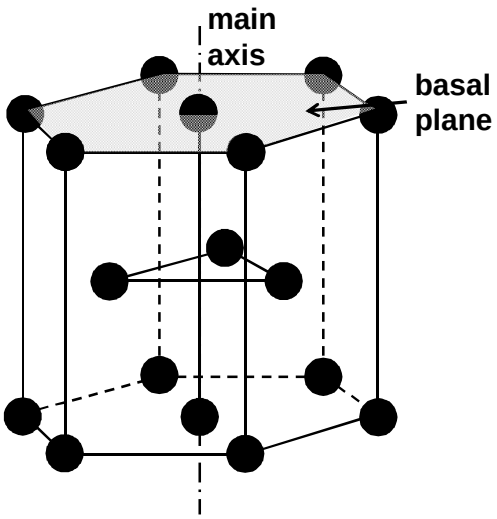

Figure 9. Atomic arrangement in hexagonal close packed (HCP) unit cell. After Callister [26].

3.1.2. Microtexture and ultrasonic wave propagation

Ultrasonic wave propagation in polycrystalline solids has been studied extensively and is reviewed in [27]. The elastic constants and therefore the acoustic velocity depend upon crystallographic orientation [28, 29]. The crystallographic orientation can vary from grain to grain, so that the acoustic impedance (the product of velocity and density) in the direction of wave propagation changes at each grain boundary. The incident ultrasonic wave is scattered, attenuating the forward propagating wave and generating 'material' or 'grain' noise. For a pulse-echo inspection, the energy scattered back towards the transducer is referred to as 'backscatter' [30]. Backscattered noise can mask reflections from defects, such as voids and inclusions and so limit the sensitivity of an ultrasonic inspection.

The attenuation coefficient due to scattering in polycrystalline solids with randomly oriented equiaxed grains has been derived for three separate frequency regions [31-33]:

Rayleigh: $\alpha \propto \overline{D}^3 f^4, \quad \lambda/\overline{D} \gg 1$ (3.1)

Stochastic: $\alpha \propto \overline{D} f^2, \quad \lambda/\overline{D} \sim 1$ (3.2)

Diffusive/geometric: $\alpha \propto 1/\overline{D}, \quad \lambda/\overline{D} < 1$ (3.3)

where $\overline{D}$ is the mean grain diameter and f and λ are the frequency and wavelength of the incident ultrasonic wave respectively.

A stochastic model for ultrasonic backscatter was developed by Rose for single phase [34, 35] and multiphase [36] polycrystalline solids. For multiphase solids, Rose assumed that the crystallographic orientation of each grain was independent from all the others; within the model no relationship can exist between the orientations of neighbouring grains. As discussed in Section 3.1.1, this is not the case for real titanium alloys; for a given crystallographic orientation of the parent BCC grain, only twelve HCP orientations can occur. Han and Thompson [37] extended Rose's model to a duplex microstructure, where the orientation of individual grains is related to the orientation of a larger parent grain, which they termed a 'macrograin'.

It is worth differentiating 'macrograins', as defined by Han and Thompson, and 'macrozones', introduced in the previous section. 'Macrograins' are specifically caused by phase transformation of large prior β grains to finer α lamellae during Stage I in Section 3.1.1. Han and Thompson describe groups of α lamellae as 'colonies'. The crystallographic orientation of the lamellae within a colony is the same. For a given prior β grain, the colonies may have one of twelve possible orientations. Their model assumes that the twelve

variants can occur with equal probability and that the prior β grains had random orientations. 'Macrozones' are areas of preferred crystallographic orientation. They may be caused by variant selection (see Section 3.1.1) during phase transformation, by thermo-mechanical processing or by a combination of these processes. The shape and preferred orientation of the macrozones gives the material its texture e.g. a rolled component may have elongated macrozones [22].

In their model for duplex microstructures, Han and Thompson [37] investigated the simplified case where the size of the α colonies is small such that each macrograin can be considered as a continuum. For equiaxed macrograins with mean radius a_m, scattering of an incident plane wave peaks for $a_m=\sqrt{3}/(2k)$, where k is the wave number. For an incident wave with a wavelength longer than the macrozone size, the medium will appear as a continuum with a single average orientation. As the frequency increases, the medium appears less like a continuum to the incident wave and scattering increases. For wavelengths much shorter than the macrograin size, the medium becomes like a single crystal and backscattering decreases. This simplified model may also be relevant for macrozones; if all the α_p and α_s crystals within a macrozone are approximately aligned then each macrozone could be approximated as a larger grain with an average effective elastic constant.

By modelling and experimentation it has been shown that both attenuation and backscattered noise depend upon the anisotropy of the crystallographic unit cell [29, 32, 33, 38-42], the grain size distribution [28, 29, 33, 38, 39, 43-45], the grain shape [44, 46, 47] and any preferred crystallographic

orientation or texture [40, 41, 48-50]. For example, for titanium alloys with elongated macrograins, the backscattered noise is highest for wave propagation normal to the elongation direction [37, 51].

Attenuation in polycrystalline solids is caused by scattering and beam spread. Once beam spread has been accounted for it is expected that higher backscattered noise will correspond to higher attenuation. Panetta *et al* [48] observed the opposite effect during pulse-echo inspection of a titanium alloy billet: propagation directions for which there was high backscattered noise corresponded to low attenuation. The attenuation was measured by averaging the amplitude of the backwall reflection. Panetta *et al* also observed that the amplitude of the backwall signal varied with position. By mapping the profile of the beam incident upon the backwall with a small 'pin' transducer [52] or a laser point detector [53] in through-transmission it was shown that, in the directions of high measured attenuation, the beam wavefront had suffered the severest phase and amplitude distortion. The actual attenuation, measured as the total energy arriving in through-transmission, was lower than that measured in pulse-echo and was independent of position. As piezoelectric transducers are phase sensitive, averaging effects across the surface of the larger element used in pulse-echo had resulted in the low measured backwall amplitude and high apparent attenuation.

Phase aberration of the propagating wavefront occurs in polycrystalline solids because the apparent velocity varies from grain to grain. For the HCP structure of α-titanium, the velocity variations between grains or macrozones can be significant. An optical scanning acoustic microscope has been

developed by Sharples [54] that allows the surface wave velocity of solids to be measured with a resolution of 100µm. A surface wave velocity map for a unidirectionally rolled sample of Ti-6Al-4V is shown in Figure 10. Elongated macrozones aligned with the rolling direction are apparent. The standard deviation in the measured velocity is 2.7% of the mean (2889m/s).

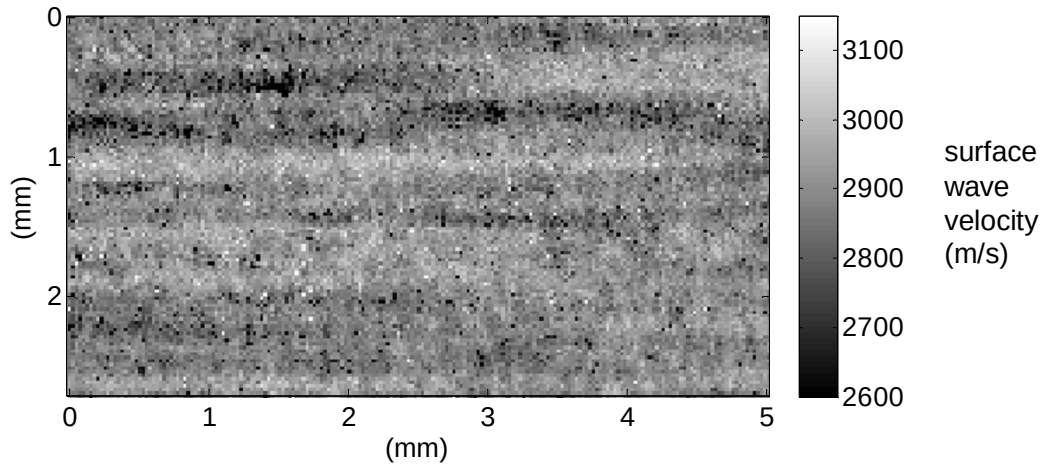

Figure 10. Surface wave velocity map of unidirectionally rolled Ti-6Al-4V sample obtained using optical-scanning acoustic microscope (O-SAM) at University of Nottingham [54]. The surface wave velocity was measured over a length of 100µm normal to the rolling direction (top-to-bottom of image). The pixel size is 25µm. Elongated macrozones can be seen aligned with the rolling direction (left to right).

In the course of this project, a series of Ti-6Al-4V blocks were cut from various positions in a disc forging (see Section 4.2). These blocks were inspected in a pulse-echo configuration. The backwall amplitude varies with position, as observed by Panetta *et al* [48]. The time of flight to the backwall also changes with position, which is expected given the anisotropy of velocity for the HCP α-titanium. The variance in the time of flight to the backwall depended upon where the Ti-6Al-4V blocks were cut from in the disc forging. Ultrasonic B-scans of the backwall of two blocks cut from different positions are shown in Figure 11. Variations in both the apparent attenuation

(amplitude) and time of flight to the backwall have implications for the inspection of diffusion bonds, as will be discussed in Section 3.2.

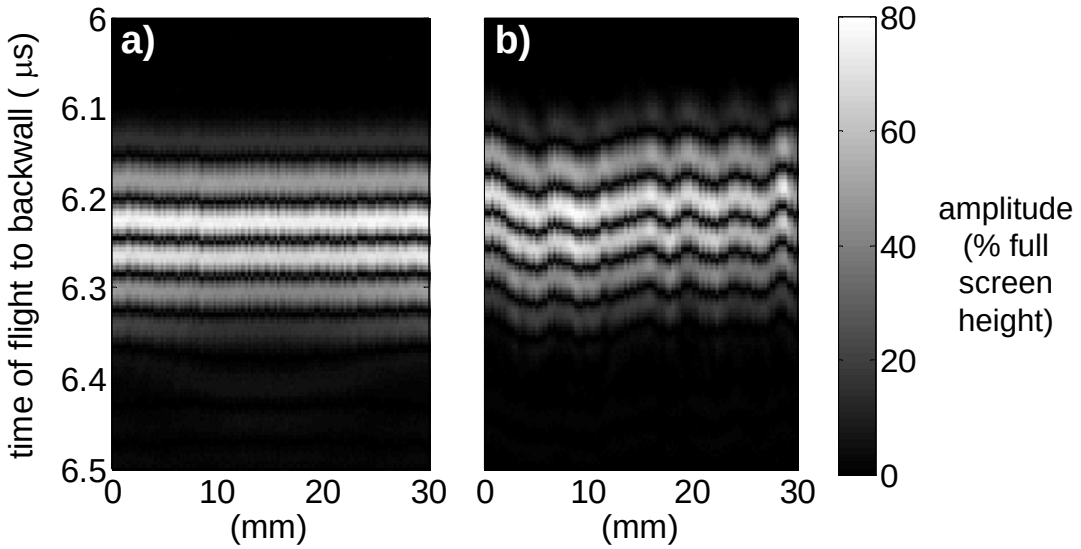

Figure 11. Ultrasonic B-scans (ultrasonic amplitude plotted against time of flight and lateral position) of backwall signal for two 19mm thick Ti-6Al-4V blocks with different microtexture. a) Time of flight to backwall is almost constant. b) Time of flight to backwall varies with position.

Assuming that the macrozones are randomly oriented, it should be possible to reduce backscattered noise by spatially averaging over areas larger than the macrozone size. The time of flight to grain boundaries varies with lateral position, as illustrated in Figure 11. Therefore backscattered signals taken from two positions, *x* and *x'*, which are separated by a sufficient distance are likely to be poorly correlated. Spatially averaging multiple signals causes cancellation due to differences in phase at a given time of flight. This is not helpful for the detection of discrete defects, where spatial averaging will reduce the reflected amplitude, however understanding the spatial correlation of backscattered noise may be useful for the inspection of diffusion bonds defects, which are distributed in a plane (see Section 3.2.6).

Thompson *et al* [55] define a normalised spatial correlation coefficient (*SCC*) for backscattered noise waveforms at positions *x* and *x'*, separated by distance |*x*–*x'*|:

$$SCC(|x - x'|) = \frac{\int V(t,x) \times V(t,x')dt}{\sqrt{\int [V(t,x)]^2 dt \times \int [V(t,x')]^2 dt}} \quad (3.4)$$

where $V(t,x)$ is the voltage vs. time, t, and position, x. Thompson *et al* show that the *SCC* depends upon the interaction of the microstructure (grain size distribution, shape etc) and the beam profile. Figure 12 illustrates the problem. For an ultrasonic ray passing through a solid with randomly oriented equiaxed grains (no macrozones) of mean diameter $\bar{D}$, the backscattered signal will change if the transducer is translated over a distance which is much greater than the microstructural length scale i.e. $|x-x'| \gg \bar{D}$. However, the ultrasonic beam is incident on a volume of microstructure, which may enclose part of one grain or a large numbers of grains. The beam diameter varies as a function of depth. Thompson *et al* defined the spatial correlation length (*SCL*) as separation |*x*–*x'*| for which the average *SCC*, calculated by comparing waveforms over many points, falls below $1/e$. The average *SCC*, calculated over many pairs of points with the same separation |*x*–*x'*|, is expected to tend to zero as |*x*–*x'*| increases i.e. there will be no correlation in the backscattered signal.

Intuitively the spatial correlation length (*SCL*) would be lowest at the focal plane, where the beam diameter is smallest. However, Yu *et al* showed [56] that, when the ultrasonic wavelength is much longer than the grain size, the *SCL* is highest at the focal plane. Away from the focal plane and particularly in the near field the phase varies more rapidly across the beam profile. The phase fluctuations within the beam diminish the correlation between two points, even if their beam profiles overlap.

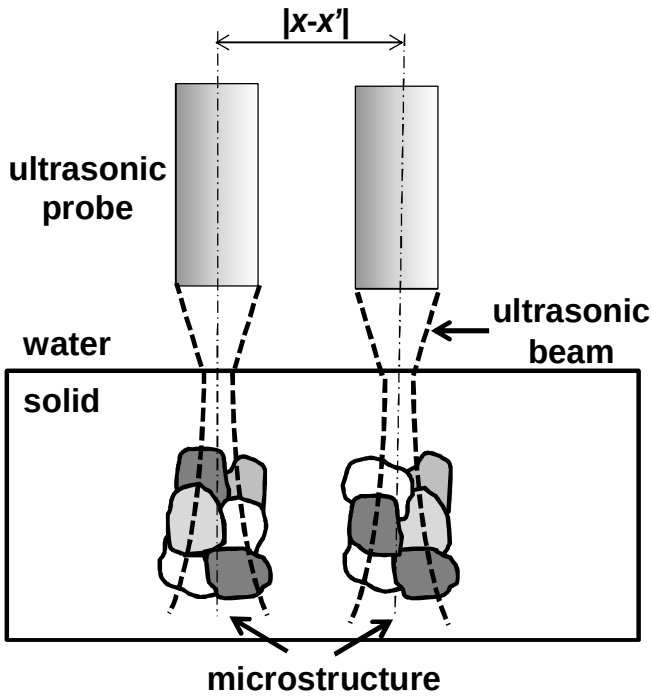

Figure 12. The correlation between backscattered ultrasonic signals from positions *x* and *x'* is affected by the microstructure and the ultrasonic beam profile. After Thompson *et al* [55]. Example backscattered noise signals are shown in Figure 13.

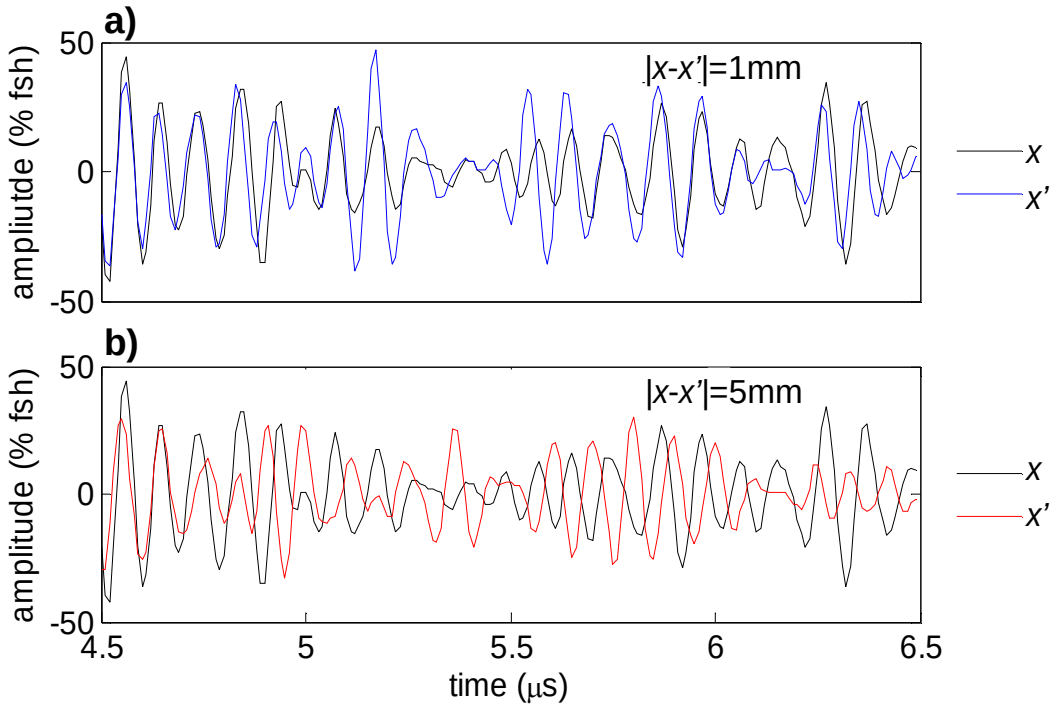

Figure 13. Backscattered noise signals at different locations over a Ti-6Al-4V block scanned with a 10MHz focussed probe for this project. Two spatial separations between the original position, *x*, and the new position, *x'* are shown. a) |*x*-*x'*|=1mm, *SCC*=0.71. b) |*x*-*x'*|=5mm, *SCC*=-0.05. Amplitude is in % of oscilloscope full screen height (fsh).

In summary, an ultrasonic wave propagating in a polycrystalline solid will be scattered, resulting in attenuation and backscattered noise. Both attenuation and backscatter are affected by the microtexture of the material, including the extent of preferential alignment within a macrozone, the size of individual grains and macrozones and the shape of the macrozones. The presence of macrozones in titanium results in higher backscattered noise levels than would be suggested by optical examination of the microstructure, where grains appear equiaxed and much smaller than the wavelengths of the interrogating ultrasonic wave [44]. Backscattered noise can mask defects such as voids and inclusions and is one of the limiting factors in the inspection of materials such as Ti-6Al-4V. The anisotropy of the HCP unit cell results in velocity variations from grain to grain, which distort the wavefront of the incident ultrasonic wave. Both the time of flight and the amplitude of a backwall reflection in pulse-echo vary as the transducer is scanned laterally. The backscattered noise will be spatially correlated due to the overlap of the incident sound field with the microstructure.

3.2. Ultrasonic Inspection of Titanium Diffusion Bonds

The most common ultrasonic method for defect detection is to look for an increase in reflected energy or a decrease in transmitted energy using a pulse-echo probe configuration or a through-transmission probe configuration respectively. The method conventionally used at Rolls-Royce plc for rectilinear forgings is a pulse-echo ultrasonic immersion technique, described in Section 2.3. In order to penetrate through the highly scattering Ti-6Al-4V, low MHz range frequencies (4-6MHz) are used. This limits the spatial resolution; defects which, in the direction normal to the incident

ultrasonic wave, are much smaller than the wavelength in size are unlikely to be detected.

Noise backscattered at the boundaries between crystalline structures (grains or macrozones) in metals further limits the sensitivity of pulse-echo inspection, as discussed in Section 3.1. The local change in microtexture at the diffusion bond could result in a spatially coherent reflection. This would make the separation of good and defective diffusion bonds even more problematic.

In this section, the microtexture at a Ti-6Al-4V diffusion bond and its effect upon incident ultrasonic waves will first be described. Next some common ultrasonic classifications of diffusion bond defects will be introduced, along with the important dimensions of defects in ultrasonic inspection. Finally the literature on the ultrasonic inspection of diffusion bonds between both similar and dissimilar metals will be reviewed.

3.2.1. Diffusion bond microtexture and backscattered ultrasound

In Section 3.1 the dependence of backscattered ultrasonic noise on microstructure was described. The concept of macrozones – regions of preferred crystallographic orientation – was introduced. For forged Ti–6Al–4V, a typical grain size is ~50μm but the macrozones can be millimetres in size.

In a good diffusion bond, there will have been grain growth across the interface. The strength of the bond [5, 7, 12] should be equal to that of the

parent metal. At the microstructural (grain) level, the interface will appear stepped (see Figure 2d). No planar discontinuity will be immediately obvious. In some cases, a chemical etch can reveal the position of the diffusion bond line, if the texture or 'flow lines' appear different on either side of the bond line. High resolution surface wave measurements can be used to map areas with the same acoustic velocity. Electron backscatter diffraction (EBSD) can be used to map the crystallographic orientation. This section shows the results of surface wave velocity measurement and EBSD for one diffusion bonded Ti-6Al-4V sample and then discusses the implications of microtexture at the bond line for the ultrasonic inspection of diffusion bond lines.

Diffusion bonded Ti-6Al-4V samples were generated by joining blanks cut from various positions in a large forging, as described in Section 4. Following pulse-echo ultrasonic inspection of the diffusion bond, Sample #2 was sectioned through the diffusion bond line and polished to allow high resolution surface wave mapping and EBSD. The polished section was 12mm thick by 20mm long and had the diffusion bond line running through at mid-thickness (~6mm). The surface wave velocity maps were generated on an optical scanning acoustic microscope [54]. For the first map (Figure 14a) the surface wave velocity was measured with a resolution of 100µm and a 100µm step size in the direction normal to the diffusion bond line over the entire sample. For the second map (Figure 14b) the velocity was measured with a resolution of 100µm and a 25µm step size over a 2mm thick x 20mm long band, which incorporated the diffusion bond line. Areas of preferred acoustic velocity can be seen in the parent metal. The diffusion bond is apparent as a planar interface between these large (millimetre scale) regions of preferred surface wave velocity halfway down Figure 14b.

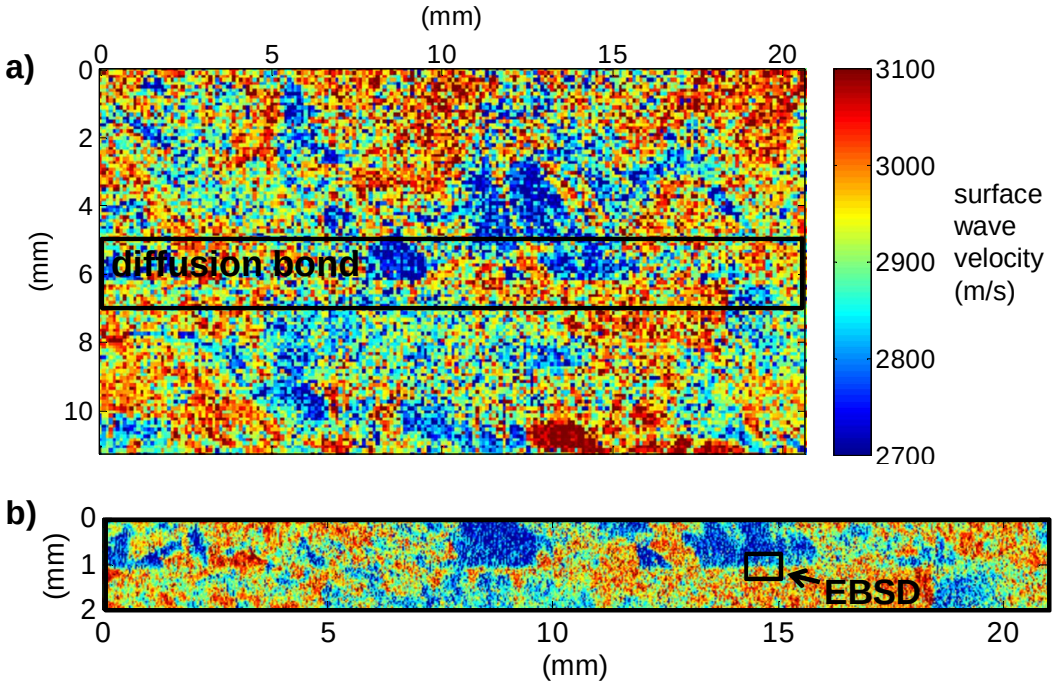

Figure 14. Surface wave velocity map of diffusion bonded Ti-6Al-4V sample (Sample #2) obtained using optical-scanning acoustic microscope (O-SAM) at University of Nottingham [54]. The surface wave velocity was measured over a length of 100µm normal to the diffusion bond line (top-to-bottom of image). a) pixel size is 100µm, macrozones are apparent either side of the bond line. Mean velocity across the entire 12mm x 20mm area is 2917m/s. b) Enlarged image of bond line region with pixel size of 25 µm. Black box indicates area of electron backscatter diffraction.

Electron backscatter diffraction (EBSD) can achieve far higher resolutions than the optical scanning acoustic microscope but it is very slow. The aim here was simply to gain a qualitative appreciation of the degree of alignment of the individual grains within a macrozone. For this project a 0.5mm x 0.7mm area (see Figure 14b) of Sample #2 on the diffusion bond line was scanned with a resolution of 1.7µm. A crystal orientation map was generated which shows the orientation of the α-titanium with respect to the sample transverse directions (Figure 15). The map shows that, above the diffusion bond line, the main axis of the HCP unit cell is strongly aligned with the sample transverse direction. Below the diffusion bond line the orientation appears random.

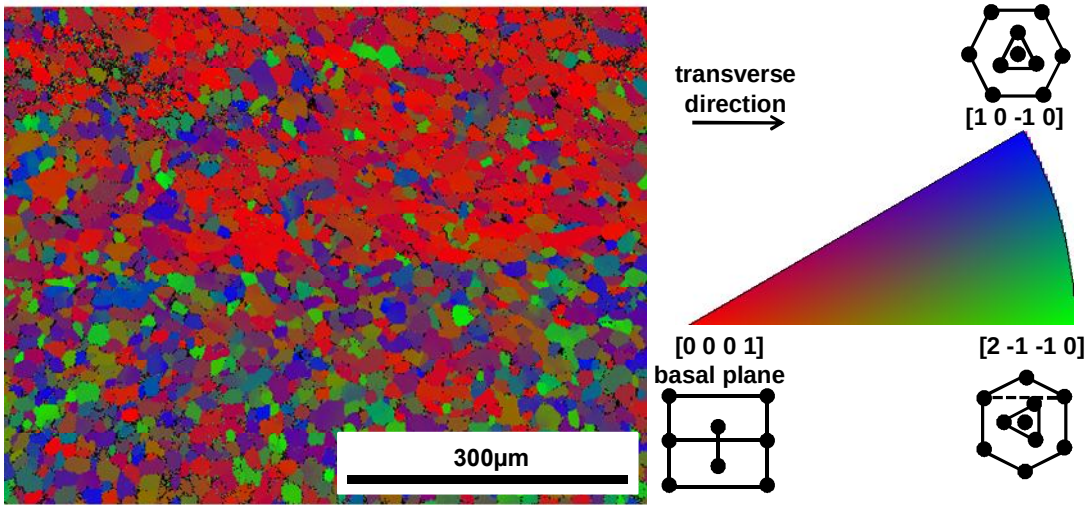

Figure 15. Crystal orientation map for 0.7mm wide by 0.5mm tall area of Sample #2 (see Figure 14) with 1.723µm resolution with respect to sample transverse direction (left to right). The colour map indicates which plane is oriented closest to the sample reference direction. The crystallographic orientation is only accurate for α-titanium (>95% in these samples – see Figure 8).

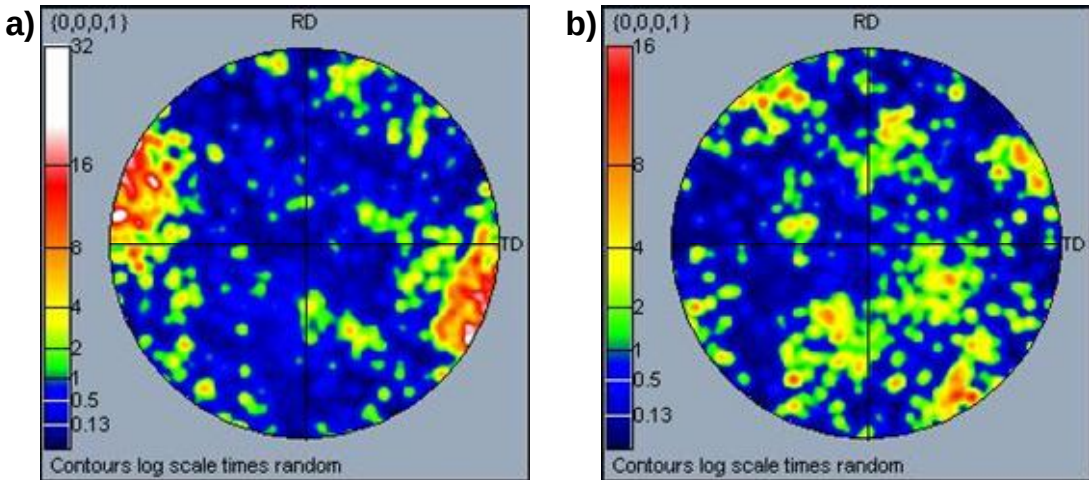

Figure 16. Pole figures for a) texture above the diffusion bond line and b) texture below the diffusion bond line, showing the distribution of orientations of the main axis of the HCP crystals [0,0,01] with respect to the sample axes of reference – rolling direction (RD), transverse direction (TD) and normal direction (central crosshair). The colour contours show the intensity of orientations over the scanned area in Figure 15 ($\log_{10}$ scale) normalised so that the intensity for a sample with random crystallographic orientation is 1 or $\log_{10}(0)$ at all points on the pole figure i.e. at each position on such a reference sample a random crystallographic orientation would be measured.

Texture can be expressed in terms of pole figures [57]. A pole figure at one spatial position shows the orientation of one crystallographic plane with

respect to the sample frame of reference e.g. the normal, transverse and rolling directions. If pole figures for all the points in the crystal orientation map are superimposed then the texture can be discerned from distribution of the points. Figure 16 shows the distribution of orientations of the main axis of the HCP unit cell for the areas above and below the bond line in Figure 15. The strong texture above the bond line is indicated by a clustering of points around the transverse direction (TD) poles.

The EBSD results show that some of the macrozones have very sharp texture with the main axes of the grains aligned while other regions have no distinct texture. Each region could be approximated as a continuum with an average elastic constant, as assumed by Han and Thompson [37]. The mean surface wave velocity normal to the diffusion bond line was calculated over the same 0.7mm x 0.5mm area. Above the bond line, the mean velocity is 2768m/s. Below the bond line, the mean velocity is 2940m/s. The mean across the entire 0.7mm x 0.5mm area is 2858m/s.

Titanium forgings are typically inspected using broadband probes with centre frequencies between 4-6MHz (Section 2.3), although higher frequencies are used for specific applications. For titanium, which has a longitudinal velocity of ~6000m/s, this corresponds to a wavelength of 1.0-1.5mm. Sample #2 therefore contains macrozones that are larger than the wavelength of the incident ultrasound. Even where the texture within a macrozone is weak, the size of the individual grains (typically 10-50µm) is much smaller than these wavelengths.

For the case where individual grains are much smaller than the wavelength and the macrozones are larger than the beam diameter, the problem becomes that of a bond between two homogeneous and dissimilar metals. The reflection coefficient, R_{12}, for a wave normally incident on a perfect interface between two homogeneous media is [58]:

$$R_{12} = \frac{z_1 - z_2}{z_1 + z_2} \tag{3.5}$$

where z is acoustic impedance (product of the material density and acoustic velocity). As more than 95% of the sample is α-titanium (see Figure 8), it is reasonable to assume that the density is constant across the entire sample. For the position scanned using EBSD, the reflection coefficient, $|R_{12}|$, due to the local change in average velocity for a wave normally incident on the bond line is 3%. The highest reflection coefficient, $|R_{12}|$, would be expected if the diffusion bond intersected two areas with high preferred crystallographic orientation and at the extremes of measured velocity. From the surface wave velocity map (Figure 14) this corresponds to local change in average velocity from 2700m/s to 3100 m/s, which would give$|R_{12}|$ equal to 6.9%. The most extreme longitudinal acoustic velocities, c_l, can be predicted from the Young's Modulus, E, using:

$$c_l = \sqrt{\frac{E(1-v)}{\rho(1+v)(1-2v)}} \tag{3.6}$$

The Young's Modulus of a titanium crystal for loading along the main axis is 145GPa and for loading orthogonal to the main axis is 100GPa [18]. The density, ρ, of the samples was known (4410kg/m^3). Poisson's ratio, v, was taken to be 0.34 [59]. Thus the corresponding acoustic velocities are 7143m/s and 5932m/s, which gives $|R_{12}|$ equal to 9.3%.

Even when the beam diameter is large compared to the macrozone size, it is likely that a proportion of the ultrasonic energy will be reflected directly back to the transducer. An ultrasonic B-scan for Sample #2, scanned in pulse-echo immersion with a longitudinal wave probe, is shown in Figure 17. There is a weakly coherent reflection at the bond depth. The mean reflection coefficient for the diffusion bond line across the entire of Sample #2 calculated at the probe centre frequency, as described in Section 5.3, was 0.8%. The maximum reflection coefficient was 4.4%. The sample was sectioned to inspect for defects; none were found. The weakly coherent reflection is thought to be due to local acoustic impedance change on the bond line.

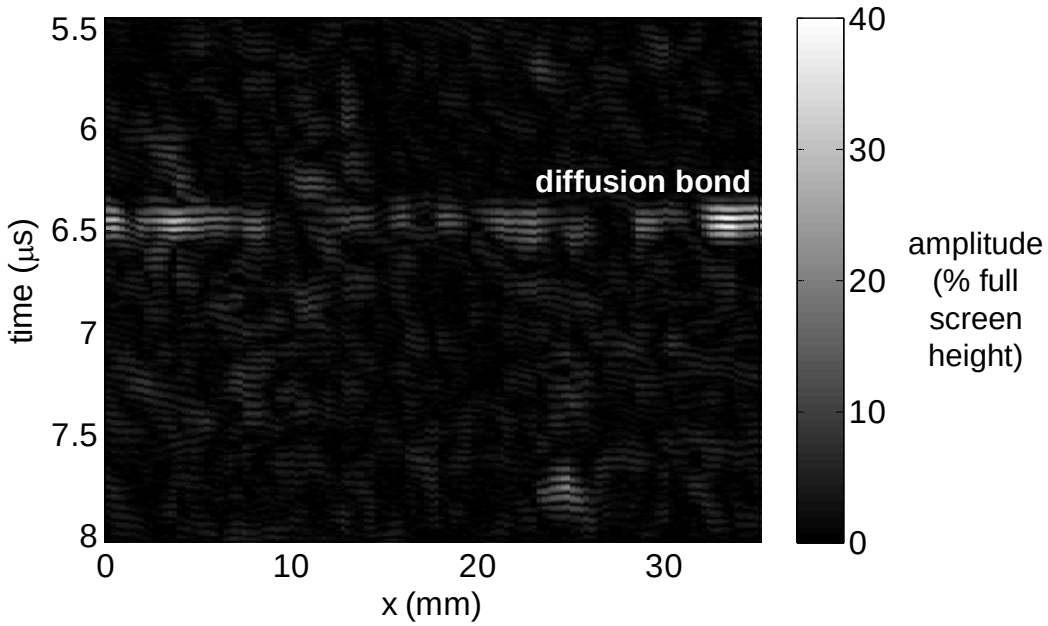

Figure 17. Ultrasonic B-scan (amplitude vs. time of flight and lateral position, *x*) of Sample #2 captured using 10.9MHz longitudinal wave probe focussed at the bond line depth. A coherent bond line reflection is apparent. The scan pitch is 0.25mm in both directions. The colour scale is linear and indicates % of oscilloscope screen height.

Similar results for all the diffusion bonded Ti-6Al-4V samples are summarised in Section 5.3. The time of flight to the bond line is not constant

i.e. the signals in the B-scan are not perfectly aligned. This could be due to the surface roughness of the original samples prior to bonding or it could be due to the anisotropy of the titanium crystallographic structure, as discussed in Section 3.1.2.

3.2.2. Diffusion bond defects and ultrasonic classification

In Section 2.2 defects which could occur during the diffusion bonding process were described. This section will attempt to classify diffusion bonding defects by their size relative to the ultrasonic wavelength and by their ultrasonic response.

Diffusion bonds are generated by pressing together two metals at high temperature and pressure. Normally the pressure is applied isostatically and so the flatness of the interface is controlled by the roughness of the two surfaces being joined. The surface finishes in this project were 1.6µm Ra or less and so the interface is thin compared to both the typical grain diameters (10-50 µm) and typical ultrasonic wavelengths.

Partial bonds, as defined by Nagy [60], are an array of unbonded spots or cracks, which are “not resolved individually by the interrogating ultrasonic beam”. A partial bond will therefore contain voids whose lateral dimensions are considerably smaller than the ultrasonic beam diameter. In this case the important dimensions are the lateral dimensions of the voids, their separation and distribution across the area to be inspected. The distribution of the voids will be affected by the process and the initial surface condition. The distribution can have some regularity if, for example, the surface

roughness of the samples to be joined has long range waviness. Sample #13 for this project (all samples are listed in Table 1, Section 4.2) was generated by joining blanks with parallel ripples on the surface with a wavelength of ~2mm. The surface condition of the blanks is shown in Figure 18. The surfaces were joined so that the ripples on one surface were 90° to the ripples on the other. An ultrasonic C-scan of the partial diffusion bond is shown in Figure 19. Horizontal bands of higher amplitude are apparent. Their spacing is ~2mm and so they are thought to be related to the surface waviness.

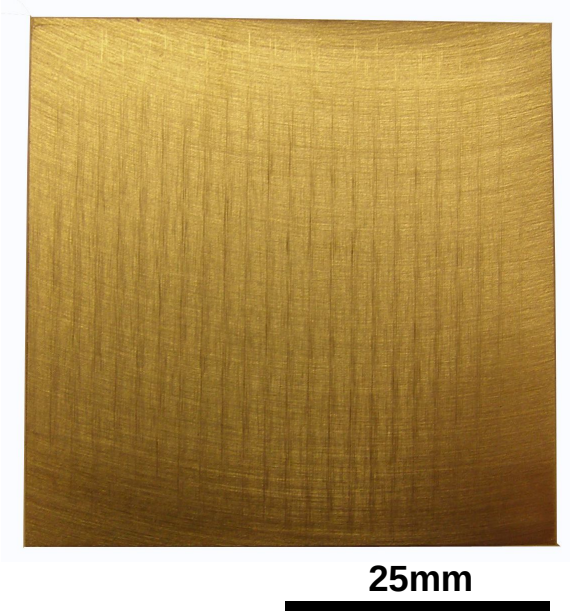

Figure 18. Photograph of Ti-6Al-4V blank with long range surface roughness. Wavelength of surface roughness ~2mm.

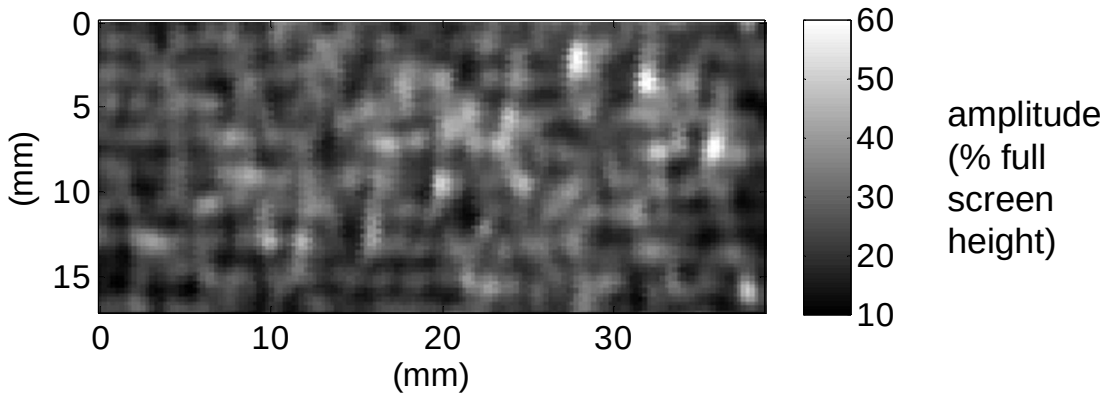

Figure 19. Ultrasonic C-scan (amplitude vs. lateral position) of diffusion bond line in Ti-6Al-4V sample #13 (see Table 1, Section 4.2). Sample #13 was generated by joining two blanks with long range surface roughness with wavelength ~2mm. The surface roughness of the unbonded blanks is shown in Figure 18. The scan pitch is 0.25mm in both directions. The colour scale is linear and indicates % of oscilloscope screen height.

'Kissing bonds' are two surfaces which are in intimate contact but have only weak 'sticking' strength [5, 7, 60, 61]. They are alternatively referred to as 'zero volume disbonds' [62]. The literature definitions of kissing diffusion bonds state either that the gap between the two faces is much less than the amplitude of the incident ultrasonic wave [60] or that there is no gap at all [5, 6, 63, 64]. In either case incident longitudinal waves can pass across the interface and therefore, in same-material bonds, the bond line is practically transparent to the incident ultrasound. Any reflection due to slight impedance mismatches or aligned grain boundaries may be amongst the noise. However, the lack of diffusion presents a line of weakness. When a load is applied perpendicular to the bond line, it is possible to pull the bond apart at stresses well below the tensile strength of the parent material [5, 6]. This line of weakness will also reduce the fracture toughness and fatigue resistance of the material [1].

The extent of the kissing bond will depend upon how it was formed. An extreme example of a kissing bond is the ‘cold inertia weld’ observed by Nagy and Adler [65]. Inertia welding is a very different process from diffusion bonding. In general, the weld is achieved by ramming a rotating tube into a stationary tube, with the tube axes aligned. Friction between the surfaces causes material mixing and the generation of a heat and plasticity affected zone, where the microstructure is significantly different from that of the parent metal. During welding, the pressure should be the same across the entire interface however the temperature increases faster towards the tube perimeter due to higher velocities. If the applied pressure is high but the temperature required for material mixing is not reached (or not maintained for long enough) then the surfaces will plastically deform and mechanically conform but no actual joining will occur. The unbonded central region is held in contact by the well bonded perimeter region.

The possibility of large (several millimetres in lateral extent) kissing bonds is a serious concern for engineers. It is conceivable that a large kissing bond could occur during diffusion bonding if the rate of diffusion was much lower than the rate of plastic deformation and insufficient time was allowed for the diffusion process, analogous to the cold weld scenario. However, attempts to generate a large kissing diffusion bond in this way at Rolls-Royce plc have not been successful to date [66]. The result was always a partial bond, with voids separated by areas where diffusion and grain growth had occurred. Kissing bonds have never been identified as the root cause of a failure. Based on the limited evidence, it is considered unlikely that problems with the diffusion bonding process will result in kissing bonds that are much larger in lateral dimension than the surface roughness.

Barnard *et al* [7] varied the total time allowed for the diffusion bond process and then inspected the bond line using a nonlinear ultrasonic method. Nonlinear methods are particularly sensitive to kissing bond type defects because, if the gap is less than the amplitude of the incident ultrasound, the void can be made to 'clap' and modulate the incident ultrasonic wave (see Section 3.2.7). In Barnard's experiments, the nonlinear parameter initially increased and then decreased with diffusion time. Barnard concluded that the nonlinear parameter reached a peak because, while diffusion occurred initially across the contacting asperities, the enclosed voids collapsed forming small kissing voids. Further diffusion resulted in the total closure of these collapsed microvoids and so a subsequent reduction in the nonlinear parameter. In this case, the kissing microvoids form as a progressive part of the diffusion bonding process and are small, of the same size scale as the surface roughness.

In the Ti-6Al-4V samples generated for this project, microvoids were observed where the gap between the two surfaces was as narrow as 0.1µm (Figure 20). If the gap is wider than the incident ultrasonic amplitude, then they cannot be considered as 'kissing'. Kawashima *et al* [67] quoted the ultrasonic amplitudes generated by their acoustic microscopy as in the order of 10nm. It was also observed that the necks of the voids in the Ti-6Al-4V diffusion bonded samples were spherical. Isolated voids with spherical necks were also observed by Wang *et al* [68] in diffusion bonded titanium specimens. In stainless steel specimens, the bond line was observed to be in intimate contact along the entire length but a gap could not be resolved using optical methods. Wang *et al* hypothesised that contamination of the steel samples prevented surface diffusion from occurring, so the dominant

mechanism was plastic collapse. For the titanium specimens, they suggested that surface diffusion had occurred faster than plastic deformation, maintaining the spherical neck and the width of the void. The likelihood of kissing bonds therefore depends upon the bonding parameters, the surface preparation and the presence of contaminants.

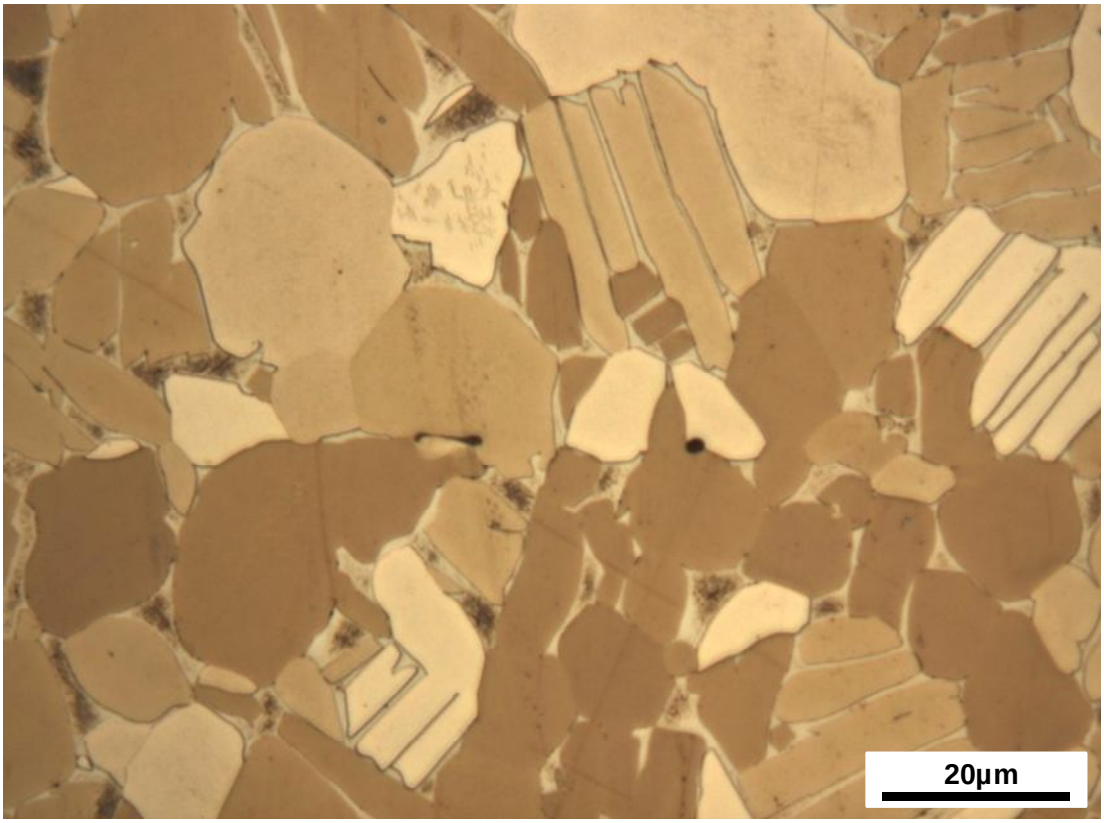

Figure 20. Micrograph showing microvoids in Ti-6Al-4V diffusion bonded sample (sample #11 – see Table 1, Section 4.2), taken at 1000x magnification under a binocular microscope. The sample has been heavily etched. The dark regions between grains are fine platelets of secondary alpha (see Section 3.1.1).

The bond strength will depend upon the degree of interdiffusion [5], the compressive stress across the bond and the percentage of the total cross-section which is unbonded [12]. Ojard *et al* [5] investigated diffusion bonding between copper and nickel. The interdiffusion distance can easily be measured in bonds between dissimilar metals. When joining was carried out at high pressures but relatively low temperatures for diffusion, they observed

that, in some samples, even though all the voids had disappeared, no interdiffusion had occurred along large regions of the bond line. The average interdiffusion distance was found to be closely linked to the ultimate tensile strength. They postulated that the surfaces were mechanically conforming but no diffusion had occurred. Due to the acoustic impedance mismatch between the two materials they could not differentiate these bonds from good bonds using conventional ultrasonic methods.

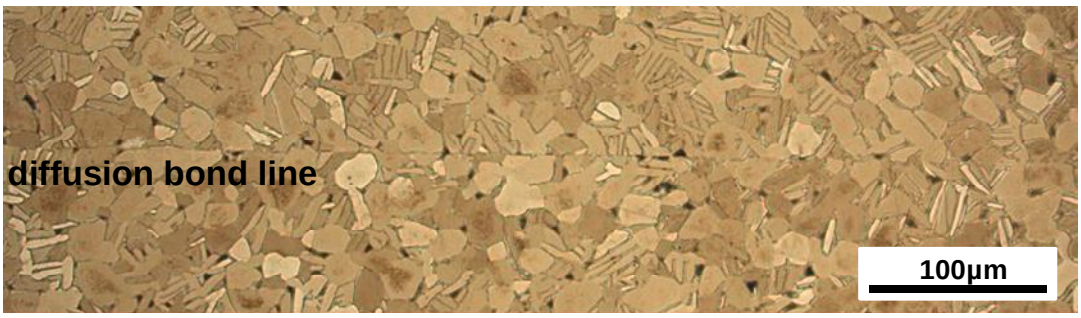

Figure 21. Micrograph of Ti-6Al-4V sample (sample #11 – see Table 1, Section 4.2) showing aligned grain boundaries at the diffusion bond line. There has been incomplete diffusion; no grain growth has occurred across the diffusion bond line. The sample has been heavily etched. The dark regions between grains are fine platelets of secondary alpha (see Section 3.1.1).

In same-material diffusion bonds, grain growth is an indication of interdiffusion. Nieters *et al* [6] observed diffusion bonds in Ti 17 where the voids had been entirely eliminated but a bond line was still apparent. These bonds may have some strength but it would be decreased below that of the parent material. In particular, aligned grains would reduce the fatigue resistance of the material. An isolated region of aligned grain boundaries was observed in the diffusion bonded Ti-6Al-4V sample #11 generated for this project (Figure 21). The rest of the sample was partially bonded – voids were interspersed along lengths of the bond line where grain growth had occurred. It is not known how to reproduce a similar sample with low

interdiffusion across a significant area. This would be extremely useful as it would allow mechanical testing to understand the strength and fatigue behaviour of this type of incomplete diffusion in Ti-6Al-4V.

Layers of contaminant can occur if the sample is not properly cleaned. Thomas and Springarn [10] observed samples with no voiding but contaminant layers less than one micron thick, which had prevented diffusion from occurring. The contaminated samples could not be differentiated from good samples by the conventional method of measuring the amplitude of the reflected ultrasonic signal. Similarly, a layer of oxide will form if the unbonded surfaces are exposed to heat and air. Such a sample was prepared during this project. The oxide layer is typically 3µm thick (see Figure 22).

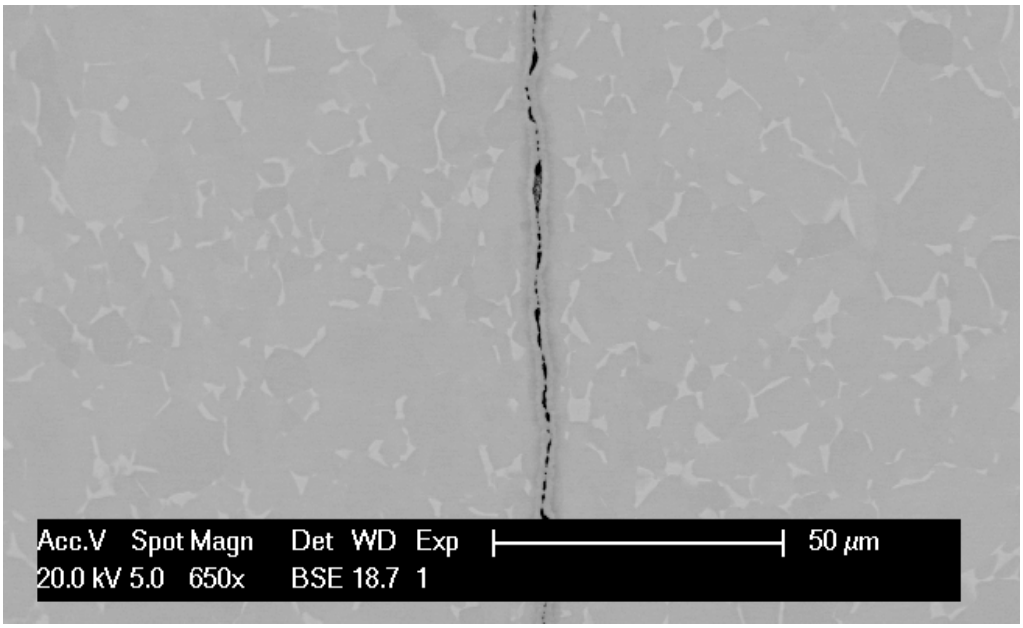

Figure 22. Micrograph of sample with severe oxidation on the bond line taken under a scanning electron microscope at 650x magnification. The bond line runs from the bottom to the top of the image. The oxide layer is typically 3µm thick.

In summary, partial bonds contain voids that are small laterally compared to the ultrasonic wavelength but that are wider than the amplitude of the

incident ultrasonic wave. Partial bonds are defined by the lateral size and distribution of the voids. Kissing bonds are narrow compared to the amplitude of the incident ultrasonic wave. They may have any lateral dimension. They may occur as a progressive part of the diffusion bonding process, in which case it is likely that 'open' voids will also be present and that the kissing voids are the same size scale as the surface roughness. Alternatively, they may be present over regions which are large compared to the size scale of the surface roughness, due to incorrect diffusion bonding parameters or the presence of contamination on the bond line. Incomplete diffusion can be considered as an interim step between a kissing and a good bond; all the voids have closed but insufficient interdiffusion or grain growth has occurred and the diffusion bond has not yet reached its maximum strength. Severe contamination or oxidation can result in a thin interlayer, separating the surfaces to be joined and severely reducing the strength of the bond.

Typical diffusion bond defects can therefore be small compared to the wavelength of the incident ultrasound in the plane of the diffusion bond. They may be narrow compared to the amplitude of the incident ultrasound in the direction orthogonal to the diffusion bond plane. There may be no material discontinuity except for aligned grain boundaries. The small size of diffusion bond defects makes their detection using ultrasonics difficult. The limitations of the pulse-echo immersion method conventionally used for the inspection of forgings have already been discussed. In the rest of this section, alternative methods that have been used for the ultrasonic inspection of diffusion bonds will be reviewed.

3.2.3. Acoustic microscopy

Scanning acoustic microscopes, which use high ultrasonic frequencies and focussed beams to achieve high spatial resolution, have been used to detect small diffusion bond line defects. Derby *et al* [69] carried out scans at 140MHz but could not differentiate the bond line from the grain noise in stainless steel samples. At 550MHz the bond line became evident [68]. The transducer was moved up and down to focus at slightly different depths, allowing the bond line to be differentiated from surface roughness effects. If the transducer is slightly out of focus at the surface then surface waves will be generated. The transmission of these surface waves can also be used to detect defects. Weglein [70] used this method to image the diffusion bond in titanium samples at 200MHz. The high frequencies involved mean that scanning acoustic microscopes can only be used for surface and slightly subsurface inspection. If the frequency is too high then the response is dominated by surface roughness effects.

3.2.4. Reflection coefficient

A common approach for the inspection of interfaces, including diffusion bonds, is the measurement of the reflection coefficient of the bond line, defined as the ratio of the reflected to the incident energy. The reflection and transmission coefficients for a perfect interface between two media with acoustic impedances z_1 and z_2 are:

$$R_{12} = \frac{Z_1 - Z_2}{Z_1 + Z_2} \tag{3.7}$$

$$T_{12} = \frac{2Z_1}{Z_1 + Z_2} \tag{3.8}$$

where *z* is the product of the material density and acoustic velocity. This assumes that both media are ideally elastic and displacement is continuous across the interface [58].

For an imperfect interface the reflection coefficient will be frequency dependent. Much research has been carried out to understand the effect of voids, inclusions and microcracks at the bond line on the frequency dependence of the reflected ultrasonic wave [12, 14, 58, 60, 63, 71-81]. At high frequencies where the wavelength, λ, is less than the spacing between defects, each defect can be assumed to scatter the incident ultrasound independently. The coherent superposition of the energy from the individual scatterers will generate a wave propagating in the specular direction. The amplitude of the reflected signal is then proportional to the bonded area [74].

If the defect spacing is on the scale of the surface roughness i.e. 5-50 μm then a wavelength of 0.5μm would be required to resolve individual defects [80]. This corresponds to frequencies of GHz in metals, which is impractical for inspection as the energy attenuates quickly. If the defect spacing, s, is close to the wavelength, λ, then multiple scattering events - where ultrasound is reflected off one defect onto another and then reflected back towards the transducer – cannot be neglected. If the spacing is equal to λ/2 then resonances will be set-up between neighbouring voids. For a regular array of voids, these resonances have been observed experimentally [14].

For low frequencies, where the wavelength is long compared to the defect size and separation [71, 79, 80] imperfect interfaces have been modelled as

a spring layer with an interfacial stiffness, *K*. For the simple case of a longitudinal or transverse wave normally incident on a bond line which is thin relative to the wavelength, so that the mass of defects is negligible, the reflection coefficient can be related to the interfacial spring stiffness by [58, 60, 71, 79-82]:

$$R_{12}(\omega) = -\frac{z_1 - z_2 + i\omega(z_1 z_2/K)}{z_1 + z_2 + i\omega(z_1 z_2/K)} \tag{3.9}$$

where ω is the angular frequency and i is $\sqrt{-1}$. For the case where the two media have the same acoustic impedance, $z_1 = z_2 = z$ [65]:

$$R(\omega) = \frac{-i\omega(z/2K)}{1 + i\omega(z/2K)} \tag{3.10}$$

Figure 23 shows the magnitude and phase of the reflection coefficient for an imperfect interface with various interfacial stiffnesses, *K*, between similar materials. The effect of various defect distributions on the interfacial stiffness, *K*, has been investigated [14, 71, 73]. Angel and Achenbach [83] derived an exact solution for the reflection coefficient due to a periodic array of planar cracks on the interface. They showed that, at low frequencies, this exact solution agreed with the spring model (Equation 3.9). Results for statistical distributions of crack were obtained by Sotoripolous and Achenbach [75] and Rose [74].

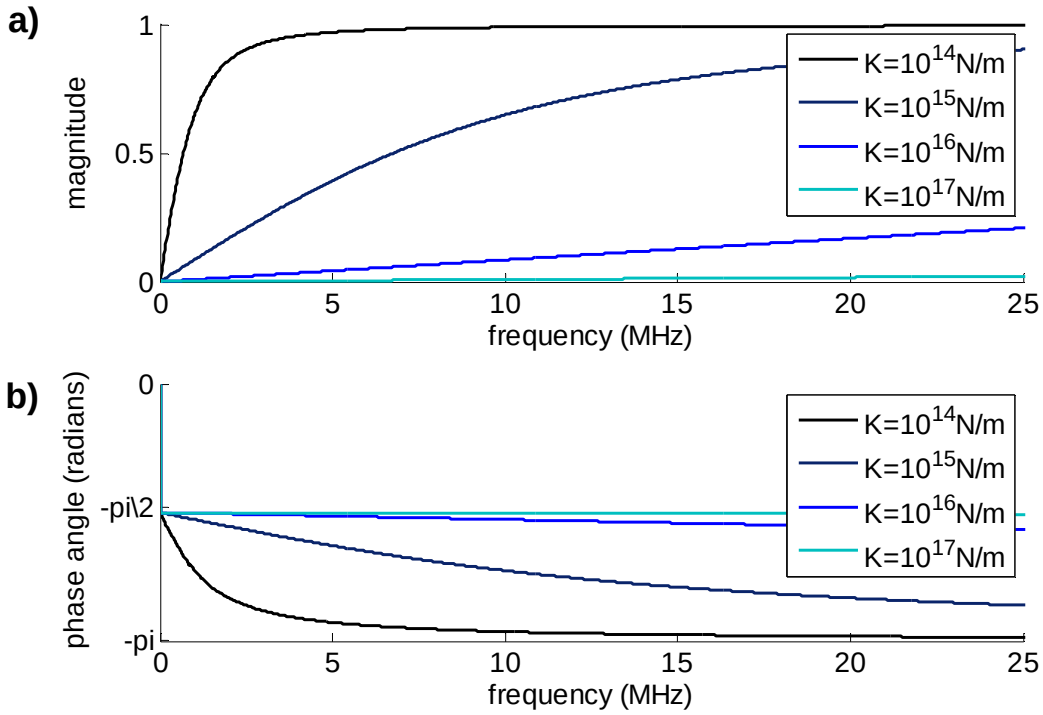

Figure 23. a) magnitude and b) phase angle of reflection coefficient, $R(\omega)$, for imperfect interface, calculated using spring model (Equation 3.9) for an interface between similar materials with acoustic impedance, z=27.3MRayls, which is a typical value for a titanium alloy.

The interfacial stiffness depends upon the defect size, shape, density and distribution [71, 74-77]. Palmer [73] *et al* measured the reflection coefficient of partially bonded Cu-Cu samples and then loaded them to failure. By examining the fracture surface they measured the ratio of unbonded to bonded surface area and therefore approximated the stiffness. For the most part they found good correlation between the measured reflection coefficient and the predictions of the spring model. The complex defect geometry cannot be determined through knowledge of the interfacial stiffness alone, making it difficult to relate the interfacial stiffness directly to mechanical properties such as strength and fatigue resistance. Still, several experimental studies have related the reflection coefficient to the bond strength [5, 12, 63,

79, 84]. Lavrentyev and Beals [79] argue that this is valid if the variation in possible bond defect geometries is limited.

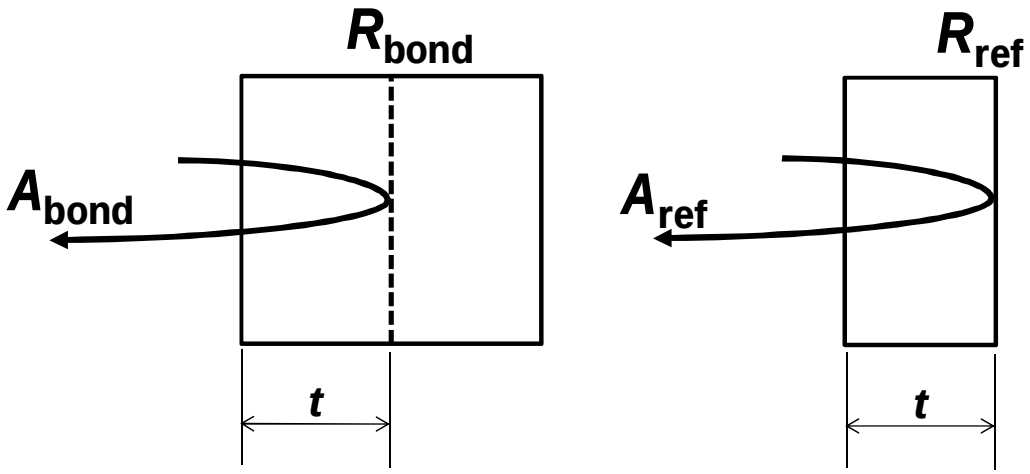

Figure 24. Illustration of the measurement of the bond line reflection coefficient, R_{bond}, by comparison of the signal amplitude reflected from the diffusion bond, A_{bond}, with the amplitude reflected from the backwall of a block of the same thickness, t, and a similar material, A_{ref}.

For a pulse-echo inspection of the bond line, the reflection coefficient for an imperfect interface, $R_{bond}(\omega)$, can be determined experimentally by comparison of the signal received from the bond line, $A_{bond}(\omega)$, to a reference reflection, $A_{ref}(\omega)$, as illustrated in Figure 24. $A_{bond}(\omega)$ is given by:

$$A_{\mathrm{bond}}(\omega) = A_1(\omega)T_{12}(\omega)Q_2(\omega,t)R_{bond}(\omega)Q_2(\omega,t)T_{21}(\omega) \qquad (3.11)$$

where A_1 is the ultrasonic waveform output by the transducer, T is the transmission coefficient, R is the reflection coefficient, Q describes the material attenuation (scattering and beam spread), ω is the angular frequency and t is time of flight or distance between the surface and the bond line. This equation assumes that the transducer frequency response is the same in transmit and receive. For a reference specimen made of the same material as the diffusion bonded sample and with thickness, t, equal to the distance between the front face and the bond line:

$$(\omega) = A_1(\omega)T_{12}(\omega)Q_2(\omega,t)R_{ref}(\omega)Q_2(\omega,t)T_{21}(\omega) \qquad (3.12)$$

By dividing Equation 3.11 by Equation 3.12 we get:

$$\frac{A_{bond}(\omega)}{A_{ref}(\omega)} = \frac{R_{bond}(\omega)}{R_{ref}(\omega)} \tag{3.13}$$

R_{ref} can be considered an ideal reflector and so the magnitude of the reflection coefficient is 1 at all frequencies. Therefore, assuming that the microstructure of the reference sample is identical to that of the diffusion bonded sample, the reflection coefficient of the bond as a function of frequency can be determined.

In the literature referenced [12, 14, 58, 60, 63, 71-81, 84], only the magnitude of the reflection coefficient as a function of frequency is measured or modelled. The phase spectrum $\varphi(t_w;\omega)$ of a signal $h(t)$ can also be extracted from the Fourier transform, H:

$$|H(t_w;\omega)|e^{i\varphi(t_w;\omega)} = \int_{t_w-T_w/2}^{t_w+T_w/2} w(t-t_w)h(t)e^{-i\omega(t-t_w)}dt \tag{3.14}$$

where w is a windowing function and t_w indicates the centre of the window relative to an absolute time scale, t, which is started at the excitation pulse. T_w is the width of the window. If the window is rectangular and long such that it does not distort the waveform, the phase, φ, at a given angular frequency, ω, will depend upon the arrival time of the pulse relative to the window centre, t_w. This is illustrated in Figure 25 and Figure 26. Figure 25 shows three broadband pulses. They are all identical except they have been shifted by 0.02µs relative to one another. The same window is used for each signal. The magnitude spectra are identical for all three signals. The phase spectra are shown in Figure 26. The phase at the centre frequency, ω_0, changes depending upon the position of the signal relative to the centre of the window.

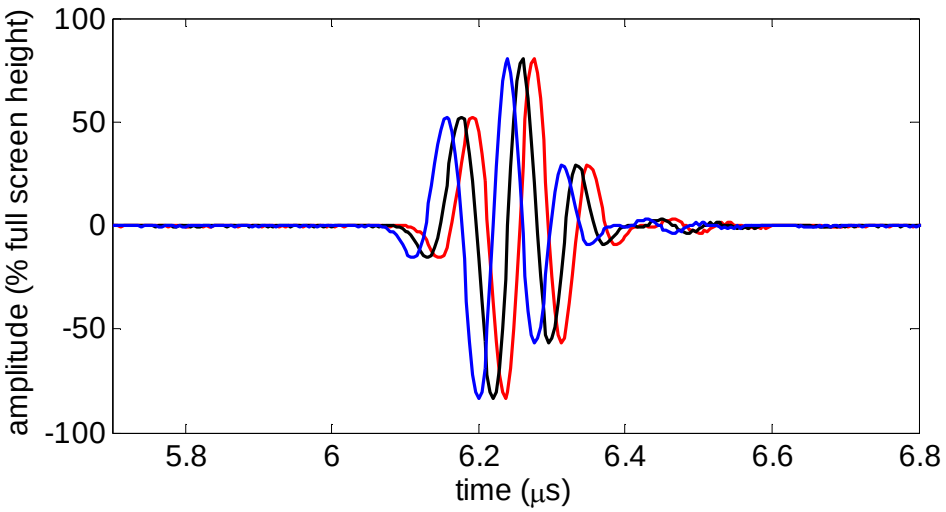

Figure 25. Original signal (red) is shifted forward in time twice 0.02μs to create two new signals (blue and black).

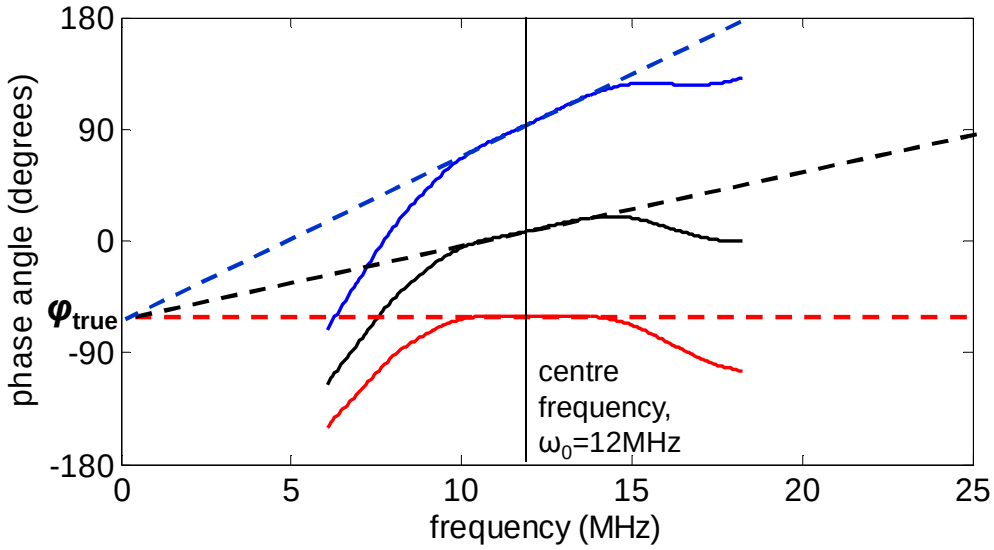

Figure 26. Phase spectra for the three signals in Figure 25, which were windowed with a rectangular window with centre t_w=6.256μs prior to calculating the Fourier transform. The phase angle, φ, depends upon the arrival time of the wave relative to the window centre, t_w. A 'true phase', φ_{true}, can be obtained that is independent of frequency.

Pilant *et al* showed that, if a line is fitted through the frequency dependent phase spectrum over a frequency range either side of the centre frequency of the broadband pulse, ω_0, and the line is extrapolated to zero, as shown in

Figure 26, the phase at the zero-crossing is independent of the arrival time of the wave [85]. Instanes *et al* termed this the 'true phase', φ_{true} [86, 87]:

$$\varphi = \varphi_{\text{true}} + \beta\omega_0 \tag{3.15}$$

β is the slope of the best-fit line and is directly proportional to the time lag between the half-energy point of the pulse and the window centre. If the windowing function distorts the pulse then it will affect $\varphi(t_w;\omega)$ and also φ_{true} [86].

Authors have investigated the use of single or combined parameters derived from the reflection coefficient as a function of frequency $R(\omega)$ to differentiate good and bad solid-state bonds [8, 63, 88-92]. Thomas and Springarn [8, 88, 89, 91, 92] measured several properties of the reflected signal, including peak amplitude and the frequency content of the reflection coefficient. They used an intelligent algorithm to differentiate between various 'good' and 'bad' diffusion bonds. They noted that although the bonds had significantly different tensile strengths the amplitude of the reflection from the bond line changed very little [91]. The algorithm only worked to differentiate between extremes of bond quality. They observed that the most sensitive indicators all measured the high frequency energy.

Nagy [60] suggested that the ratio of the longitudinal reflection coefficient, R_L, to the transverse reflection coefficient, R_T, could be used to differentiate between partial and kissing bonds. Nagy showed that interfaces with a smaller out-of-plane dimension have a higher transverse stiffness. He assumed that partial bonds are essentially arrays of flat cracks surrounded by well bonded regions whereas kissing bonds have a larger out-of-plane dimension, as they are formed by greater plastic flow. Therefore R_L/R_T is

expected to be higher for partial bonds than for kissing bonds. Brotherhood *et al* [93, 94] calculated the ratio R_L/R_T for dry kissing bonds between aluminium plates of various surface roughness under compressive load. As the compressive load increased, the ratio of R_L/R_T was also seen to increase. This corroborates Nagy's prediction; as the pressure is increased, air voids are flattened and so the shear stiffness is expected to increase.

Relating the bond quality to the reflection coefficient becomes particularly difficult for dissimilar materials, where there is always a reflection from the interface [5, 63], or for anisotropic polycrystalline materials (see Section 3.1.2), where the reflection from defects may not appear above the material noise. Thomas and Springarn [92] used a similar intelligent algorithm to that described previously to separate 'good' and 'bad' aluminium to steel diffusion bonds. Two different types of aluminium were used to generate the samples. If the inspection was carried out in pulse-echo from the steel side of the diffusion bonded samples then the good and bad samples could be separated. They could not be separated if the inspection was carried out from the aluminium side. This was attributed to the differences in microstructure between the two types of aluminium. Jamieson [63] fit a straight line to the reflection coefficient $|R(f)|$ over the range 5 to 15MHz and extrapolated back to zero. Jamieson attempted to correlate the rate of change of $|R|$ and the value of the best-fit line at zero frequency with the tensile strength of copper to beryllium diffusion bonds. At low frequencies, the slope of $|R(f)|$ is proportional to the interfacial stiffness [79]. The correlation of the rate of change of $|R|$ with ω with the tensile strength was poor. The correlation of the zero crossing of the best fit line was better but

other measures were reported to be more sensitive to variations in ultimate tensile strength.

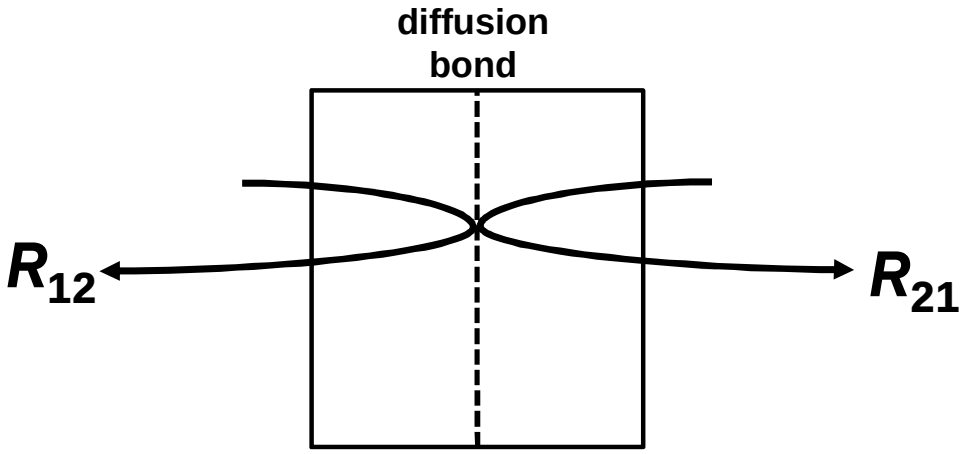

Figure 27. Illustration of the symmetric reflection technique. Two reflection coefficients are measured; one from each side of the sample (R_{12} and R_{21}).

Nagy and Adler suggested the symmetric reflection technique [65] for the inspection of imperfect interfaces between dissimilar materials. The reflection coefficient is measured from both sides of the interface, as illustrated in Figure 27. The reflection coefficient, R_{12}, for a perfect interface is given in Equation 3.7. If the acoustic impedance of medium 1 is higher than that of medium 2, the reflection coefficient R_{12} will be negative. For a wave propagating in the opposite direction, the reflection coefficient, R_{21} will be positive. For long wavelengths, the reflection coefficient for a defective interface is given in Equation 3.9. The first part of the term, $(z_1 - z_2)/(z_1 + z_2)$, is due to the acoustic impedance mismatch. The second part of the term is the reduction in stiffness due to the presence of defects and is identical for both R_{12} and R_{21}. The symmetric reflection coefficient is:

$$R_s(\omega) = \frac{R_{12}+R_{21}}{2} \tag{3.16}$$

$$R_s(\omega) = \frac{\frac{i\omega}{z_1+z_2}\left(\frac{z_1 z_2}{\mathrm{K}}\right)}{1+\frac{i\omega}{z_1+z_2}\left(\frac{z_1 z_2}{\mathrm{K}}\right)} \tag{3.17}$$

For long wavelengths:

$$R_s(\omega) \approx \frac{i\omega}{z_1+z_2}\left(\frac{z_1 z_2}{K}\right) \tag{3.18}$$

In the long wavelength regime the symmetric coefficient is wholly imaginary. The asymmetric reflection coefficient is:

$$R_a(\omega) = \frac{R_{12}-R_{21}}{2} \tag{3.19}$$

$$R_a(\omega) = \frac{z_2-z_1}{z_1+z_2+i\omega\left(\frac{z_1 z_2}{K}\right)} \tag{3.20}$$

For long wavelengths:

$$R_a(\omega) \approx \frac{z_2-z_1}{z_1+z_2} \tag{3.21}$$

The asymmetric coefficient is approximately equal to that of the perfect interface and is wholly real. Therefore the component of the reflection due to the acoustic impedance change at the interface will be π/2 radians out of phase with the component of the reflection due to the presence of defects. Nagy and Adler used the symmetric reflection technique for the inspection of stainless steel-aluminium friction welds and stainless steel-copper inertia welds. R_s was more sensitive to the nominal lack of bonded area than the one-sided reflection coefficient R_{12}. They spatially averaged measurements over an area to reduce the error in the signal amplitude.

In summary, the reflection coefficient for a perfect interface is independent of frequency. The reflection coefficient of an imperfect interface is frequency dependent. The frequency dependence is complex and depends upon the lateral size of the defects and their distribution. At conventional inspection frequencies, the wavelength will be long compared to the size of the defects and the interfacial thickness. The spring or quasi-static model can therefore be used to relate the frequency dependent reflection coefficient to an

interfacial stiffness, which is indicative of the bond quality. The interfacial stiffness does not, however, give us direct information about the defect geometry and, without *a priori* knowledge, cannot be used to predict the mechanical properties of the bond. For long wavelengths, the component of the reflection coefficient due to any acoustic impedance mismatch will be real while the component due to defects will be imaginary i.e. there will be a phase separation of $\pi/2$ radians. If the phase of the reflected wave can be determined independent of arrival time or window position, then it may be possible to use this phase separation to distinguish good and poor bonds. In the symmetric reflection technique, reflection coefficients are obtained from both sides of the bond line. The components due to acoustic impedance mismatch are both real but opposite in sign i.e. they are asymmetric. The components due to the defects are both imaginary and have the same sign. In the symmetric reflection coefficient, the real components due to the acoustic impedance mismatch cancel leaving the imaginary components due to the defect.

3.2.5. Backscatter coefficient

The backscatter coefficient measures the energy reflected from the sample that travels directly back towards the probe. Ojard *et al* [95] used the backscattered energy to detect defects in Cu-Ni diffusion bonds. They measured the normalised energy reflected from the bond line, which can be calculated by squaring and integrating the spectrum in the frequency domain. This parameter is proportional to the square of the reflection coefficient. It is therefore more sensitive to an increase in high frequency backscatter and thus the presence of small defects at the bond line.

Parseval's theory states that the energy of the wave in the time domain is equal to the energy in the frequency domain. Therefore the normalised energy can also be calculated by squaring and integrating the time domain signal.

3.2.6. Spatial techniques: spatial averaging, cross-correlation and time of flight variance

Spatial averaging can be used to reduce the contribution of backscattered material noise from the parent metal either side of a diffusion bond. In the parent metal, even when there is strong texture, grains and macrozones are distributed somewhat irregularly. If the ultrasonic transducer is moved a distance that is large compared to the beam diameter and the size of the largest crystallographic unit (grain or macrozone), then the signals captured in the original and the new position will be poorly correlated in phase; the arrival times from grain boundaries in each position is different. The time of flight to a planar weld should be constant. When signals are spatially averaged, phase cancellation will reduce the backscattered noise but the weld reflection, which arrives at the same time in phase, will remain as shown in Figure 28.

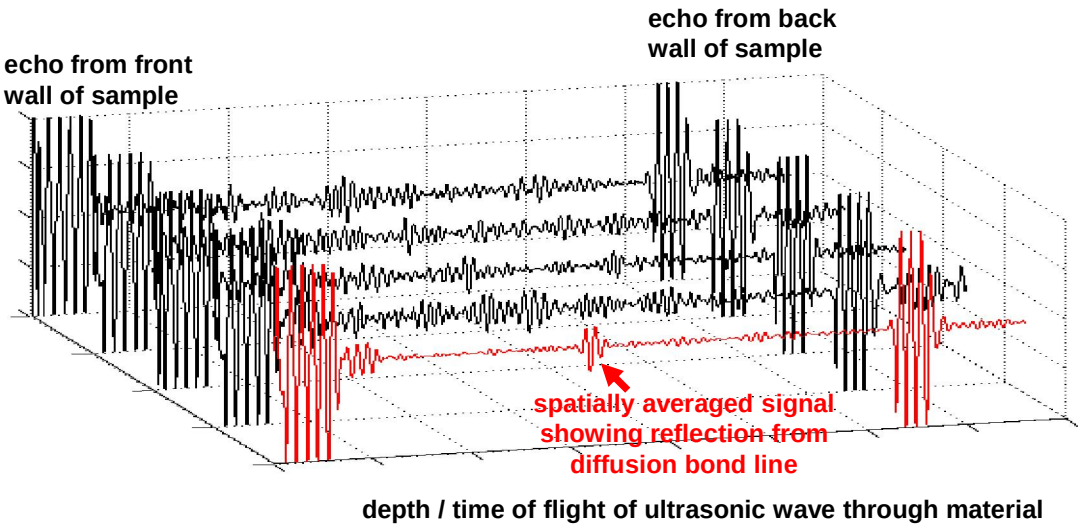

Figure 28. Illustration of spatial averaging. Signals captured from four different positions over a diffusion bonded Ti-6Al-4V block are in black. The spatially averaged signal (625 positions across 25mm x 25mm area) is shown in red. Material noise is cancelled out but the reflection from the bond line remains.

The assumption that the weld reflection arrives in phase is only valid if:

1. the time of flight to the bond line is constant;
2. the weld reflection is due to either acoustic impedance mismatch or defects, but not both.

Figure 11 showed that, for Ti-6Al-4V, where the crystallographic unit cell is highly anisotropic, the time of flight to the bond line can vary. The variance depends not only on the metal alloy but upon the microtexture. Time of flight also varies if the weld is not planar. As discussed in the previous section, for a partial bond, if the wavelength is long compared to the lateral defect size, then the phase due to acoustic impedance mismatch will be $\pi/2$ radians different from the phase due to a defect. Spatial averaging will then reduce the amplitude and distort the phase of the weld signal. If the wavelength is short compared to the lateral defect size, the phase due to acoustic impedance mismatch will be the same or π radians different from that due to a defect. Spatial averaging will reduce the amplitude of the weld signal.

Another method used to detect distributed defects is time of flight variance, suggested by Nieters *et al* [6, 96]. By looking at the B-scan representation in Figure 17 it is easy to distinguish the weakly coherent signal reflected from the bond line. It is more difficult, however, to pick the bond line reflection out from the material noise in a single A-scan (amplitude vs. time) or a C-scan of gated peak amplitudes. Time of flight variance (TOF measures the time to the peak in a section of each received A-scan signal and then measures the variance of this time of flight – effectively doing what an inspector might by eye. Nieters *et al* used [6] this method to detect incomplete diffusion in Ti-17 samples. The technique is only applicable to diffusion bonds where the bond is at a constant or known depth, and for bonds between similar materials, where no coherent reflection is expected from the bond line. For bonds between dissimilar materials or materials with coarse microtexture, such as the Ti-6Al-4V samples investigated in this project, it may not be possible to separate the coherent signal due to acoustic impedance mismatch from that due to defects. Jamieson found that time of flight variance and backscatter coefficient were mostly closely related to the tensile strength of beryllium-copper diffusion bonds [63].

The normalised spatial correlation coefficient, *SCC*, has been introduced already in Equation 3.4. It is used to describe the spatial correlation of ultrasonic backscatter in polycrystalline materials [55]. Rinker *et al* [64] used the spatial correlation coefficient (*SCC*) to detect aligned grain boundaries in upset-forge welds in stainless steel. For the 'marginal' welds the average *SCC* was higher than for the good welds. Reflections from aligned grain boundaries in the marginal welds were thought to cause spatial correlation of the reflected signals. They also looked at average *SCC* as a function of the

spacing between measurement positions ($|x-x'|$ in Equation 3.4). If grain growth had occurred across the weld then, as $|x-x'|$ is increased, the average *SCC* is expected to tend towards zero. For the 'marginal' welds, the *SCC* tended to some residual value, suggesting that a weak spatially coherent reflector (the aligned grain boundaries) was present over a large area. The *SCC* can also be calculated as a function of a time lag, φ; the shape of two signals is then compared as they are shifted relative to one another in time. This means that the technique could be altered to work for a weld line that is not perfectly planar.

For all ultrasonic inspection methods that depend upon the response of the bond line being constant with space, signals must be averaged or correlated over distances longer than the spatial correlation length (*SCL*) of the backscattered noise (see Section 3.1.2), in order to get an improvement in the signal to noise ratio. Defects that are distributed over regions with dimensions shorter than the *SCL* may not be detected. These techniques are therefore only relevant for distributed defects.

3.2.7. Nonlinear inspection

Nonlinear ultrasonic methods measure the nonlinear stress-strain response of the material. This nonlinearity may be a material property, such as the dislocation density, or it may be a discontinuity, such as a fatigue crack or a kissing bond.

For ultrasound incident upon a discontinuity, if the gap is larger than the amplitude of the incident ultrasound, then all of the energy will be reflected.

However, if the amplitude of the incident ultrasonic stress wave is sufficient, it will cause the gap to open and close slightly. The transmitted and reflected waves will be distorted. The frequency spectrum of this distorted waveform will contain upper harmonics [97] of the fundamental frequency of the incident wave. The ratio between the amplitude of the fundamental harmonic A_1 and the square of the amplitude of the second harmonic $A_2{}^2$ is a measure of the nonlinearity [98].

If two waves with different fundamental frequencies are incident on the discontinuity, then the lower frequency f_1 will cause the gap to open and close. As the gap opens and closes, the proportion of the high frequency wave f_2 transmitted across the gap will be modulated in amplitude and/or phase. In this case sidebands with frequency $f_2 \pm f_1$ will be generated as well as harmonics [99, 100]. If there is a compressive load across the discontinuity, pushing the surfaces into intimate contact, then this load has to be overcome before harmonic generation [93, 97, 101, 102] or parametric modulation [100, 103] will occur.

Solodov *et al* attributed the nonlinear stress-strain response of an elastic wave incident on an unbonded but contacting interface to Hertzian contact, as well as the clapping mechanism described above [101]. They termed surfaces which are 'in close proximity or even touching each other' as 'contact acoustic nonlinearities' (CANs). Kissing bonds and partially closed fatigue cracks are real examples of CANs. Due to this behaviour, nonlinear ultrasonic inspection is expected to be more sensitive to these types of defects than linear inspection [98].

The generation of upper harmonics of the incident ultrasonic wave has been demonstrated for two surfaces in dry contact [101, 102], for fatigue cracks [104, 105], for kissing adhesive bonds [93, 94] and for diffusion bonds defects [7, 15, 67, 106, 107]. Parametric modulation has mainly been used for the detection of cracks to date [99, 100, 103]. Nonlinear techniques have been specifically used to assess diffusion bonds in dissimilar materials, the nonlinearity due to the bulk material or acoustic impedance mismatch being orders of magnitude lower than the nonlinearity due to the CAN [15, 67].

3.2.8. Technique selection

The aim of this EngD programme is to improve the sensitivity of ultrasonic inspection to diffusion bond line defects and, in particular, to attempt to separate well-bonded samples with a texture mismatch at the bond line from partially bonded samples. The application is diffusion bonds between forged pieces of Ti-6Al-4V. The choice of which techniques to pursue was based upon several considerations, which are briefly outlined here.

The aim is to develop a technique for the detection of distributed voiding in diffusion bonds between pieces of forged Ti-6Al-4V. A schematic of the inspection is shown in Figure 29. Normal to bond line inspection is possible. This is preferable because, at normal incidence, energy reflected from the bond line is likely to be scattered directly back to the probe. There is access to one side of the diffusion bond line so the inspection must be in pulse-echo. The metal path to the bond line is likely to be ~10-100mm. Low frequency inspections are preferable as the ultrasound will not be attenuated during propagation. Finally, as explained in the preface to this thesis, the

timescale of this project was only two years. It was considered unrealistic to pursue a nonlinear inspection within this period, given the added complexity of those systems.

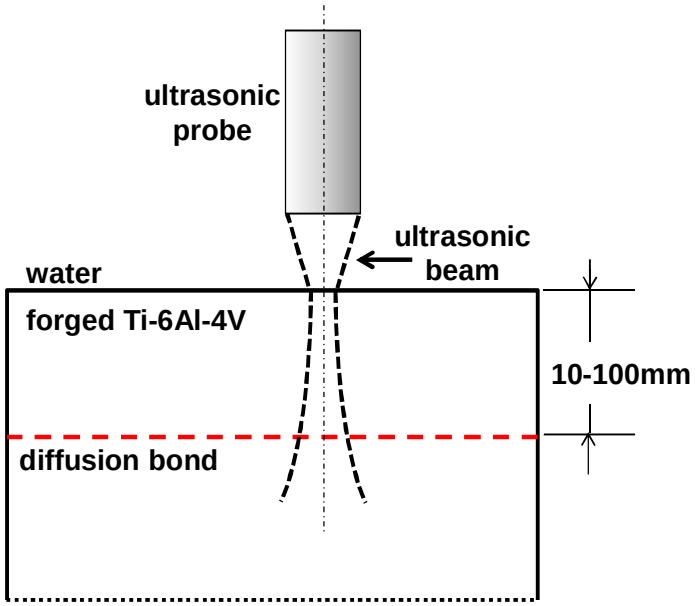

Figure 29. Schematic of geometry for inspection of diffusion bond between pieces of Ti-6Al-4V.

Suitable techniques therefore include the reflection coefficient, the backscatter coefficient and spatial techniques, such as spatial averaging, time of flight variance and spatial cross correlation. Ti-6Al-4V is highly scattering; backscattered noise amplitudes can mask reflections from small voids. Furthermore, the diffusion bond line between pieces of forged Ti–6Al–4V acts as a weak reflector to the incident ultrasound, as described in Section 3.2.1. The problem is analogous to that of a diffusion bond between dissimilar materials, except that the acoustic impedance mismatch varies locally and so the amplitude reflected from a perfect bond will not be constant. Industrially, a useful outcome of this project will be the description of the percentage voiding that can be reliably detected using the conventional pulse-echo immersion technique.

For a defective bond where the voids are short and narrow compared to the wavelength of the incident ultrasound, the simple interfacial spring model (Equation 3.9) predicts that it is possible to differentiate between the component of the reflection due to acoustic impedance mismatch and that due to the defect from the phase of the reflected signal. In this project, the true phase of the wave, which is independent of its arrival time, was measured. Given the amplitude and the phase, a complex reflection coefficient could be calculated. Spatial averaging of the imaginary and real components in the frequency domain can then be used to reduce the contribution of spatially incoherent backscattered noise in the parent metal either side of the diffusion bond line. Nagy and Adler's symmetric reflection technique will also be investigated for the diffusion bonded samples generated. It cannot be applied where there is access to one side of the diffusion bond, however it can be used to separate good and well-bonded samples and for other industrial applications.

4. Manufacture and Characterisation of Diffusion Bonded Ti-6Al-4V Samples

In Section 3.2.1, the microtexture at a diffusion bond line between two pieces of forged Ti-6Al-4V was described. It was shown that, even for a good titanium diffusion bond, there could be a low-amplitude spatially-coherent reflection from the bond line and that this could be mistaken for a defect. The objectives of this EngD project were to demonstrate the effect of microtexture on the sensitivity of the ultrasonic inspection of diffusion bonds in forged Ti-6Al-4V and to develop an inspection strategy to differentiate between well bonded and partially bonded samples.

Two different types of sample were required:

1. Well bonded samples with various levels of microtexture.
2. Partially bonded samples. The aim was to obtain samples with low percentage voiding, where the reflections were difficult to differentiate from either spatially incoherent backscattered noise in the parent metal or from spatially coherent backscattered noise at the diffusion bond line by amplitude alone.

One partially bonded sample (serial # HUCK01) made from cross-rolled Ti-6Al-4V plate had been manufactured prior to the start of the EngD project. The microtexture of cross-rolled Ti-6Al-4V is significantly different from that of forged Ti-6Al-4V. A series of samples was made by joining blanks cut from segments of two Ti-6Al-4V forgings. Finally, a number of different strategies were investigated to obtain partially bonded samples.

In this section the general diffusion bonding process and the geometry of the samples will be described. Photographs of etched sections of forgings and surface wave velocity maps for the same areas are included to qualitatively illustrate the microtexture of the bulk material. Blanks representative of those used in the diffusion bonded samples were evaluated ultrasonically, to determine their acoustic velocity and the variation of attenuation with lateral position. The results of a conventional ultrasonic inspection – where only the amplitude of the reflected signal is measured - are presented. The strategies adopted for obtaining partially bonded samples are described. Finally, the partially bonded samples are metallurgically examined and the percentage voided area is assessed. This is compared to the ultrasonic results.

4.1. Diffusion Bonding Process

The diffusion bonded samples were made by joining two blanks of Ti-6Al-4V. 50x50x19mm blanks were cut from the segments of forgings or from rolled plate by wire electrodischarge machining. The blanks cut from forgings were ground to the specified dimensions and surface finish. Grinding also removed the recast layer remnant from the wire cutting process. The surface finish after grinding to a nominal finish of 1.6µm Ra is shown in Figure 30a. A 6.35mm diameter hole was drilled in one of the blanks and a pipe close-fitted into the hole. Technical drawings of the blanks are included in Appendix A.

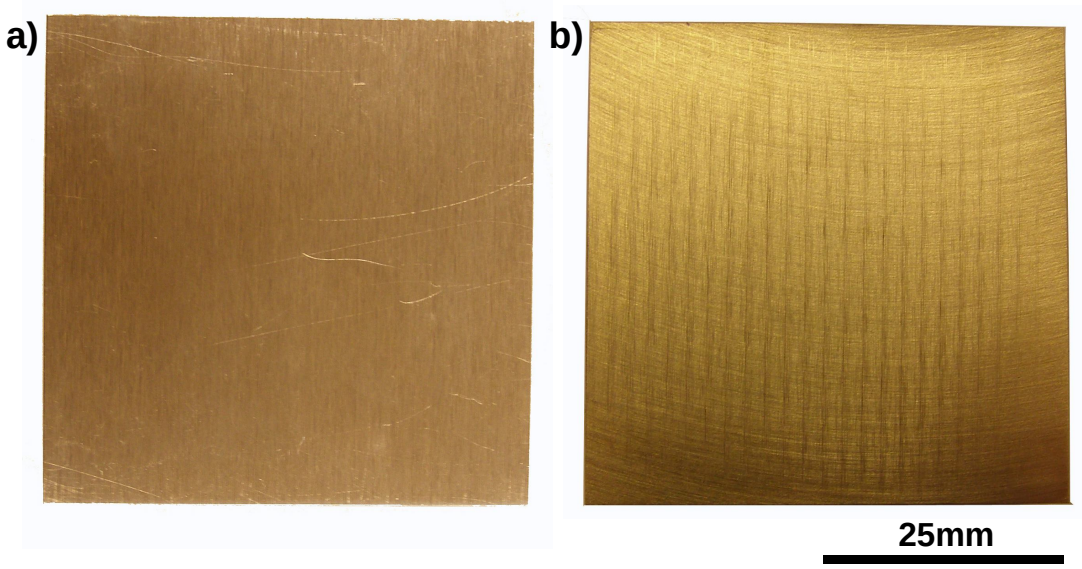

Figure 30. a) Photograph of blank sample after wire cutting and grinding to a nominal surface roughness of 1.6µm Ra. b) Photograph of same blank sample after light polish with FEPA 180 grit paper, revealing 'corrugated' surface finish with wavelength of ~2mm.

The two 50x50mm faces on each blank were finished by grinding with 180 FEPA grit paper (equivalent to 0.62µm Ra). A light polish of the surfaces after wire cutting and grinding to 1.6µm Ra revealed a long-range waviness or 'corrugated' surface finish (Figure 30b) that was not obvious prior to polishing. The wavelength was approximately 2mm. It is suspected that this waviness is an artefact of the wire cutting process. The samples were polished until this waviness was entirely removed. Using a centre punch, dimples were placed either side of the hole on the surface that would be diffusion bonded. The raised edges around the dimple prevented the surfaces 'ringing' together and so allowed complete evacuation of the air. The surfaces to be joined were ultrasonically cleaned with acetone and then swab etched using 2% HF, 10% HNO_3 in water. The samples were rinsed under running tap water and then ultrasonically washed in demineralised water. They were dried under a hot air blower. The two blanks were seam welded together, with the dimpled surface at the interface, and the pipe was

welded in place by manual TIG with an argon purge. The samples were then 'baked out' to evaporate any residual moisture from the internal surfaces and to evacuate the gas. They were placed in a furnace at 550°C. The pipe was connected to a vacuum pump running at a manifold pressure of below 10^{-6} bar and left for one hour. Before turning off the vacuum pump, the ends of the pipes were spot welded to seal the internal vacuum.

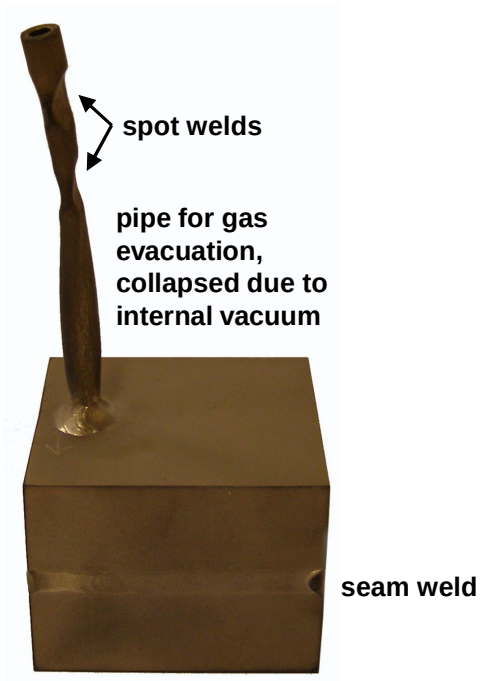

Figure 31. Photograph of diffusion bonded Ti-6Al-4V sample with evacuation pipe still attached. Once all of the air has been evacuated the pipe collapses due to the internal vacuum. This is used as an indicator that the gas has been evacuated successfully.

Diffusion bonding was carried out by hot isostatic press (HIP). The samples were placed in a pressurised furnace for a period of time. The diffusion bonding parameters are proprietary to Rolls-Royce plc. A diffusion bonded sample is shown in Figure 31. The evacuation pipe has collapsed, which indicates that the vacuum had been maintained during the HIP. Prior to ultrasonic inspection, the pipe was sawn off and ground down to a 1mm high stub.

4.2. Microtexture and Ultrasonic Characterisation of Blanks

4.2.1. Microtexture of blanks

Most of the blanks were machined from segments of forged Ti-6Al-4V, including:

- Segments of an aeroengine disc forging: J,M and N
- Segments of two small pancake forgings, used for development: D1 and D2.

The position of the 50x50x19mm blanks (FORG01-09) in each segment is shown in Appendix A. Blanks taken from the same radial position were assumed to have similar microtexture.

One radial slice was cut from each segment. The slices were swab etched with 10% HF, 50% HNO_3 in water to reveal the forging flow lines and the average texture. A photograph of the etched slice of segment N is shown in Figure 32.

Figure 32. Photograph of forged Ti-6Al-4V segment N, swab etched with 10% HF, 50% HNO_3 in water to reveal the forging flow lines.

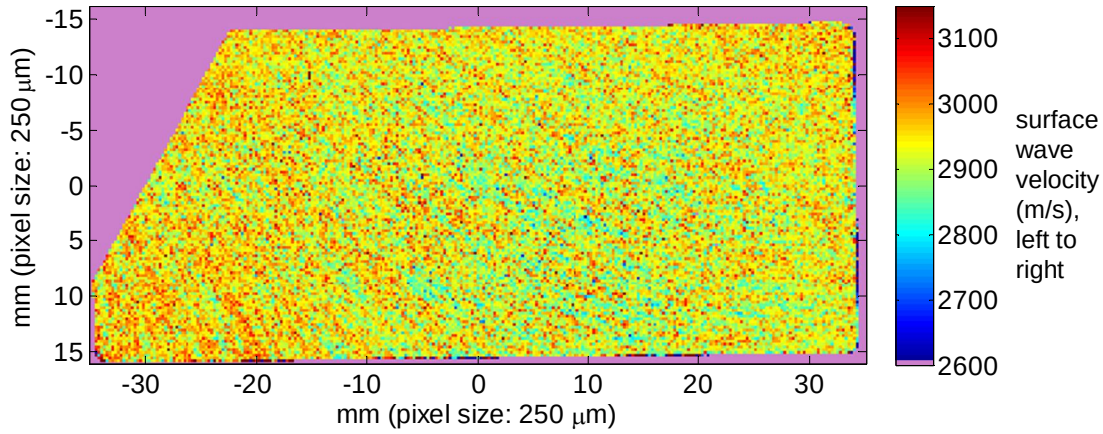

Figure 33. Surface wave velocity map of slice through forged Ti-6Al-4V segment N, obtained using optical-scanning acoustic microscope (O-SAM) at University of Nottingham [54]. The surface wave velocity was measured left-to-right over a length of 250μm with a pixel size of 250μm.

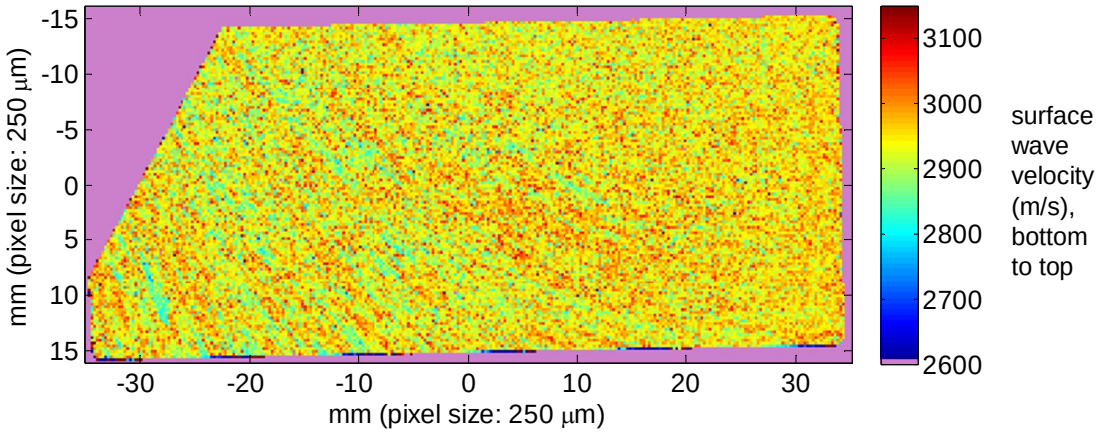

Figure 34. Surface wave velocity map of slice through forged Ti-6Al-4V segment N, obtained using optical-scanning acoustic microscope (O-SAM) at University of Nottingham [54]. The surface wave velocity was measured bottom-to-top over a length of 250μm with a pixel size of 250μm.

Surface wave velocity maps of the samples were also created using an optical scanning acoustic microscope [54]. The surface wave velocity was measured with a resolution of 250μm and a 250μm pixel size in two perpendicular directions. The velocity maps in the two directions for a slice of segment N are shown in Figure 33 and Figure 34. These two velocities can be combined in a single map (Figure 35a). A two-dimensional colour map (Figure 35b) is

used to indicate the magnitude of the two perpendicular velocities. For example, red indicates that the velocity is high in the horizontal direction (from the left hand side to the right hand side of the image) but low in the vertical direction (from the bottom to the top of the image). Blue indicates that the velocity is high in both directions. Photographs of the etched slices for all the forged segments – J, M, N, D1 and D2 - and their surface wave velocity maps are included in Appendix B.

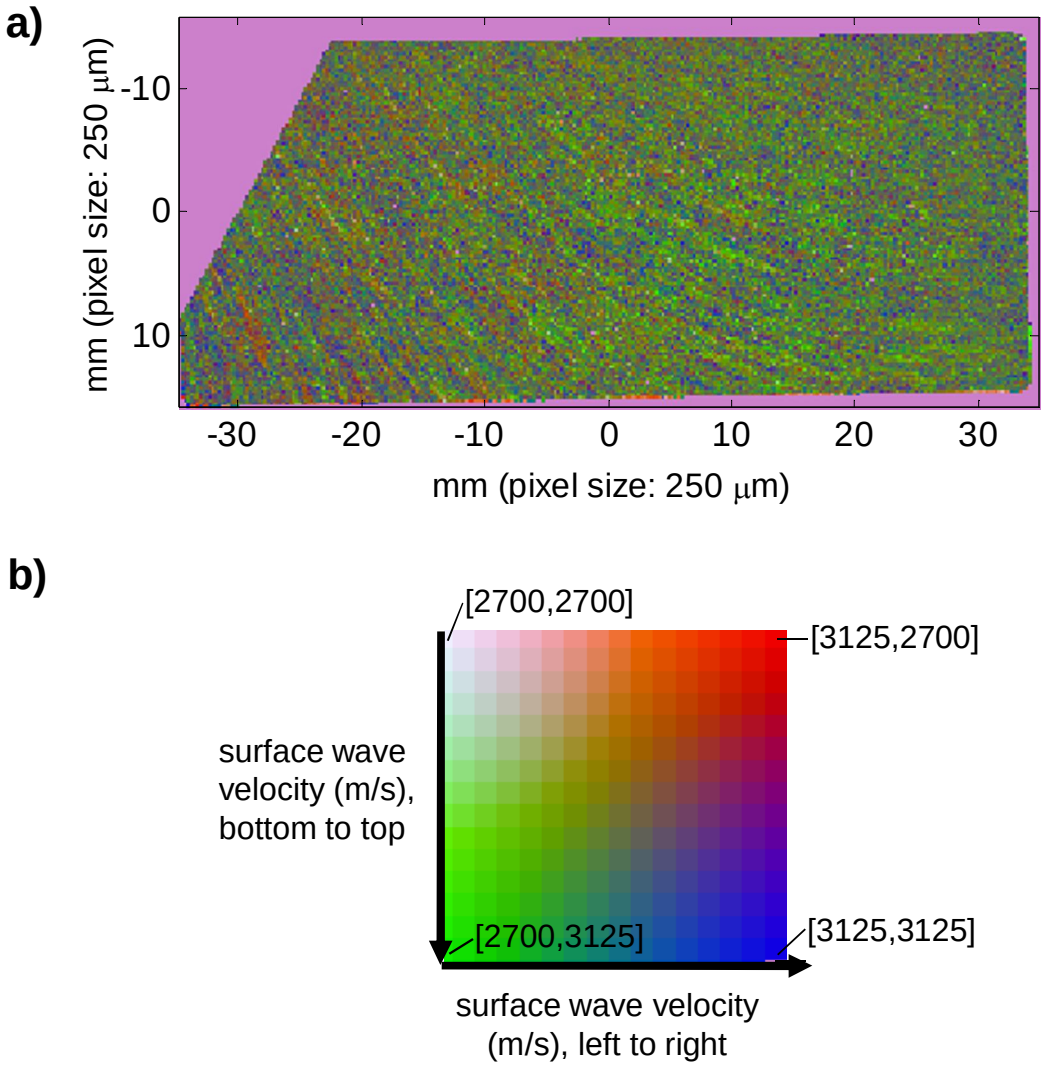

Figure 35. a) Combined surface wave velocity map of slice through forged Ti-6Al-4V segment N, obtained using optical-scanning acoustic microscope (O-SAM) at University of Nottingham [54]. The map was generated by combining the maps in Figure 33 and Figure 34. b) The 2D colour map shows the surface wave velocity in two directions: left-to-right and top-to-bottom. Blue indicates that the velocity is high in both directions.

4.2.2. Ultrasonic characterisation of blanks

Blanks had been cut from nine different radial positions in the forged Ti−6Al−4V segments, indicated by the serial numbers FORG01-FORG09. Blanks cut from the same radial position were assumed to have similar microtexture. Therefore the attenuation and ultrasonic backscatter for the reference sample were expected to be representative of all the blanks with the same serial number. However, this is not entirely correct. The microstructure produced in forgings is often banded; different quadrants having different levels of backscattered ultrasonic noise [108].

Blanks were also cut from unidirectionally rolled plate. The square blanks (50x50x19mm) were cut so that the large face was parallel with the rolling plane and one side was aligned with the rolling direction. Three blanks were retained as ultrasonic reference samples and given the serial numbers UD01-UD03. Cross-rolled plate was used to manufacture one sample prior to the start of this project (sample HUCK01). However, no extra cross-rolled plate was available to manufacture a reference specimen. All of the blanks were ground to a surface finish of 0.62µm Ra with 180 FEPA grit paper prior to ultrasonic inspection.

In this section, the measurement of the longitudinal wave velocity of the blanks in the thickness direction is described. The acoustic velocity is used to set the water path of the pulse-echo immersion inspection. It can also be used to estimate the acoustic impedance of the blanks. The blanks are then inspected in pulse-echo immersion. The mean amplitude and the standard deviation in mean amplitude of the backwall reflection are compared.

The acoustic velocity of the blocks for a longitudinal wave travelling in the through thickness direction was measured using contact ultrasonics. A 0.25" diameter 10MHz compressive wave probe was coupled to the surface with gel. The time of flight between the positive maxima of the 1st and 2nd backwall reflections was measured. The time of flight was measured in five different positions across the 50x50mm surface. The measurement was repeated three times in each position. The thickness of the blocks (~19mm) was measured with a ball micrometer in the same five positions as the acoustic velocity. Note that differences in time of flight between different positions on the same block could be due to variations in thickness or due to anisotropy (see Section 3.1.2). The average longitudinal velocity for each block is plotted in Figure 36.

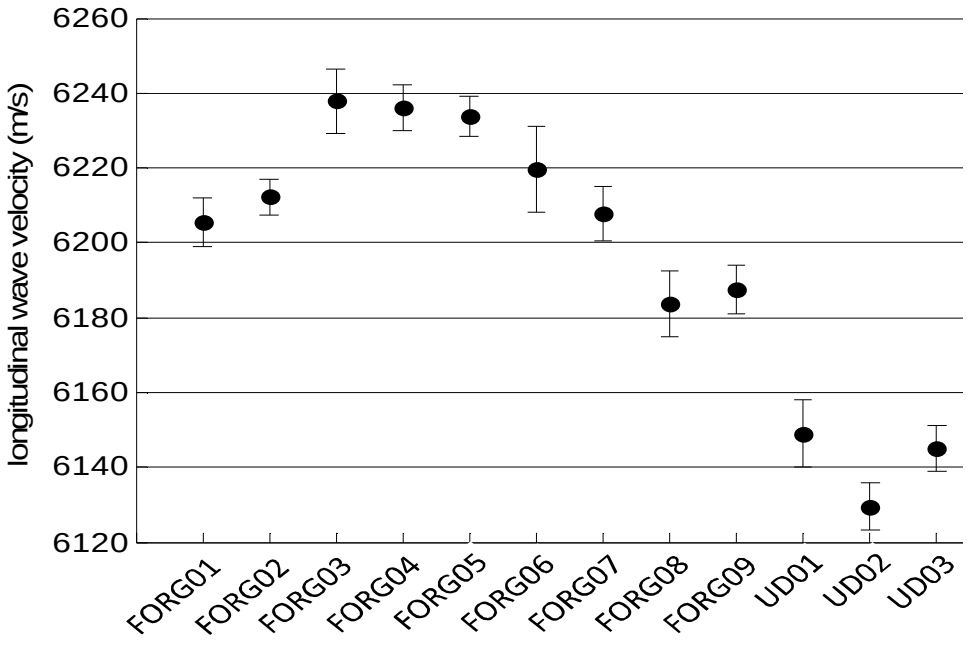

Figure 36. Longitudinal wave velocity (m/s) in thickness direction of reference blocks (50x50x19mm) cut from forged Ti-6Al-4V (FORG**) and unidirectionally rolled plate (UD**).

The difference in the longitudinal wave velocity between blocks is higher than the measurement error. The variation in velocity between blocks is

attributed to the anisotropy of titanium and the preferred crystallographic orientation of grains over large length scales within the block. The average longitudinal wave velocity across all of the forged samples (FORG**) is 6214m/s.

Each of the 50x50x19mm reference blocks was scanned in pulse-echo immersion with a 10.9MHz 6.3"F 0.75" probe. The probe characterisation is described in Appendix C. The probe axis was normal to the front wall. The water path was calculated so that the beam was focussed on the backwall, given the measured longitudinal wave velocity of the titanium and the water. The scan pitch was 0.25mm. An area 30x30mm from the centre of the block, which was not affected by edge effect, was isolated. The amplitude of the signal reflected from the backwall of the reference blocks was observed to vary across the scanned area.

The mean backwall amplitude and the standard deviation across the scanned area for each reference block are shown in Figure 37. Differences in acoustic impedance between the blocks can affect the measured backwall amplitude. Based upon the variation in acoustic velocity between the blocks (Figure 36), this is expected to be ~1.5%. which is much smaller than the observed variation between blocks. Attenuation is caused by beam spread and scattering of the ultrasonic wave by the material microstructure. The measured attenuation is also affected by distortion of the wavefront as it propagates through anisotropic material (see Section 3.1.2). For the unidirectionally rolled reference samples (UD01-03) the macrozones are 100-300µm wide (see Figure 38) orthogonal to the rolling plane and in the direction of wave propagation and so significant wavefront distortion is not

expected. However, in this direction the microstructure is highly scattering (see Section 5.1). The scattering accounts for the low backwall amplitude.

The backscatter for the forged reference blocks (FORG01-09) was ~15-20dB below that for the unidirectionally rolled plate. Blocks FORG07-09 were cut from forged segments M and N. The individual macrozones could not be resolved in the surface wave velocity maps (Figure B 16 and Figure B 20), which were done with a 250µm scan pitch, indicating a fine homogeneous microstructure. Wavefront distortion would therefore be low, giving the high measured value of backwall amplitude.

Blocks FORG03-06 were all cut from forging segment J. The surface wave acoustic velocity map for this segment (Figure B 12) indicates that it has the coarsest microtexture of all the segments used as stock material, with macrozones up to 2mm in size. These blocks have the lowest mean backwall amplitude and the largest standard deviation in the backwall amplitude. The high standard deviation indicates that the wavefront is being distorted by the highly anisotropic Ti-6Al-4V, which accounts for the low backwall amplitude.

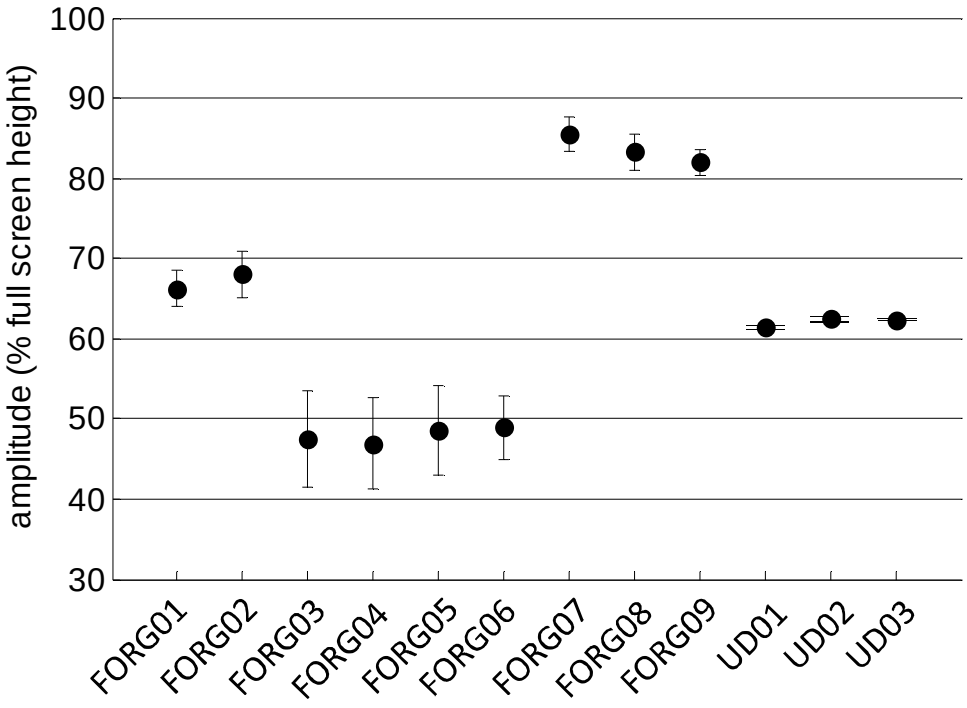

Figure 37. Mean back wall amplitude from 19mm thick forged (FORG**) and unidirectionally rolled (UD**) reference samples. Bars show one standard deviation in backwall amplitude over the scanned area (35mm x 35mm) above and below the mean.

4.2.3. Combinations of blanks used to manufacture diffusion bonded samples

Nine samples (samples #1-#9) were generated by joining blanks cut from the Ti-6Al-4V forged segments and using the process described in Section 4.1. They are thought to be well bonded. One partially bonded sample was available at the beginning of the project (HUCK01). It was manufactured by joining blanks cut from Ti-6Al-4V cross-rolled plate. To obtain more partially bonded samples, the surface preparation of the blanks was altered from that described in Section 4.1. The various surface preparations investigated are described in Section 0. Four partially bonded samples (samples #10-#13) were generated by joining blanks cut from forged

segments. Two samples (HUCK02 and HUCK03) were manufactured by joining blanks cut from Ti-6Al-4V unidirectionally rolled plate. Despite altering the surface preparation, these two samples are thought to be well-bonded. The combination of blanks used to create diffusion bonded samples is listed in Table 1.

Table 1. Combination of blanks cut from forged (FORG**) and rolled Ti-6Al-4V used to make diffusion bonded samples. Technical drawings showing position of FORG** in the forging segments are included in Appendix A. Pieces of unidirectionally rolled plate were joined with the rolling directions aligned.

Sample #	Well bonded or partially bonded?	Blank 1(pipe side)	Blank 2
1	Good	FORG05	FORG05
2	Good	FORG06	FORG04
3	Good	FORG07	FORG09
4	Good	FORG03	FORG09
5	Good	FORG01	FORG01
6	Good	FORG02	FORG01
7	Good	FORG02	FORG02
8	Good	FORG08	FORG07
9	Good	FORG03	FORG09
10	Partially bonded	FORG04	FORG03
11	Partially bonded	FORG07	FORG08
12	Partially bonded	FORG01	FORG01
13	Partially bonded	FORG02	FORG01
HUCK01	Partially bonded	Cross-rolled plate	Cross-rolled plate
HUCK02	Good	Unidirectionally rolled plate	Unidirectionally rolled plate
HUCK03	Good	Unidirectionally rolled plate	Unidirectionally rolled plate

4.3. Manufacture of Partially Bonded Samples

The process described in Section 4.1 was used to obtain nine well-bonded samples. Partially bonded samples were also required. The aim was to obtain samples where the ultrasonic reflection amplitude due to voiding was similar to that due to the material noise or due to acoustic impedance mismatch at the bond line e.g. it should not be possible to separate the partially bonded samples from the well bonded samples by ultrasonic amplitude alone.

One partially bonded sample, made from cross-rolled Ti-6Al-4V plate, had been manufactured prior to the start of the EngD project. It was given the serial number HUCK01. The blanks used had dimensions 45 x 40 x 14mm. No pipe was used to evacuate gas from between the surfaces. The surfaces of the sample had been cleaned as normal and then the blanks were put through a standard hot isostatic press (HIP) cycle. The sample had already been sectioned and polished to show the extent of the disbond on the bond line. As only limited inspection could be carried out on the remnants of the sample and because cross-rolled plate has very different microtexture from forged Ti-6Al-4V, this sample was not used for the bulk of the work in this project. However, the sample was used to relate the absolute reflection coefficient, $|R|$, to the percentage bonded area (see Section 4.5).

Sample HUCK01 was severely voided. The nine well bonded samples were all put through a standard HIP cycle. It was not possible to vary the pressure, temperatures or times as samples went through with a batch. To create more partially bonded samples but with lower levels of bond line voiding, changes were made in the surface preparation.

Due to limited stock material and time, only a few attempts could be made at achieving poor bonds. Four different methods were tried:

1. Not swab etching the surfaces to be joined.
2. Oxidising the surfaces to be joined prior to joining.
3. Leaving out the final grinding step with 180 FEPA grit paper.
4. Scratching the surface of the samples.

For methods 1 and 2, the blanks used were cut from unidirectionally rolled Ti-6Al-4V plate, rather than forged Ti-6Al-4V. The blanks were joined with the rolling directions aligned. One sample was produced by each method: HUCK02 using method 1 and HUCK03 using method 2 (see Table 1). For method 1, one of the blanks went through the normal sample preparation. The other blank was ultrasonically cleaned in acetone as normal, but was not swab etched. All other steps were as described in Section 4.1. For method 2, after ultrasonic cleaning, one of the blanks was placed in a furnace at 475°C for 45 minutes. The surface oxidised to a light straw colour. The oxide did not form scale. The sample was then diffusion bonded as normal.

Both samples HUCK02 and HUCK03 were ultrasonically inspected in pulse-echo immersion and sectioned, as described in Section 4.4. No defects were found on the bond line of either sample. A spatially coherent reflection at the bond line was not observed for these samples. A surface wave velocity map of the sectioned surface of HUCK02 for wave propagation in the direction normal to the bond line is shown in Figure 38. The microtexture is highly anisotropic due to rolling; the macrozones are present as elongated plates aligned with the rolling direction. This texture is not representative of the forged Ti-6Al-4V used to manufacture blisks. These samples were therefore not used for the bulk of the ultrasonic inspections in this project. However,

the microstructure is homogeneous for wave propagation in the direction normal to the bond line (orthogonal to the rolling plane). The backscattered noise for sample HUCK02 is compared to that for the forged samples in Section 5.1.

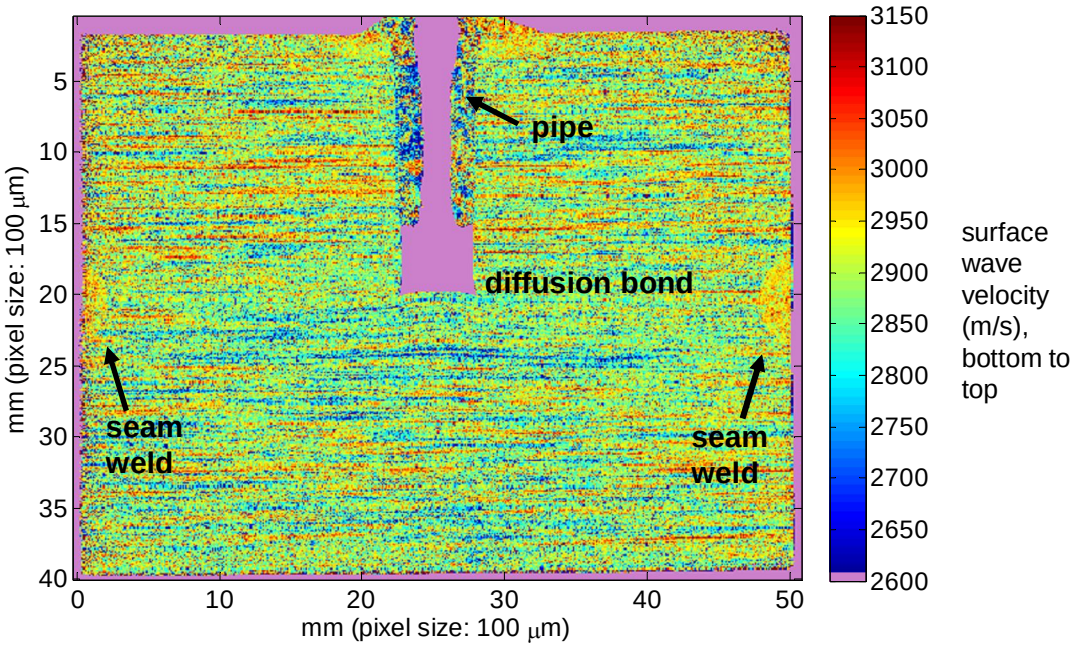

Figure 38. Surface wave velocity map of slice through sample HUCK02, obtained using optical-scanning acoustic microscope (O-SAM) at University of Nottingham [54]. The surface wave velocity was measured bottom-to-top over a length of 100μm with a pixel size of 100μm. The sample was sliced through the evacuation pipe and hole. The diffusion bond extends horizontally in both directions from the bottom corners of the hole. HUCK02 was made by joining two pieces of unidirectionally rolled Ti-6Al-4V, with the rolling directions aligned. The macrozones are elongated and aligned with the rolling direction (left-to-right).

For method 3, the final grinding process was not carried out. The surfaces to be joined will have the 'corrugated' finish observed in Figure 30. Two partially bonded samples – sample #12 and #13 - were manufactured in this way.

Method 4 was opportunistic. The samples were prepared as normal but, following the final grinding process to a surface roughness of 0.62µm Ra and during transportation from the machine shop, the surfaces of the blanks became scratched. The scratches were in random orientations. It was decided to diffusion bond these blanks together in the hope of achieving partial bonds. Two partially bonded samples – sample #10 and #11 – were obtained. The exact process parameters for all the samples are available in the R-R NDE report [66].

4.4. Ultrasonic Inspection and Sectioning of Samples

All sixteen of the samples listed in Table 1 were ultrasonically inspected in pulse-echo immersion using a 10.9MHz 6.3”F 0.75” diameter probe. The probe characterisation is described in Appendix C. The probe axis was normal to the bond line and the water path was chosen such that the beam was focussed at the bond line depth. A C-scan (area scan) was carried out with a scan pitch of 0.25mm in both lateral directions. Full waveform data sampled at 250MS/s was captured at each position. The data for the region directly below the evacuation pipe shown in Figure 31 was not used. The microtexture of the pipe material is not representative and, for some of the samples, voids were still present at the bond line depth at the base of the hole. Near the sample edges, the ultrasonic beam is intersected by the vertical sides of the sample. Data within 10mm of the edges of the sample was therefore also discarded. For each ultrasonic scan a region of 30mm x 20mm was isolated, as shown in Figure 39. Unfortunately, samples #12 and #13 had been sectioned prior to ultrasonic inspection. The scanned areas for the remnants of these samples were smaller: 13x30mm for sample #12 and

16x30mm for sample #13. The smaller area should not affect any of the calculations in this project.

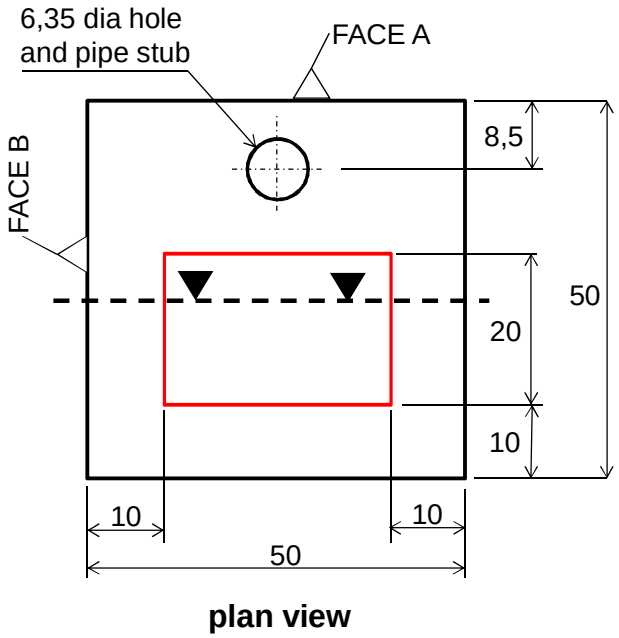

Figure 39. Plan view of Ti-6Al-4V diffusion bonded sample. The full waveform data for the 30x20mm region highlighted in red was used. The distance of the ultrasonic probe from faces A and B was determined with the 6dB drop method. The samples were sectioned perpendicular to the diffusion bond line and parallel to face A, as indicated by the thick dashed line. One surface was polished to allow metallurgical examination, as indicated by the arrows.

Ultrasonic C-scan images for some of the diffusion bonded samples are included in this section. At each scan position, the amplitude is the maximum amplitude in a 0.48µs gate centred at the diffusion bond depth. The colour scale indicates the amplitude in decibels relative to the reflection amplitude from a 0.050" diameter flat-bottomed hole a depth of 20.3mm in a stainless steel calibration block. It should be remembered that the diffusion bonded samples were generated by joining blanks of various microtexture. The attenuation, indicated by the mean backwall amplitude of the blanks across the scanned area (see Figure 37, Section 4.2.2), varies with

microtexture. It is therefore not rigorous to directly compare the amplitude of the signal between blocks. Values are provided here for information. The reflection coefficient, R_{bond}, takes the apparent attenuation into account. R_{bond} is calculated in Section 5.3 and these values can be directly compared.

C-scans of the diffusion bond line for two well-bonded samples (samples #1 and #7) are shown in Figure 40 and Figure 41. For all the well-bonded samples measured reflection amplitudes are below -25dB.

C-scans for samples #10 and #11, which were generated by joining blanks whose surfaces were scratched (Method 4 – see Section 0), are shown in Figure 42 and Figure 44 respectively. For sample #10, the peak amplitude is -26dB. The peak amplitude on sample #11 is -21dB. Samples #10 and #11 were also scanned with a 25MHz 3”F 0.75” diameter probe, which gives better spatial resolution than can be achieved with the 10.9MHz probe. The 25MHz C-scans are shown in Figure 43 and Figure 45. Linear features (the scratches on the diffusion bonded surfaces) are evident in both images.

Ultrasonic C-scans for samples #12 and #13, which were generated by joining blanks whose surfaces had long range waviness (Method 3 – see Section 0), are shown in Figure 46 and Figure 47 respectively. The peak measured amplitude is -11dB for sample #12 and -15dB for sample #13.

A C-scan of sample HUCK01 is shown in Figure 48. No evacuation pipe was used in this sample, so the entire sample could be scanned. The peak amplitude is +9dB compared to the 0.050” flat-bottomed hole. The peak and average absolute amplitudes across the C-scans for all the diffusion bonded samples are summarised in Figure 49 and Figure 50 respectively.

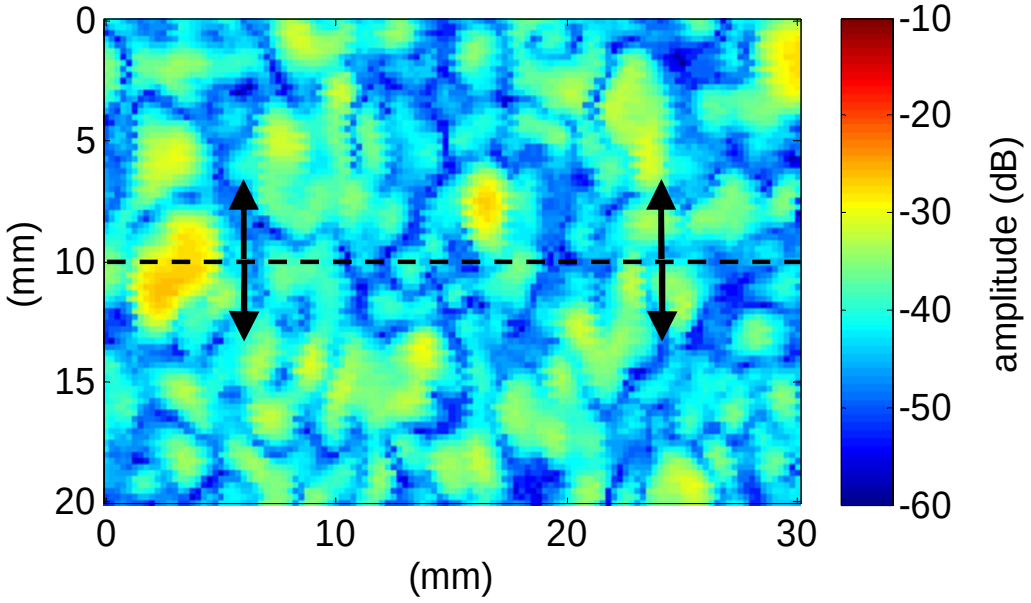

Figure 40. Sample #1. Ultrasonic C-scan of 20x30mm area of diffusion bond line with 0.25mm scan pitch. The scan was carried out in pulse-echo immersion with a 10.9MHz 6.3"F 0.75" focussed at the bond line depth. The colour scale is in decibels (dB) relative to the reflection amplitude from a 0.050" diameter 20.3mm deep flat-bottomed hole in a stainless steel calibration block. The sample was sectioned and prepared to allow metallurgical examination along the black dashed line, which intersects the point of highest ultrasonic amplitude. It was then incrementally polished four times in 1mm increments in both the directions indicated by the arrows.

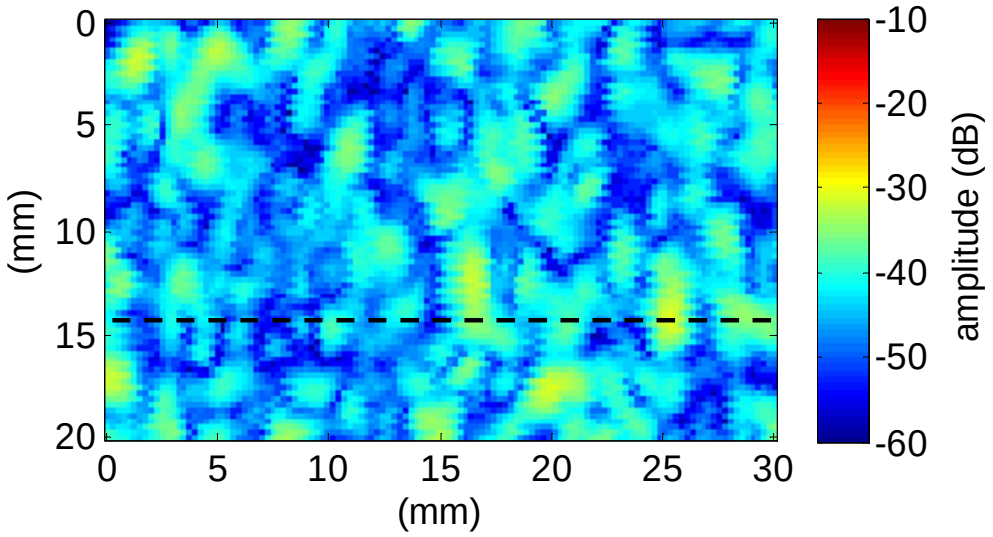

Figure 41. Sample #7. Ultrasonic C-scan of 20x30mm area of diffusion bond line with 0.25mm scan pitch. The scan was carried out in pulse-echo immersion with a 10.9MHz 6.3"F 0.75" focussed at the bond line. The colour scale is in decibels (dB) relative to the amplitude from a 0.050" flat-bottomed hole 20.3mm deep in a stainless steel calibration block. The sample was sectioned and prepared to allow metallurgical examination along the black dashed line, which intersects the point of highest ultrasonic amplitude.

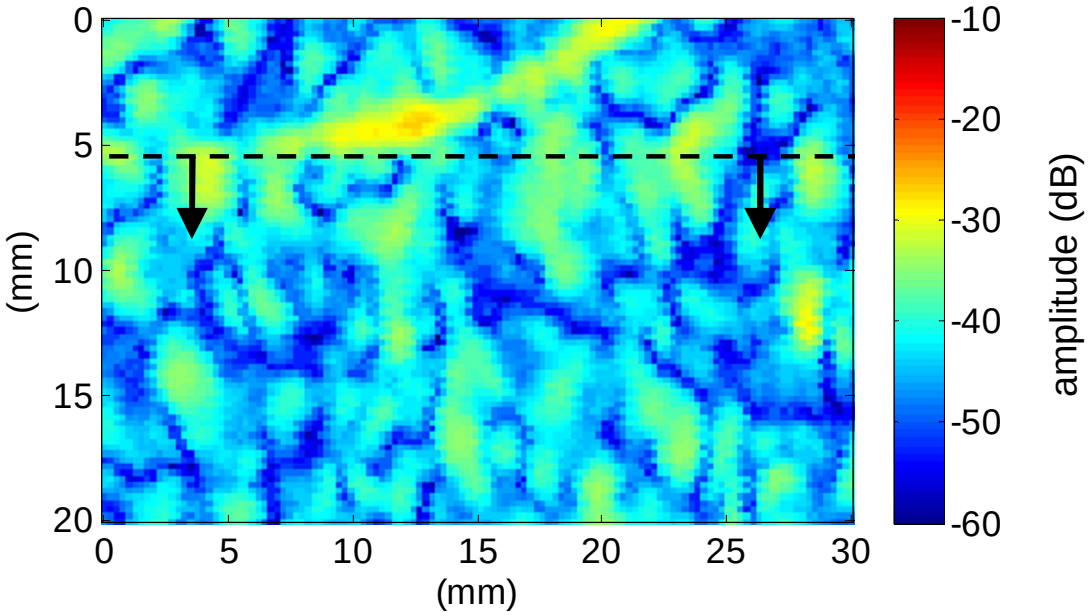

Figure 42. Sample #10. Ultrasonic C-scan of 20x30mm area of diffusion bond line with 0.25mm scan pitch. The scan was carried out in pulse-echo immersion with a 10.9MHz 6.3"F 0.75" focussed at the bond line depth. The colour scale is in decibels (dB) relative to the reflection amplitude from a 0.050" flat-bottomed hole 20.3mm deep in a stainless steel calibration block. The sample was sectioned and prepared to allow metallurgical examination along the black dashed line. It was then incrementally polished in 2mm increments in the direction indicated by the arrows.

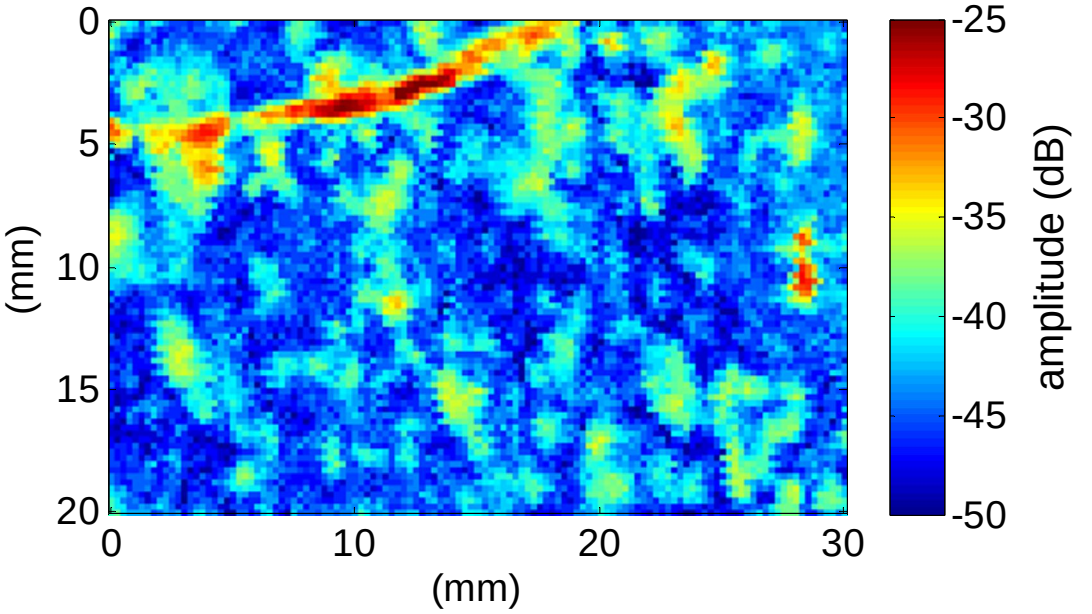

Figure 43. Sample #10. Ultrasonic C-scan of 20x30mm area of diffusion bond line with 0.25mm scan pitch. The scan was carried out in pulse-echo immersion with a 25MHz 3"F 0.75"diameter probe. The colour scale is in decibels (dB) relative to the reflection amplitude from a 0.050" flat-bottomed hole 20.3mm deep in a stainless steel calibration block.

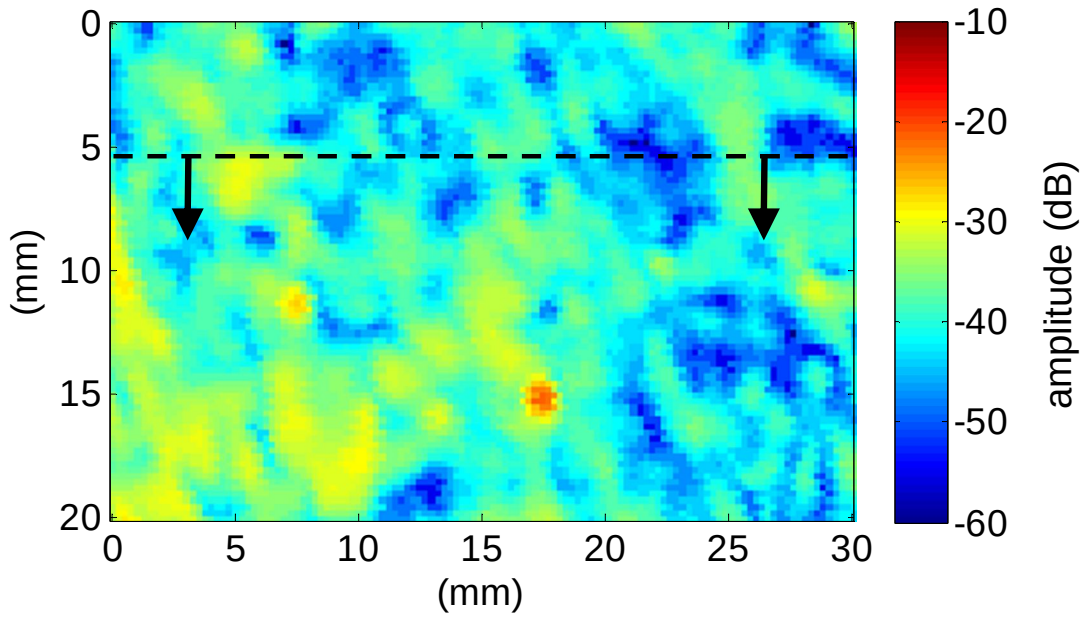

Figure 44. Sample #11. Ultrasonic C-scan of 20x30mm area of diffusion bond line with 0.25mm scan pitch. The scan was carried out in pulse-echo immersion with a 10.9MHz 6.3"F 0.75" focussed at the bond line depth. The colour scale is in decibels (dB) relative to the reflection amplitude from a 0.050" flat-bottomed hole 20.3mm deep in a stainless steel calibration block. The sample was sectioned and prepared to allow metallurgical examination along the black dashed line. It was then incrementally polished in 2mm increments in the direction indicated by the arrows.

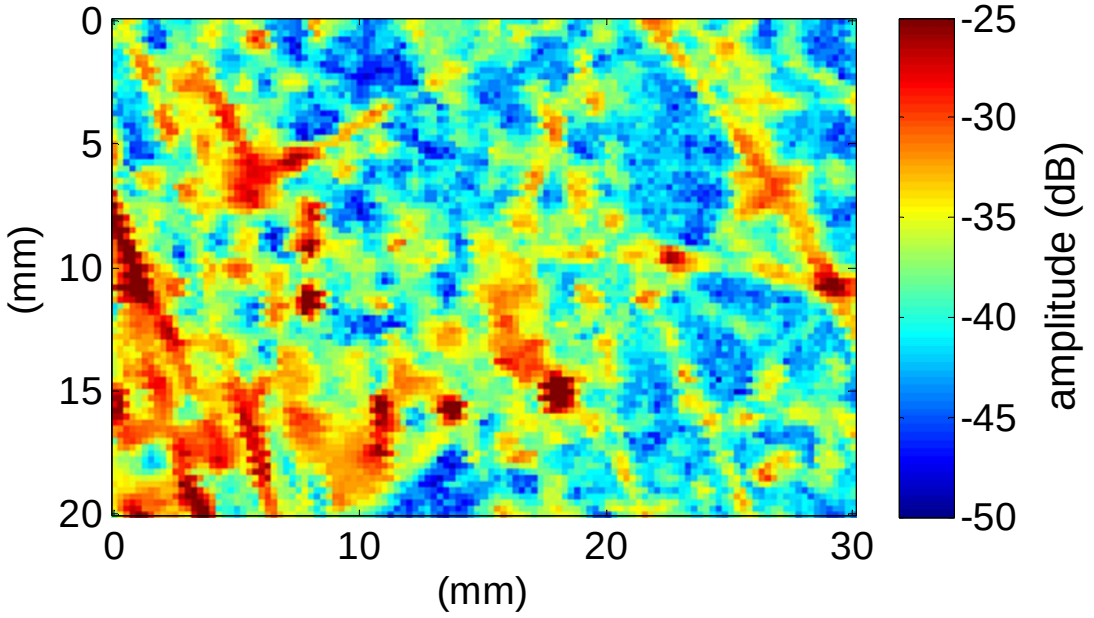

Figure 45. Sample #11. Ultrasonic C-scan of 20x30mm area of diffusion bond line with 0.25mm scan pitch. The scan was carried out in pulse-echo immersion with a 25MHz 3"F 0.75"diameter probe. The colour scale is in decibels (dB) relative to the reflection amplitude from a 0.050" flat-bottomed hole 20.3mm deep in a stainless steel calibration block. The maximum reflection amplitude in this scan saturated the digitizer.

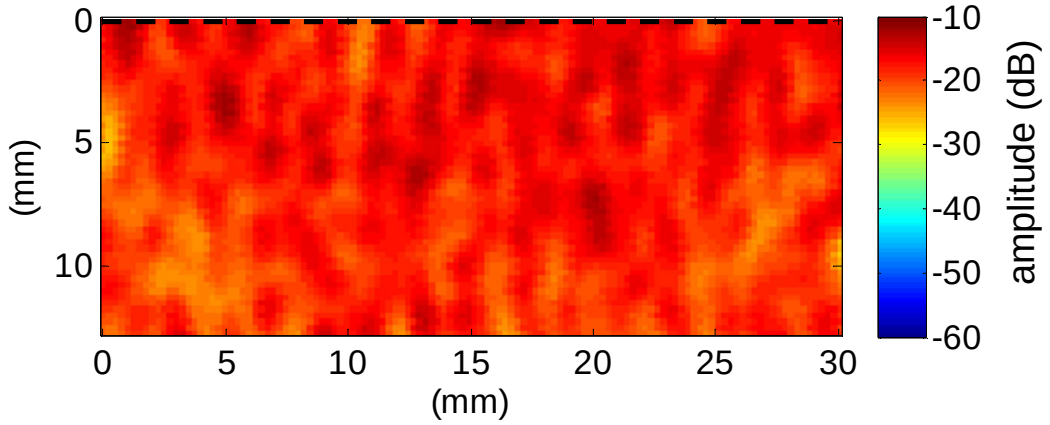

Figure 46. Sample #12. Ultrasonic C-scan of 20x30mm area of diffusion bond line with 0.25mm scan pitch. The scan was carried out in pulse-echo immersion with a 10.9MHz 6.3"F 0.75" focussed at the bond line depth. The colour scale is in decibels (dB) relative to the reflection amplitude from a 0.050" flat-bottomed hole 20.3mm deep in a stainless steel calibration block. The black dashed line is parallel to and 27mm from Face A (see Figure 39). The sample was sectioned and prepared to allow metallurgical examination along the black dashed line.

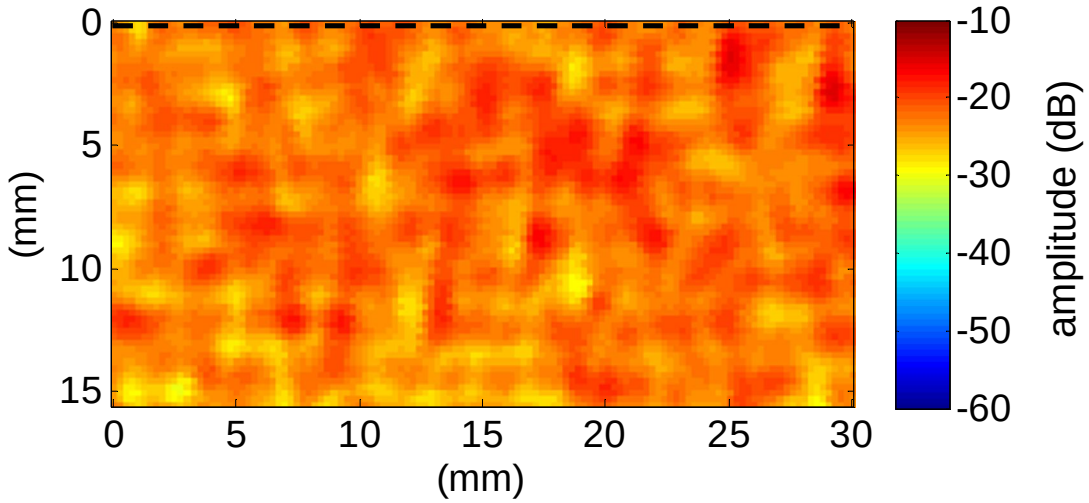

Figure 47. Sample #13. Ultrasonic C-scan of 20x30mm area of diffusion bond line with 0.25mm scan pitch. The scan was carried out in pulse-echo immersion with a 10.9MHz 6.3"F 0.75" focussed at the bond line depth. The colour scale is in decibels (dB) relative to the reflection amplitude from a 0.050" flat-bottomed hole 20.3mm deep in a stainless steel calibration block. The black dashed line is parallel to and 24mm from Face A (see Figure 39). The sample was sectioned and prepared to allow metallurgical examination along the black dashed line

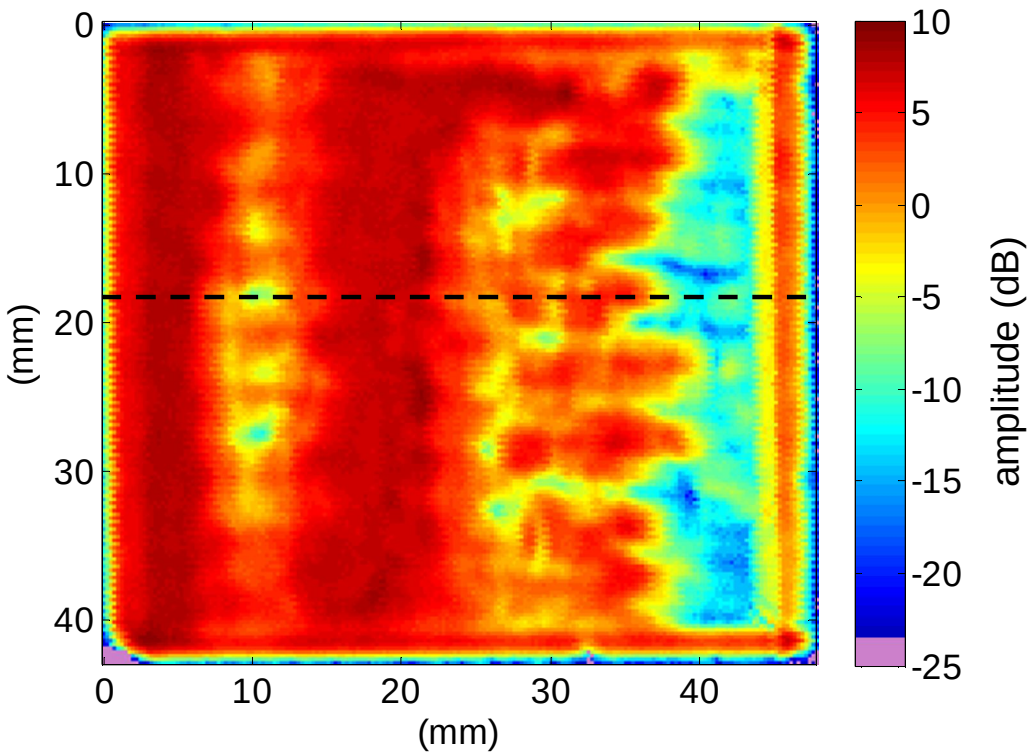

Figure 48. Sample HUCK01. Ultrasonic C-scan of diffusion bond line with 0.25mm scan pitch. The scan was carried out in pulse-echo immersion with a 10.9MHz 6.3"F 0.75" focussed at the bond line depth. The colour scale is in decibels (dB) relative to the reflection amplitude from a 0.050" flat-bottomed hole 15.2mm deep in a stainless steel calibration block.

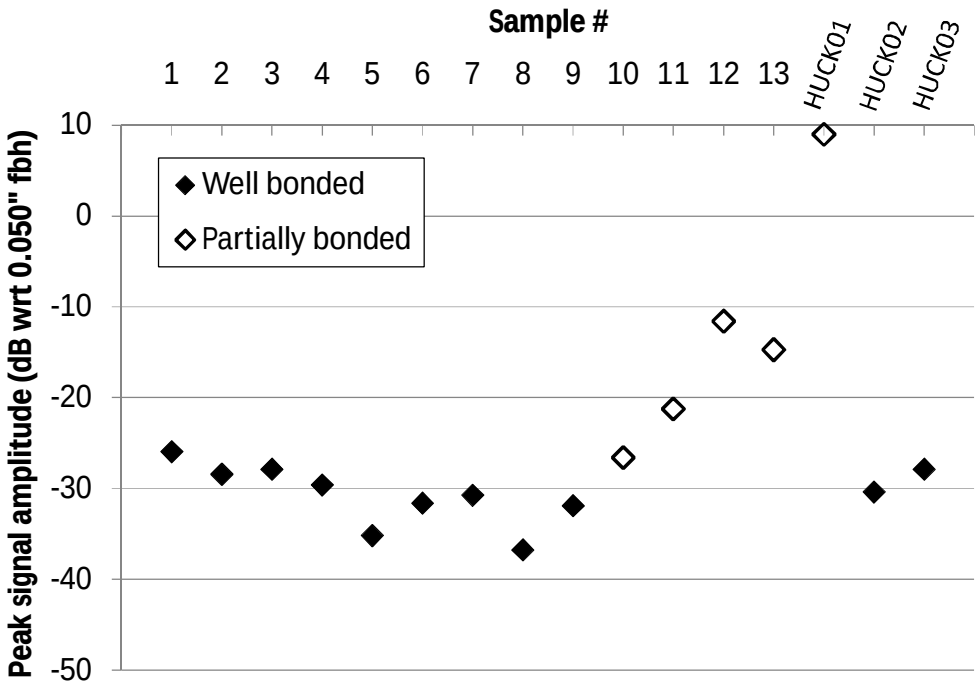

Figure 49. Peak absolute signal amplitude across scanned area of both well bonded (solid diamonds) and partially bonded (empty diamonds) Ti-6Al-4V samples. The absolute amplitude at each scan position was determined as the maximum signal amplitude in a 0.48μs gate centred at the diffusion bond depth.

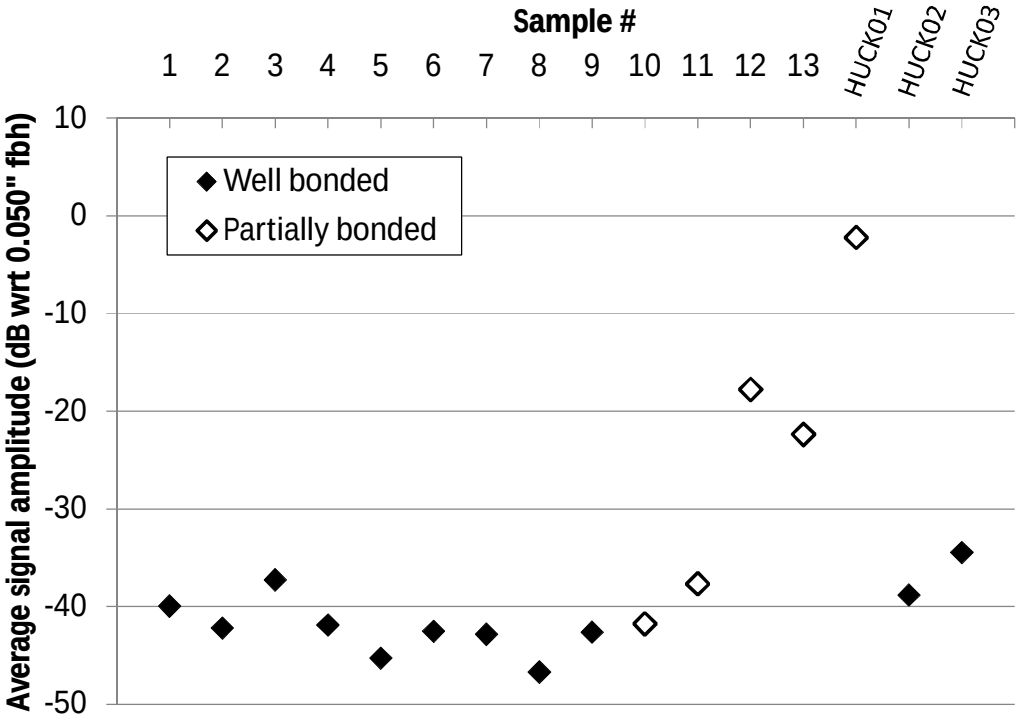

Figure 50. Average absolute signal amplitude across scanned area of both well bonded (solid diamonds) and partially bonded (empty diamonds) Ti-6Al-4V diffusion bonded samples. The absolute amplitude at each scan position was determined as the maximum signal amplitude in a 0.48μs gate centred at the diffusion bond depth.

For each of the well bonded samples (sample #1-9, HUCK02 and HUCK03), the position of the highest amplitude reflection was found and its distance relative to faces A and B (Figure 39) was measured. The 6dB drop method was used to determine the position of the sample edges. The samples were sectioned perpendicular to the diffusion bond line and parallel to face A, as shown in Figure 39. It was polished so that the prepared surface intersects the position of highest ultrasonic amplitude. These positions are shown on the ultrasonic C-scans for samples #1 and #7 in Figure 40 and Figure 41. Due to errors in the ultrasonic measurement and the cut-up process, the positional accuracy is no better than ±0.6mm. No defects were found in any of the well bonded samples. However, in the partially bonded samples, typical defect sizes ranged from 1-200µm (see Section 4.5). Given the positional inaccuracy, it is possible that any defects may have been missed. Incremental polishing is time consuming and expensive. It was only carried out for sample #1. A 10mm wide section ±5mm of the original section (see Figure 40), which corresponded to the position with the highest amplitude reflection, was polished through with 1mm increments. No defects were found. Polishing increments of a few microns would be required to guarantee that these samples are actually free of voids.

The sectioning and metallurgical examination of the partially bonded samples are described in the next section.

4.5. Metallurgical Examination of Partially Bonded Samples

Five of the Ti-6Al-4V samples were partially bonded: HUCK01, which was generated by joining pieces of cross-rolled Ti-6Al-4V plate, and samples #10 - #13, which were generated by joining pieces of forged Ti-6Al-4V (see Section 0).

Sample HUCK01 (45x40x28mm) was sectioned perpendicular to the bond line in the position shown in Figure 48 and one surface was polished, so that the different severities of disbond could be assessed. The amplitude of the ultrasonic C-scan varies by approximately 25dB from left to right. The bond was voided. Sample #12 was sectioned parallel to and 27mm from Face A (see Figure 39), in the position shown in Figure 46. A typical micrograph is shown in Figure 51: isolated voids were distributed along the bond line, separated by well-bonded regions. Sample #13 was sectioned parallel to and 24mm from Face A (see Figure 39), in the position shown in Figure 47.

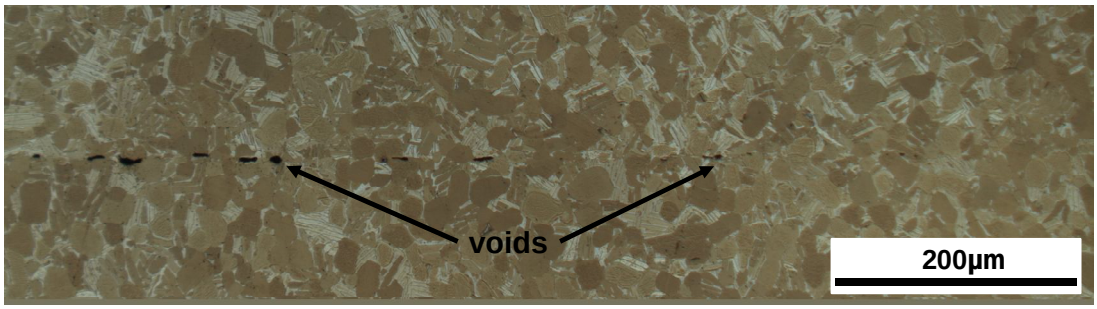

Figure 51. Typical micrograph at 200× magnification of partially voided sample #12.

In order to estimate the percentage voiding at those sections in samples HUCK01, #12 and #13, images were taken at 200× magnification under a binocular microscope at intervals of 2mm. The void lengths were measured. At this magnification the pixel size is 0.34µm. The smallest void length

measured was 0.69µm (2 pixels long). However, at this pixel resolution, such a short feature cannot be confirmed to be a void, rather than a dust particle or adjacent dead pixels. Voids greater than 3 µm long could be resolved easily. The mean void length and the standard deviation for each of the three samples (HUCK01, #12 and #13) are listed in Table 2.

Each image covered a 0.9mm length of the bond line. The total length of the voids in the bond line plane was measured for each image. The linear percentage voiding at each position was then calculated as the total length of the voids divided by the length of the image. Figure 52 shows a region of total unbond. The mean percentage voiding and the standard deviation in the percentage voiding across all the images was calculated. These results are also included in Table 2.

Table 2. Linear percentage voiding and void length distribution for Sample #12, Sample #13 and HUCK01.

Sample #	Mean linear percentage voiding	Maximum linear percentage voiding	Standard deviation in linear percentage voiding	Mean void length (µm)	Standard deviation in void length (µm)
12	15.9	21.4	3.6	11.6	9.2
13	7.9	32.0	9.0	10.9	10.8
HUCK01	58.3	100.0	21.9	33.3	140.0

The measured length does not necessarily correspond to the largest dimension of the void out of the plane of the image (or in the plane of the diffusion bond). The void may be truncated at the edge of the image. If it is assumed that the voids are not truncated at the edge of the image and that they are circular then the largest out of plane dimension would be the diameter. It is more probable that the section has intersected a chord other than the diameter. The most probable length of the chord can be calculated.

The derivation is included in Appendix D. The ratio between the void diameter and the most probable chord length is $4/\pi$. Therefore, assuming that the voids are circular, that they do not overlap and that they are not truncated by the edge of the image, the measured length probably underestimates the void diameter.

In some places on HUCK01 it appeared as if the gap between the two surfaces had been 'filled' by a layer of material ~5µm wide (see Figure 52). This could have occurred as part of the diffusion process or material may have been smeared into the gap during polishing. If a gap between the interlayer and the surfaces could be resolved, then these regions were measured as one long void.

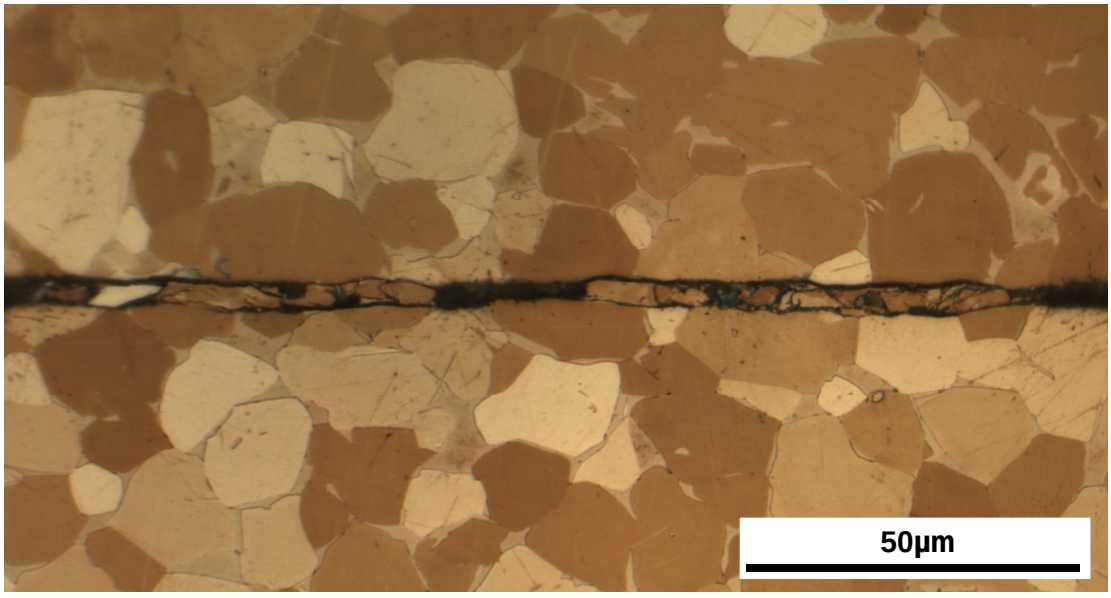

Figure 52. Micrograph of sample HUCK01 showing 'filling' of the interface by titanium.

For HUCK01, sample #12 and sample #13 the linear percentage voiding, calculate as the measured length of the voids divided by the image length, was plotted against the absolute reflection coefficient, $|R_{bond}|$, calculated for

the same position. The method used to calculate $|R_{bond}|$ is described in Section 5.3. The absolute reflection coefficient increases monotonically with the linear percentage voiding (see Figure 53), but there is considerable scatter. The scatter is greatest for sample HUCK01. The signal amplitude (see Section 4.4) and linear percentage voiding (see Table 2) vary more for HUCK01 with position than for samples #12 and #13. The linear percentage voiding was calculated over the 0.9mm length of the image. The ultrasonic beam diameter was 1.29mm (see Appendix D). There is also error in the relationship between the position on the C-scan and on the section, introduced by the ultrasonic 6dB drop measurement of the positions of the two reference faces. The positional inaccuracy is ±0.6mm. The scatter in Figure 53 is probably caused by these factors.

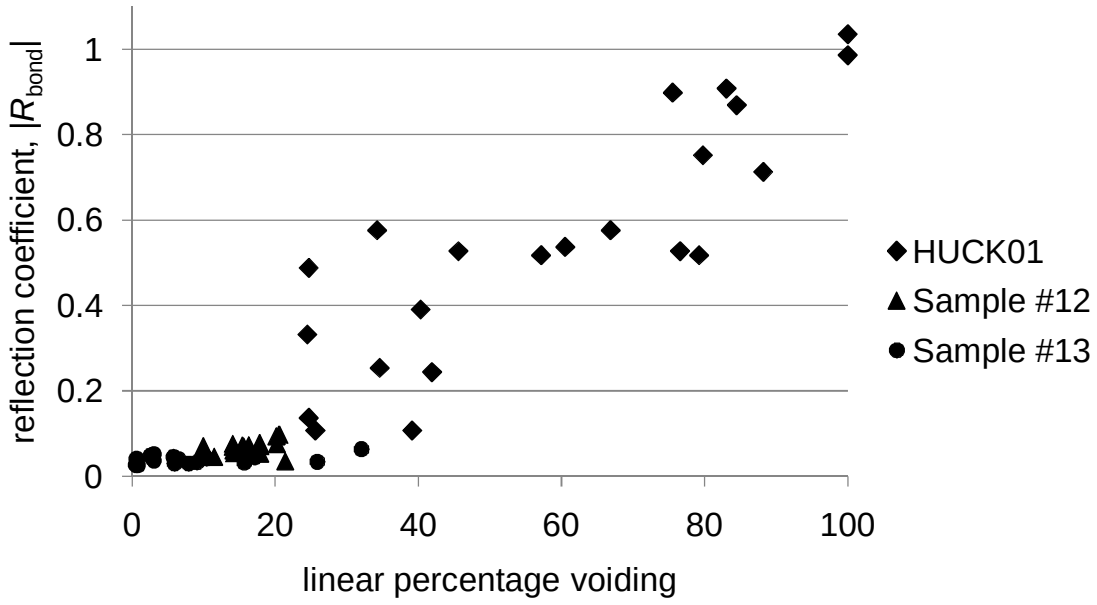

Figure 53. Absolute reflection coefficient, $|R_{bond}|$, for partially bonded sample against linear percentage voiding for: HUCK01in 22 different positions spaced at 2mm intervals along the dashed line shown in Figure 48, sample #12 in 15 different positions spaced at 2mm intervals along the dashed line shown in Figure 46 and sample #13 in 15 different positions spaced at 2mm intervals along the dashed line shown in Figure 47.

Samples #12, #13 and HUCK01 all contained relatively high percentage voiding and could be easily separated from the well-bonded samples based upon the amplitude of the ultrasonic signal reflected from the bond line (see Figure 49). Samples #10 could not be separated from the well-bonded samples based upon the amplitude of the reflected signal and sample #11 was marginal. Both samples #10 and #11 were sectioned parallel to and 25mm from Face A and polished for metallurgical examination (see Figure 39). The part of the sample without the pipe stub was then polished with increments of 2mm at a subcontractor. In total nine sections were metallurgically examined. Due to cost, images were not taken at regular intervals along the bond line at each polishing increment. The polishing increments at which voids were found were noted. Where voids were found, images of typical distributions were taken.

In the first two sections of sample #10 (25mm and 27mm from Face A), no voids were observed but there were regions of incomplete diffusion, where little or no grain growth had occurred across the interface. A photograph is shown in Figure 54. Voids were observed for all subsequent sections randomly distributed along the bond line. The voids ranged from 0.9µm - 92.4µm in diameter. The highest percentage voided area calculated for any of the images was 12.2%.

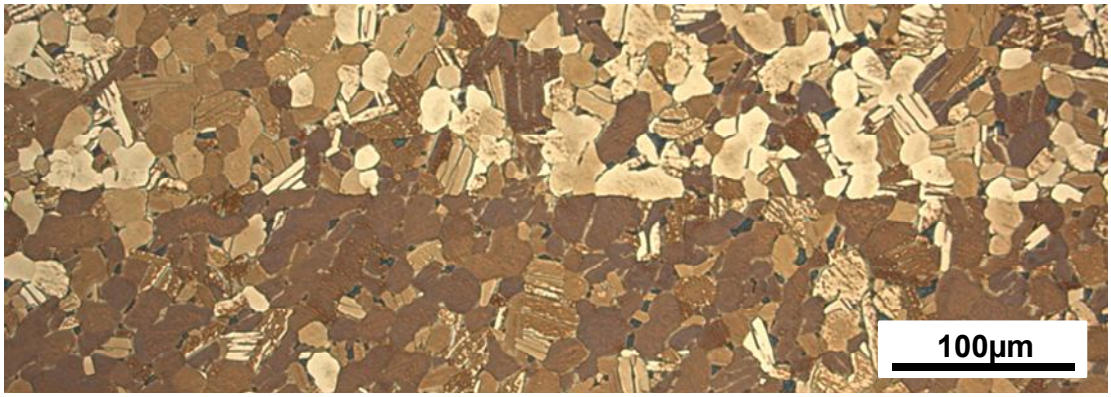

Figure 54. Sample #10: Photograph of bond line at first section, 25mm from Face A (see Figure 39). Limited grain growth has occurred across the interface. The sample has been heavily etched. The dark regions between grains are fine platelets of secondary alpha (see Section 3.1.1).

In sample #11, no voids were observed at the first two sections but incomplete diffusion or lack of grain growth was observed in some positions. A photograph is shown in Figure 55. Voids were observed randomly distributed along sections 3-9. The voids ranged from 1.0µm -59.6µm in diameter. The highest percentage voided area calculated for any of the images was 37.7%. The percentage voiding generally increased closer to Face B and further from Face A (Figure 39), which corresponds to the bottom left-hand side of the ultrasonic C-scan in (Figure 44).

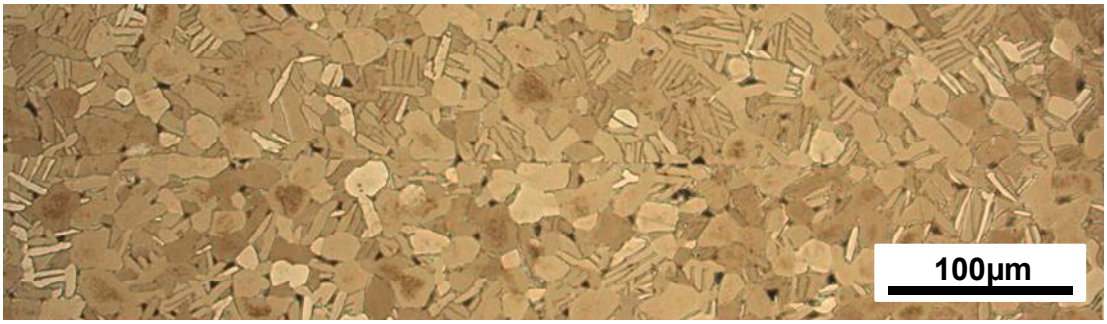

Figure 55. Sample #11. Photograph of bond line at second section, 27mm from Face A (see Figure 39). Limited grain growth has occurred across the interface. The sample has been heavily etched. The dark regions between grains are fine platelets of secondary alpha (see Section 3.1.1).

In summary, sixteen Ti-6Al-4V diffusion bonded samples were ultrasonically inspected for this project. Thirteen (samples #1-#13) were generated by joining pieces of forged Ti-6Al-4V. HUCK01 was manufactured before the start of this project and was made by joining pieces of cross-rolled Ti-6Al-4V plate. HUCK02 and HUCK03 were manufactured by joining pieces of unidirectionally rolled Ti-6Al-4V plate. HUCK01 was known to be partially bonded. Four new partially bonded samples (#10-#13) were generated by controlling the surface roughness of the blanks. Sectioning and metallurgical examination allowed the percentage voiding from samples HUCK01, #12 and #13 to be measured and related to the absolute reflection coefficient, $|R_{bond}|$. In general, the ultrasonic reflection coefficient increased monotonically with the percentage voiding. However, there is considerable scatter which is attributed to the measurement method. The reflection amplitude of samples #10 and #11 was lower than that for HUCK01, #12 and #13. Samples #10 and #11 were sectioned and polished in two millimetre increments. The general trend in bond condition was noted. The maximum amplitude in the C-scan for sample #10 was lower than the maximum in one of the well-bonded samples. However, the reflected amplitude cannot be directly compared for these samples due to differences in microtexture. The absolute reflection coefficient for all blocks is calculated in Section 5.3.

5. Advanced Methods for Detection of Partial Bonds in Ti–6Al–4V

The requirements of the ultrasonic inspection for the diffusion bonds between forged Ti-6Al-4V were outlined in Section 3.2.8. They include:

- normal to bond line inspection;
- pulse-echo configuration, as there is only access to one side of the diffusion bond;
- metal paths between ~10-100mm.

The conventional ultrasonic inspection of titanium diffusion bonds is limited by the amplitude of the backscattered noise from the parent material and by the reflection due to acoustic impedance mismatch between macrozones with different crystallographic alignment either side of the interface. The pulse-echo immersion inspection of the thirteen diffusion bonded blocks in Section 4, showed that two of the partially bonded samples (#12 and #13) could readily be separated from the well bonded samples based upon the maximum amplitude of the ultrasonic signal across the scanned area. Samples #11 was marginal and sample #10 could not be differentiated from the well bonded samples. In the first part of this section, the ultrasonic backscatter in the samples is measured, both in the parent metal and at the diffusion bond depth. The signal amplitude is corrected relative to a 0.050" flat-bottomed hole, as is done for a standard forging inspection. The aim is to understand whether backscatter from the parent material or the interface reflection is the limiting factor for the inspection.

For a partial bond that is distributed across an area larger than the size of the macrozones, techniques that measure the spatial distribution of the reflected ultrasound are appropriate, including spatial averaging, spatial

cross correlation and time of flight variance. The weak spatially coherent reflection due to acoustic impedance mismatch at the interface may limit the applicability of these methods. In Section 5.2, the spatial cross correlation coefficient is calculated for each of the diffusion bonded samples.

In Section 4, the amplitude of the reflected ultrasonic signal was measured. However, the apparent attenuation for the blanks used to manufacture the samples (FORG**) varies. The reflection coefficient accounts for this attenuation, by calculating the ratio between the magnitude of the frequency spectrum for the diffusion bond, $|A_{bond}(\omega)|$, and that for a reference signal from the backwall of a block with similar microtexture, $|A_{ref}(\omega)|$. The magnitude or absolute value of the reflection coefficient is frequently used to assess the quality of diffusion bonds (see Section 3.2.4). In Section 5.3 the absolute reflection coefficient, $|R_{bond}(\omega)|$, as a function of frequency is calculated for each sample. The frequency dependence of the reflection from the diffusion bond and the limitations of the absolute reflection coefficient as a method are discussed. Since, for the diffusion bonded samples, there is access to both sides of the diffusion bond the reflection coefficient was calculated for normal incidence on both sides: R_{12} and R_{21}.

For a defective bond where the voids are short and narrow compared to the wavelength of the incident ultrasound, the simple interfacial spring model (Equation 3.9) predicts that it is possible to differentiate between the component of the reflection due to acoustic impedance mismatch and that due to a defect from the phase of the reflected signal. In Section 5.4, the 'true phase', φ_{true}, of the reflection from the diffusion bond – a measure that is independent of arrival time - is calculated. The effect of gating and beam

focussing on φ_{true} is investigated. A complex reflection coefficient, R_{bond}, is calculated from the magnitude, $|R_{bond}|$, and phase of the reflection coefficient, φ_{true}, around the centre frequency of the probe. Spatial averaging is used to reduce the contribution of spatially incoherent backscattered noise in the parent metal either side of the diffusion bond. The imaginary and real components of R_{bond} are compared.

Finally, in Section 5.5 the symmetric reflection technique [65] is investigated. For this method, the reflection coefficient for normal incidence inspection from both sides of the diffusion bond – R_{12} and R_{21} – are combined. As access to both sides of the diffusion bond is required, this cannot be applied to the specific inspection geometry, however it can be used to separate good and well-bonded samples and for other industrial applications.

5.1. Ultrasonic Backscatter

In Section 4.4, the amplitude of the ultrasonic signal reflected from the bond line depth was compared for the diffusion bonded samples. These samples were generated by joining pieces of Ti-6Al-4V with various textures. In an industrial scenario, forgings are inspected by looking for reflections above the ‘grass’, which is the sound backscattered by the microstructure (see Section 2.3). The signal to backscattered noise ratio varies with metal path due to focussing and beam spread (Figure 6). Distance amplitude correction (DAC) is used to bring reflections from a standard reflector to the same amplitude over a range of metal paths. A single threshold can then be applied over this range. DAC does not improve the signal to backscattered noise ratio but it simplifies the inspection. The threshold is specific to that

forging and the selected inspection parameters (the probe and water path). It is chosen to ensure that the false call rate is low. The lowest achievable signal to backscattered noise ratio therefore determines the inspection threshold across the entire metal range.

The aims of this section are:

1. Understand the effect of the beam profile on the amplitude of the backscattered ultrasonic noise.
2. Understand the effect of DAC on the amplitude of the backscattered noise.
3. Determine whether the inspection sensitivity is limited by backscatter from the parent metal and the use of DAC, as in a conventional forging inspection, or by the planar interface between differently oriented macrozones caused by diffusion bonding Ti-6Al-4V, which acts as a weakly coherent reflector.

DAC will be applied to the full waveform data captured for the diffusion bonded samples: HUCK02 and samples #1-#13.

Sample HUCK02 was manufactured by joining two pieces of unidirectionally rolled plate with the rolling directions aligned. Figure 56a shows a surface wave velocity map for wave propagation normal to the diffusion bond for a slice through the sample. The macrozones are present as elongated plates, which are aligned with the rolling direction. The plates are typically 100-300µm thick. The surface wave velocity in the macrozones varies by up to 15%. Han and Thompson predict that scattering will be highest for wave propagation orthogonal to the long axis of the elongated plates [37]. Figure 56b shows a higher resolution image of a small region on the diffusion bond

line. There is no clear discontinuity in the microtexture at the diffusion bond line, as is observed in the surface wave velocity maps for a diffusion bond between forged Ti-6Al-4V (see Figure 14 – sample #2). As the interface is parallel with the rolling direction, the bond line cannot be differentiated from the boundaries between macrozones in the parent metal. HUCK02 is therefore a homogeneous block of Ti-6Al-4V with no change in microtexture at the diffusion bond. The full waveform data captured for sample HUCK02 was processed to help understand the effect of beam profile and distance amplitude correction (DAC) on the amplitude of the backscattered noise.

All diffusion bonded samples were ultrasonically inspected as described in Section 4.4 with a 10.9MHz 6.3”F 0.75” diameter probe focussed at the bond line depth. The scanned area was 30x20mm. The root mean square (RMS) backscattered noise was calculated across this area as a function of time of flight for sample HUCK02. The captured waveform was windowed with a 0.48µs long cosine-taper, where the ratio of constant to tapered sections was 0.2. The root mean square of the windowed waveform was calculated. The window was then shifted by the sampling interval – 0.004µs – and an RMS was calculated for each window position. This was repeated to obtain RMS against time of flight at each scan position. The RMS against time of flight was then averaged over the scanned area.

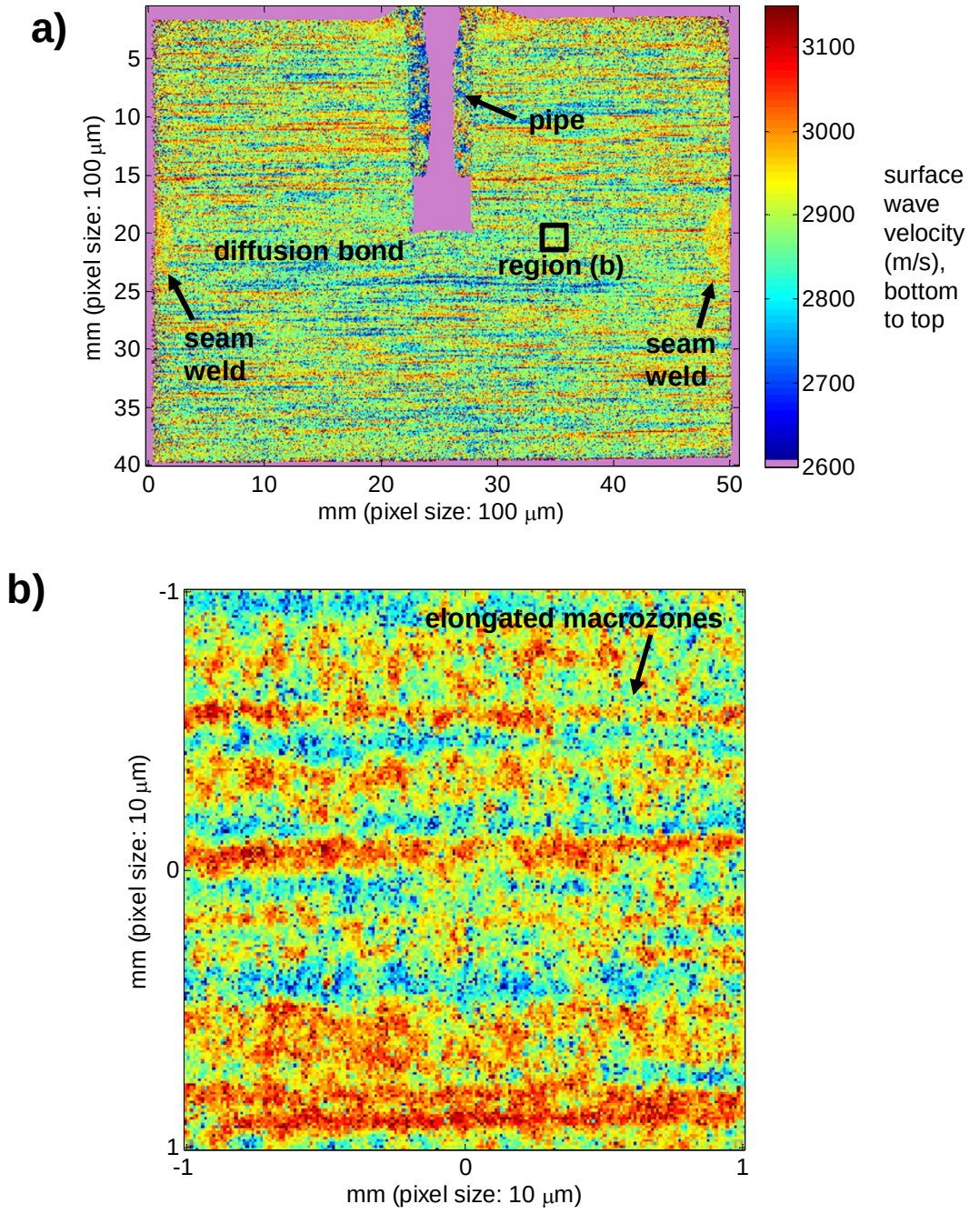

Figure 56. Surface wave velocity maps of sample HUCK02, obtained using optical-scanning acoustic microscope (O-SAM) at the University of Nottingham [54]. The surface wave velocity was measured from top to bottom of the image. a) HUCK02 was made by joining two pieces of unidirectionally rolled Ti-6Al-4V, with the rolling directions aligned. The sample was sliced through the evacuation pipe and hole. Surface wave velocity was measured over a length of 100μm with a pixel size of 100μm. b) Higher resolution image of region (b) showing elongated macrozones aligned with the rolling direction (left-to-right). Surface wave velocity was measured over a length of 50μm with a pixel size of 10μm.

A distance amplitude curve for that probe and water path was generated (see Appendix C) and is plotted in Figure 57a. The standard reflector was a 0.050" flat-bottomed hole. Each point corresponds to the amplitude reflected from a 0.050" flat bottomed hole at a different depth (or metal path) in the calibration block. Figure 57a shows the RMS backscattered noise for HUCK02 without distance amplitude correction. The highest amplitude backscattered noise is around the focal zone. Figure 57b shows the RMS backscattered noise with distance amplitude correction. The amplitude has been corrected so that the reflection from a 0.050" is constant across the entire range of metal paths. The RMS backscattered noise is now reasonably flat over the range of metal paths but it is lowest around the focal zone.

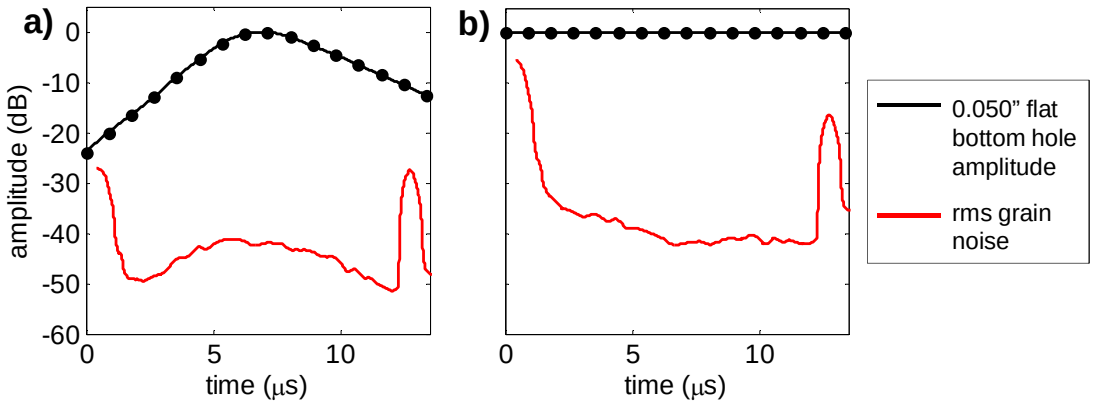

Figure 57. a) Flat-bottomed hole amplitude (black) and RMS backscattered noise (red) for HUCK02 against time of flight (a function of depth). b) Corrected so that flat-bottomed hole amplitude is 0dB for all time. 0dB is the amplitude of the reflection from a 0.050" flat-bottomed hole at a depth of 20.3mm in stainless steel.

The RMS and maximum backscattered noise was calculated in the same way for samples #1-#13, which were manufactured by joining blanks cut from segments of Ti-6Al-4V forgings. Figure 58 shows the RMS backscattered noise against time of flight for samples #1, #4, #5 and HUCK02, which are all

thought to be well bonded. The plots for these samples only are included here as they highlight specific issues, which will be discussed in the remainder of this section. The RMS and maximum backscattered noise against time of flight for all samples (#1 -#13 and HUCK02) are included in Appendix E.

For sample #4, the RMS backscattered noise is ~5dB higher immediately after the diffusion bond than immediately before it. This sample was generated by joining two blanks which were cut from different segments of forging and so had different microtexture (see Table 1 in Section 4.2). The step-change in backscattered noise is caused by the different microtexture either side of the diffusion bond. For sample #5 there is also a step-change in backscattered noise at the diffusion bond depth; the RMS backscattered noise is ~5dB lower immediately after the diffusion bond than immediately before it. However, Sample #5 was generated by joining two blanks cut from the same radial position in a forging (see Table 1 in Section 4.2). The step-change in RMS backscattered noise for this sample suggests that the microtexture changes with depth through the block. It could also indicate that microtexture varies with circumferential position in the forging and that the microtexture of the two joined blanks is different. This is important because, in Section 5.3 and Section 5.4, blocks cut from the same circumferential position in the forged segment are ultrasonically scanned to obtain reference signals which are used in the calculation of the reflection coefficient. If the microtexture of the reference block is not representative then error is introduced into the calculation. The blanks for sample #1 were also cut from similar regions in the same forging segment. For this sample there is no step-change in the RMS backscattered noise either side of the diffusion bond depth.

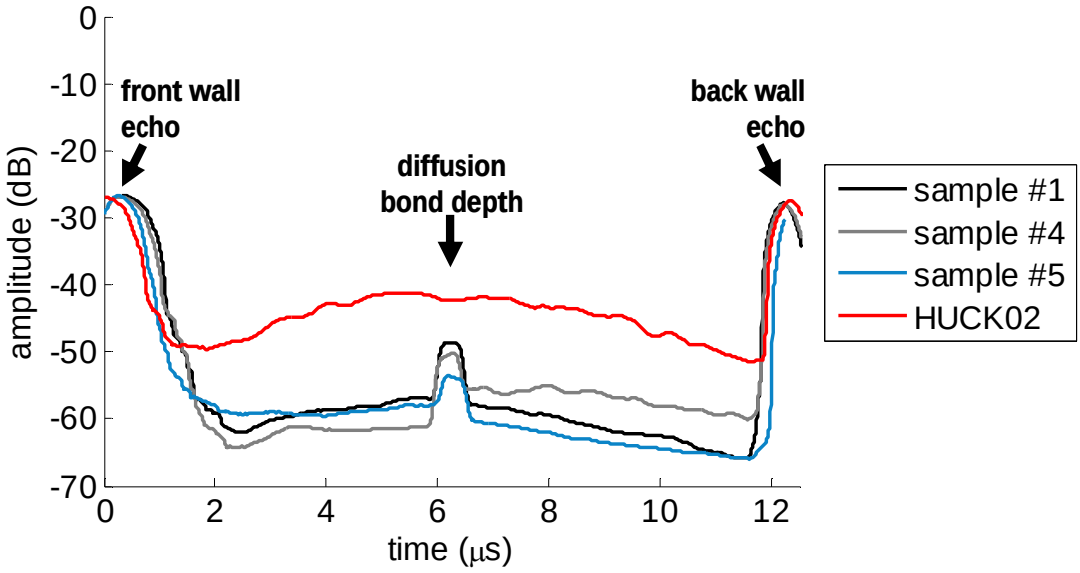

Figure 58. Root mean square of backscattered ultrasonic noise in samples #1, #4, #5 and HUCK02 vs time of flight (a function of depth) with probe focussed at diffusion bond depth. 0dB is the amplitude of the reflection from a 0.050" flat-bottomed hole at a depth of 20.3mm in stainless steel.

The RMS backscattered noise in the forged samples either side of the diffusion bond is ~15-20dB lower than in HUCK02. It should therefore be possible to detect much smaller defects in the bulk of the forged material than in the bulk of the unidirectionally rolled plate with wave propagation normal to the rolling plane. For all samples the backscattered noise is highest at the depth of the diffusion bond, as the probe was focussed at that depth. For samples #1, #4 and #5 there is an abrupt peak in the RMS backscattered noise at the depth of the diffusion bond which is not present for sample HUCK02. This peak is up to 15dB higher than the RMS backscattered noise immediately before or after the bond line depth. Samples #1, #4 and #5 are thought to be well bonded but, as stated in Section 4.5, the samples were not incrementally polished at sufficiently fine increments to guarantee this. The peak in RMS backscattered noise may be due to the presence of defects but could also be attributed to the planar

interface between large macrozones at the diffusion bond line, as discussed in Section 3.2.1.

At the diffusion bond depth, the RMS backscattered noise in HUCK02 is similar to that for sample #1. For the forged samples, the macrozone boundaries in the parent metal are randomly oriented (see surface wave velocity maps of forged segments in Appendix B). The incident ultrasound will be scattered in all directions. The diffusion bond creates a planar interface between macrozones. Also, the beam diameter was smallest at the diffusion bond depth due to focussing. Before and after the bond plane, it is less likely that the entire beam is incident upon one boundary at a time, simply because the beam diameter is larger. There is a higher likelihood that, at the diffusion bond depth, energy will be reflected back towards the probe. In HUCK02, the macrozones are parallel to the diffusion bond and tens of millimetres in length, as shown in Figure 56. For this sample, the ultrasonic wave will be reflected directly back towards the probe at all depths. The likelihood of this occurring is no greater at the diffusion bond depth. This will cause the lower RMS backscattered noise in the parent metal and the abrupt peak at the bond depth for the forged samples #1-#13, compared to the rolled sample HUCK02.

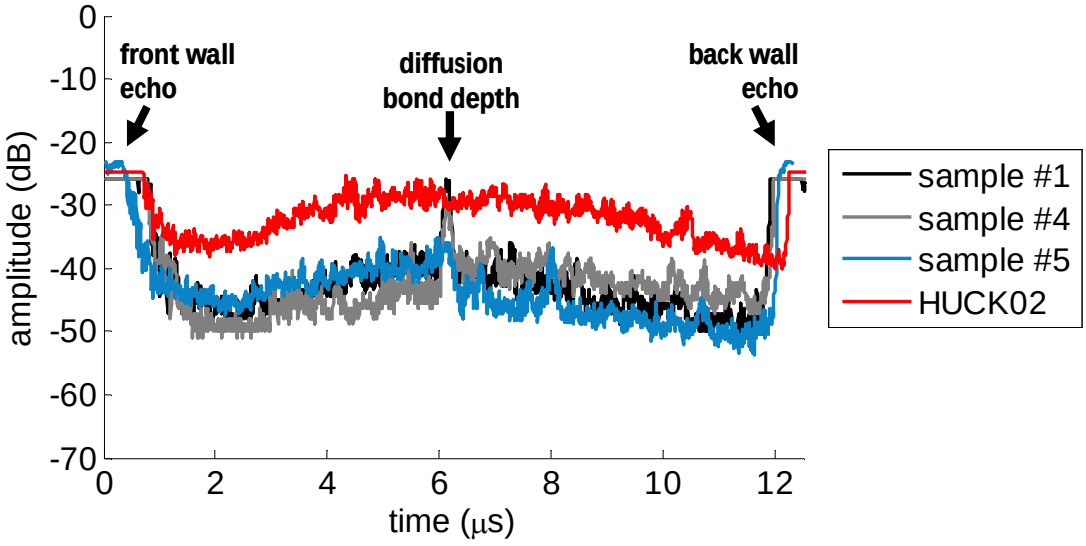

Figure 59. Maximum backscattered ultrasonic noise in samples #1, #4, #5 and HUCK02 vs time of flight (a function of depth) with probe focussed at diffusion bond depth. 0dB is the amplitude of the reflection from a 0.050" flat-bottomed hole at a depth of 20.3mm in stainless steel.

The maximum amplitude of the backscattered noise determines the threshold for the inspection. Figure 59 shows the maximum backscattered noise over the scanned area against time of flight for samples #1, #4, #5 and HUCK02. The results look similar to those for RMS backscattered noise in Figure 58; the backscatter amplitude is highest at the bond line depth, where the probe was focussed, and, for the forged samples #1 and #4 there is also an abrupt peak at the bond line depth. The increase in maximum backscattered noise is not obvious for sample #5. For sample #5 there is also a peak after the diffusion bond depth, which is similar to the amplitude at the diffusion bond. This may be a reflection from a large macrozone whose boundary happens to be normal to the incident wave.

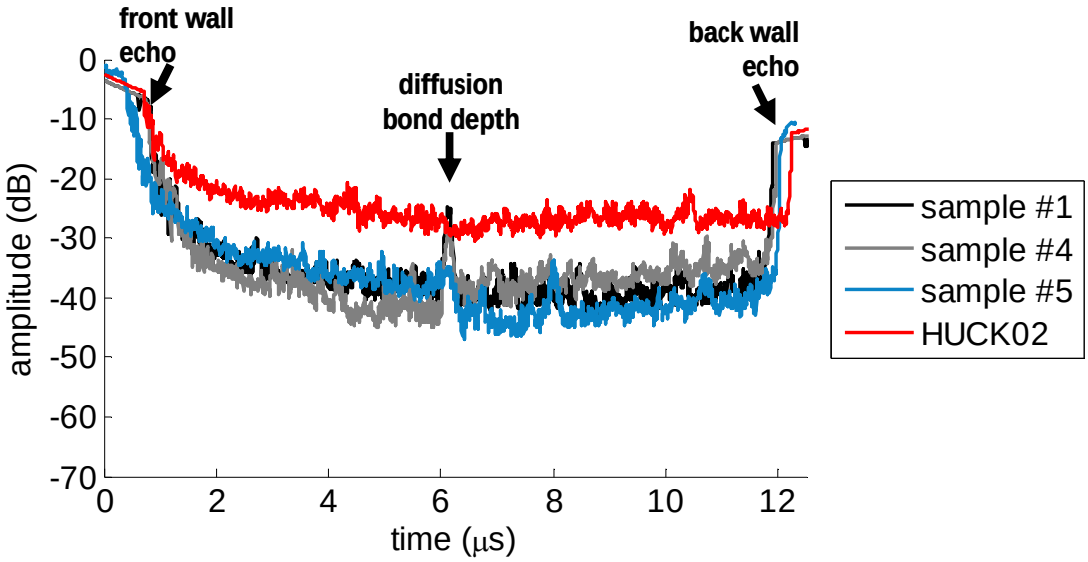

Figure 60. Maximum backscattered ultrasonic noise in samples #1, #4, #5 and HUCK02 vs time of flight (a function of depth) with probe focussed at diffusion bond depth and distance amplitude correction. 0dB is the amplitude of the reflection from a 0.050" flat-bottomed hole at the same time of flight in stainless steel.

Figure 60 shows the maximum backscattered noise against time of flight with distance amplitude correction. For sample HUCK02, the maximum backscattered noise is now reasonably flat across all depths. For samples #1 and #4 the maximum backscattered noise is highest at the bond line depth, even with distance amplitude correction. Assuming that samples #1 and #4 are defect free and that the peak can be attributed to acoustic impedance mismatch between adjacent macrozones at the bond line, then the inspection threshold has to set above this amplitude to avoid false calls. For sample #5, the maximum backscattered noise at depths both before and after the diffusion bond depth is higher than at the diffusion bond depth. It can be concluded that, for samples #1 and #4, the ultrasound backscattered by the interface limits the sensitivity of the inspection. For sample #5 the ultrasound backscattered in the parent metal limits the sensitivity of the inspection.

A method for determining the inspection threshold for diffusion bonds between forged pieces of Ti-6Al-4V would be useful in industry. Across samples #1-9, which are all thought to be well-bonded, the maximum reflected amplitude at the diffusion bond line depth varied by up to 10dB (see Figure 49). The amplitude of the backscattered signal is determined by a combination of the acoustic impedance mismatch at the diffusion bond depth and the beam diameter.

If the beam diameter is smaller than the macrozones then the amplitude of the backscattered signal will be determined by the local acoustic impedance mismatch. In Section 3.2.1, the highest possible longitudinal wave reflection coefficient due to acoustic impedance mismatch in Ti-6Al-4V was estimated assuming that on one side of the interface all the grains are aligned with their main axis parallel to the diffusion bond and on the other side of the interface the grains are aligned with their main axis orthogonal to the diffusion bond. The acoustic impedance mismatch was then 9.3%, which is −17dB compared to a 0.050” diameter flat-bottomed hole in stainless steel for these inspection parameters. In a real microstructure this level of texture may not occur. The texture in the material can then be characterised by measurement, either using a technique such as electron backscatter diffraction or by local measurement of the acoustic velocity. Surface wave velocities were measured with a resolution of 250µm for slices of the forged segments (see Section 4.2.1 and Appendix B). The highest surface wave reflection coefficient due to acoustic impedance mismatch between adjacent macrozones in sample #2 was estimated to be 6.9% (see Section 3.2.1). A reflection coefficient of 6.9% for a longitudinal wave corresponds to −19dB compared to a 0.050” flat-bottomed hole in stainless steel.

If the beam diameter is larger than the macrozones, the acoustic impedance mismatch will be averaged and such high amplitude backscattered signals are less likely. The actual peak measured for sample #2 was −28dB (Figure 49). It is clearly important to ultrasonically inspect diffusion bonded samples or components with representative microtexture and the selected inspection parameters in order to set an inspection threshold that does not result in false calls but that achieves the highest possible sensitivity to defects.

5.2. Spatial Correlation Coefficient

In the previous section it was shown that the ultrasonic backscatter in well bonded forged samples #1-#9 at the bond line can be higher than before or after the bond line, even with distance amplitude correction. This was attributed to an acoustic impedance mismatch at the diffusion bond. If the acoustic impedance change is low to high, the reflection coefficient will be positive i.e. the reflected wave will be in phase with the incident wave. If the acoustic impedance change is high to low, the reflected wave will be π radians out of phase with the incident ultrasonic wave. If the microtexture of the two pieces that have been joined is similar then both phases will be equally probable. As the probe is moved over the bond line, the phase of the reflected wave will flip. If the beam diameter is larger than the macrozone size, then these two phase changes will cancel one another out to some extent.

The normalised spatial correlation coefficient, *SCC*, (Equation 3.4) measures how similar signals are in phase and amplitude between two points, x and x'. If $|x-x'|=0$mm, then the two signals are the same and the *SCC* is 1. Two

signals that are far apart, $|x-x'|\rightarrow\infty$, are expected to be poorly correlated and the *SCC* will be closer to 0. For an area scan the *SCC* can be calculated for many pairs of points with the same measurement spacing $|x-x'|$ (see Figure 61) and an average can be found. If the signals for two different positions over a good diffusion bond are compared then they will either be in phase, giving a positive *SCC*, or out of phase, giving a negative *SCC*. The average *SCC* is expected to tend to zero.

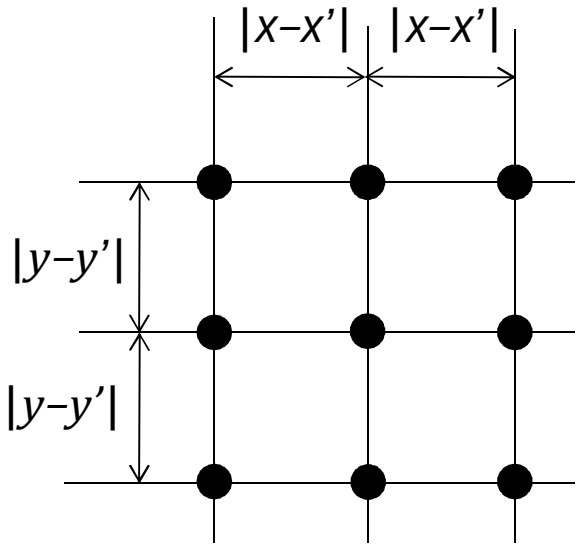

Figure 61. The spatial correlation coefficient, *SCC*, was calculated for all pairs of points spaced $|x-x'|$ and $|y-y'|$ apart across the scanned area. An average *SCC* was calculated for two perpendicular directions, *x* and *y*.

Rinker *et al* [64] showed that for good upset-forge welds in stainless steel the average *SCC* tends towards zero as the measurement spacing, $|x-x'|$, increases. For welds that are marginal over length scales greater than $|x-x'|$, the reflection will be correlated, since the reflection due to the defects arrives back in phase. $SCC(|x-x'|\rightarrow\infty)$ tends to a non-zero residual value.

The average spatial correlation coefficient as a function of measurement spacing was calculated for the forged diffusion bonded samples #1-#13. Full

waveform data for all the samples had been captured, as described in Section 4.4. A time series 0.4μs long and centred on the diffusion bond line was extracted from the full waveform data. The *SCC* was calculated by comparing each 0.4μs time series spaced $|x-x'|$ apart using Equation 3.4. An average *SCC* was calculated in two perpendicular directions, $|x-x'|$ and $|y-y'|$ (see Figure 61). This was done for $|x-x'|$ and $|y-y'|$ over the range 0mm-10mm in 0.25mm steps. The spatial correlation coefficient is calculated without shifting the signals relative to one another in time. Therefore the bond line must be flat and normal to the incident beam.

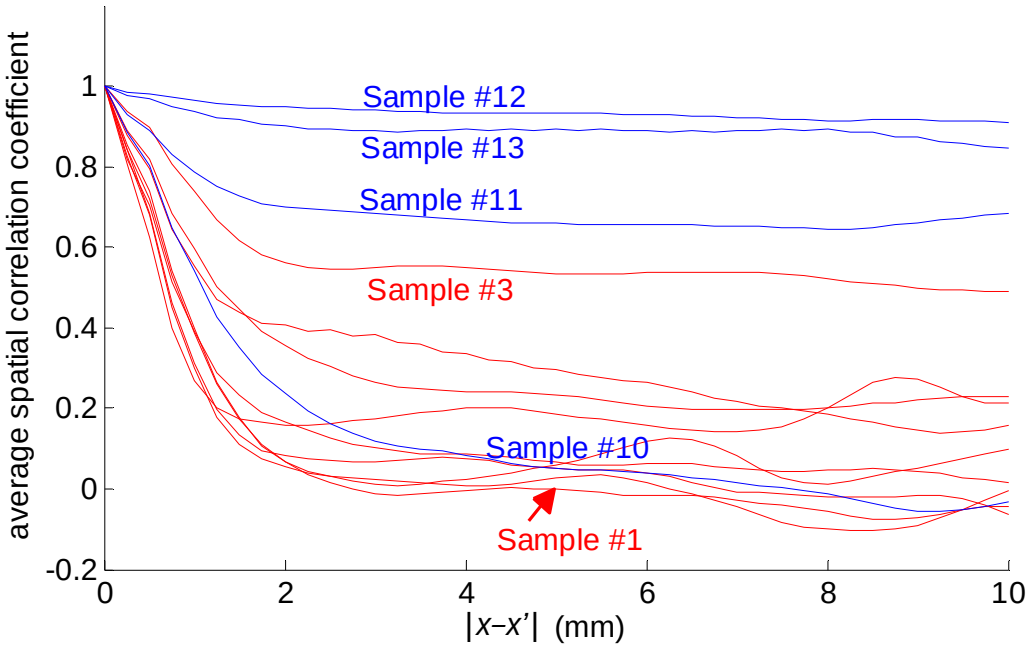

Figure 62. Average spatial correlation coefficient, *SCC*, vs spacing of measurement positions, $|x-x'|$ over 30x20mm scan area for samples #1-#13. Well bonded samples (#1-#9) are shown in red. Partially bonded samples (#10-#13) are shown in blue.

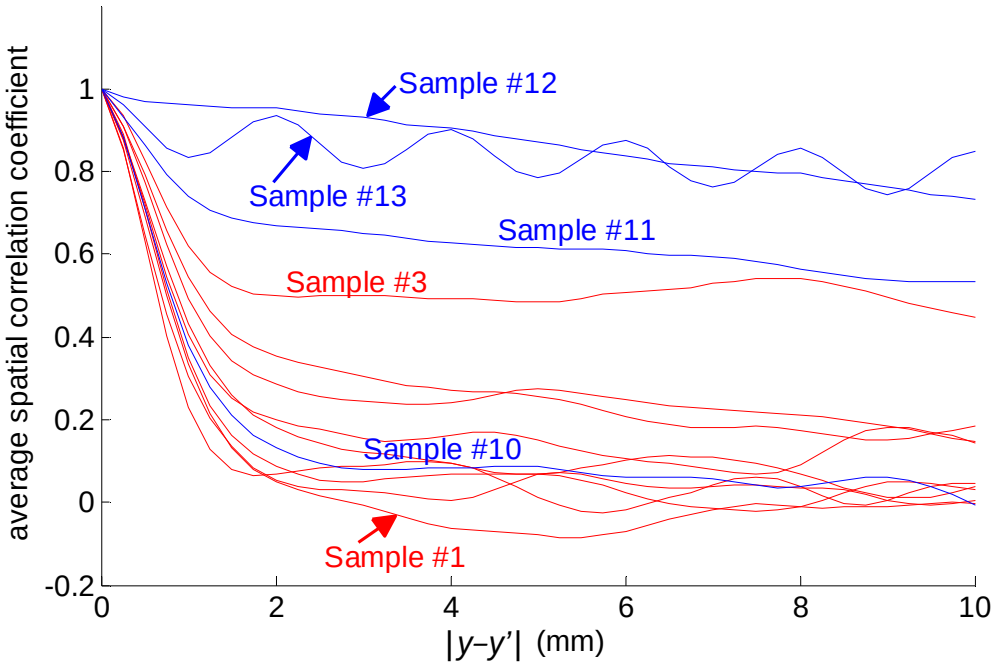

Figure 63. Average spatial correlation coefficient, *SCC*, vs spacing of measurement positions, |*y*-*y'*| over 30x20mm scan area for samples #1-#13. Well bonded samples (#1-#9) are shown in red. Partially bonded samples (#10-#13) are shown in blue. *SCC*(|*y*-*y'*|) for sample #13 has periodicity of ~2mm, which is thought to be related to the long range surface roughness of the blanks.

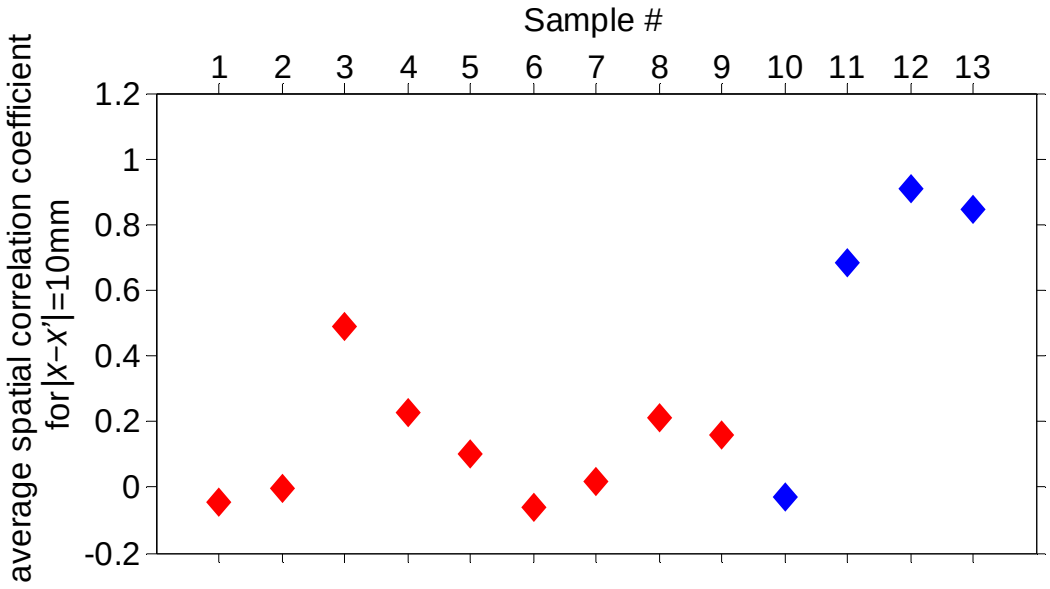

Figure 64. Average spatial correlation coefficient, *SCC*, |*x*-*x'*| =10mm for samples #1-#13. Well bonded samples (#1-#9) are shown in red. Partially bonded samples (#10-#13) are shown in blue.

The average *SCC* against measurement spacing in each direction - $|x-x'|$ and $|y-y'|$ - for samples #1-#13 are shown in Figure 62 and Figure 63 respectively. The average *SCC* for the measurement spacing $|x-x'|=10$mm is plotted for each sample in Figure 64. Samples #12 and #13, which have high percentage voiding, have the highest average $SCC(|x-x'|=10\text{mm})$. This implies that the bond line signal is coherent. For sample #13, $SCC(|y-y'|)$ has a periodicity of ~2mm. An ultrasonic C-scan is shown in Figure 47. There are horizontal bands of higher reflectivity, which are thought to be related to the long range surface roughness of the blanks. The periodicity in $SCC(|y-y'|)$ is due to these bands.

Sample #1 has the second highest average bond line amplitude for all the well-bonded samples (Figure 50) and yet it has one of the lowest average $SCC(|x-x'|=10\text{mm})$. This implies that the phase of the bond line signal varies significantly with position. Sample #3 has the highest average bond line amplitude for all the well-bonded samples (Figure 50). Except for the partially bonded samples, it has the highest average $SCC(|x-x'|=10\text{mm})$. This implies that the phase hardly varies with position. Figure 65 shows B-scans for samples #1 and #3. As expected, the reflection for sample #3 appears straighter or more ‘in phase’ than that for sample #1.

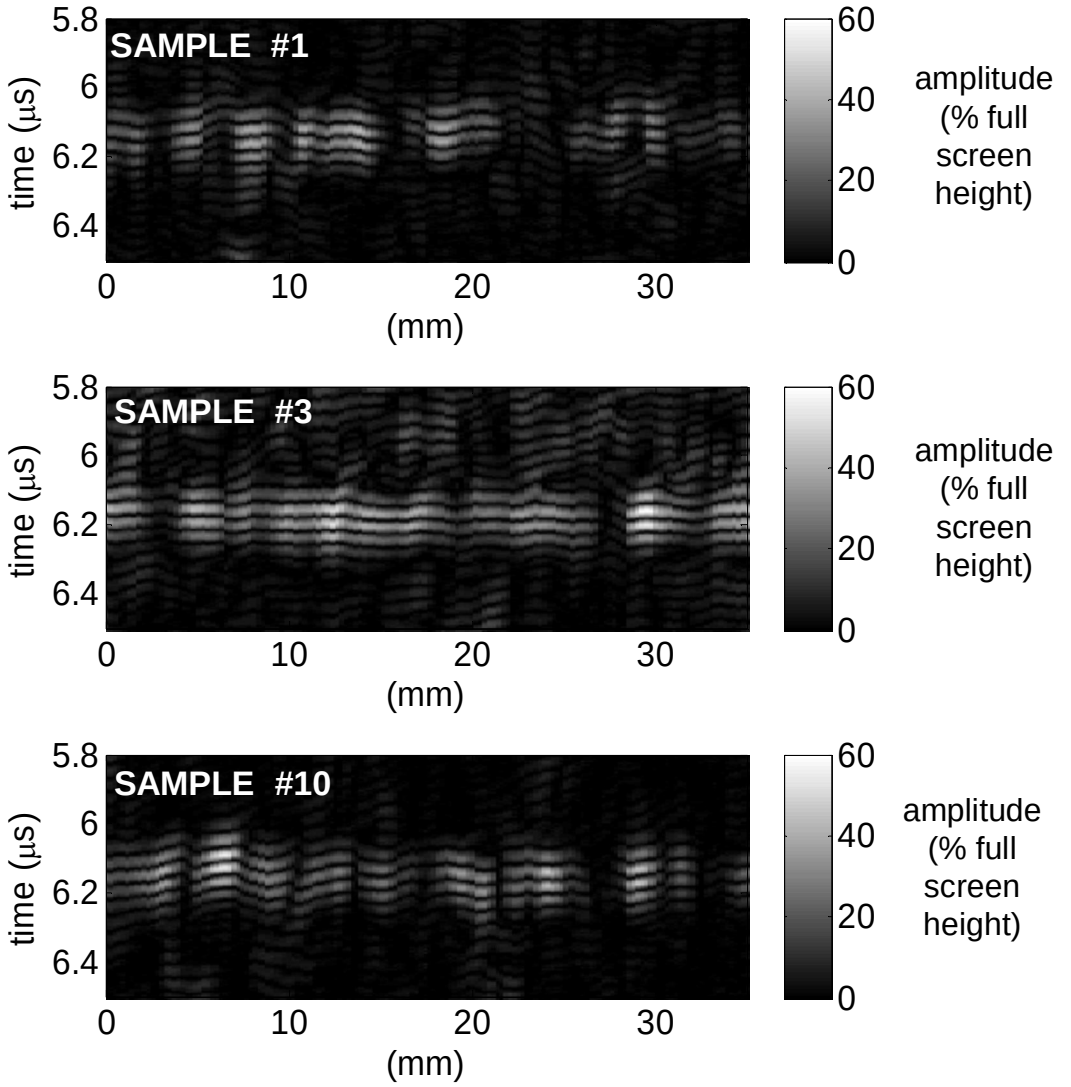

Figure 65. Ultrasonic B-scans of samples #1, #3 and #10. The reflection from sample #3 arrives in phase for almost all lateral positions. It has the correspondingly highest average spatial correlation coefficient for large measurement spacings, $SCC(|x-x'|\rightarrow\infty)$.

Sample #1 was generated by diffusion bonding two blanks cut from forged segment J (FORG05 – see Table 1). Sample #3 was generated by diffusion bonding blanks FORG07 and FORG09 cut from forged segments M and N. The surface wave velocity maps for slices from these forgings are included in Appendix B. They show that the microtexture of segment J (Figure B 10) is coarser than that of segments M and N (Figure B 14 and Figure B 18). The coarse microtexture in segment J and sample #1 means that the arrival time

of the wave at the bond line varies, as observed in the ultrasonic B-scan in Figure 65, reducing the spatial correlation coefficient.

Even if the arrival time is constant, which is expected when the propagation distance is much larger than the macrozone size, the phase of the reflection should flip between 0 and π radians for a well bonded interface between pieces of textured Ti-6Al-4V, as discussed above. The average *SCC* would then be expected to tend to zero for large measurement spacings. However, if there is an overall preference in crystallographic orientation in the blanks, such that the two blanks have different average acoustic impedances in the propagation direction normal to the bond line, then the phase of the reflected signal will be more consistent. $SCC(|x-x'|\rightarrow\infty)$ would then be non-zero, as observed for sample #3. The measured longitudinal velocity of blanks FORG07 and FORG09 in the through thickness direction differed by only 0.33% (Figure 36).

The average $SCC(|x-x'|=10\text{mm})$ for sample #10, which is known to be partially bonded, is lower than that for many of the well bonded samples. An ultrasonic B-scan for sample #10 is also shown in Figure 65. The phase of the reflected signal appears to vary with lateral position. Like sample #1, the blanks for sample #10 (FORG03 and FORG04) were both cut from segment J. The coarse microtexture could cause the 'wobbly' echo and the low spatial correlation coefficient. For partially bonded samples, the spring model predicts that the reflected signal will be $\pi/2$ out of phase with the incident signal for wavelengths that are long compared to the defect size (Equation 3.9). There will also be reflections in phase and π out of phase with the incident wave due to the acoustic impedance mismatch at the bond line. The

net result is that the phase varies with lateral position and $SCC(|x-x'|=10\text{mm})$ for sample #10 is very low.

Like sample #3, sample #11 was manufactured by joining two blanks cut from forged segment J (FORG07 and FORG08). The measured longitudinal velocity of blanks FORG07 and FORG08 differed by 0.39% (Figure 36). $SCC(|x-x'|=10\text{mm})$ for sample #11 is only marginally higher than $SCC(|x-x'|=10\text{mm})$ for sample #3. This could be attributed to the presence of defects on the bond line or $SCC(|x-x'|\rightarrow\infty)$ could be dominated by the acoustic impedance mismatch at the bond line. If the phase of the reflection due to acoustic impedance mismatch was consistent, then the presence of defects ($\pi/2$ out of phase with the incident signal) could cause $SCC(|x-x'|\rightarrow\infty)$ to decrease.

These results suggest that measuring the *SCC* as a function of measurement spacing is not a suitable method for differentiating between good and partial diffusion bonds between pieces of Ti-6Al-4V. Weakly coherent signals may be present at the diffusion bond due to acoustic impedance mismatch between macrozones or due to the presence of defects. Also, for sections that are thin compared to the macrozone size, the variation in the arrival time of the ultrasonic wave with lateral position can be significant, such that the signals appear uncorrelated. The technique may be applied if microtexture at the diffusion bond is consistent and the material is well characterised.

Straightforward spatial averaging and time of flight variance, which were introduced in Section 3.2.6, are similar methods to spatial cross correlation.

They also depend upon the backscatter from the bulk material returning to the probe out of phase but the backscatter from the defects in the bond plane returning in phase. For the same reasons described above, their application might be limited for diffusion bonds in Ti-6Al-4V.

Spatial averaging is often used in combination with other techniques to reduce the contribution of backscattered noise from the parent material. It is used to this end in Section 5.4 and Section 5.5, alongside the calculation of the complex reflection coefficient. Thompson *et al* [55] defined the spatial correlation length, *SCL*, for bulk material as the measurement spacing $|x-x'|$ for which the average *SCC* falls to $1\backslash e$ (see Section 3.1.2). The *SCL* depends upon the grain or macrozone size and upon the beam profile. In Section 3.2.6, it was suggested that the *SCL* could be used to estimate the minimum length scales over which spatial averaging must be carried out. This also dictates the minimum size of distributed defect that could be detected. Thompson *et al*'s definition of *SCL* assumed that the average *SCC* would tend towards zero for large measurement spacings. $SCC(|x-x'|\rightarrow\infty)$ at the diffusion bond depth is non-zero for several of the well bonded Ti-6Al-4V samples #1-#9, plotted in red in Figure 62 and Figure 63. For the well bonded samples between pieces of textured Ti-6Al-4V, the spatial correlation length could instead be defined as:

$$SCL = |x - x'| \quad \text{where } SCC = SCC(|x - x'| \rightarrow \infty) + \frac{1}{e}(1 - SCC(|x - x'| \rightarrow \infty)) \quad (5.1)$$

For samples #1-#13 this value is ~1.25mm, which is very close to the beam diameter (1.29mm). For this project, spatial averaging was carried out over areas of 20x30mm, which is much larger than the spatial correlation length.

The spatial correlation length is also affected by the microtexture of the bulk material. *SCC* as a function of measurement spacing was calculated for

sample HUCK02 for two perpendicular directions: one perpendicular to the rolling direction ($|x-x'|$) and one aligned with the rolling direction ($|y-y'|$). The results are shown in Figure 66. For both directions the *SCC* tends towards zero for large measurement spacings, suggesting that there is no average acoustic impedance mismatch. The *SCL* in the direction perpendicular to the rolling direction is the same as that for samples #1-#13: ~1.25mm. In the direction aligned with the rolling direction the *SCL* is ~4mm. This high spatial correlation length is attributed to the elongated macrozones generated by the rolling process (see surface wave velocity map in Figure 38).

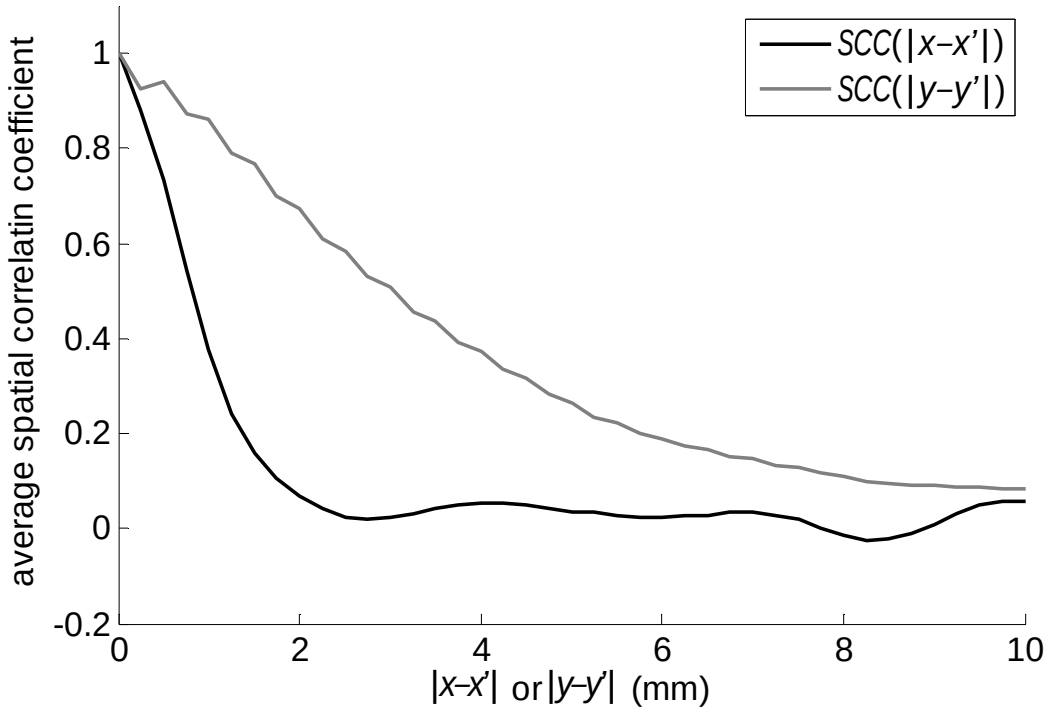

Figure 66. Average spatial correlation coefficient, *SCC*, vs spacing of measurement positions for two directions, $|x-x'|$ and $|y-y'|$ over 30x20mm for sample HUCK02. *x* was aligned with the rolling direction and *y* was perpendicular.

In conclusion, the average spatial correlation coefficient for large measurement spacings, $SCC(|x-x'|\rightarrow\infty)$, can be non-zero for diffusion bonds

between textured Ti-6Al-4V and the value is thought to depend upon the microtexture of the blanks that are joined. The presence of defects could cause $SCC(|x-x'|\rightarrow\infty)$ to increase or decrease. $SCC(|x-x'|\rightarrow\infty)$ or similar methods, such as spatial averaging or time of flight variance, could be used to differentiate well bonded and partially bonded samples but *a priori* knowledge of the microtexture either side of the interface is required.

The spatial correlation length, *SCL*, as defined by Thompson *et al* cannot be calculated for diffusion bonds in textured Ti-6Al-4V, if there is a difference in the average acoustic impedance of the material either side of the bond line. An alternative *SCL* can be defined, which is related to $SCC(|x-x'|\rightarrow\infty)$ by Equation 5.1. The spatial correlation coefficient or any technique which uses spatial averaging is only applicable to distributed defects. The diffusion bond must be defective over length scales greater than the spatial correlation length for the techniques to be effective.

5.3. Absolute Reflection Coefficient

The absolute reflection coefficient, $|R_{bond}(\omega)|$, and its frequency dependence are commonly used to assess the quality of diffusion bonds (see Section 3.2.4). For normal incidence on a diffusion bond it can be defined as the magnitude of the frequency spectrum of the signal reflected from the bond, $|A_{bond}(\omega)|$, divided by the magnitude of the frequency spectrum of a reference signal, $|A_{bond}(\omega)|$ (Equation 3.13).

The reflection from the backwall of a block whose thickness is equal to the diffusion bond depth and with identical microtexture can be used as a

reference signal (see Section 3.2.4). In this project, blanks cut from the same radial but different circumferential positions in the forged segments were used as reference blocks. The microtexture is expected to be similar but not identical to that in the diffusion bonded sample. In this section, the calculation of the reference frequency spectrum $|A_{ref}(\omega)|$ is described first. The absolute reflection coefficient $|R_{bond}(\omega)|$ is then calculated for the diffusion bonded samples #1-#13. The aim is to understand the frequency dependence of the reflections from defects.

The capture of full waveform data for the reference blocks FORG01-09 was described in Section 4.2.2. For each lateral position in the ultrasonic scan, the backwall signal was gated using a 1.2μs long cosine-taper window, as shown in Figure 67a. The centre of the window was fixed relative to the front wall reflection using an interface gate. The magnitude of the frequency spectrum at each position, $|A_{ref}(\omega)|$, was calculated by Fast Fourier Transform (FFT). $|A_{ref}(\omega)|$ varied with scan position. The frequency spectra were spatially averaged across the scan area to obtain a single reference spectrum.

The absolute reflection coefficient was also calculated for sample HUCK01 (Figure 53) but no cross-rolled plate was available as a reference. A saw cut was made at the bond line depth in the actual sample to act as a reference reflector, giving the magnitude of the frequency spectrum at only one point.

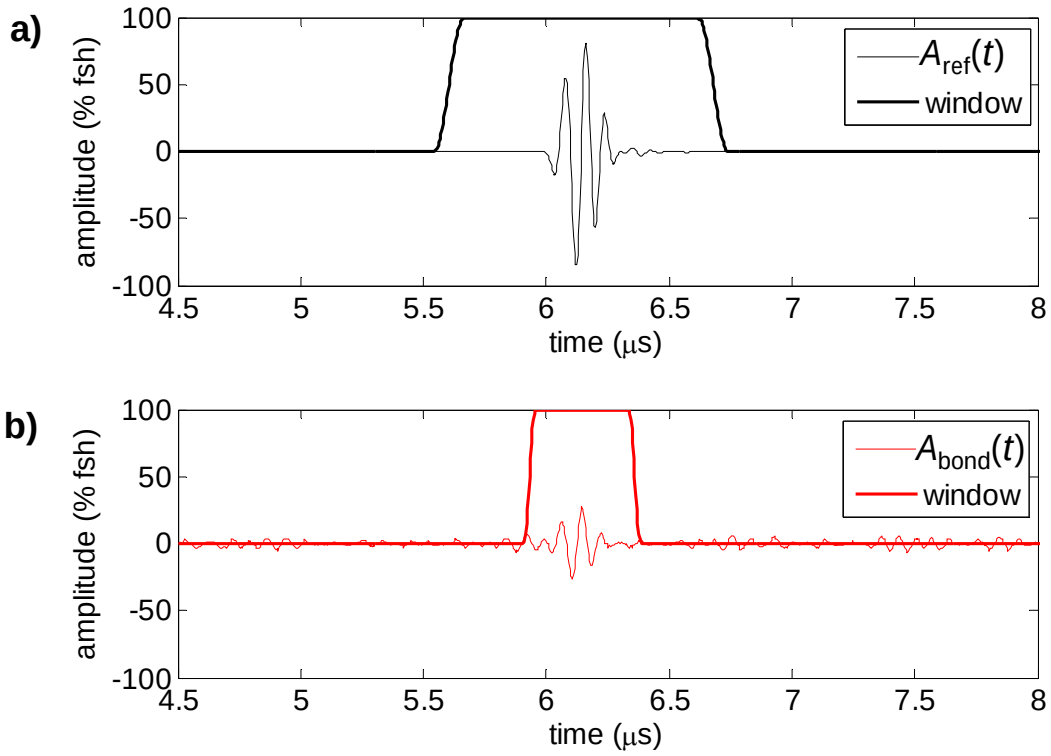

Figure 67. a) Typical backwall reflection for FORG07 and 1.2μs cosine-taper window b) Typical bond line reflection and 0.48μs cosine-taper window. Amplitude is in % full screen height (% fsh).

Full waveform data for diffusion bonded samples #1-#13 had been captured as described in Section 4.4. A 0.48μs long cosine-taper window was used to window the signal at the diffusion bond depth in each scan position, as shown in Figure 67b. A shorter window was used for the bond reflection, A_{bond}, than for the reference reflection, A_{ref}, to limit the contribution of the backscattered noise before and after the diffusion bond line. The centre of the window was fixed relative to the front wall reflection using an interface gate. The magnitude of the frequency spectrum, $|A_{bond}(\omega)|$, was found by Fast Fourier Transform. The reflection coefficient, $|R(\omega)|$, can be found by dividing $|A_{bond}(\omega)|$ by the magnitude of the frequency spectrum of the appropriate reference block, $|A_{ref,FORG**}(\omega)|$, as shown in Figure 68. The blanks joined to make each diffusion bonded sample are listed in Table 1.

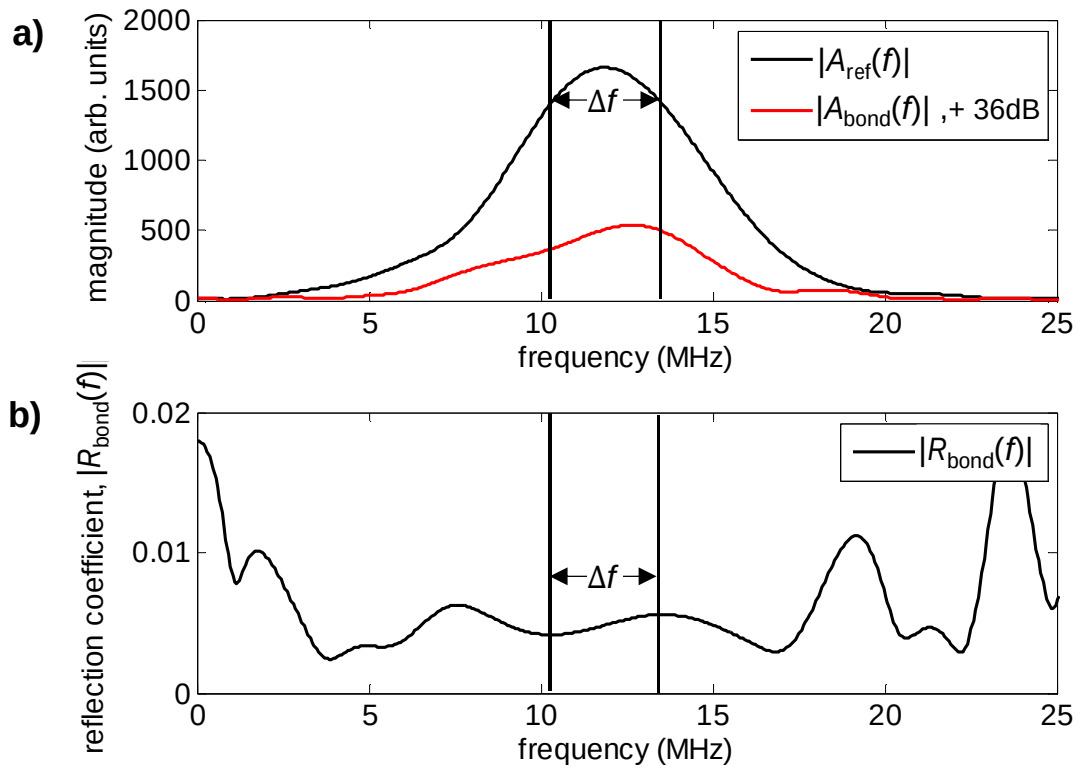

Figure 68. a) Magnitude of frequency spectrum for backwall reflection from a reference block, $|A_{ref}(f)|$, and for a bond line reflection $|A_{bond}(f)|$. $|A_{bond}(f)|$ was captured at a gain +36dB compared to that for the reference block. b) The reflection coefficient $|R_{bond}(f)|$ is the ratio of the two functions. A mean reflection coefficient can be calculated over a specified frequency range Δf.

The maximum magnitude of the frequency spectrum was found and the frequency range that corresponds to a 1dB decrease in magnitude was determined. The mean reflection coefficient across this frequency range was calculated for all samples. This frequency range was used as it corresponds to the range over which the phase and magnitude of the reflection coefficient are determined in Section 5.4 and is used to allow direct comparison of the results. The samples were scanned from both sides. The reflection coefficient for inspection from the side with the pipe stub (see Figure 31) is termed R_{12}. The reflection coefficient from the opposite face is termed R_{21}. An image correlation method was used to ensure that the reflection coefficient was being calculated over an identical area of the diffusion bond for scans from

both sides (see Appendix F). The maximum absolute reflection coefficient across the scanned area, $|R_{bond}|$, for inspection from each side of the sample is plotted for all samples in Figure 69. Partially bonded samples #12 and #13 can be easily differentiated from the well bonded samples. The maximum $|R_{bond}|$ for partially bonded samples #10 and #11 is lower than that for sample #1, which is thought to be well bonded. The difference in the measured reflection coefficient from either side of the sample - R_{12} and R_{21} - is due to variation in the apparent attenuation of the signal with scan position (see Figure 37, Section 4.2.2) and error in the measurement system.

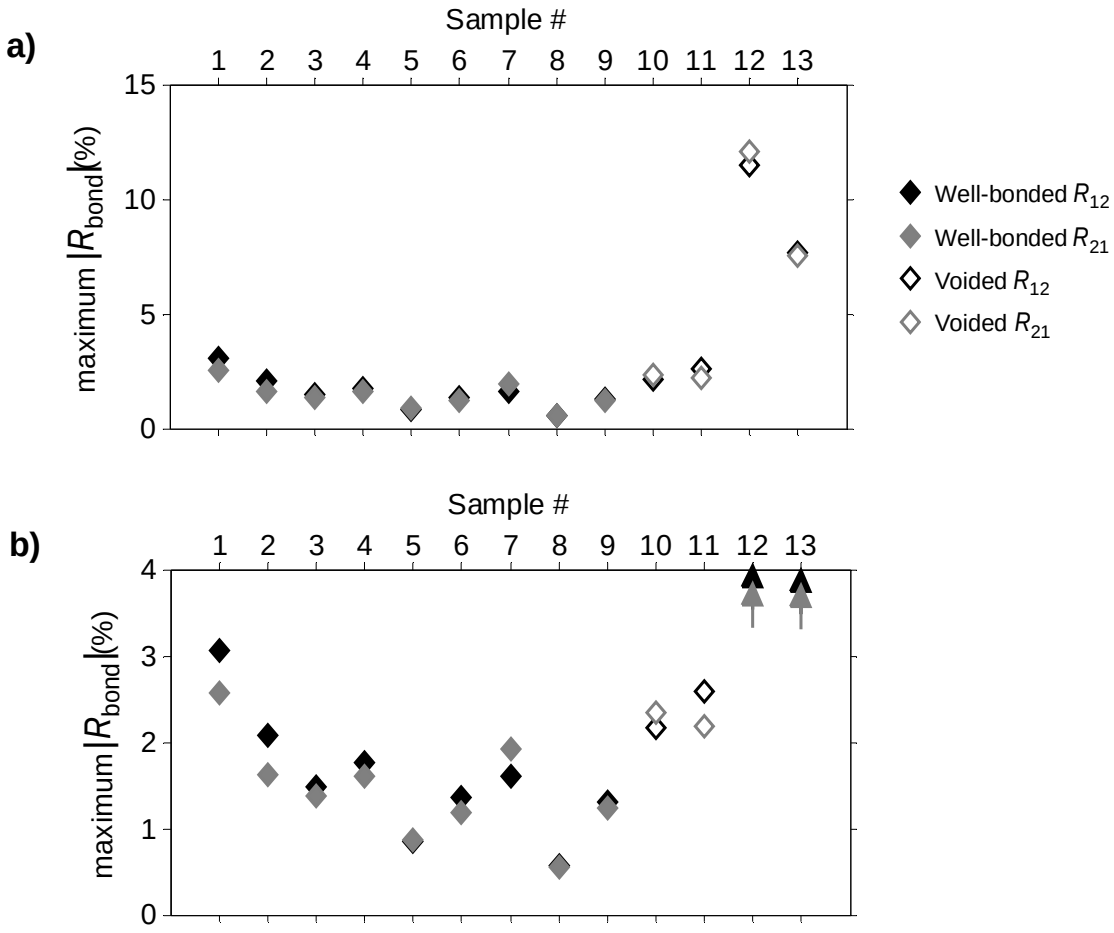

Figure 69. a) Maximum absolute reflection coefficient across entire ultrasonic scan for both well-bonded (#1-#9) and voided samples (#10-#13). The samples were scanned from each side to obtain R_{12} and R_{21} b) Same figure with expanded scale.

The absolute reflection coefficient was also averaged over the area of the scan. In this report, angle brackets <> are used to denote a spatial average. Therefore the spatial average of the absolute reflection coefficient is written as $<|R_{bond}|>$. $<|R_{bond}|>$ for each sample is plotted in Figure 70 for completeness and for comparison to the complex reflection coefficient in Section 5.4.

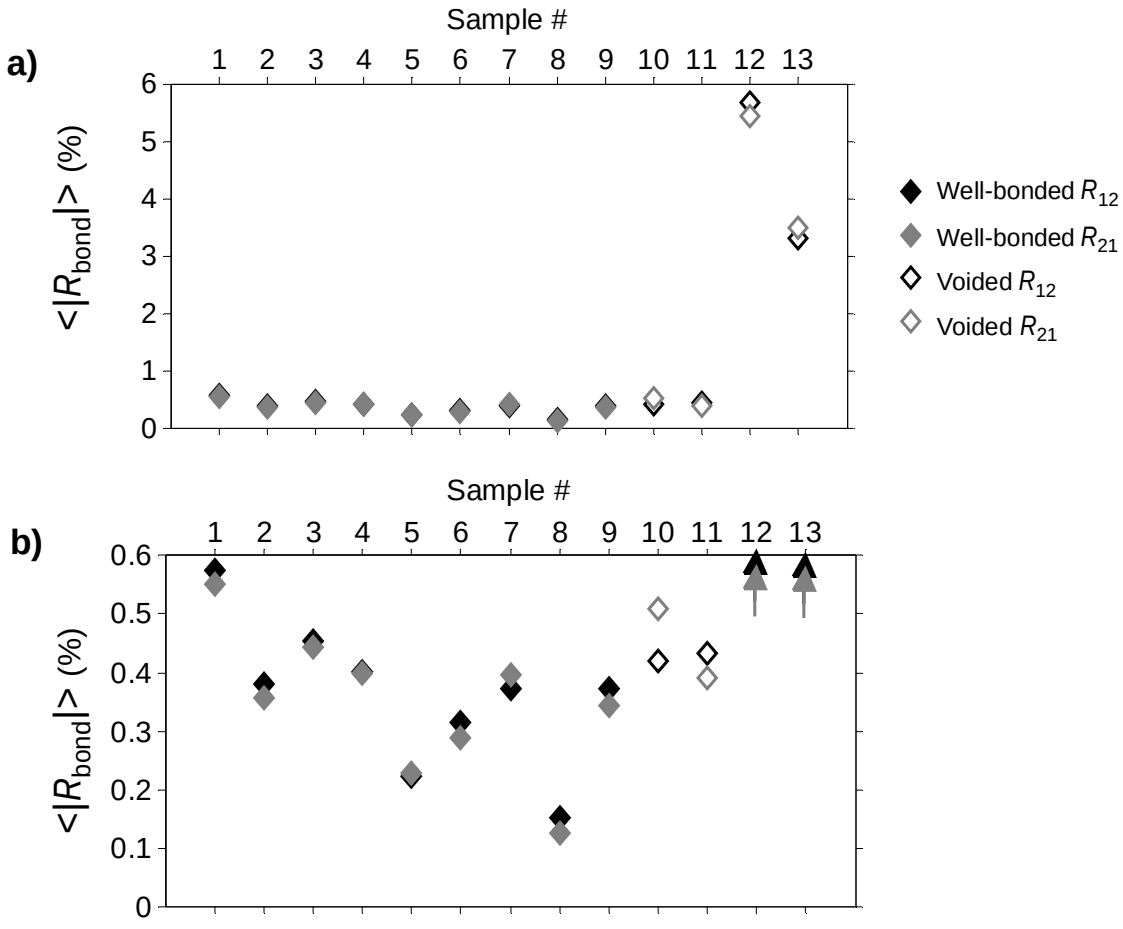

Figure 70. a) Absolute reflection coefficient spatially averaged across entire ultrasonic scan for both well-bonded (#1-#9) and voided samples (#10-#13). The samples were scanned from each side to obtain R_{12} and R_{21} b) Same figure with expanded scale.

A map of the mean reflection coefficient over a specified frequency range, Δf, against scan position can be created. Examples of $|R_{bond}|$ against scan position are shown in Figure 71, Figure 72, Figure 73 and Figure 74 for samples #1, #2, #10 and #11 respectively. The maps show the frequency

ranges 7-8MHz, 12-13MHz and 17-18MHz. Samples #1 and #2 are thought to be well bonded. At higher frequencies, the lateral size of the indications becomes smaller, which is a result of the improved spatial resolution. Samples #10 and #11 were generated by joining blanks whose surfaces had been scratched (see Section 0). At higher frequencies linear indications can be resolved from the background noise. These indications are thought to be scratches remnant after the diffusion bonding process. At high frequency these defect signals dominate and the reflections due to backscatter in the bulk material and acoustic impedance mismatch at the interface fall into the background.

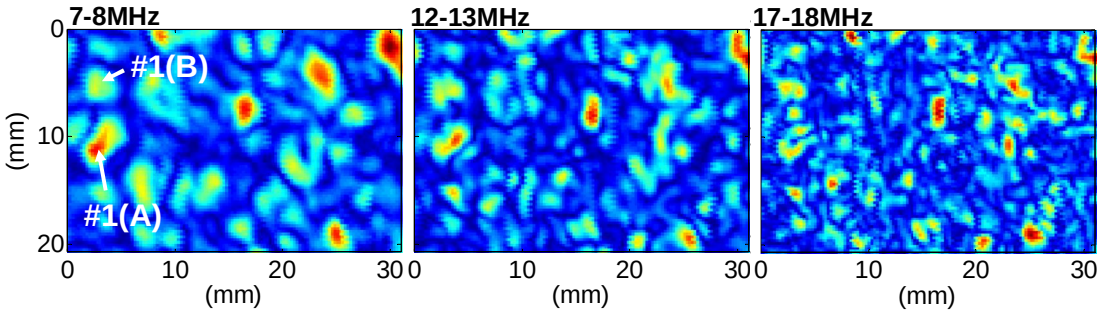

Figure 71. Sample #1. Map of absolute reflection coefficient $|R_{bond}(f)|$ averaged over three different frequency ranges: 7-8MHz, 12-13MHz and 17-18MHz. Colour scale is linear. Red indicates high magnitude. All three maps have been scaled relative to the maximum value in that map. $|R_{bond}(f)|$ for points #1(A) and #1(B) are plotted in Figure 76.

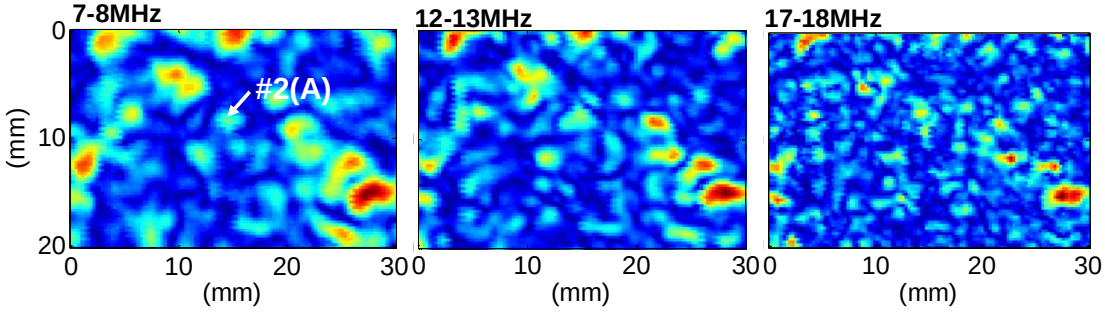

Figure 72 Sample #2. Map of absolute reflection coefficient $|R_{bond}(f)|$ averaged over three different frequency ranges: 7-8MHz, 12-13MHz and 17-18MHz. Colour scale is linear. Red indicates high magnitude. All three maps have been scaled relative to the maximum value in that map. $|R_{bond}(f)|$ for point #2(A) is plotted in Figure 76.

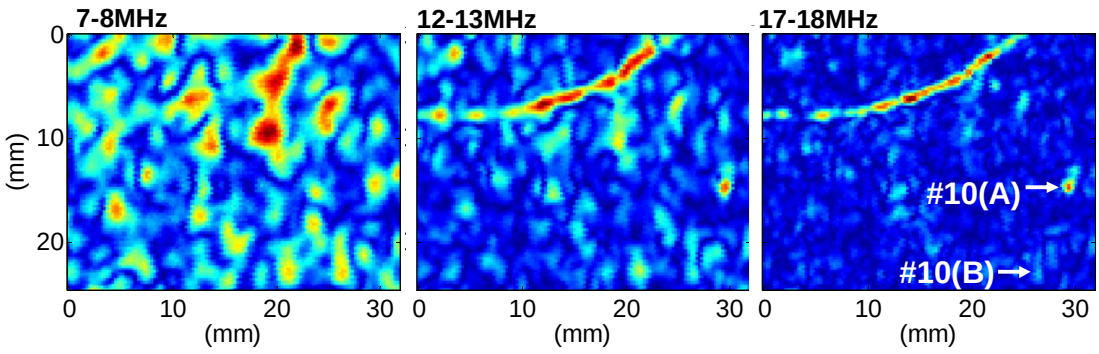

Figure 73. Sample #10. Map of absolute reflection coefficient $|R_{bond}(f)|$ averaged over three different frequency ranges: 7-8MHz, 12-13MHz and 17-18MHz. Colour scale is linear. Red indicates high magnitude. All three maps have been scaled relative to the maximum value in that map. Linear indications are apparent in the higher frequency maps (12-13MHz and 17-18MHz). $|R_{bond}(f)|$ for points #10(A) and #10(B) are plotted in Figure 76.

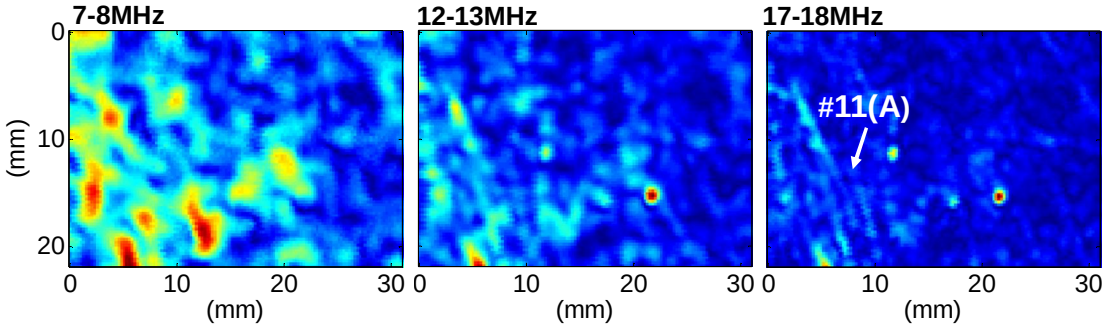

Figure 74. Sample #11. Map of absolute reflection coefficient $|R_{bond}(f)|$ averaged over three different frequency ranges: 7-8MHz, 12-13MHz and 17-18MHz. Colour scale is linear. Red indicated high magnitude. All three maps have been scaled relative to the maximum reflection coefficient for that map. Linear indications are apparent in the higher frequency maps (12-13MHz and 17-18MHz). $|R_{bond}(f)|$ for point #11(A) is plotted in Figure 76.

The spring model was used in Equation 3.9, Section 3.2.4 to describe the behaviour of partial bonds containing defects which are small compared to the ultrasonic wavelength. For an ideal interface the reflection is expected to have no frequency dependence. For a partially bonded interface, the presence of defects is expected to reduce the interfacial stiffness and the magnitude of the reflection coefficient will increase with frequency. Figure 75 and Figure 76 show the absolute reflection coefficient, $|R_{bond}(f)|$, at multiple

points in the partially bonded samples HUCK01and #10-#13. In Figure 76, the scale is expanded to show points with a lower reflection coefficient. $|R_{bond}(f)|$ from the marginal samples #10 and #11 are labelled and their position is indicated on the maps of absolute reflection coefficient in Figure 71 and Figure 72 respectively. These positions are all in regions where metallurgical examination had indicated a high likelihood of voiding. They were chosen simply to show a range of magnitudes of the reflection coefficient. The predictions of the spring model for a partial bond between two pieces of homogeneous isotropic titanium are also plotted. There is reasonable agreement between the spring model and the measured frequency dependence of the reflection coefficient, $|R_{bond}(f)|$, for the partial bond. As the interfacial stiffness increases, the predicted and measured frequency spectra become flatter.

In Figure 76, the absolute reflection coefficient, $|R_{bond}(f)|$, for positions in samples #1 and #2, which are thought to be well-bonded, is also plotted. $|R_{bond}(f)|$ from samples #1 and #2 are labelled in Figure 76 and its corresponding position is indicated on the maps of absolute reflection coefficient in Figure 73 and Figure 74 respectively. Position #1(A) has the highest absolute reflection coefficient for any of the well-bonded samples. The other points were chosen to show a range of magnitudes of the reflection coefficient. $|R_{bond}(f)|$ is flatter over the frequency range, which may indicate that the reflection is due to an acoustic impedance mismatch rather than a defect.

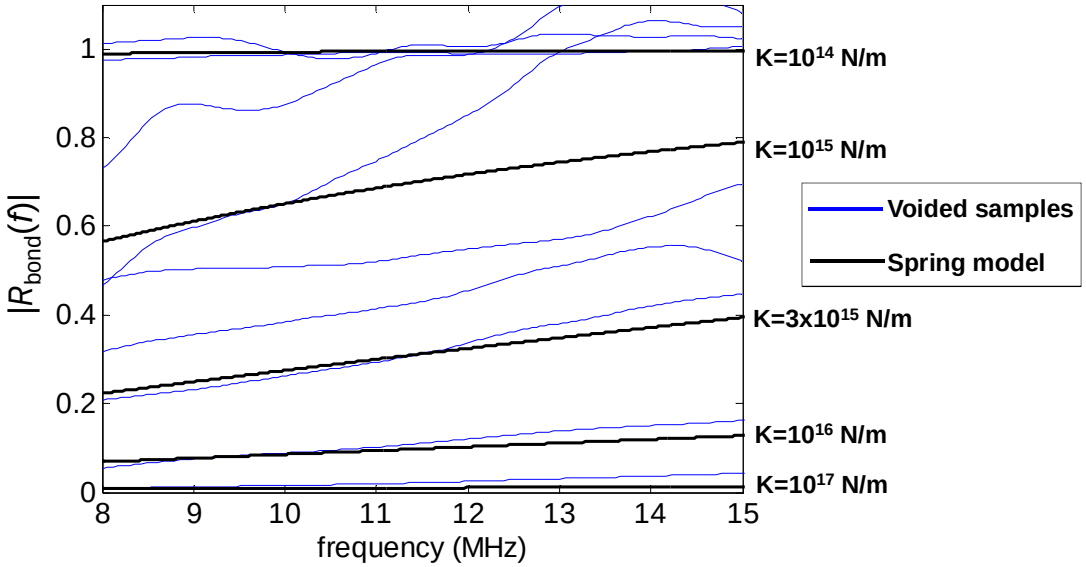

Figure 75. Reflection coefficient, $|R_{bond}(f)|$, measured at multiple points over the voided samples HUCK01, sample #10, sample #11, sample #12 and sample #13 and the prediction of the simple spring model (Equation 3.9) for an imperfect interface between similar pieces of material with acoustic impedance, z=27.3MRayls.

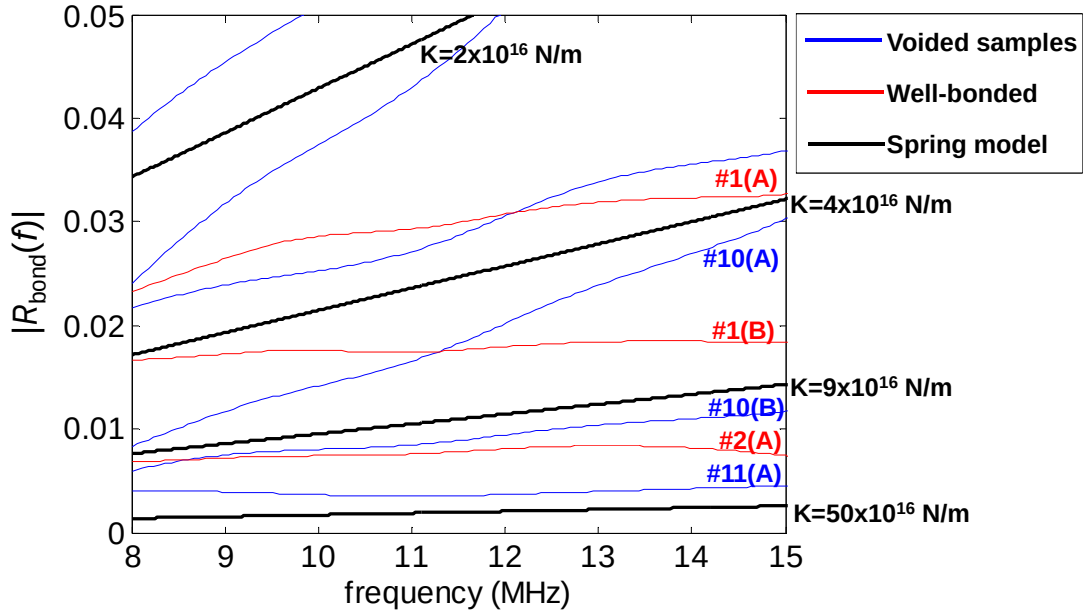

Figure 76. Reflection coefficient, $|R_{bond}(f)|$, measured at multiple points over the voided samples HUCK01, sample #10, sample #11, sample #12 and sample #13 and the well-bonded samples #1 and #2. $|R_{bond}(f)|$ from samples #1, #2, #10 and #11 are labelled and their position is marked in Figure 71 to Figure 74. The prediction of the simple spring model (Equation 3.9) for an imperfect interface between similar pieces of material with acoustic impedance, z=27.3MRayls is also shown. Expanded scale compared to Figure 75.

It is well known that high frequency inspection is more sensitive to small defects since higher spatial resolution can be achieved. Even when the wavelength is long compared to the defect size, the absolute reflection coefficient will increase with frequency as predicted by the spring model. Some method of quantifying the improvement in signal to noise ratio of the absolute reflection coefficient with increasing frequency was required. For each sample, the mean reflection coefficient was calculated over a 1MHz frequency range between 7-8MHz, 8-9MHz etc, increasing to 17-18MHz. These frequencies cover the working bandwidth of the probe. Below 7MHz and above 18MHz the electrical noise became dominant. For each frequency range, the maximum absolute reflection coefficient across the scanned area was calculated. A signal to noise ratio was calculated, defined as the maximum absolute reflection coefficient across the scanned area for that sample divided by the maximum absolute reflection coefficient across the scanned area for sample #1 at each frequency range. Sample #1 was chosen arbitrarily from the well bonded samples. The same trends in SNR are also observed if any of the other well bonded samples is used as a reference. The signal to noise ratio (SNR) against frequency is plotted in Figure 77. The defective samples (#10-#13) have clear frequency dependence while the well bonded samples (#1-#9) appear flatter across all frequencies. Below 13MHz the SNR is <1 for both samples #10 and #11.

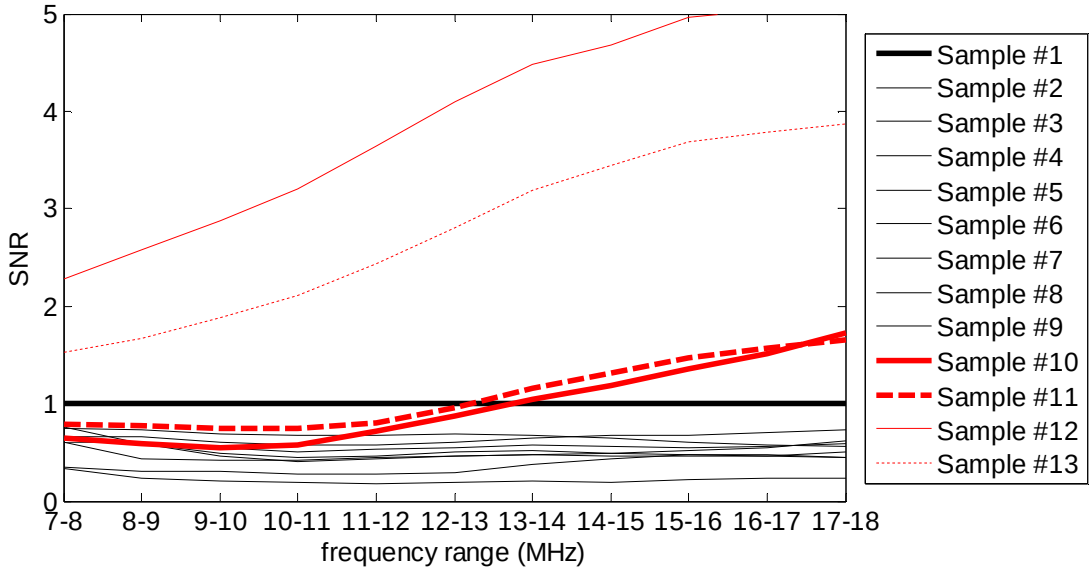

Figure 77. Signal to noise ratio (defined as maximum absolute reflection coefficient for frequency range across scanned area at each relative to the same value for sample #1) against frequency range.

In this section the absolute reflection coefficient $|R_{bond}|$ was calculated. The maximum value of $|R_{bond}|$ across partially bonded samples #10 and #11 was lower than in well bonded sample #1. This implies that the reflection coefficient due to acoustic impedance mismatch at the bond line can be larger than that due to partial bonding. The absolute reflection coefficient was also calculated as a function of frequency. $|R_{bond}(\omega)|$ for defective regions in samples #10 and #11 showed more frequency dependence than $|R_{bond}(\omega)|$ in the well bonded samples, as predicted by the spring model. Better separation between the well bonded and partially bonded samples was achieved by isolating higher frequency components $|R_{bond}(\omega)|$. At high frequency, better separation could be achieved than by conventional amplitude based methods, described in Section 4.4, or the spatial methods, discussed in Section 5.2.

These results suggest that the rate of change of $|R_{bond}|$ with frequency can be used to assess the quality of diffusion bonds. However, for low percentage voiding and correspondingly low $|R_{bond}|$, $\partial|R_{bond}|/\partial\omega$ is reasonably flat over working range of the probe used. Also, the contribution of backscattered noise from the bulk material becomes higher. Work by other authors has had limited success relating $\partial|R_{bond}|/\partial\omega$ to bond quality [63]. The complex reflection coefficient takes advantage of the frequency dependence of both the magnitude and the phase of the reflected signal for partial diffusion bonds and is described in the next section.

5.4. Complex Reflection Coefficient

The central objective of this project was to attempt to differentiate between reflections due to partial bonding and reflections due the acoustic impedance change that occurs at the diffusion bond for anisotropic Ti-6Al-4V. As discussed in the introduction to Section 5, it would be preferable to develop a solution that allows one-sided inspection and that allows detection of defects at greater metal paths. The latter requirement implies the use of lower frequencies, which are less attenuated during propagation.

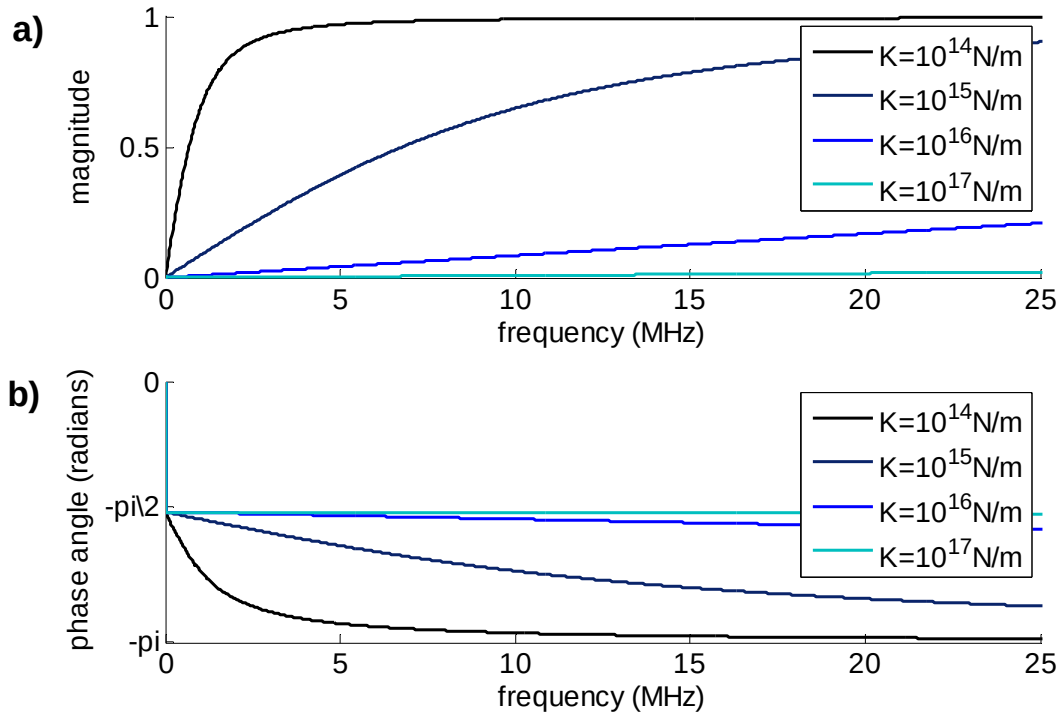

Figure 78. a) Magnitude and b) Phase angle of reflection coefficient, $R(\omega)$, for an imperfect interface with stiffness, K, calculated using spring model (Equation 3.9) for an interface between similar materials with acoustic impedance, z=27.3MRayls, which is a typical value for a titanium alloy.

The magnitude and phase of the reflection coefficient for a partial bond between two pieces of titanium with the same acoustic impedance, calculated using the spring model (Equation 3.9), are shown in Figure 78. The magnitude of the reflection coefficient increases with frequency, as was observed for the partially bonded samples in Section 5.3. The spring model also predicts that, for long wavelengths, the wave reflected from a partial bond will be $\pi/2$ radians out of phase with the incident wave. The phase of the wave reflected at an ideal interface between two materials with different acoustic impedances will be either in phase or π radians out of phase with the incident wave. Typical void lengths observed in the partially bonded samples were in the order of tens of microns (Table 2). At 10MHz the wavelength in titanium is ~600µm. The response from these samples for the 10.9MHz probe used in this project is therefore expected to be in the long

wavelength regime, suggesting that the phase could be used to discriminate good and partial bonds. Lower frequencies such as those conventionally used for forging inspections (4-5MHz) are equally applicable.

For the highest amplitude reflection on the partially bonded sample #12, $|R_{bond}|$ at the probe centre frequency (10.9MHz) was 10%. This corresponds to an interfacial stiffness of 0.93×10^{16}N/m. From Equation 3.9, for a partial bond between two pieces of Ti-6Al-4V with acoustic impedance 27.3MRayls the phase for this interfacial stiffness and at a frequency of 10.9MHz is −95.8°. Over the range 7-18MHz, the phase varies from −93.7° to −99.5°. For the lower amplitude signals in samples #10, #11 and #13, the phase is expected to be closer to -90° over the same frequency range, as illustrated in Figure 78b. Therefore, for the four partially bonded samples manufactured by joining blanks cut from forged segment (samples #10-#13) there should be good separation in phase between the component of the reflection due to partial bonding and the component of the reflection due to acoustic impedance mismatch.

If the magnitude, $|R_{bond}|$, and the phase, φ_{bond}, of the frequency spectrum are known then these can be combined as a complex number:

$$R_{bond} = |R_{bond}|(\cos\varphi_{bond} + i\sin\varphi_{bond}) \quad (5.2)$$

The components of R_{bond} at one frequency are plotted on the complex plane in Figure 79. At any position in a partially bonded sample there will be a component due to impedance mismatch, $R_{bond,imp}$, a component due to the defect, $R_{bond,flaw}$, and a component due to backscattered noise from the microstructure before and after the diffusion bond, R_{noise}. $R_{bond,imp}$ is in phase with the incident wave or π radians out of phase and so is wholly real. $R_{bond,imp}$

and $R_{bond,flaw}$ are separated by $\pi/2$ radians. $R_{bond,flaw}$ is wholly imaginary. The component due to backscattered noise will have random phase, which should vary with position. This component can therefore be reduced by spatial averaging over lengths greater than the spatial correlation length, which was calculated for the diffusion bonded samples in Section 5.2.

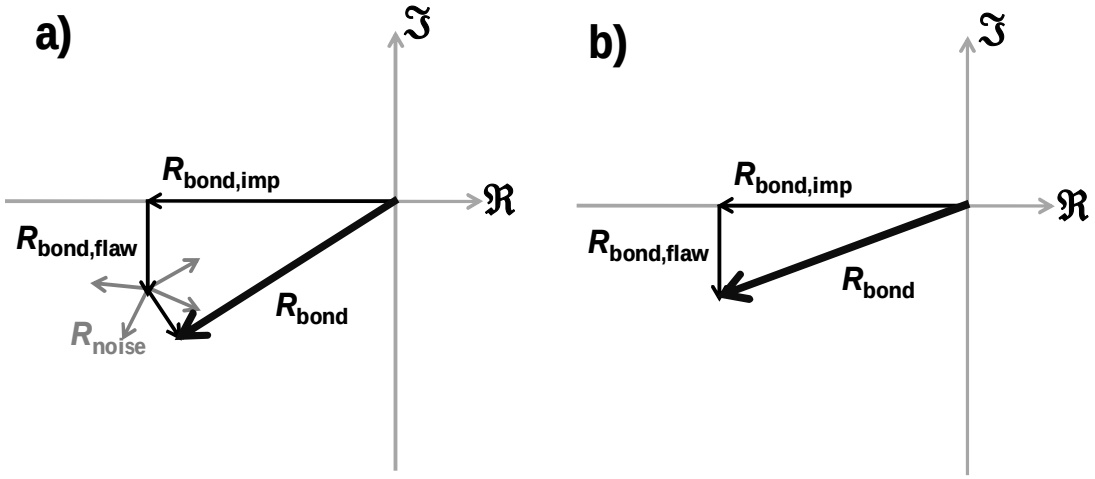

Figure 79. Decomposition of complex reflection coefficient, R_{bond}, at a single frequency for diffusion bond in Ti-6Al-4V sample. a) Vector decomposition for a single point. b) Vector decomposition for the spatially averaged complex reflection coefficient; the component due to backscattered noise cancels out.

For the spatially averaged signal, only the component due to the defect is imaginary. By decomposing the complex reflection coefficient into its real and imaginary components, taking advantage of both the phase and magnitude of the reflected signal, it may be possible to separate the well bonded and the partially bonded Ti-6Al-4V samples.

Determination of the phase of a broadband pulse is problematic. It depends upon frequency and time of arrival. In Section 3.2.4, the 'true phase', φ_{true}, was introduced, which allows the phase to be measured independent of arrival time. In this section the magnitude and true phase of the frequency spectrum are calculated first for the Ti-6Al-4V reference blocks (FORG01-

09). The effect of microtexture, beam focussing and gating on the true phase is investigated. Then the magnitude and true phase of the frequency spectrum for diffusion bonded samples #1-#13 is found and used to calculate the complex reflection coefficient. The absolute, real and imaginary components of the spatially averaged complex reflection coefficient are compared.

5.4.1. Calculation of the magnitude and true phase of reference signal

The magnitude, $|A_{ref}(\omega)|$, and phase, $\varphi_{ref}(\omega)$, as a function of frequency, of a reference signal are both required to determine the complex reflection coefficient of the diffusion bonded samples. In this project the backwall reflection from blocks with representative microtexture were used as reference signals. From Equation 3.7, the reflection coefficient at an ideal interface between two materials with acoustic impedance z_1 and z_2, where $z_1 > z_2$ as for the reflection from the backwall of a titanium block in water, is real and negative. The phase relative to the incident wave is therefore 180°. In the pulse-echo immersion inspection, the system (filters, amplifiers, transducers etc) has a frequency dependent phase delay [86]. The measured phase of the wave reflected from the backwall of a block of titanium will not be 180°. To allow the complex reflection coefficient to be separated into its real and imaginary components, the phase of the signal must be found relative to this measured value.

For each lateral position in the ultrasonic scan, the captured backwall signal was gated using a 1.2μs long cosine-taper window, as shown in Figure 80a.

The arrival time of the pulse from the backwall varies relative to the window centre, t_w, varies due to crystallographic anisotropy of the parent metal. The window length was chosen so that it was significantly longer than the pulse length and any variation in time of arrival, so that none of the backwall signals were distorted by windowing. The centre of the window, t_w, was fixed relative to the front wall reflection using an interface gate. The windowed data was placed into a series of zeros 2^12 points long (16.385µs), as shown in Figure 80b. The magnitude and phase of the frequency spectrum were calculated by Fast Fourier Transform (FFT). The zero padding increases the frequency resolution of the spectrum from 0.833MHz for the 1.2µs time series to 0.061MHz for the 16.385µs time series.

The delay between the start of the time series at t=0 and the centre of the window, t_w, adds a linear term to the phase spectrum $\varphi(t_w;\omega)$ (Equation 3.14), which is proportional to the delay, t_w. To remove this linear term from the phase spectrum, the windowed signal is chopped at the window centre in the time domain. The second half of the windowed pulse is moved to the beginning of the 16.385µs time series and the first half is moved to the end, as shown in Figure 80b.

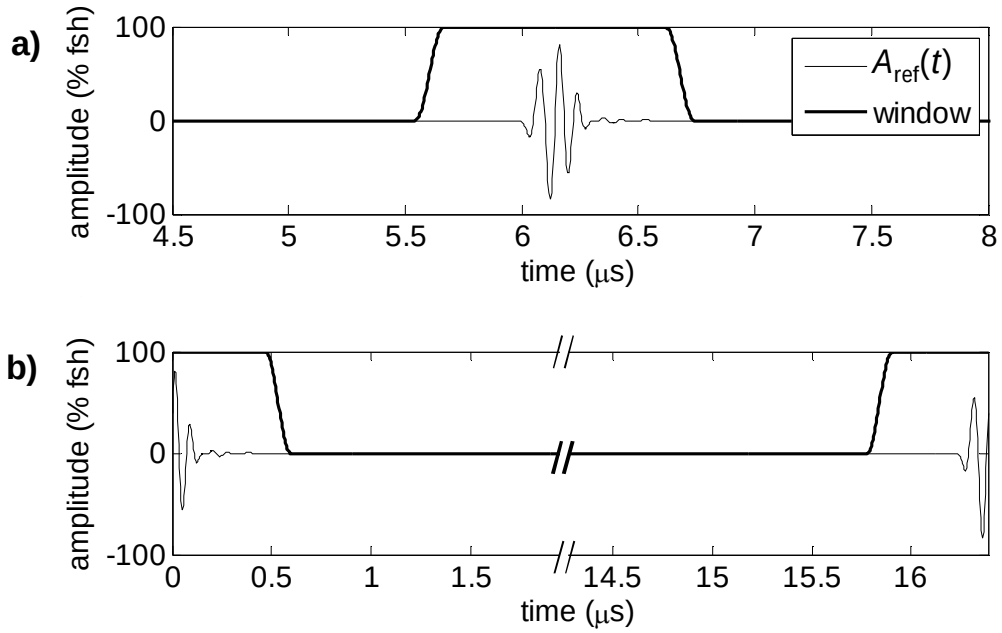

Figure 80. a) Typical reflection from backwall of reference block FORG07 and 1.2μs cosine-taper window. b) Signal chopped to remove linear phase component and zero-padded to 2^12 points (16.385 μs) to improve frequency resolution. Amplitude is in % full screen height (% fsh).

The magnitude and phase spectra for one position on the reference sample FORG07 are shown in Figure 81. As described in Section 3.2.4, the phase at the centre frequency of the reflected signal also depends on the position of the half-energy point of the pulse relative to the centre of the window. Variations in arrival time of the backwall reflection could occur due to surface roughness, non-parallel faces or due to crystallographic anisotropy (see Section 3.1.2). The first two can be controlled by preparation of the samples prior to ultrasonic inspection. The crystallographic anisotropy is a material property. The true phase of the pulse, φ_{true}, defined in Equation 3.15, has the advantage that it can be calculated independent of arrival time, so long as the pulse has not been distorted by convolution with the window. It was observed that the phase spectrum is reasonably linear around the centre frequency of the reference signal. The maximum magnitude of the frequency spectrum and the frequency range, Δf, that corresponds to a 1dB decrease in

magnitude were determined. A straight line was fitted across this frequency range and the true phase was taken to be $\varphi_{true}(f=0MHz)$, as shown in Figure 81. This calculation was carried out for each scan position and so a map of true phase was created.

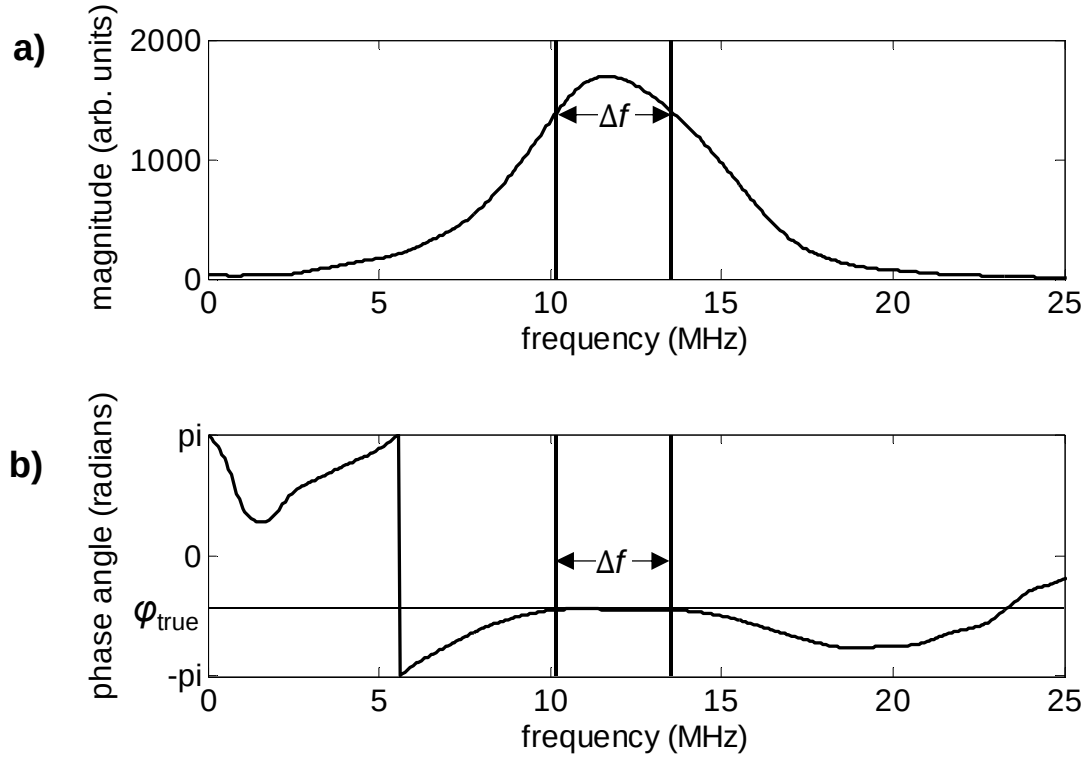

Figure 81. a) Magnitude of frequency spectrum for backwall signal shown in Figure 80. b) Phase of frequency spectrum for same signal. The true phase of the signal can be calculated by fitting a straight line over a frequency range, Δf, and finding φ(f=0MHz).

The inspection of the Ti-6Al-4V reference block is described in Section 4.2.2. A nickel block with the same dimensions (50x50x19mm) was inspected in the same way. The stock nickel had been manufactured by hot isostatic press from powder and so the sample has a fine and homogeneous microstructure. True phase maps for the backwall of the nickel block and Ti-6Al-4V reference block FORG01 are shown in Figure 82. The true phase for the nickel block is almost constant with lateral position; the standard

deviation in true phase across the scanned area is 1.26°. For FORG01, the standard deviation in true phase across the scanned area is 6.18°.

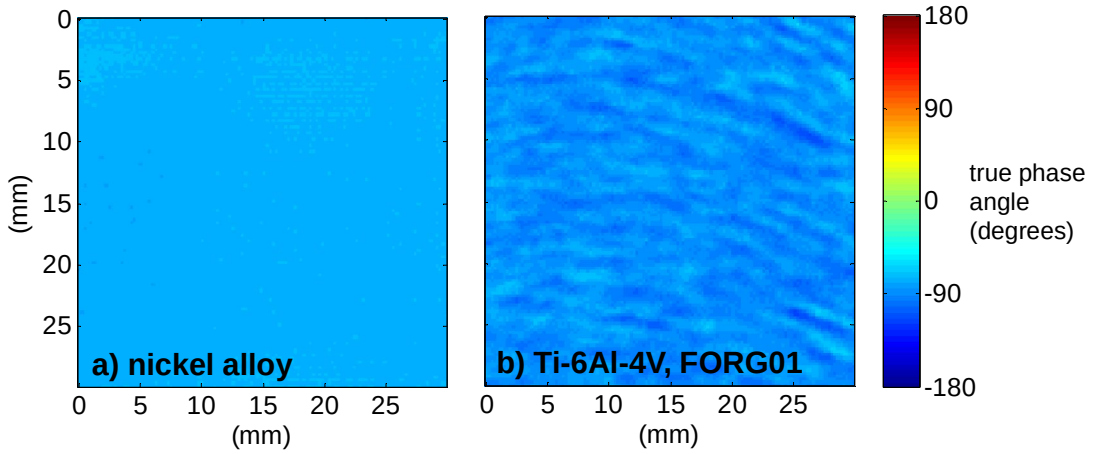

Figure 82. True phase maps for backwall reflection of a) nickel block and b) Ti-6Al-4V reference block, FORG01. The standard deviation in true phase is 1.26° for the nickel block and 6.38° for FORG01.

Similar true phase maps were generated for reference blocks FORG01-09. The mean true phase and the standard deviation are plotted for each block in Figure 83. The highest standard deviation was 28.2° for reference block FORG05. FORG03-06 all had high standard deviations in true phase. These blocks were cut from forged segment J. The surface wave velocity maps of the slice of segment J showed that it had the coarsest microtexture of the forged segments (see Figure B 10). Reference blocks FORG03-06 also have the highest standard deviation in backwall amplitude (see Figure 37). The variation in the measured true phase with scan position for the Ti-6Al-4V reference blocks is thought to be caused by wavefront distortion during propagation through the textured material. This will be discussed further in the next section (Section 5.4.2).

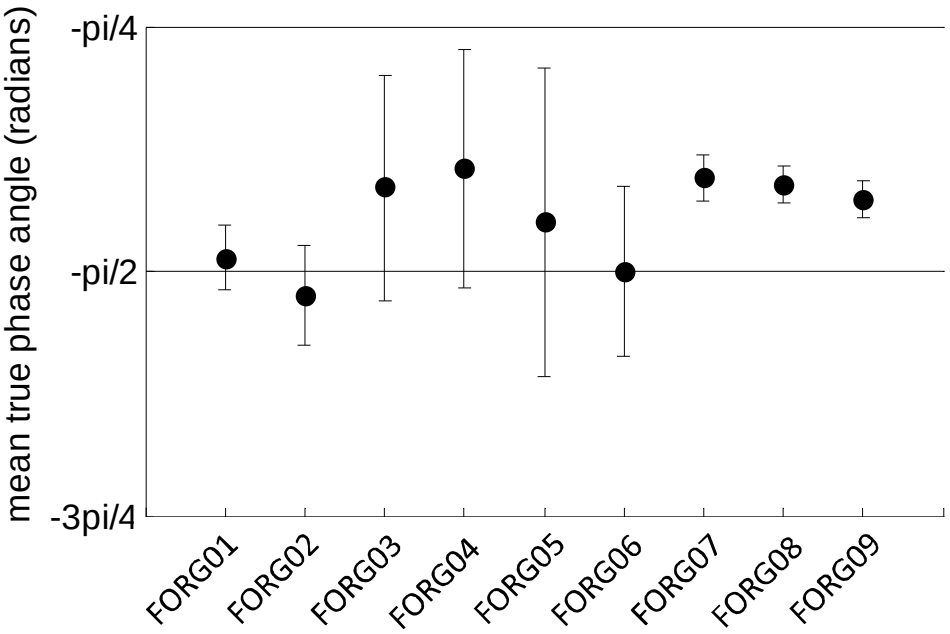

Figure 83. Mean true phase angle of backwall of forged reference samples, FORG01-09. Error bars shown one standard deviation above and below the mean.

Phase spectra at multiple positions across the nickel block and the Ti-6Al-4V blocks FORG01 and FORG03 are shown in Figure 84. To find the true phase a straight line is fitted over the frequency range, Δf, as described above. The points were selected to show phase spectra corresponding to the full range of calculated values of true phase. $\varphi_{ref}(f)$ is straighter for the nickel block over the range Δf than for the two Ti-6Al-4V blocks (FORG01 and FORG03). For the Ti-6Al-4V blocks, the frequency dependence over this range also varies with the scan position. Error is introduced by carrying out the linear fit. The variation in true phase with scan position for the two Ti-6Al-4V blocks is greater than for the RR1000 blocks.

The spatially averaged magnitude, $|A_{ref}(\omega)|$, of the frequency spectrum was calculated for each of the reference samples cut from forged Ti-6Al-4V (FORG**). The spatially averaged true phase angle plotted in Figure 83, was used as the reference true phase, $\varphi_{ref}(\omega)$.

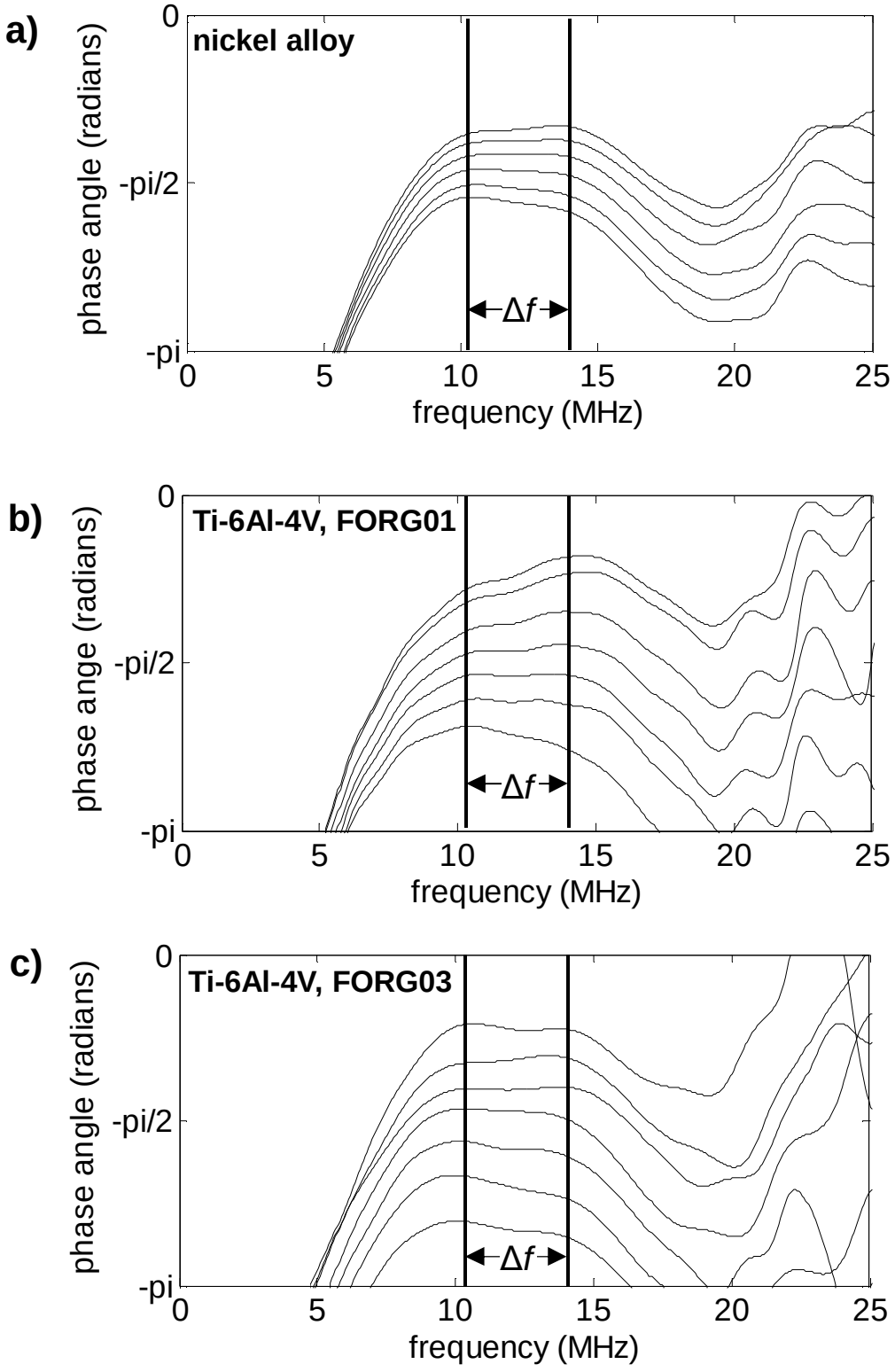

Figure 84. Phase spectra at various scan positions across a) the nickel alloy block b) the Ti-6Al-4V block, FORG01, and c) the Ti-6Al-4V block, FORG03. The true phase angle, φ_{true}, is found by fitting a straight line over the frequency range, Δf, and finding $\varphi(f=0\text{MHz})$.

5.4.2. True phase for focussed ultrasonic beams

As described in the previous section, by convention the phase of the wave reflected from the backwall of a titanium to water interface is 180°. The measured phase, $\varphi_{ref}(\omega)$, will not be 180° due to the frequency dependent phase delay of the measurement system. For a plane wave emitted by an infinitely wide source $\varphi(\omega)$ should be constant for all propagation distances. A spherically focussed transducer with a finite aperture diameter was used in this project. In this section the effect of beam focussing on the measured reference phase, $\varphi_{ref}(\omega)$, is briefly investigated.

A nickel block and a Ti-6Al-4V block of the same thickness (19mm) were ultrasonically inspected with a 10.9MHz 6.3" 0.75" diameter spherically focussed probe, as described in Section 4.2.2. The true phase at each scan position was calculated by fitting a straight line over a frequency range, Δf, which corresponds to a 1dB decrease in the magnitude, as described in Section 5.4.1. This was done for a range of water paths (distance between transducer element and the front wall of the blocks), so that the focal depth of the probe was varied.

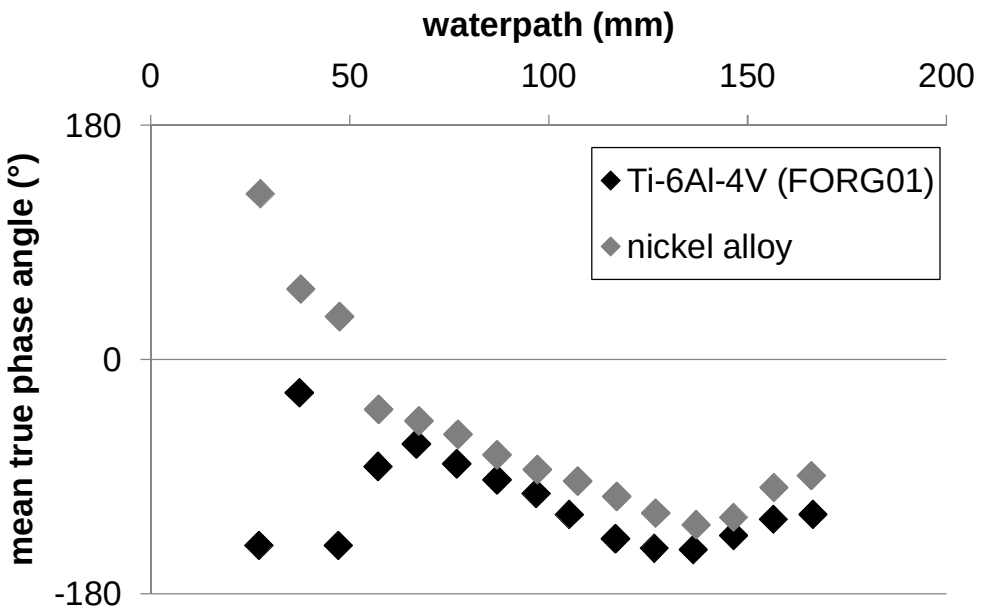

Figure 85. Mean true phase angle (°) calculated over scanned area against water path between probe face and front wall of block for Ti-6Al-4V and nickel block, both with thickness 19mm. The true phase angle, φ_{true}, is found by fitting a straight line over the frequency range ,Δf, and finding $\varphi(f=0\text{MHz})$. Δf is the frequency range corresponding to a 1dB decrease in the magnitude of the frequency spectrum. The focal plane for Ti-6Al-4V block is 79mm.

The mean true phase against water path for the backwall reflection is plotted in Figure 85. The mean true phase varies with water path for both the titanium and the nickel block. The true phase of the received signal will be that of each ray arriving back at the probe, integrated over the area of the element. In the nearfield of the probe (water paths<79mm), where the beam is formed by constructive and destructive interference, the measured true phase fluctuates erratically. In the far field (water paths>79mm) the true phase changes steadily. The change in true phase with increasing distance from the focal plane is attributed to wavefront curvature. At different water paths the backwall of the blocks intersects a different plane of the ultrasonic beam and so the measured phase changes, as shown in Figure 86.

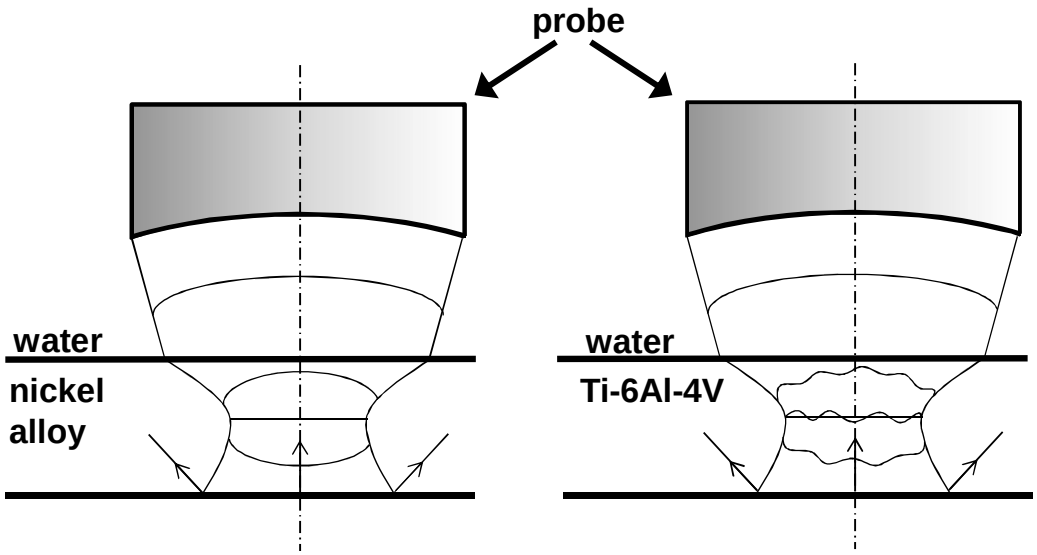

Figure 86. Propagation of a focussed beam in a homogeneous nickel block (left) and an anisotropic Ti-6Al-4V block (right).

The standard deviation in true phase against water path for both blocks is plotted in Figure 87. For both blocks the standard deviation is lowest at the focal plane. It increases quickly in the nearfield (water path<79mm) and slower in the farfield (water path>79mm). For the nickel alloy it was expected that the standard deviation in the farfield would be constant. Away from the focal plane, the beam diameter at the backwall increases. It might therefore become more sensitive to changes in probe alignment and the flatness of the backwall. The standard deviation for the Ti-6Al-4V block is significantly higher than for the nickel alloy block at all water paths. In the Ti-6Al-4V block the anisotropy of the material causes distortion of the propagating wavefront. The phase of the ultrasonic rays arriving back at the transducer will depend upon the volume of microtexture that the beam has passed through. Thus the measured true phase changes with spatial position.

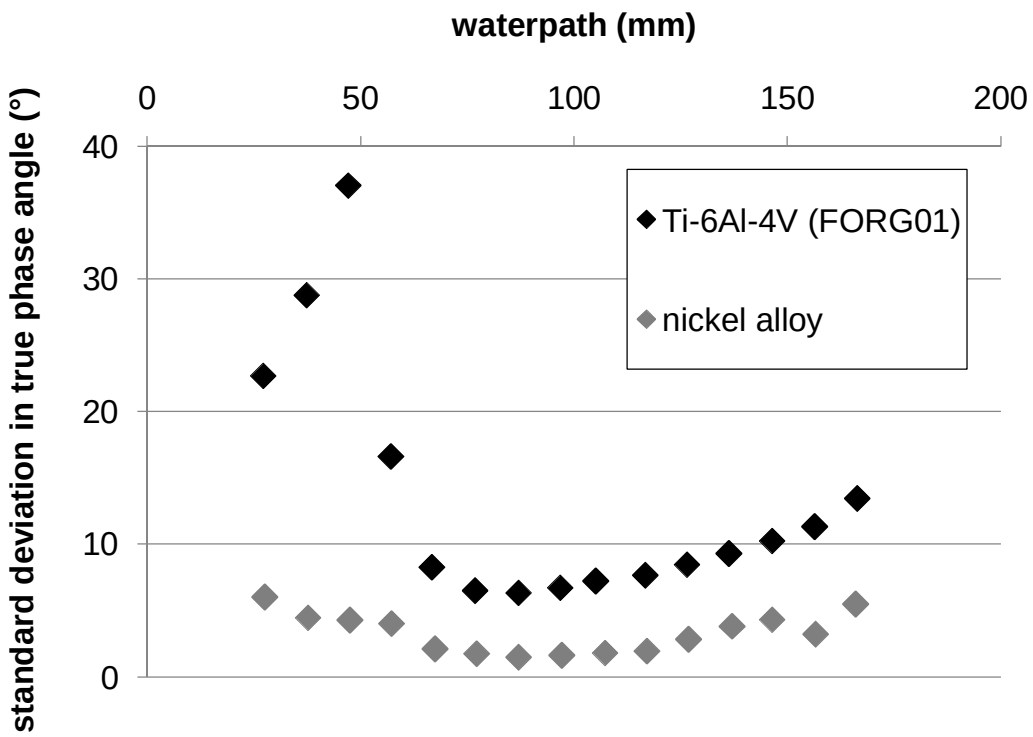

Figure 87. Standard deviation in true phase angle (°) over scanned area against water path between probe face and front wall of block for Ti-6Al-4V and nickel block, both with thickness 19mm.

5.4.3. Calculation of the magnitude and true phase of diffusion bond signal

In this section the method used for the calculation of the complex reflection coefficient for the diffusion bonded samples #1-#13 is described. A reference magnitude, $|A_{ref}|$, and true phase, φ_{ref}, were calculated as described in Section 5.4.1. The magnitude, $|A_{bond}|$, and the true phase spectrum, φ_{bond}, of the reflection from the diffusion bond are required to calculate the complex reflection coefficient.

For each lateral position in the ultrasonic scan, the captured backwall signal was windowed with a cosine-taper, as shown in Figure 80a. The centre of the window, t_w, was fixed relative to the front wall reflection using an interface

gate. The windowed bond reflection was processed in the same way as the reference signal (Section 5.4.1). The isolated time series was chopped at the window centre, t_w. The first half of the time series was placed at the end of a series of zeros 2^12 points long (16.385µs), as shown in Figure 80b. The second half of the time series was placed at the beginning of the series of zeros. This removed the linear phase term caused by the delay between the start of the time series and the window centre, t_w, from the frequency spectrum. The magnitude and phase of the frequency spectrum were calculated by Fast Fourier Transform (FFT).

To find the true phase of the bond line reflection, φ_{bond}, a straight line was fitted across the frequency range, Δf, which corresponds to a 1dB drop in the magnitude of the reference frequency spectrum from its peak value, as shown in Figure 81. The true phase for the diffusion bond was taken to be $\varphi(f=0\text{MHz})$. The magnitude of the reflection coefficient was found by dividing $|A_{bond}(\omega)|$ by $|A_{ref}(\omega)|$. The mean reflection coefficient, $|R_{bond}|$, was found over the same frequency range, Δf.

The window used to isolate the backwall reflection $A_{ref}(t)$ of the reference blocks could be any length, so long as it does not distort the pulse [86]. A typical signal for the backwall of the reference block is shown in Figure 88a. Typical signals for the reflection from the diffusion bond are shown in Figure 89a and Figure 90a. For the diffusion bond signals, the amplitude of the backscattered noise from the bulk material relative to the amplitude of the interface signal is higher than for $A_{ref}(t)$. Windowed backscattered noise from the bulk material immediately before and after the diffusion bond contributes to the calculated magnitude, $|A_{bond}(\omega)|$, and the phase spectrum,

$\varphi_{bond}(\omega)$. Therefore it is preferable to have a short window, which limits the contribution of backscattered noise but which is long enough so that it does not distort the pulse. The arrival time of the pulse from the diffusion bond relative to the window centre, t_w, varies due to crystallographic anisotropy of the parent metal. If the window is too short then the pulse could be distorted in some spatial positions. The window length must be chosen with care.

The effect of window length on the calculated value of true phase was investigated for three signals: the backwall signal from a reference block (Figure 88) and two signals reflected from diffusion bond in sample #1 (Figure 89 and Figure 90). For five different lengths of cosine-taper window the effect of shifting the arrival time of the pulse relative to the window centre on the calculated value of true phase was investigated. The time between the window centre and the 'centre' of the pulse (e.g. half-energy or 6dB down point) is termed the 'lag'. For the reflection from the backwall of a reference block, the calculated true phase at zero lag was the same for all window lengths. This was assumed to be the correct value of true phase. For the diffusion bond signals, the calculated value of true phase at zero lag depends upon the window length. Longer windows incorporate more backscattered noise. The calculated value of true phase for the shortest window (0.32µs) is assumed to be the most accurate. The variation of true phase with window length is higher for the signal shown in Figure 90 than for the signal in Figure 89, because the ratio of the amplitude of the bond signal to the amplitude of the ultrasonic backscatter is lower.

For the reference signal, $A_{ref}(t)$, as the lag between the half-energy point of the pulse and the window centre is increased, the calculated true phase

begins to deviate from the correct value because the window starts to distort the pulse. Long windows are therefore less sensitive to the variation in the arrival time of the pulse. However, short windows are preferred to limit the contribution of ultrasonic backscatter to the complex reflection coefficient. The average longitudinal wave velocity in the through thickness direction for each of the reference blocks is plotted in Figure 36. For the blanks cut from forged segments, the longitudinal wave velocity is highest for FORG03 (6238m/s) and lowest for FORG08 (6183m/s). This difference in velocity would result in a difference in arrival time of 0.054µs. For the results presented here a 0.48µs long window was used. For the diffusion bond reflection shown in Figure 90, with the lowest signal to backscattered noise ratio, the true phase varies by 40° for a window length of 0.48µs and lags between -0.054µs and + 0.054µs. For reflections with an even lower signal to backscattered noise ratio, the error in true phase is expected to be larger.

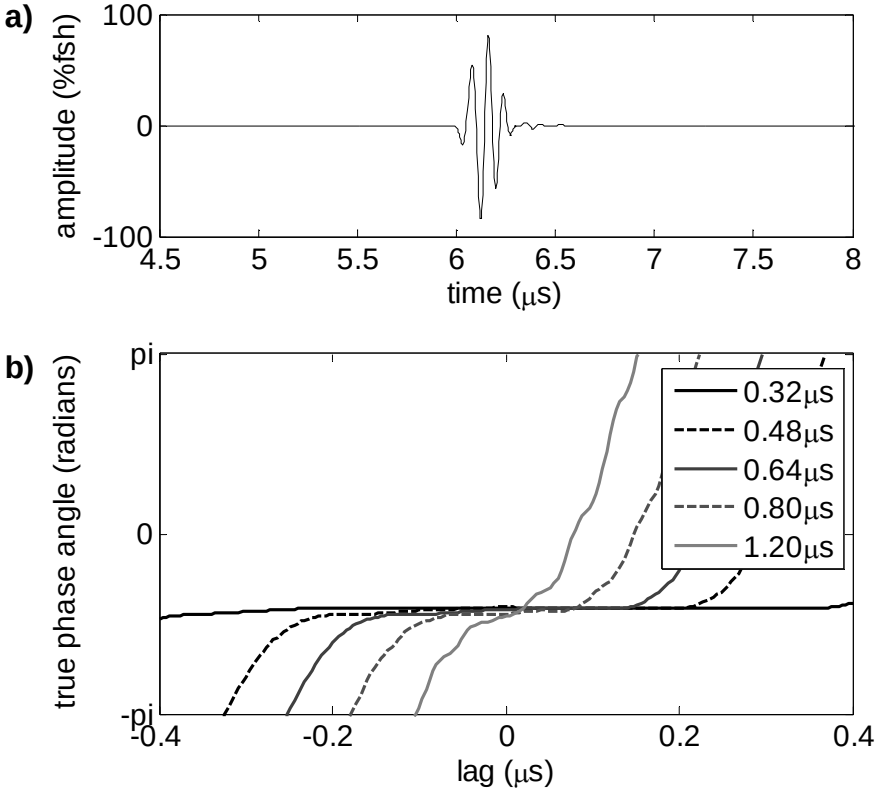

Figure 88. a) Typical $A_{ref}(t)$ - signal reflected from backwall of reference block FORG01. b) True phase for $A_{ref}(t)$ against lag for various lengths of cosine-taper window: 0.32µs, 0.48µs, 0.64 µs, 0.80µs and 1.20µs.

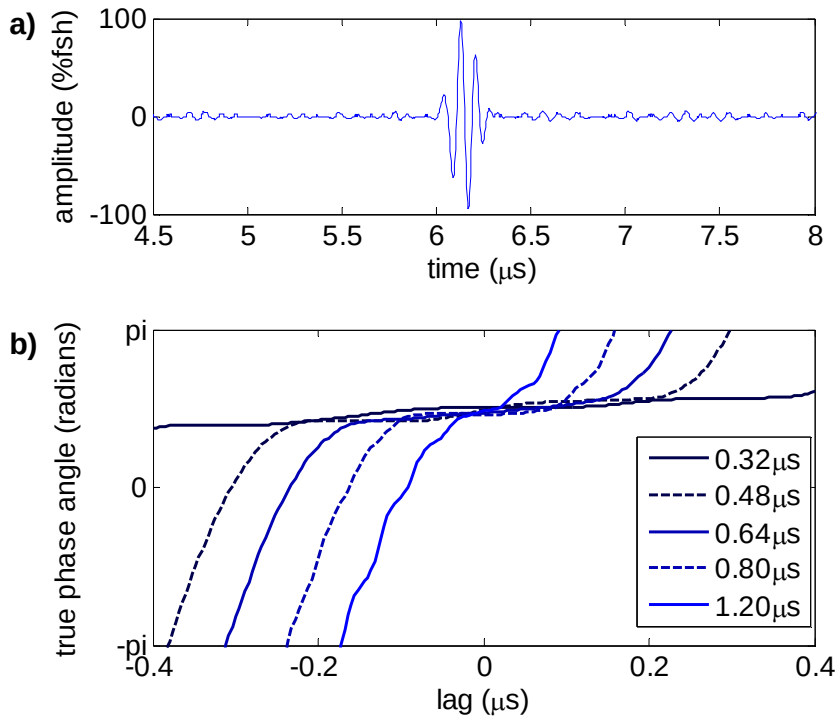

Figure 89. a) Signal reflected from diffusion bond of sample #1, $A_{bond}(t)$, with high signal to backscattered noise ratio. b) True phase for $A_{bond}(t)$ against lag for various lengths of cosine-taper window: 0.32μs, 0.48μs, 0.64 μs, 0.80μs and 1.20μs.

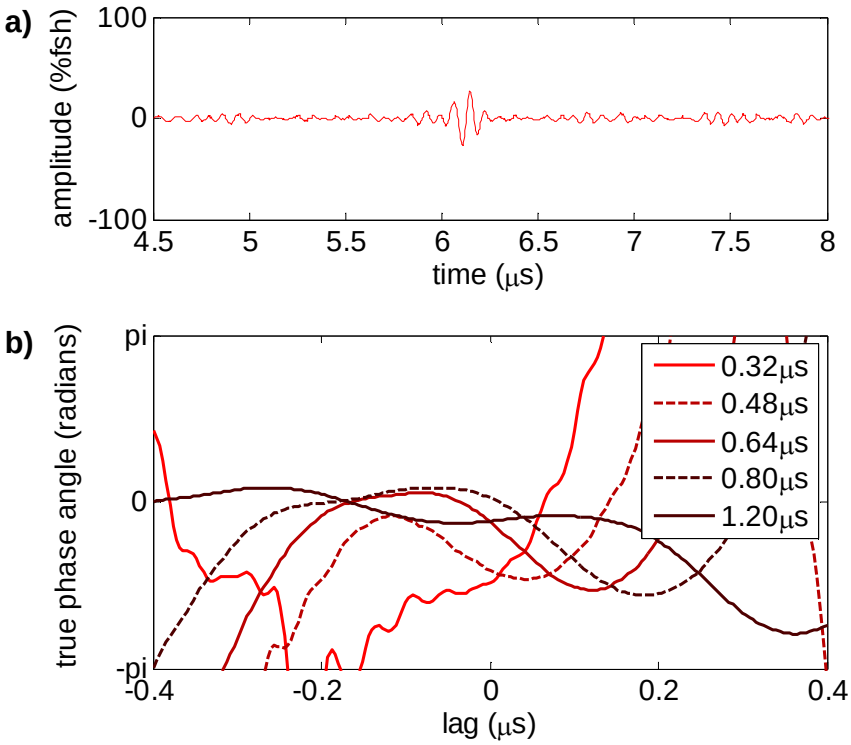

Figure 90. a) Signal reflected from diffusion bond of sample #1, $A_{bond}(t)$, with low signal to backscattered noise ratio. b) True phase for $A_{bond}(t)$ against lag for various lengths of cosine-taper window: 0.32μs, 0.48μs, 0.64 μs, 0.80μs and 1.20μs.

In summary, the presence of backscattered ultrasonic noise introduces error into the calculated magnitude and true phase. The error is higher when the ratio of the amplitude of the interface signal to the ratio of the backscattered noise is low. A short window can be used to limit the contribution of backscattered noise but, if the window is too short, it will distort the ultrasonic pulse which also introduces error. A short window is particularly an issue when the arrival time of the backwall varies due to crystallographic anisotropy in the material. The window length chosen must be a compromise between these two factors.

The true phase of the diffusion bond signal, φ_{bond}, was corrected by subtracting the true phase of the reference signal, φ_{ref}, and adding π radians, so that a backwall reflection has a true phase angle of π radians. The true phase for the backwall of the reference sample was shown to vary with lateral position. A single spatially averaged true phase was used as a reference, as described in Section 5.4.1. The error in the calculated value of true phase will depend upon the variation of true phase for the reference block, which is thought to depend upon the microtexture of the block. Error will also be introduced if the water path is incorrect, if the thickness of the reference block is different from the depth of the diffusion bond or if the mean velocity of the diffusion bonded blank is different from that of the reference block. Finally, a value for the complex reflection coefficient was calculated from φ_{bond} and $|R_{bond}|$ using Equation 5.2.

5.4.4. Complex reflection coefficient for diffusion bonded samples

The ultrasonic inspection of the diffusion bonded sample is described in Section 4.4. Samples #1-#13 were inspected from both sides of the diffusion bond, as illustrated in Figure 91. The reflection coefficient from the side with the pipe stub was termed R_{12} while the reflection coefficient from the opposite side was termed R_{21}. An image correlation method was used to ensure that the reflection coefficient was calculated over an identical area of the diffusion bond for scans from both sides (see Appendix F). The true phase and the magnitude of the complex reflection coefficient were calculated relative to a reference true phase and magnitude, as described in Section 5.4.3.

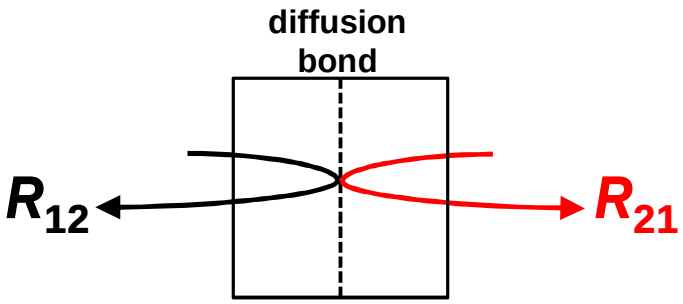

Figure 91. Configuration for inspection from both sides of the diffusion bond: R_{12} and R_{21}.

Figure 92 shows a schematic of the components of the complex reflection coefficient for inspection from both sides of a well-bonded sample, R_{12} and R_{21}. Figure 92a illustrates the scenario for one position on the diffusion bond. The reflected signal has a component due to an acoustic impedance mismatch at the diffusion bond depth and a component due to the windowed backscattered noise before and after the diffusion bond. For inspection from one side, the component due to the impedance mismatch, $R_{12,imp}$, is 180° out of phase with the incident wave. The true phase is the same as that for the reference signal (titanium to water interface). For inspection from the

opposite side, the component due to impedance mismatch $R_{21,imp}$, is in phase with the incident wave. $R_{12,imp}$ and $R_{21,imp}$ are both real. $\Re(R_{12,imp})$ and $\Re(R_{21,imp})$ are expected to have the same magnitude but be opposite in sign i.e. the components due to the acoustic impedance mismatch are symmetric for inspection from opposite sides of the diffusion bond.

The component due to backscattered noise, R_{noise}, has a random phase. The phase is different for inspection from opposite sides of the diffusion bond and is unknown. $R_{12,imp}$ and $R_{21,imp}$ can be estimated by taking the real component of the reflection coefficient. However, the accuracy of the estimated values depends upon the relative magnitude of $R_{12,imp}$ and $R_{21,imp}$ and R_{noise}. Since the phase of the windowed backscattered noise varies with lateral position, R_{noise} can be reduced by spatial averaging. In this report $<>$ denotes a spatial average. Figure 92b shows the spatially averaged signal. For a well-bonded sample, the only component is due to the acoustic impedance mismatch at the diffusion bond depth, $<R_{12,imp}>$ and $<R_{21,imp}>$, as the noise component has cancelled.

The phase of the component due to the acoustic impedance mismatch at the bond for one scan position will either be in phase with the incident wave or 180° out of phase, depending upon whether there is an increase or decrease in the acoustic impedance. $R_{12,imp}$ at two different scan positions may therefore be 180° out of phase with one another. Spatial averaging may result in cancelling of the component due to acoustic impedance mismatch. If there is a change in the average acoustic impedance at the diffusion bond then one phase (either 0° or 180°) will occur more frequently. In this case the

component due to acoustic impedance mismatch will not be cancelled by spatial averaging.

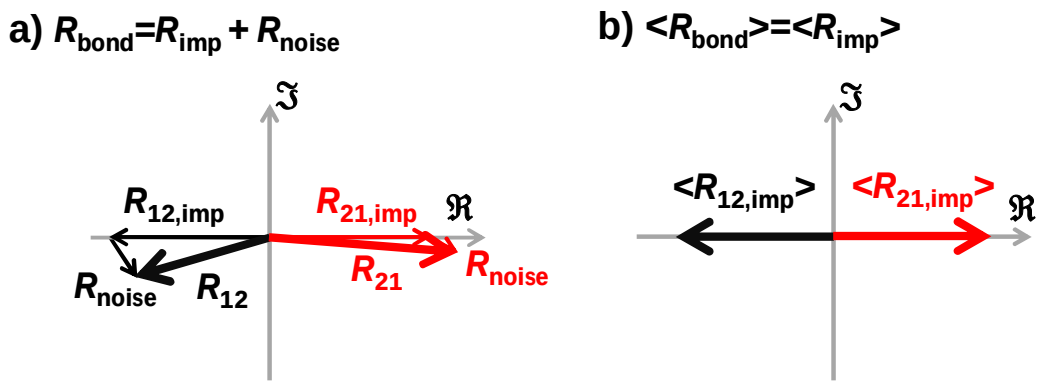

Figure 92. Vector decomposition for complex reflection coefficients, R_{12} and R_{21}, at a single frequency for a well bonded region of a diffusion bond. a) Reflection with components due to acoustic impedance, R_{imp}, and backscattered noise, R_{noise}. b) Spatially averaged signal with a component due to acoustic impedance, $<R_{imp}>$, only. The backscattered noise has cancelled.

Figure 93a illustrates the scenario for a partially bonded region. Again the component due to an acoustic impedance mismatch for incidence from opposite sides of the diffusion bond, $R_{12,imp}$ and $R_{21,imp}$ are real, equal in magnitude and opposite in sign. The components due to the flaw, $R_{12,flaw}$ and $R_{21,flaw}$, are −90° out of phase with the incident wave for inspection from both sides. $R_{12,flaw}$ and $R_{21,flaw}$ are both imaginary. $\Im(R_{12,flaw})$ and $\Im(R_{21,flaw})$ are expected to have the same magnitude and the same sign i.e. the component due to the flaw is asymmetric. The aim is to take advantage of the 90° separation between $R_{bond,imp}$ and $R_{bond,flaw}$ to differentiate between well bonded and partially bonded samples. The phase of the component due to backscattered noise, R_{noise}, is random and can again be cancelled by spatial averaging (Figure 93b).

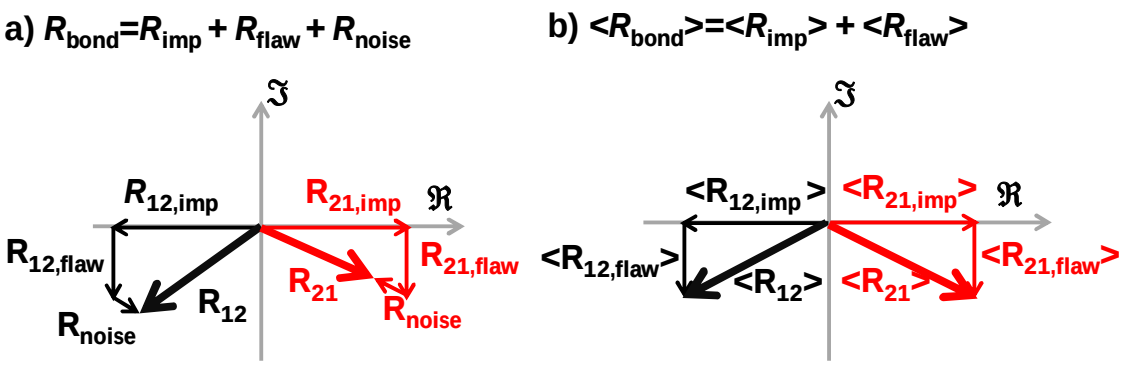

Figure 93. Vector decomposition for complex reflection coefficients, R_{12} and R_{21}, at a single frequency for a partially bonded region of a diffusion bond a) with components due to acoustic impedance, R_{imp}, the flaw, R_{flaw}, and backscattered noise, R_{noise}. b) Spatially averaged signal with components due to acoustic impedance, $\langle R_{imp}\rangle$, and the flaw, $\langle R_{flaw}\rangle$. The backscattered noise has cancelled.

In this section, maps of the real and imaginary components of the complex reflection coefficient against scan position for sample #10 are examined. The response for a region that is thought to be partially bonded is compared to that for a region that is void-free, in order to show that the components fit the theory locally. The complex reflection coefficient is spatially averaged to reduce the contribution of backscattered noise. The spatially averaged complex reflection coefficient for the well bonded and partially bonded samples are compared.

Maps of the real and imaginary component of the complex reflection coefficient for sample #10 for scans from both sides of the diffusion bond (R_{12} and R_{21}) are shown in Figure 94. Sample #10 contains a linear indication running diagonally across the top-left corner of the sample, which is thought to be a scratch on the surface remnant from the diffusion bonding process. This region has not been sectioned. The magnitude of the reflection coefficient at position #10(C) on the scratch is plotted in Figure 95. $|R_{bond}(f)|$ shows strong frequency dependence, which indicates that it is voided.

Directly below the scratch there is a region which is thought to be void-free. This region has been sectioned. No voids were observed, however the grain boundaries are aligned (see Figure 54, Section 4.5). The magnitude of the reflection coefficient at position #10(D) in the void free region is also plotted in Figure 95; $|R_{bond}(f)|$ is relatively independent of frequency suggesting that the interface is well-bonded here.

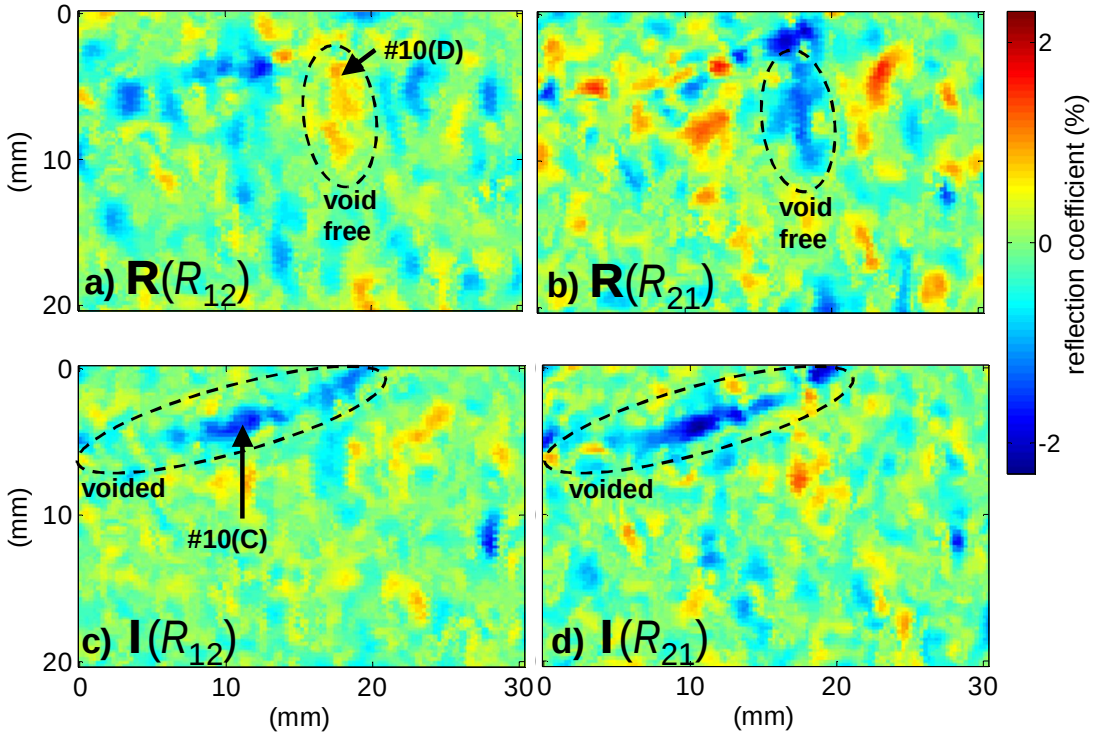

Figure 94. Map of real ($\Re$) and imaginary ($\Im$) components of complex reflection coefficient against spatial position for sample #10. a) Real component for inspection from the side of the sample with the pipe stub, $\Re(R_{12})$. A region that is thought to be void free and a point #10(C) in that region are is highlighted. $|R_{12}(f)|$ at #10(C) is plotted in Figure 95. b) Real component for inspection from the opposite side of sample, $\Re(R_{21})$. Same void-free region is highlighted. c) Imaginary component, $\Im(R_{12})$. A region that is thought to be voided and a point #10(D) in that region are highlighted. $|R_{12}(f)|$ at #10 (D) is plotted in Figure 95. d) Imaginary component, $\Im(R_{21})$. Same voided region is highlighted.

The real component of the void-free region (Figure 94a and Figure 94b) is similar in magnitude and opposite in sign for inspection from opposite sides of the diffusion bond, as expected for a well bonded region. The imaginary

component of the same region (Figure 94c and Figure 94d) is non-zero. This could be caused by the contribution of backscattered noise, as shown in Figure 92a, or by error introduced by the fact that a spatially averaged reference phase has been used and, in reality, the reference phase varies with lateral position. The latter will be discussed in more detail for the spatially averaged results. The imaginary component of the voided region (Figure 94c and Figure 94d) is similar in magnitude and is negative for inspection from both sides of the diffusion bonds, as expected for a partially bonded region.

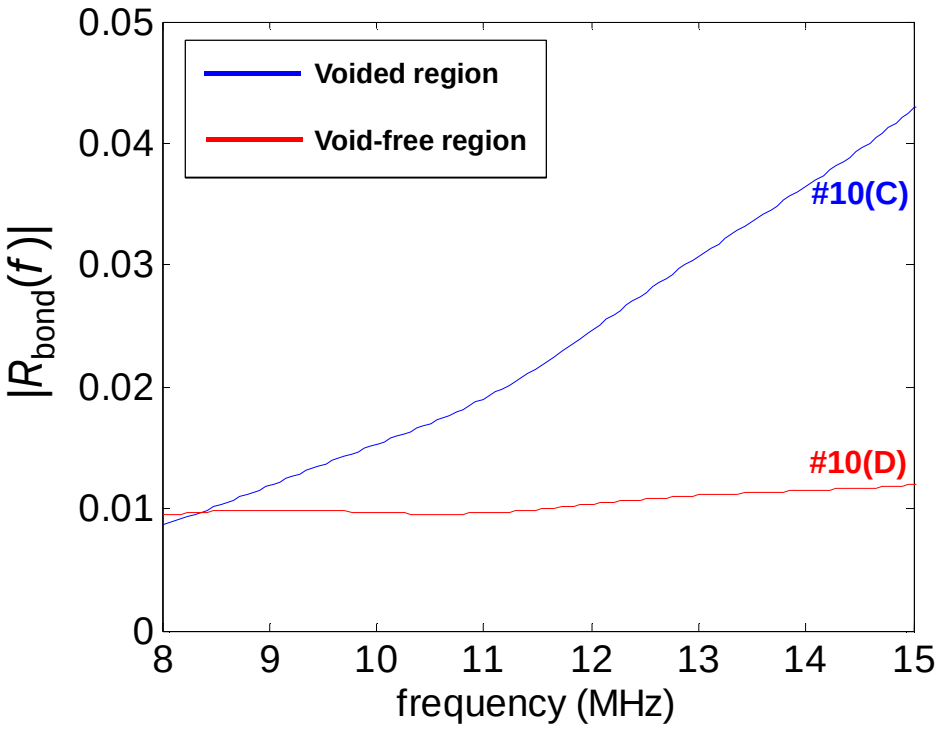

Figure 95. Magnitude of reflection coefficient against frequency, $|R_{bond}(f)|$, for positions #10(C) and #10(D) on sample #10, indicated in Figure 94. The sample is thought to be voided at #10(C); $|R_{bond}(f)|$ shows strong frequency dependence. The sample is thought to be void-free at #10(D); $|R_{bond}(f)|$ is flat over the frequency range.

The complex reflection coefficient was spatially averaged over the scanned area for samples #1-#13 in order to reduce the contribution of the

backscattered noise. The spatial average of the real component of the complex reflection coefficient for scans from both sides of the diffusion bond, $<\Re(R_{12})>$ and $<\Re(R_{21})>$ are shown in Figure 96 for samples #1-#13. The spatial averages of the imaginary component of the complex reflection coefficient, $<\Im(R_{12})>$ and $<\Im(R_{21})>$ are shown in Figure 97.

For samples #1-#9, which are thought to be well bonded, $<\Re(R_{12})>$ and $<\Re(R_{21})>$ are approximately symmetric (equal in magnitude and opposite in sign), as expected for a reflection due to an acoustic impedance mismatch (see Figure 92b). The imaginary component of the spatially averaged complex reflection coefficient, $<\Im(R_{12})>$ and $<\Im(R_{21})>$, is expected to be zero, as the backscattered noise should cancel out. Figure 97 shows that the imaginary component is non-zero and, for some of the well-bonded samples, similar in magnitude to the imaginary component for the partially bonded samples #10 and #11. This implies that some of the well-bonded samples are defective or that there is error in the complex reflection coefficient.

Error may be introduced into the calculation of the complex reflection coefficient due to:

1. Differences between the thickness or average acoustic velocity of the reference block and the diffusion bonded blank. As discussed in Section 5.4.2, for a focussed beam and due to wavefront curvature the true phase for an interface depends upon the position of the backwall along the beam axis.
2. The effect of wavefront distortion during propagation through the anisotropic Ti-6Al-4V on the measured amplitude. The amplitude of

the backwall reflection for the reference blocks was observed to change with scan position (see Figure 37). Therefore the spatially averaged value, $|A_{ref}|$, is not correct for every scan position.

3. The effect of wavefront distortion during propagation through the anisotropic Ti-6Al-4V on the measured true phase. The true phase of the backwall reflection for the reference blocks was observed to change with scan position (see Figure 83). Therefore the spatially averaged value, φ_{ref}, is not correct for every scan position.
4. The frequency dependence of the phase spectrum over the range, Δf, over which the straight line is fit (see Section 5.4.1), in order to determine the true phase. The frequency dependence varies with scan position for Ti-6Al-4V, as shown in Figure 84b and Figure 84c. Windowed backscattered noise also affects the frequency dependence of the phase spectrum and introduces error into the calculated value of true phase. The error in the true phase depends upon the relative amplitude of the interface signal to the backscattered noise (see Figure 89 and Figure 90).
5. The contribution of the backscattered noise to the measured magnitude of the reflection coefficient, $|A_{bond}|$.

More work is required to understand the contribution of these various factors.

For samples #10 and #11, which had low fraction voiding, $<\Im(R_{12})>$ and $<\Im(R_{21})>$ are similar in magnitude and both negative, which agrees with the prediction of the spring model for partially bonded samples (see Figure 93b). The imaginary component for the well-bonded samples #3 and #4 is lower than the imaginary component for samples #10 and #11, for inspection from

at least one side. The result is that the imaginary component of the complex reflection coefficient cannot be used to differentiate the well bonded samples from the partially bonded samples as had been hoped. $<\Re(R_{12})>$ and $<\Re(R_{21})>$ for samples #10 and #11 are symmetric, which indicates that a component of the signal is caused by acoustic impedance mismatch. $<\Im(R_{12})>$ and $<\Im(R_{21})>$ are asymmetric (similar in magnitude and with the same sign) for all the partially bonded samples, as expected, but approximately symmetric for the well-bonded samples. The asymmetry of the imaginary component of the reflection coefficient for the partially bonded samples and symmetry of the imaginary component for the well-bonded samples will be taken advantage of in Section 5.5, where the symmetric reflection coefficient is calculated.

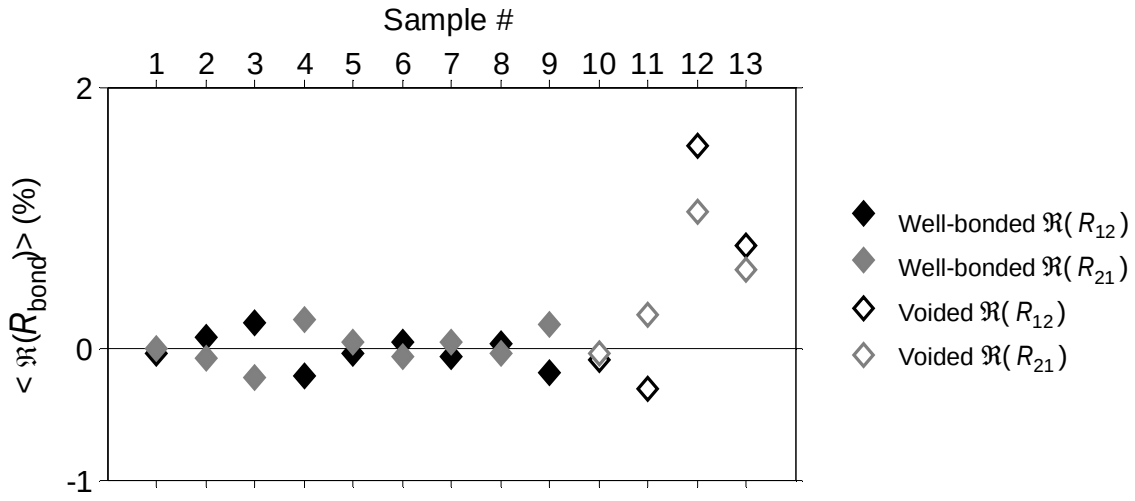

Figure 96. Real component of spatially averaged complex reflection coefficient for both well-bonded (#1-#9) and voided samples (#10-#13). The samples were scanned from each side to obtain R_{12} and R_{21}.

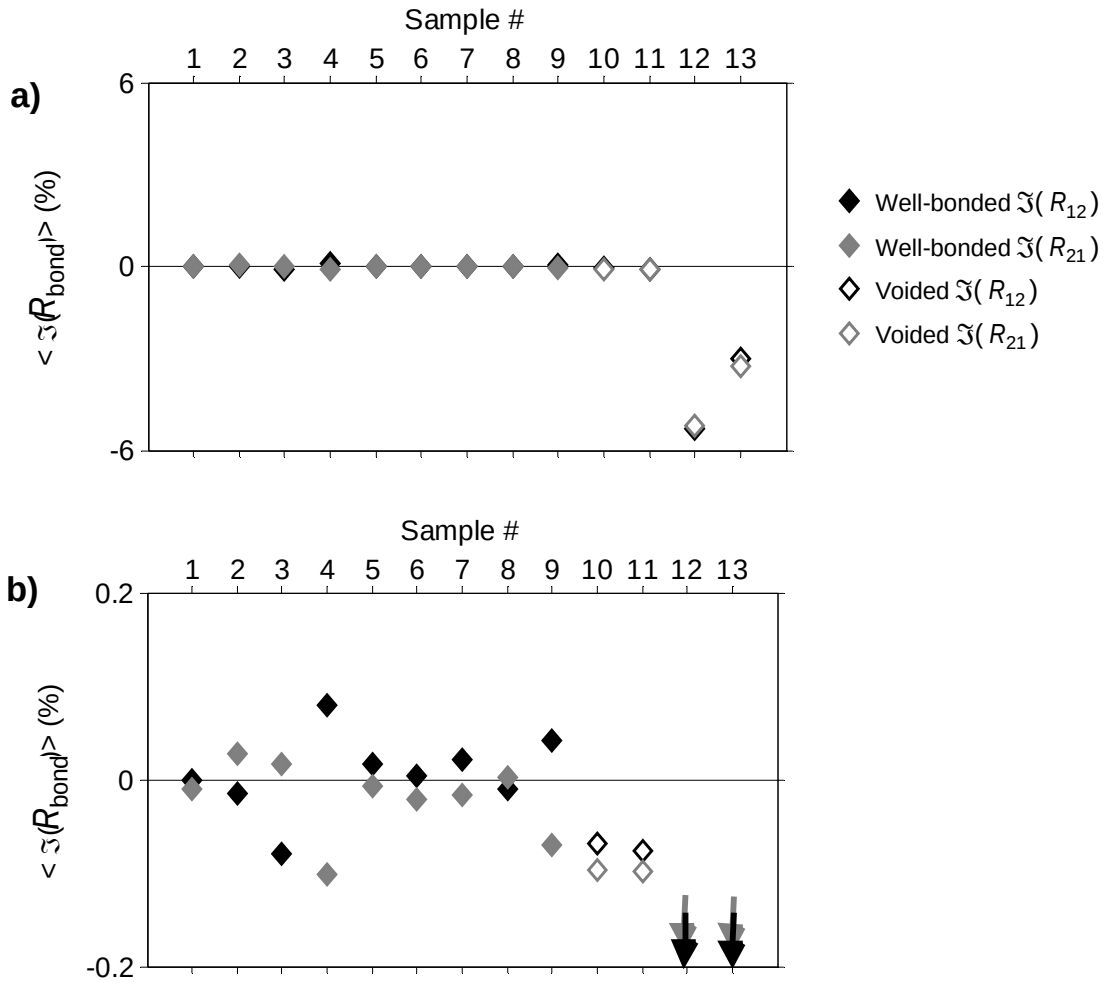

Figure 97. a) Imaginary component of spatially averaged complex reflection coefficient for both well-bonded (#1-#9) and voided samples (#10-#13). The samples were scanned from each side to obtain R_{12} and R_{21}. b) Same figure with expanded scale.

For high fraction voiding, the true phase is expected to deviate from -90°, as discussed in the introduction. The spring model (Equation 3.9) predicts that the true phase will decrease, eventually reaching -180° (a full disbond). Of the partially bonded samples #10-#13, samples #12 and #13 had the highest fraction voiding see (Section 4.4). The interfacial stiffness for the point with the highest amplitude reflection in sample #12 was estimated at 0.93×10^{16}N/m, which corresponds to a true phase of -95.8° at the probe centre frequency (10.9MHz). The mean true phase and standard deviation in true phase for the diffusion bond reflection across the scanned area for

samples #12 and #13 are listed in Table 3. The mean true phase is ~-75° for both samples for inspection from both sides. $<\Re(R_{12})>$ and $<\Re(R_{21})>$ are both positive. Assuming that the component due to the flaw is much larger than the component due to acoustic impedance mismatch for these samples, then the difference between the measured and predicted true phase is a result of experimental error. An error in the measured true phase means that the component due to the flaw appears in both the imaginary and real parts of the complex reflection coefficient. However ~20° is still much less than the 90° difference between components due to the flaw and due to an acoustic impedance mismatch. The imaginary components for inspection from both sides, $<\Im(R_{12})>$ and $<\Im(R_{21})>$, are therefore both negative as would be expected for a partial bond. The difference between the measured and predicted true phase could be a result of one or a combination of the factors 1-6 listed above. More work is required to understand and reduce the experimental error.

Table 3. Mean true phase and standard deviation relative to backwall echo for $A_{bond}(t)$ for samples #12 and #13.

	Sample #12		Sample # 13	
Side	**Mean true phase (°)**	**Standard deviation in true phase (°)**	**Mean true phase (°)**	**Standard deviation in true phase (°)**
R12	-74.7	12.5	-76.4	19.2
R21	-79.6	14.2	-79.6	17.4

The magnitude of the spatially averaged complex reflection coefficient, $|<R_{bond}>|$, was also calculated for each sample. This is not the same as the spatially averaged absolute reflection coefficient, $<|R_{bond}|>$, calculated in Section 5.3. The complex reflection coefficient contains phase information. As discussed above, for inspection from the same side of the diffusion bond

the reflection at one scan position may be in phase with the incident wave while at another scan position the phase is 180°. Spatial averaging of the complex reflection coefficient at these two positions would result in cancelling. Phase cancellation will not occur if the absolute reflection coefficient is spatially averaged. The spatially averaged absolute reflection coefficient $<|R_{bond}|>$ can be considered as a measure of the total energy reflected from the diffusion bond averaged across the scan area. The magnitude of the spatially averaged complex reflection coefficient $|<R_{bond}>|$ is rather a measure of the coherency of the reflected signal.

The magnitude of the spatially averaged complex reflection coefficient, $|<R_{bond}>|$, is plotted for each sample for inspection from both sides in Figure 98. Again, samples #10 and #11 cannot be differentiated from the well-bonded samples #1-#9 on the basis of $|<R_{bond}>|$. The spatially averaged absolute reflection coefficient, $<|R_{bond}|>$, for sample #1 was high (Figure 70), which indicates that a lot of energy has been reflected from the bond. However, the spatially averaged complex reflection coefficient $|<R_{bond}>|$ is low, suggesting that the true phase of the signals varies with lateral position. For samples #3 and #4 the spatially averaged complex reflection coefficient $|<R_{bond}>|$ (Figure 98) and absolute reflection coefficient $<|R_{bond}|>$ are similar in magnitude (Figure 70). Spatial averaging has not resulted in cancelling of the complex reflection coefficient. This indicates that there is a difference in the average acoustic impedance either side of the diffusion bond. A coherent (in-phase) reflection from the bond was also observed for some samples in the measurement of the spatial correlation coefficient (see Figure 64, Section 5.2).

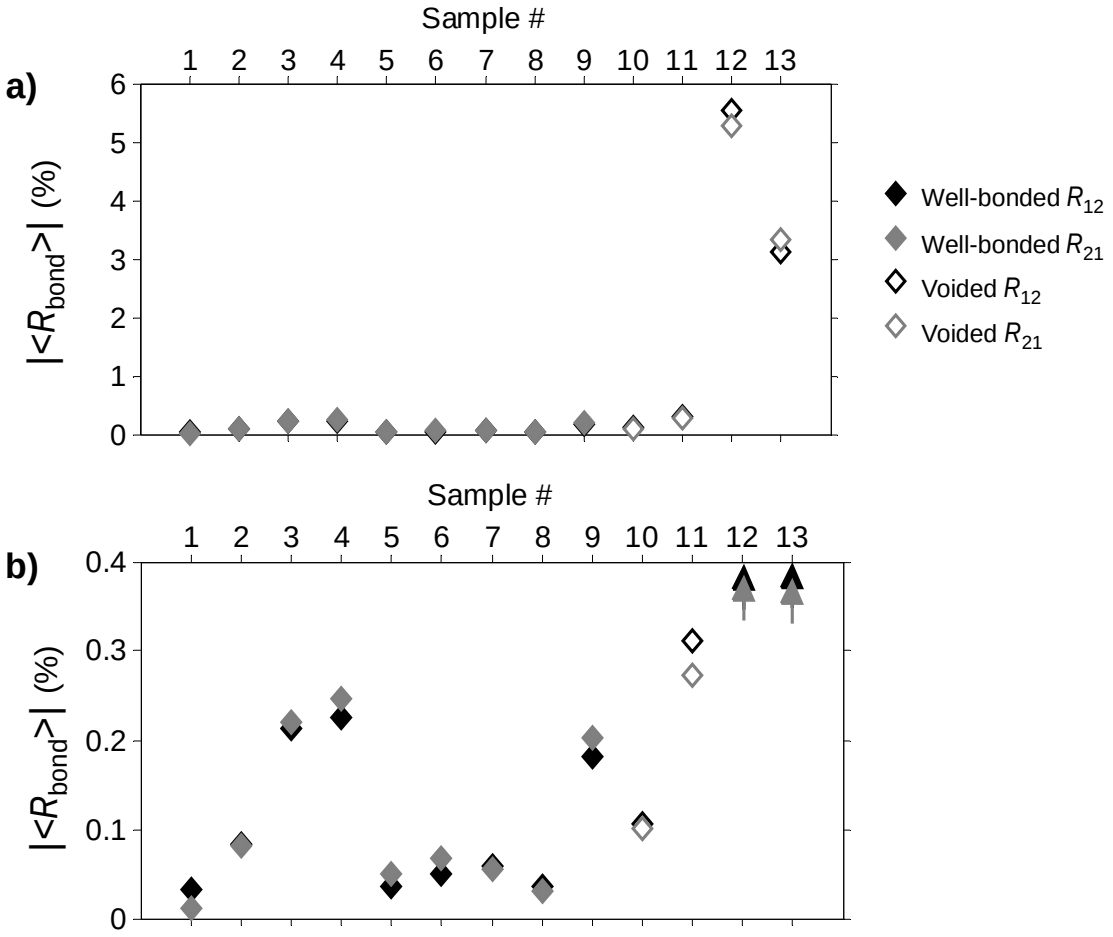

Figure 98.a) Magnitude of spatially averaged complex reflection coefficient for both well-bonded (#1-#9) and voided samples (#10-#13). The samples were scanned from each side to obtain R_{12} and R_{21}. b) Same figure with expanded scale.

In Section 5.3, the spatially averaged absolute reflection coefficient, $<|R_{12}|>$, of the well-bonded and partially bonded samples was compared. The partially bonded samples #10 and #11 could not be separated from the well-bonded samples #1-#9. A signal to noise ratio is defined as $<|R_{12}|>$ for the partially bonded sample divided by the maximum $<|R_{12}|>$ for any of the well-bonded samples. The signal to noise ratio for each of the partially bonded samples is plotted on a logarithmic scale in Figure 99. This indicates the sensitivity that can be achieved by the conventional pulse-echo inspection methods at the centre frequency of the probe. Higher signal to noise ratios can be achieved by moving to higher frequencies.

In this section, the magnitude $|<R_{12}>|$, real $<\Re(R_{12})>$ and imaginary $<\Im(R_{12})>$ components of the spatially averaged reflection coefficient were compared. Signal to noise ratios for these three parameters are defined in Table 4 and plotted alongside those for the absolute reflection coefficient, $<|R_{12}|>$, in Figure 99. The imaginary component of the complex reflection coefficient, $<\Im(R_{12})>$, gives a consistently higher signal to noise ratio than the spatially averaged absolute reflection coefficient at the centre frequency of the probe. However, the SNR is still less than unity for samples #10 and #11. The imaginary component of the spatially averaged reflection coefficient $<\Im(R_{12})>$ is expected to be almost zero for the well-bonded samples, as it should be insensitive to acoustic impedance mismatch at the bond line and the backscattered noise should be reduced by spatial averaging (see Figure 93). Errors in the measured value of true phase, discussed above, will result in a non-zero imaginary component for the well-bonded specimens, resulting in a SNR<1.

The real component of the spatially averaged reflection coefficient $<\Re(R_{12})>$ should not be sensitive to flaws at the interface. However, due to errors in the measured true phase, the real component for samples #12 and #13 is much higher than that for any of the well-bonded samples, giving an SNR>>1.

Table 4. Definition of signal to noise ratio for various parameters of one sided reflection.

Parameter	Signal to noise ratio
Spatially averaged absolute reflection coefficient, $<\|R_{12}\|>$	$\frac{\langle\|R_{12}\|\rangle \text{ of voided sample}}{\text{maximum } \langle\|R_{12}\|\rangle \text{ for well bonded samples}}$
Magnitude of spatially averaged complex reflection coefficient, $\|<R_{12}>\|$	$\frac{\|\langle R_{12}\rangle\| \text{of voided sample}}{\text{maximum } \|\langle R_{12}\rangle\| \text{ for well bonded samples}}$
Spatially averaged real component of complex reflection coefficient, $<\Re(R_{12})>$	$\frac{\|\langle\Re(R_{12})\rangle\| \text{of voided sample}}{\text{maximum } \|\langle\Re(R_{12})\rangle\| \text{for well bonded samples}}$
Spatially averaged imaginary component of complex reflection coefficient, $<\Im(R_{12})>$	$\frac{\langle\Im(R_{12})\rangle \text{of voided sample}}{\text{minimum } \langle\Im(R_{12})\rangle \text{for well bonded samples}}$

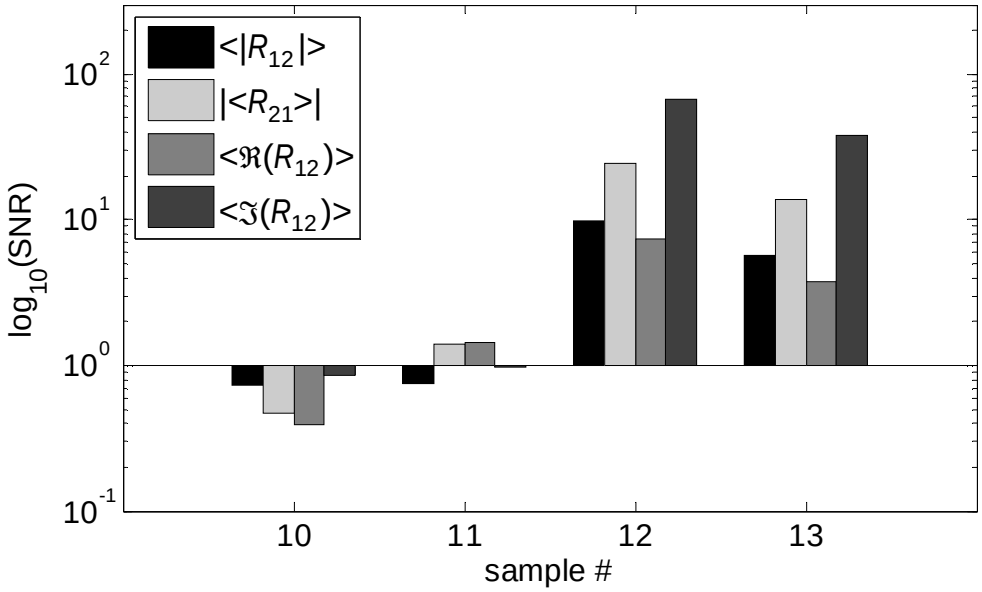

Figure 99. Signal to noise ratio, as defined in Table 4, for the spatially averaged absolute reflection coefficient, $<|R_{12}|>$, and the magnitude ,$|<R_{12}>|$, real component, $<\Re(R_{12})>$, and imaginary component $<\Im(R_{12})>$ of the spatially averaged complex reflection coefficient for partially bonded samples #10-#13. The scale is logarithmic.

In summary, the true phase and the magnitude of the reflection coefficient were measured at each position of the sample and converted to the imaginary and real components relative to a reference true phase. The real

component for the well-bonded samples #1-#9 was symmetric (similar in magnitude and opposite in sign) for inspection from opposite sides of the diffusion bond, which agrees with the theory for an ideal interface. The imaginary component was non-zero, which is not predicted by the spring model and suggests an error in the measured value of the true phase. The imaginary component of the partially bonded samples #10-#13 was asymmetric (similar in magnitude and negative) for inspection from both sides of the diffusion bond, which agrees with the prediction of the spring model for an imperfect interface. The real component of the partially bonded samples #12-#13, which contained high fraction voiding, was positive for inspection from both sides of the diffusion bond, which again suggests error in the measured true phase.

The sensitivity of the imaginary component of the complex reflection coefficient to partial bonds will therefore depend upon the relative size of the contribution due to the partial bond and the acoustic impedance mismatch and on the error in the measured reference phase. The latter could be caused by variations of phase with position due to the texture in Ti-6Al-4V, by errors in probe waterpath or by differences between the texture or thickness of the reference block and the diffusion bonded blank. If this error could be reduced then a one sided inspection, which uses the imaginary component of the complex reflection coefficient to differentiate between well-bonded and partially bonded samples, could be possible.

5.5. Symmetric Reflection Technique

Nagy and Adler [65] suggested the use of the symmetric reflection coefficient, R_S, for the inspection of welds between dissimilar materials. R_S is defined in Equation 3.16. It relies upon the fact that, for an acoustic impedance mismatch, the reflection coefficient is symmetric i.e. equal in magnitude and opposite in sign for inspection from opposite sides of the diffusion bond, and therefore cancels out. This behaviour was observed for the real component of the spatially averaged complex reflection coefficient in Section 5.4.

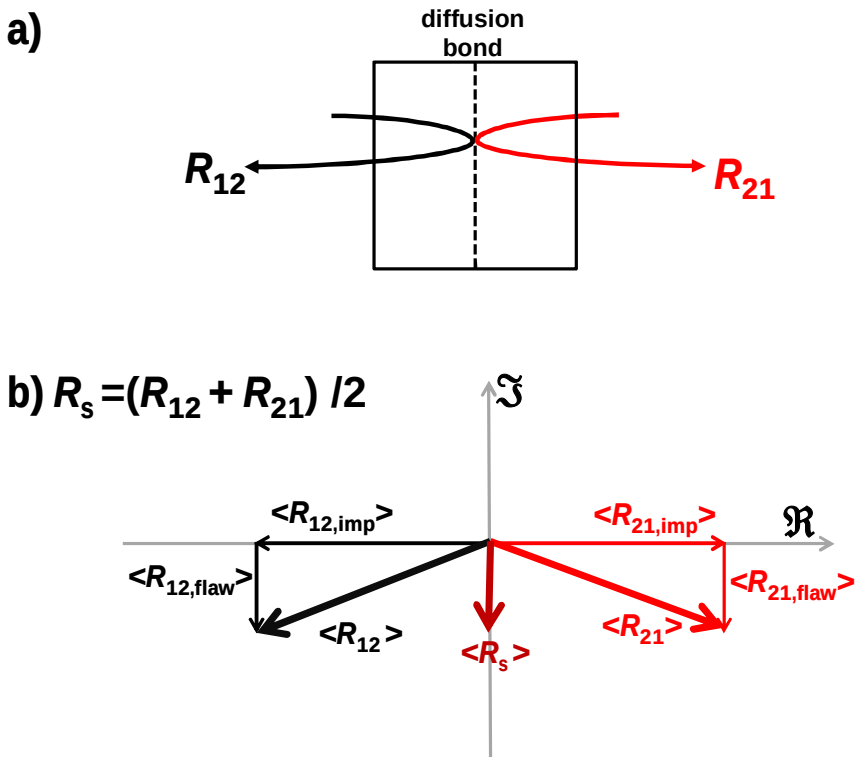

Figure 100. Symmetric reflection technique. a) Configuration for inspection from both sides of the diffusion bond. b) Vector decomposition of spatially averaged complex reflection coefficient, $<R_{12}>$ and $<R_{21}>$, at a single frequency for a diffusion bond in a partially bonded sample for inspection from both sides and calculation of the spatially averaged symmetric reflection coefficient, $<R_S>$.

The reflection coefficient due to a flaw is expected to be asymmetric, as illustrated in Figure 100. The reflection coefficient will not cancel and the symmetric reflection coefficient, R_s, will be imaginary and negative. In this section, the real and imaginary components and the magnitude of the spatially averaged symmetric reflection are calculated for each of the forged diffusion bonded samples #1-#13.

In order to calculate the symmetric reflection coefficient, the same region of the diffusion bond must be inspected from both sides and the complex reflection coefficients for each point summed. An image correlation method was used to ensure that the reflection coefficient was calculated over an identical area of the diffusion bond for scans from both sides and to align the points (see Appendix F). Misalignment of position will introduce error in the calculated value of R_s.

The complex reflection coefficient was calculated around the centre frequency of the probe (10.9MHz) at each scan position for all samples, as described in Section 5.4. The symmetric reflection coefficient, R_s, was calculated at each position using Equation 3.16. A map of the real component of R_s for the partially bonded sample #10 is shown in Figure 101a. The imaginary component of R_s is shown in Figure 101b. The real component of the symmetric reflection coefficient, $\Re(R_s)$, is near zero for all spatial positions. The linear indication highlighted at the top-left of the map in Figure 101a is thought to be voided. The absolute reflection coefficient, $|R_{12}(f)|$, shows strong frequency dependence, which is indicative of a partial bond (see Figure 95, Section 5.4.4). Correspondingly, the imaginary component, $\Im(R_s)$, is negative in this region. The component due to acoustic

impedance mismatch has cancelled out but the component due to flaws, which are asymmetric, remains and is imaginary and negative as expected (see Figure 100). A region directly below the linear indication and highlighted in Figure 101a is thought to be void-free. This region was sectioned and no voids were observed. Also, the absolute reflection coefficient, $|R_{12}(f)|$, is flat over the working bandwidth of the probe (see Figure 95, Section 5.4.4). The imaginary component, $\Im(R_s)$, is near-zero in this region.

In the maps shown in Figure 101, the complex reflection coefficient is calculated for each scan position. The component of the signal due to backscattered noise (see Figure 92.a and Figure 93.a) will be present in the calculation of the complex reflection coefficients R_{12} and R_{21}. The phase of the backscattered noise is random. Therefore, for the calculation of the symmetric reflection coefficient for a single point, it is not expected to cancel. For the real components of the signal to cancel at a single position, the component due to backscattered noise must be small relative to that due to acoustic impedance mismatch at the diffusion bond depth.

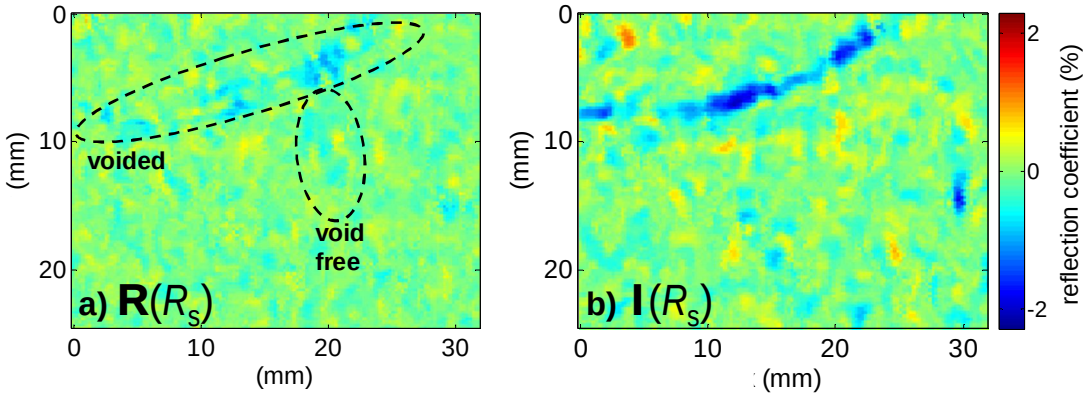

Figure 101. a) Real ($\Re$) and b) imaginary ($\Im$) components of symmetric reflection coefficient, R_s, against spatial position for sample #10. R_{12} and R_{21}, were calculated around the centre frequency of the probe (10.9MHz), as described in Section 5.4.3. A region that is thought to be voided and a region that is thought to be void-free are highlighted in (a). Both (a) and (b) are scans of the same region. Colour bar is linear and indicates reflection coefficient in percent.

The difference between the voided and void-free regions is more obvious in Figure 102. Since $\Re(R_s)$ is near-zero in all positions for sample #10, the magnitude $|R_s|$ can be taken to show the severity of voiding at each lateral position. A map of the absolute reflection coefficient $|R_{12}|$ around the centre frequency of the probe (10.9MHz) is shown in Figure 102a. A map of $|R_s|$ is plotted in Figure 102b. Both the voided and void-free regions are highlighted in Figure 102a. In Figure 102b, $|R_s|$ for the region that is thought to be voided is high. $|R_{12}|$ and $|R_s|$ are similar in magnitude for this region (~2%). In the void-free region $|R_s|$ is much lower than $|R_{12}|$, suggesting that the reflection is due to acoustic impedance mismatch alone and R_{12} and R_{21} have cancelled (see Figure 100).

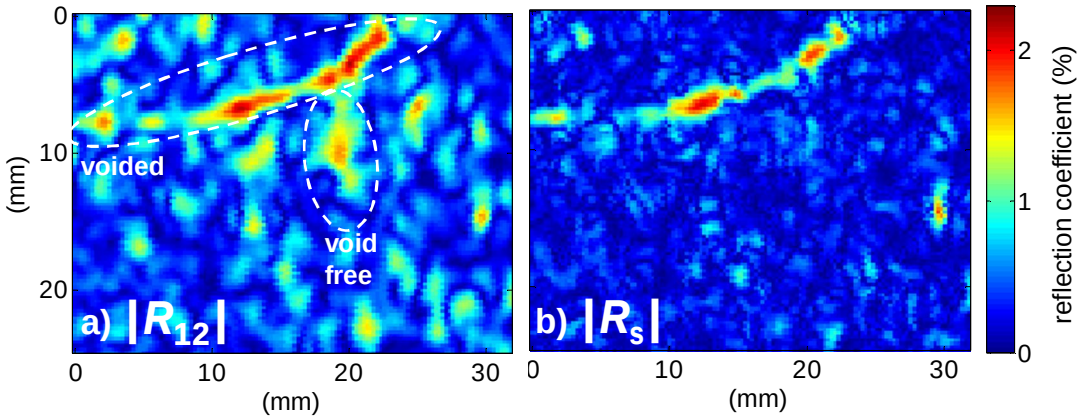

Figure 102. Sample #10. a) Absolute reflection coefficient for inspection from one side only $|R_{12}|$ at the centre frequency of the probe (10.9MHz), as described in Section 5.3. b) Magnitude of symmetric reflection coefficient, $|R_s|$. R_{12} and R_{21} were calculated around the centre frequency of the probe (10.9MHz), as described in Section 5.4.3. A region that is thought to be voided and a region that is thought to be void-free are highlighted in (a). Both (a) and (b) are scans of the same region. Colour bar is linear and indicates reflection coefficient in percent.

The relative amplitudes of the voided region and void-free region are similar in Figure 102b to that in Figure 73 for the absolute reflection coefficient over the frequency range 17-18MHz. A similar improvement in separation between the regions thought to be voided and those thought to be void-free

has been achieved using the symmetric reflection coefficient, $|R_s|$, as by moving to higher frequency.

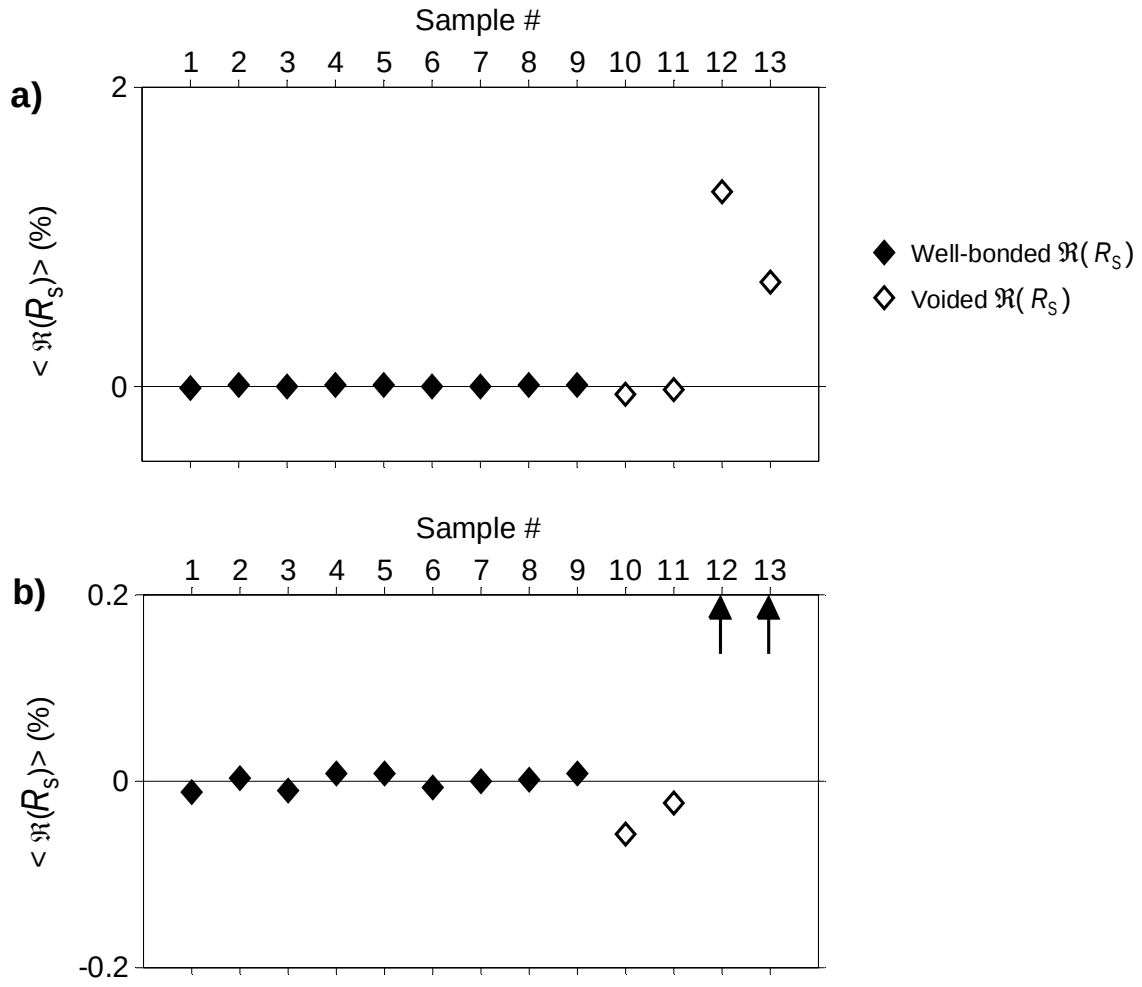

Figure 103. a) Real component of spatially averaged symmetric reflection coefficient for both well-bonded (#1-#9) and voided samples (#10-#13). The samples were scanned from each side to obtain R_{12} and R_{21}. b) Same figure with expanded scale.

The spatially averaged symmetric reflection coefficient, $<R_s>$, was calculated for each sample. The real component $<\Re(R_s)>$ is plotted in Figure 103. In Section 5.4, the real component of the spatially averaged complex reflection coefficient for samples #10 and #11 was observed to be similar in magnitude and opposite in sign for inspection from opposite sides of the diffusion bond, $<\Re(R_{12})>$ and $<\Re(R_{21})>$ (see Figure 96). The real component of the symmetric reflection coefficient, R_s, is near zero for these samples (Figure

103). For samples #12-#13, $<\Re(R_{12})>$ and $<\Re(R_{21})>$ were both positive. This was attributed to error in the measured value of the true phase. Consequently $\Re<R_{12}>$ and $\Re<R_{21}>$ do not cancel and $<\Re(R_s)>$ is much larger than that for samples #1-#11.

The imaginary component of the symmetric reflection coefficient, $\Im(R_s)$, for the partially bonded samples is expected to be negative, as shown in Figure 100. $<\Im(R_s)>$ for samples #1-#13 is plotted in Figure 104. For the partially bonded samples #10-#13, $<\Im(R_s)>$ is negative. For the well-bonded samples #1-#9 $<\Im(R_s)>$ is near-zero and there is now good separation between samples #1-#9 and the partially bonded samples #10 and #11. $<\Im(R_{12})>$ and $<\Im(R_{21})>$ cancelled for the well-bonded samples #1-#9 because they were similar in magnitude but opposite in sign (see Figure 97). The magnitude of the spatially averaged symmetric reflection coefficient, $|<R_s>|$, for samples #1-#13 is also plotted in Figure 105. Again, there is good separation between the well-bonded and partially bonded samples.

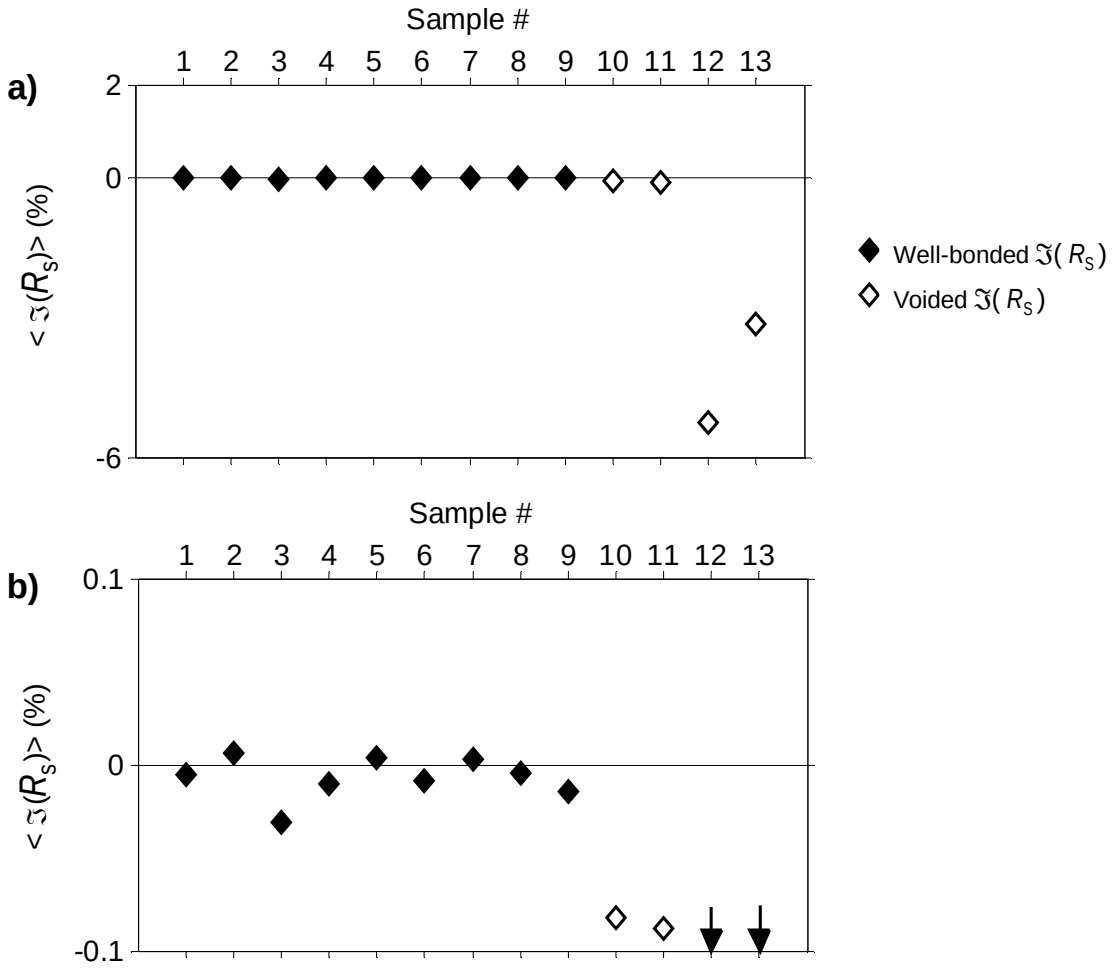

Figure 104. a) Imaginary component of spatially averaged symmetric reflection coefficient for both well-bonded (#1-#9) and voided samples (#10-#13). The samples were scanned from each side to obtain R_{12} and R_{21}. b) Same figure with expanded scale.

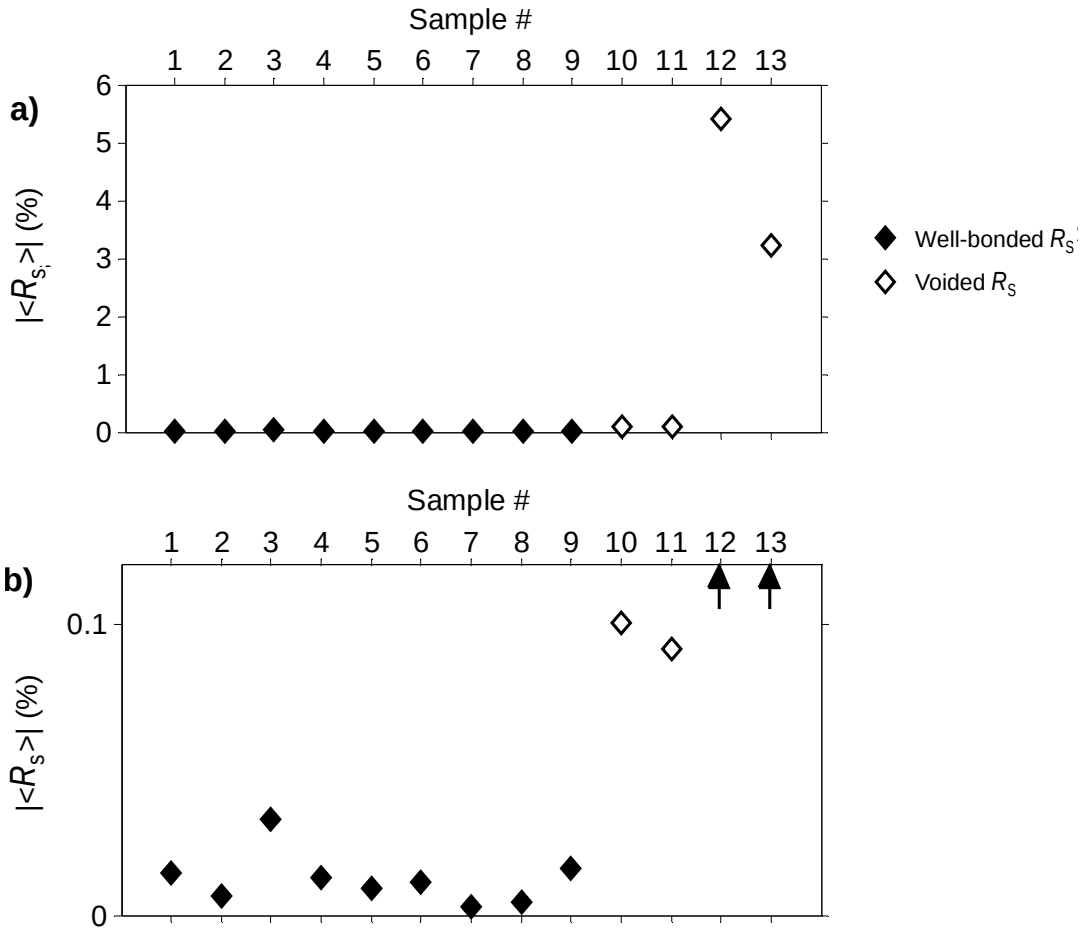

Figure 105. a) Magnitude of spatially averaged symmetric reflection coefficient for both well-bonded (#1-#9) and voided samples (#10-#13). The samples were scanned from each side to obtain R_{12} and R_{21}. b) Same figure with expanded scale.

In Section 5.3, the spatially averaged absolute reflection coefficient, $<|R_{12}|>$, of the well-bonded and partially bonded samples was compared. The partially bonded samples #10 and #11 could not be separated from the well-bonded samples #1-#9. A signal to noise ratio was defined as $<|R_{12}|>$ for the partially bonded sample divided by the maximum $<|R_{12}|>$ for any of the well-bonded samples. This indicates the sensitivity that can be achieved by the conventional pulse-echo inspection methods at the centre frequency of the probe. Higher signal to noise ratios can be achieved by moving to higher frequencies.

In this section, the real, $<\Re(R_s)>$, and imaginary, $<\Im(R_s)>$, components and the magnitude $|<R_s>|$ of the symmetric reflection coefficient were compared. Signal to noise ratios each of these parameters are defined in Table 5 and are plotted alongside that for $<|R_{12}|>$ in Figure 106 for each of the partially bonded samples #10-#13.

Table 5. Definition of signal to noise ratio for various parameters of one sided and symmetric reflection technique.

Parameter	Signal to noise ratio
Spatially averaged absolute reflection coefficient, $<\|R_{12}\|>$	$\frac{\langle\|R_{12}\|\rangle \text{ of voided sample}}{\text{maximum } \langle\|R_{12}\|\rangle \text{ for well bonded samples}}$
Magnitude of spatially averaged symmetric reflection coefficient, $\|<R_s>\|$	$\frac{\|\langle R_s\rangle\| \text{of voided sample}}{\text{maximum } \|\langle R_s\rangle\| \text{ for well bonded samples}}$
Spatially averaged real component of symmetric reflection coefficient, $<\Re(R_s)>$	$\frac{\|\langle\Re(R_s)\rangle\| \text{of voided sample}}{\text{maximum } \|\langle\Re(R_s)\rangle\| \text{for well bonded samples}}$
Spatially averaged imaginary component of symmetric reflection coefficient, $<\Im(R_s)>$	$\frac{\langle\Im(R_s)\rangle \text{of voided sample}}{\text{minimum } \langle\Im(R_s)\rangle \text{for well bonded samples}}$

The signal to noise ratio for the imaginary component of the symmetric reflection coefficient, $<\Im(R_s)>$, is greater than unity for all four partially bonded signals and gives a consistently higher signal to noise ratio than the spatially averaged one-sided absolute reflection coefficient, $<|R_{12}|>$ (see Figure 106). For sample #10, the signal to noise ratio for $<\Im(R_s)>$ is 2.64 showing that there is now good separation between the well bonded samples and all the partially bonded samples. Spatial averaging has also considerably improved the signal to noise ratio for samples #12 and #13. The contribution of backscatter from the parent metal and acoustic impedance mismatch at the bond line for the well bonded samples has almost vanished. The

component due to the flaw in samples #12 and #13 is still present. The result is signal to noise ratios of >100.

The signal to noise ratio for the real component, $<\Re(R_s)>$, and the magnitude, $<|R_s|>$, of the spatially averaged symmetric reflection coefficient are also plotted in Figure 106. The spring model predicts that $<|R_s|>$ will be due to the imaginary component only since $<\Re(R_s)>$ should be zero for both well bonded and partially bonded samples (see Figure 100). However, as shown in Figure 103, the real component is non-zero for the partially bonded samples. This is thought to be due to error in the measured true phase. $<\Im(R_s)>$ is more than three times larger than $<\Re(R_s)>$ for the partially bonded samples. This component will dominate the magnitude of symmetric reflection coefficient. Therefore the SNR for $<|R_s|>$ is very close to that for $<\Im(R_s)>$.

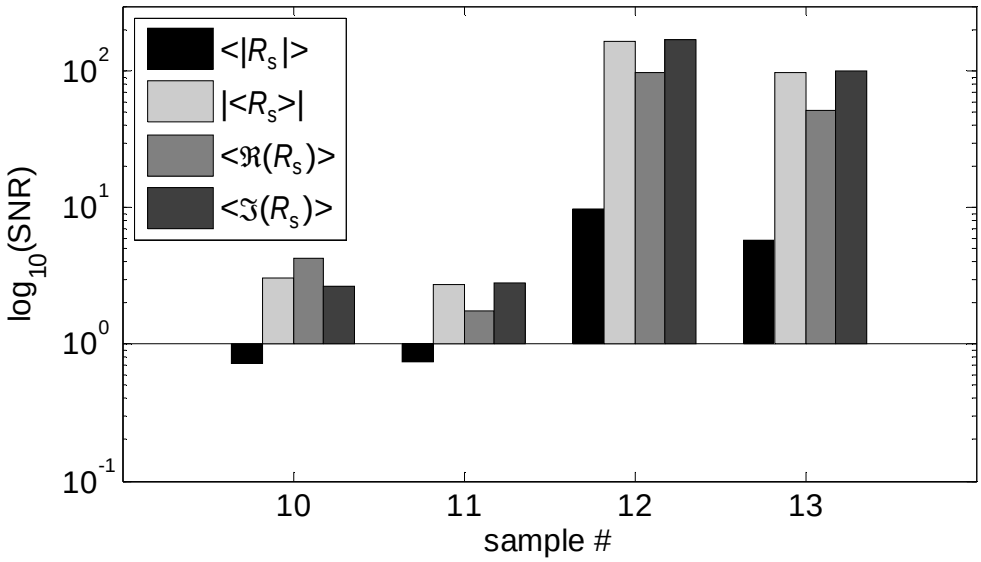

Figure 106. Signal to noise ratio, as defined in Table 5, for the spatially averaged absolute reflection coefficient, $<|R_{12}|>$, and the magnitude ,$|<R_{12}>|$, real component, $<\Re(R_{12})>$, and imaginary component $<\Im(R_{12})>$ of the spatially averaged complex reflection coefficient for partially bonded samples #10-#13. The scale is logarithmic.

In summary, the symmetric reflection coefficient was measured in each position across the sample and also spatially averaged. The imaginary component of the symmetric reflection coefficient was negative, as predicted for an imperfect interface by the spring model. Good separation between the partially bonded samples and the well bonded samples was achieved with the spatially averaged reflection coefficient. The real component of the spatially averaged reflection coefficient, $<\Re(R_s)>$, should be zero as backscattered noise should cancel due to spatial averaging and acoustic impedance mismatch should cancel due to inspection from opposite sides of the diffusion bond. $<\Re(R_s)>$ was not zero and was larger in magnitude for the partially bonded samples #10-#13 than for the well bonded samples. This was attributed to error in the measured true phase. The imaginary component $<\Im(R_s)>$ was shown to give the better separation between the partially bonded and well bonded samples than the real component $<\Re(R_s)>$ or the magnitude $|<R_s>|$ of the spatially averaged reflection coefficient.

5.6. Conclusions

In this section various signal processing methods were investigated for improving the sensitivity of ultrasonic inspection to partial diffusion bonds in titanium. In Section 5.1 it was shown that, for the 10.9MHz 6.3”F 0.75” diameter probe used for inspection in this project, the interface reflection could further limit the inspection sensitivity, depending upon the microtexture of the blocks that were joined. The interface reflection is a result of the joining of macrozones with different preferred crystallographic alignments and so different acoustic impedances. The samples were generated by joining material with various microtextures. The amplitude of

the signal reflected from the interface varied between samples. This is probably related to microtexture of the parent metal. This work highlights the importance of determining the likely amplitude of the interface reflection in good diffusion bonds for microtexture representative of the actual component, in order to set the inspection threshold and avoid false calls. Based upon the amplitude of the backscattered ultrasound, partially bonded sample #10 could not be separated from the well bonded samples.

In Section 5.2, the possibility of using the spatial correlation coefficient as a function of measurement spacing, $SCC(|x-x'|)$, as a means of differentiating between well bonded and partially bonded samples was investigated. $|x-x'|$ is the spacing between in measurements. $SCC(|x-x'|)$ was found to depend upon the microtexture of the blanks that were joined, as well as upon the presence of voids. If two pieces of material with identical but coarse microtexture were joined then the *SCC* would tend to zero for large $|x-x'|$, even if amplitude of the backscattered signal is high. If two pieces of material with different microtexture and different average acoustic impedances were joined then the $SCC(|x-x'|)$ would tend to a non-zero value for large measurement spacings, even if the amplitude of the backscattered signal is low. There is potential for using the $SCC(|x-x'|)$ for differentiating between well bonded and partially bonded samples. However, *a priori* knowledge of the microtexture in the component would be required. $SCC(|x-x'|)$ did not separate sample #10 from the well bonded samples. Techniques which measure the spatial correlation of the reflected signal, including the *SCC*, spatial averaging and time of flight variance, can only be used to detect distributed defects. The defects must be distributed over an area greater than the spatial correlation length.

The absolute reflection coefficient was calculated for samples #1-#13 in Section 5.3. At the centre frequency (10.9MHz) of the probe, neither sample #10 nor sample #11 could be separated from the well-bonded samples. The signal to noise ratio increased with frequency. At frequencies above 14MHz, the partially bonded samples could be separated from the well bonded samples. This confirms that higher sensitivity to diffusion bond defects can be achieved at higher frequency. If the metal path allows high frequency inspection then this is clearly the most straightforward and sensitive inspection.

The true phase – a measure of the phase of the interface reflection, independent of arrival time - was introduced in Section 5.4. Given the magnitude and the true phase of the signal, the reflection coefficient can be decomposed into its real and imaginary components. The spring model predicted that, for long wavelengths, the component of the reflection due to a partial bond would be wholly imaginary but that the component due to an acoustic impedance mismatch would be wholly real. The hypothesis behind this technique was that the imaginary component of the complex reflection coefficient could be used to separate the well bonded and partially bonded samples. The complex reflection coefficient was calculated for a frequency range around the centre frequency of the probe (10.9MHz). Spatial averaging was used to eliminate the contribution of backscattered noise. For some samples, it also eliminated the reflection due to acoustic impedance mismatch which could be either 0 radians or π radians, depending upon the scan position. The imaginary component was negative for inspection from both sides of the diffusion bond for all the partially bonded samples. For the well bonded samples the imaginary component was approximately

symmetric, suggesting that there was some error in the reference true phase. Due to the non-zero imaginary component for the well-bonded samples, neither sample #10 nor sample #11 could be separated from the well-bonded samples.

The imaginary component of the complex reflection coefficient has potential as a method for one-sided inspection, if the errors can be reduced. For partial bonds between material where the change in acoustic impedance at the interface is consistent (highly textured titanium or solid-state welds between different materials) the error in the reference true phase will be lower. If the amplitude of the interface signal is high relative to that of the backscattered noise before or after the interface then spatial averaging may not be required.

The symmetric reflection technique was used in Section 5.5. The technique requires measurement of the magnitude and true phase of the reflection coefficient for normal incidence on both sides of the diffusion bond. It would therefore not be applicable to the inspection geometry described in 3.2.8. However, it could be used for determining the condition of samples and for other industrial applications. All the partially bonded samples could be separated from the well bonded samples using this method.

Unlike high frequency inspection, the complex reflection coefficient and symmetric reflection technique could be applicable to inspection at greater metal paths. The probe used for this project had a centre frequency of 10.9MHz. At lower frequencies the backscattered noise is expected to reduce (Equation 3.2). The ratio between the component of the reflection due to

acoustic impedance mismatch and the component due to the flaw will decrease at lower frequencies. Therefore, low frequency inspection might be more sensitive to error in the reference phase. The complex reflection coefficient and symmetric reflection coefficient have not yet been calculated at a lower frequency for these samples. Future work could look at both reducing the error in the phase measurement and lower frequency inspection.

6. Conclusions

6.1. Review of Part II of Thesis

The aim of this project was to improve the sensitivity of ultrasonic inspection of titanium diffusion bonds. The inspection geometry will allow normal to bond line inspection. However, the metal paths may be large and there is only access from one side of each diffusion bond.

The factors limiting the sensitivity of conventional ultrasonic pulse-echo immersion inspection were described in Section 3.1 and Section 3.2. In Ti–6Al–4V the grains are arranged in regions of preferred crystallographic orientation. These regions or 'macrozones' may be millimetres in size. For the ultrasonic frequencies commonly used for the inspection of metals in industry (1-50MHz depending upon application), the size and anisotropy of these macrozones, rather than the individual grains, determines the amplitude of the backscattered ultrasound. This backscatter limits the sensitivity of conventional inspection, as the amplitude of the reflection from a small defect will not appear above the 'grass'.

A diffusion bond creates a planar interface between these macrozones. Ultrasound will be reflected due to the change in preferred crystallographic alignment and the associated change in acoustic impedance. This reflection further limits the sensitivity of the conventional ultrasonic inspection. In Section 5.1 it was shown that the reflection from this interface is, on average, higher than the reflection from the bulk material before and after the diffusion bond for a series of well-bonded samples manufactured by joining Ti-6Al-4V of rolled and forged microtextures (Section 4). The presence of

these macrozones has been demonstrated using high resolution surface wave measurements and electron backscatter diffraction (Section 3.2.1).

A series of partially bonded samples were generated, as described in Section 4. Two of these partially bonded samples could be readily separated from the well bonded samples by the amplitude of the reflected ultrasonic signal. One sample was marginal and the fourth could not be separated by the amplitude of the reflected ultrasonic signal. Various signal processing methods were investigated for improving the sensitivity of the ultrasonic inspection to these partially bonded samples.

The spatial correlation coefficient, *SCC*, measures the correlation between signals over a region of the diffusion bond. For good same-metal diffusion bond, the average *SCC* is expected to tend to zero for large measurement spacings. However, for some of the well bonded Ti-6Al-4V samples (Section 5.2) this did not occur. This was attributed to a slight difference in the average acoustic impedance either side of the diffusion bond. The *SCC* for a well bonded Ti-6Al-4V sample therefore depends upon the preferred orientation of the macrozones as well as their size relative to the area over which the *SCC* is calculated. For the well bonded samples where the *SCC* did not tend to zero for large measurement spacings, the presence of flaws could decrease or increase the *SCC*. This method could be applied for the detection of defects distributed over a region of a diffusion bond; however it depends upon *a priori* knowledge of the *SCC* expected for a good diffusion bond, which is specific to the microtexture of the joined material.

The absolute reflection coefficient (Section 5.3) was observed to increase with frequency for voided regions of the partially bonded samples but not for void-free regions of the same sample or for the well bonded samples. At frequencies above 14MHz all the partially bonded samples could be separated from the well bonded samples. As expected, higher sensitivity to diffusion bond defects can be achieved at higher frequency. If the metal allows high frequency inspection then this is clearly the most straightforward and sensitive option.

The frequency dependence of the magnitude of the reflection coefficient also implies that the ultrasonic wavelength is long compared to the defect size. For this regime, the spring model (Equation 3.9) predicts that the reflection due to a partial bond will be $\pi/2$ radians out of phase with the reflection due to acoustic impedance mismatch. The true phase of the diffusion bonds was measured in Section 5.4 relative to a reference phase (the backwall of a sample with similar microtexture). On the reference blocks, the effect of focussing and microtexture on the measured true phase was investigated. The true phase varies with the position of the interface relative to the probe face for a focussed probe due to wavefront curvature. For an anisotropic material such as Ti-6Al-4V, the true phase also varies with scan position due to wavefront distortion. This variation was not accounted for in the measurement of the true phase for the diffusion bonded samples and introduces an error. The size of the error will depend upon the microtexture of the material and is larger for samples with coarse microtexture. Error in the true phase is also introduced due to the presence of backscattered noise from the parent metal immediately before and after the diffusion bond. The

error increases as the relative ratio of the diffusion bond signal and the backscattered noise decreases.

From the magnitude and true phase of the reflected signal, a complex reflection coefficient was calculated for the samples in Section 5.4. Spatial averaging was used to reduce the contribution of backscattered noise. The spatial correlation length of the diffusion bond signal was measured in Section 5.2 and was found to be 1.25mm. The complex reflection coefficient must be spatially averaged over distances greater than the spatial correlation length in order to eliminate the backscattered noise. In this sample the complex reflection coefficient was averaged over the entire area (20x30mm). The size of the distributed defect that can be detected is limited by the area over the signal is averaged.

The imaginary component of the complex reflection coefficient is expected to be zero for the well bonded samples and negative for the partially bonded samples. As expected, it was negative for the partially bonded samples for inspection from both sides of the diffusion bond. For the well bonded samples the imaginary component was non-zero and approximately equal in magnitude but opposite in sign. The symmetric imaginary component for the well bonded samples suggested that there is an error between the true phase measured for the reference blocks and the actual true phase at the diffusion bond, as described above. Due to the non-zero imaginary component for the well-bonded samples, neither sample #10 nor sample #11 could be separated from the well-bonded samples. The imaginary component of the complex reflection coefficient has potential as a method for one-sided

inspection of Ti-6Al-4V diffusion bond, but only if these errors can be significantly reduced.

The symmetric reflection technique (Section 5.5) was less sensitive to the error in measurement phase. All of the partially bonded samples could be separated from the well bonded samples by comparing the imaginary component of the symmetric reflection coefficient. Further work is required to understand the sensitivity of the symmetric reflection technique to error in the measured true phase for Ti-6Al-4V samples. The technique requires measurement of the magnitude and true phase of the reflection coefficient for normal incidence on both sides of the diffusion bond. It would therefore not be applicable to the inspection geometry. However, it could be used for determining the condition of development samples, and for other industrial applications. Unlike high frequency inspection, the complex reflection coefficient and symmetric reflection technique could be applicable to inspection at greater metal paths.

6.2. Brief Summary of Main Contributions

The main contributions of Part II of this thesis can be summarised as follows:

- a series of good and partial Ti-6Al-4V diffusion bonds were generated. The joined blanks had a range of microtexture, which was qualitatively characterised by high resolution surface wave measurement. One of the partially bonded samples could not be separated from the well bonded samples based upon the amplitude of the reflected signal.

- the spatial correlation of signals over a region of the diffusion bond was measured as a function of measurement spacing for well bonded and partially bonded Ti-6Al-4V samples. For well bonded samples the spatial correlation coefficient tended to a residual value for large measurement spacings. This was attributed to the acoustic impedance averaged over the scanned area before the diffusion bond being different to that after it i.e. the diffusion bond is analogous to a join between two different materials. If the microtexture of the parent metal is consistent then the spatial correlation coefficient could be used to detect defects.

- the reflection from void-free regions of diffusion bonded samples was shown to be frequency independent, implying that the reflection is caused by acoustic impedance mismatch. This was attributed to the planar interface between macrozones with different preferred crystallographic alignments created by the diffusion bond. The amplitude of this reflection was shown to limit the sensitivity of the conventional ultrasonic inspection.

- the reflection from voided regions of diffusion bonded samples was shown to be frequency dependent. Separation between the well bonded and partially bonded samples could be achieved at high frequencies. The frequency dependence implied that the defect size is smaller than the ultrasonic wavelength. Metallurgical examination of the diffusion bonds confirmed this.

- the ‘true phase’ – a measurement of pulse phase, independent of arrival time – was applied to the assessment of diffusion bond quality. The magnitude and true phase of the reflection coefficient were combined to calculate the imaginary and real components of the reflection coefficient. The imaginary component of the reflection coefficient was negative for voided areas, as predicted by the spring model for long wavelengths.

- the true phase was shown to be dependent upon wavefront curvature (caused by beam focussing and spread) and wavefront distortion (caused by crystallographic anisotropy of the parent metal).

- the symmetric reflection technique was successfully used to discriminate between the partially bonded samples and the well bonded samples.

6.3. Future Work

From an industrial point of view, this project has highlighted the fact that there may be a weakly coherent reflection at a titanium diffusion bond due to the planar interface between macrozones. Before even a conventional ultrasonic inspection can be applied, a good diffusion bond between pieces of representative forged material is required. Ultrasonic inspection of such representative samples or development components should be carried out so that an inspection threshold that will avoid false calls can be set.

In this project the well bonded and partially bonded samples could not be separated based on the imaginary component of the complex reflection coefficient. The complex reflection coefficient has two major advantages. Firstly, it requires access to only one side of the diffusion bond, thereby meeting the requirements of the inspection. Secondly, by using the true phase and the magnitude of the reflected signal, the complex reflection coefficient should be able to achieve higher signal to noise ratios at lower frequencies.

Three different causes of error in the measured value of true phase have been identified:

1. Wavefront curvature. The effect of focussing and beam spread on the true phase of the propagating wave pulse for various probe geometries could be modelled and measured experimentally for a homogeneous material. This would also allow the error in reference phase caused by the variations in water path of sample thickness to be estimated. Modelling should be carried out to achieve a better understanding of the problem.
2. Wavefront distortion. The true phase varies with lateral position in an anisotropic material due to wavefront distortion. Rather than using blanks with similar microtexture, the reference phase could be measured on the actual blanks prior to diffusion bonding. This would allow a point-by-point correction in the true phase. Modelling of an anisotropic system should be carried out to promote better understanding of the problem. This could be supported by direct measurement of the microtexture using, for example, local surface wave velocity measurements or electron backscatter diffraction.

3. Backscattered noise. Backscattered noise adds a random error to the calculated value of true phase. Spatial averaging reduces the backscattered noise. The area over which the reflection coefficient is averaged should be varied for the data that has been captured.

At lower frequencies, the ratio between the component of the reflection due to acoustic impedance mismatch and the component due to the flaw is expected to increase. Therefore, low frequency inspection might be more sensitive to error in the reference phase. However, if the error can be limited then it may be possible to achieve similar results at even lower frequencies. Forging inspection is typically carried out at 4-6MHz, compared to 10.9MHz used for this project.

In two of the partially bonded samples (#10 and #11), regions were observed where there was no voiding but the grain boundaries were aligned. The results presented here suggest that the imaginary component of the reflection coefficient is not sensitive to these regions. However, they could present a mechanical weakness in the material. If possible, samples with incomplete diffusion but no voiding should be generated. The effect of this type of defect on the fatigue performance of the material should be investigated. The sensitivity of the various ultrasonic inspections to this should be assessed. If the aligned grain boundaries result in a significant loss of interfacial stiffness then it may be possible to detect it using the symmetric reflection technique.

In the actual inspection geometry, it is possible that the depth of the diffusion bond will vary slightly with lateral position. The depth tolerance will

be known. The effect of crystallographic anisotropy and depth variations on the sensitivity of the various techniques should be investigated prior to industrial application.

The symmetric reflection technique was demonstrated by Nagy and Adler for application to inertia welds between dissimilar metals. The method could similarly be applied to diffusion bonds between dissimilar metals. A one-sided inspection of dissimilar metals may also be possible, if the error in the true phase measurement can be understood and corrected for.

In summary, in the course of this project the magnitude and phase of the reflection coefficient were measured and used to differentiate Ti–6Al–4V samples that were partially bonded from Ti–6Al–4V samples that were well bonded. By measuring the reflection coefficient from both sides of the diffusion bond the well bonded and partially bonded samples were successfully separated. However, more work is required to determine whether a single-sided inspection of titanium diffusion bonds is possible. A single-sided technique would be extremely advantageous for industrial application. It is recommended that:

- Modelling and experimental work is carried out to understand the effect of wavefront curvature (focussing) and wavefront distortion due to propagation through an anisotropic material on the measured true phase of the reflection coefficient.
- The effect of varying the area over which the reflection coefficient is spatially averaged is investigated.

- The reflection coefficient is calculated for well bonded and partially bonded samples for data captured at 4-6MHz, as these frequencies are typically used for the inspection of forgings in industry [3].

This project focussed on methods for improving the sensitivity of ultrasonic inspection to partial bonds. However, regions of incomplete diffusion were observed in two of the diffusion bonded samples. Samples containing this type of defect over the entire diffusion bond line would be extremely useful, both to understand the effect on the mechanical properties and to determine the sensitivity of the various ultrasonic inspection methods discussed here. Industry should attempt to manufacture samples with incomplete diffusion.

It is also strongly recommended that the complex reflection coefficient – where both the magnitude and phase of the reflected wave are determined – and the symmetric reflection technique are applied to the inspection of solid state welds between dissimilar materials.

Appendix A – Technical Drawing for Ti-6Al-4V Blanks

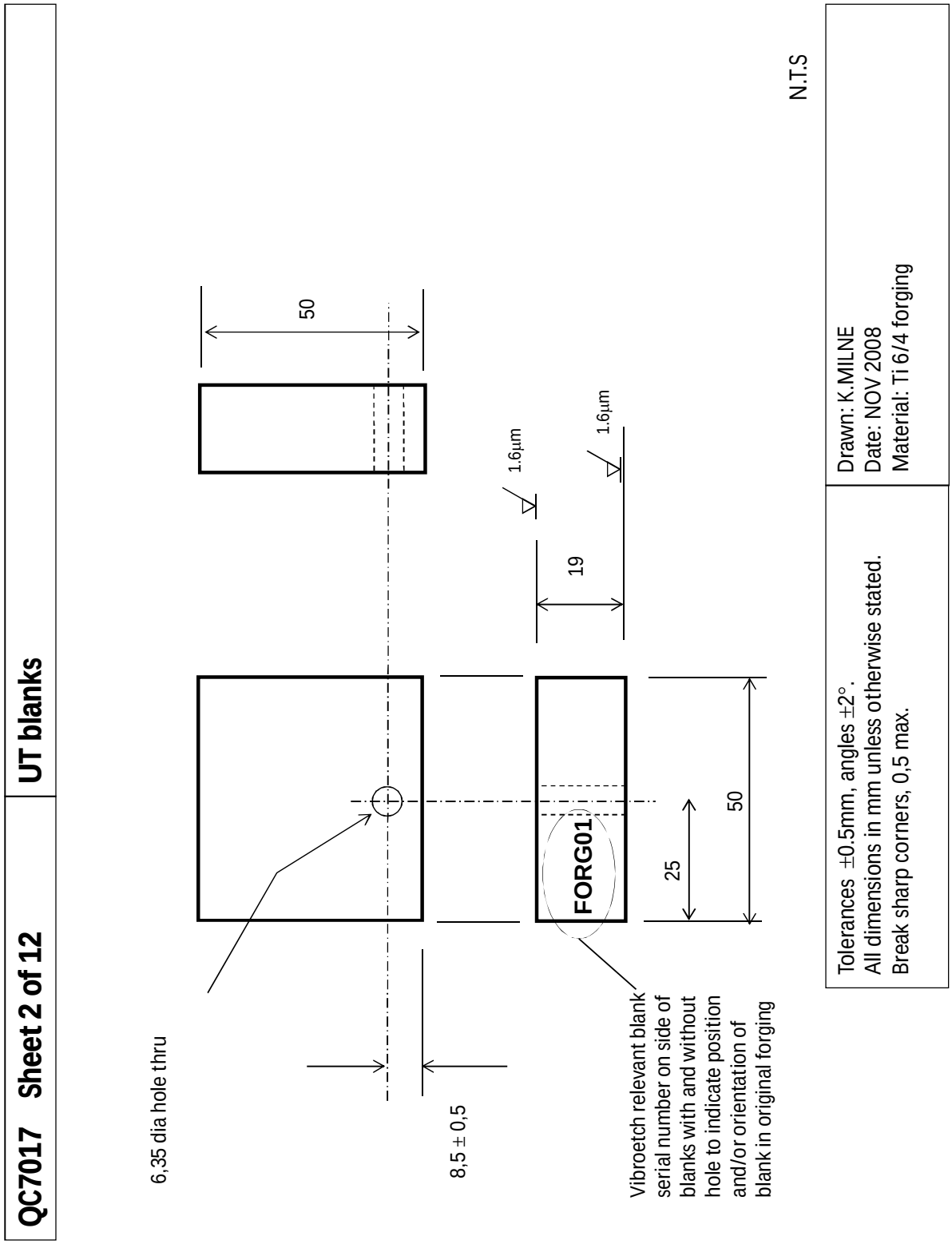

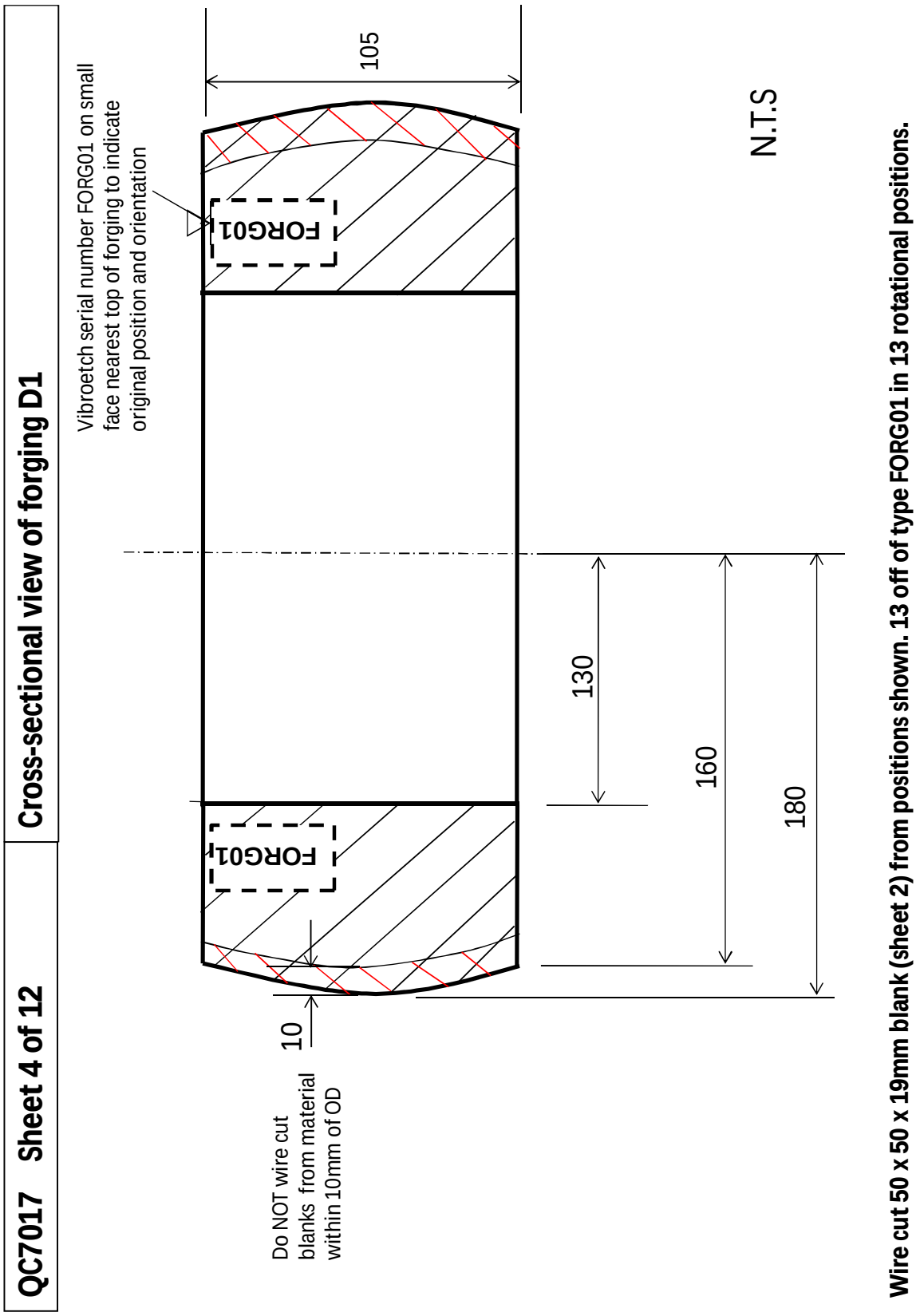

Wire cut 50 x 50 x 19mm blank (sheet 2) from positions shown. 13 off of type FORG01 in 13 rotational positions.

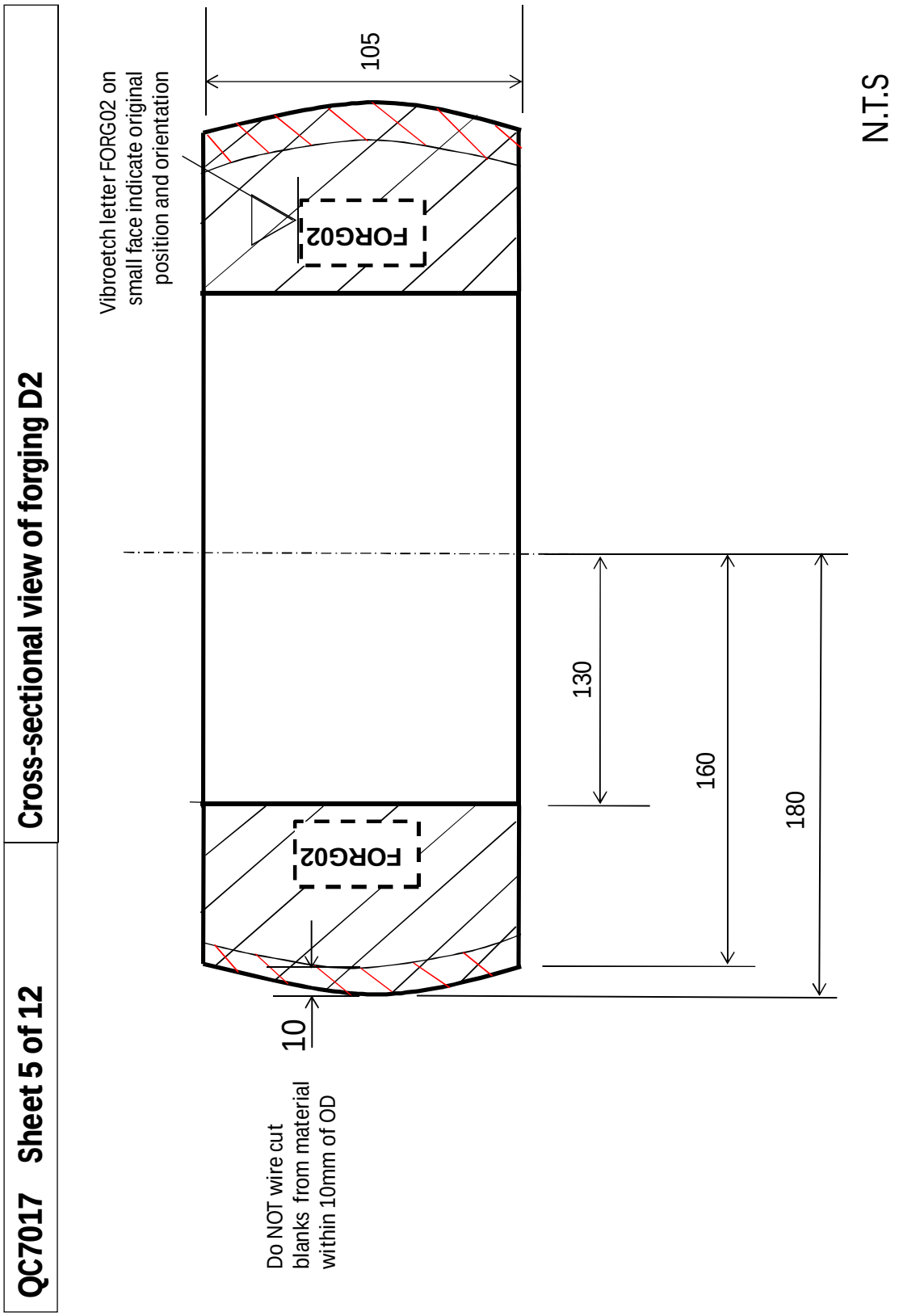
QC7017 Sheet 5 of 12
Cross-sectional view of forging D2
Vibroetch letter FORG02 on small face indicate original position and orientation
105
FORG02
FORG02
130
160
180
10
Do NOT wire cut blanks from material within 10mm of OD
N.T.S
Wire cut 50 x 50 x 19mm blank (sheet 2) from positions shown. 13 off type FORG02 in 13 rotational positions.

QC7017 Sheet 8 of 12	Cross-sectional view of forged segment J

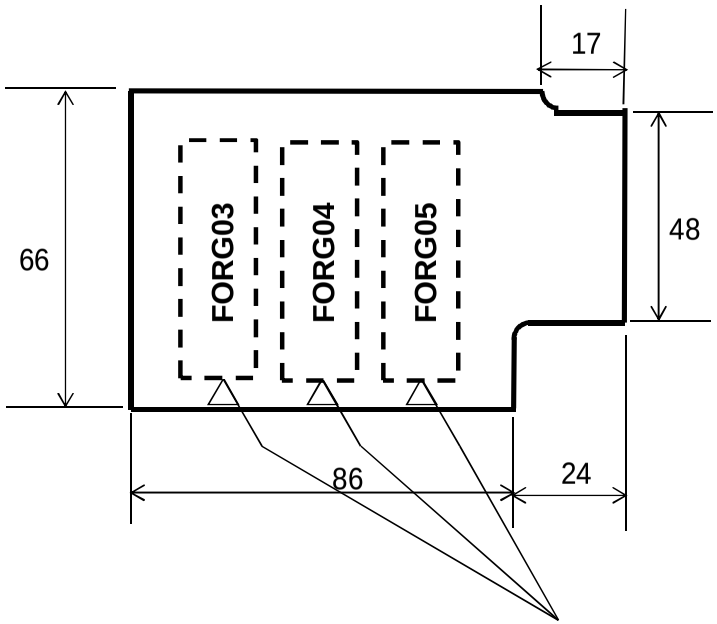

100° sector

Vibroetch blank serial number (FORG03, FORG04, FORG05) respectively on this face of blanks to indicate original position and orientation

N.T.S

Wire cut 50 x 50 x 19mm blank (sheet 2) from positions shown. 3 off type FORG03, FORG04 and FORG05 in 3 rotational positions

QC7017 Sheet 9 of 12	Cross-sectional view of forged segment J

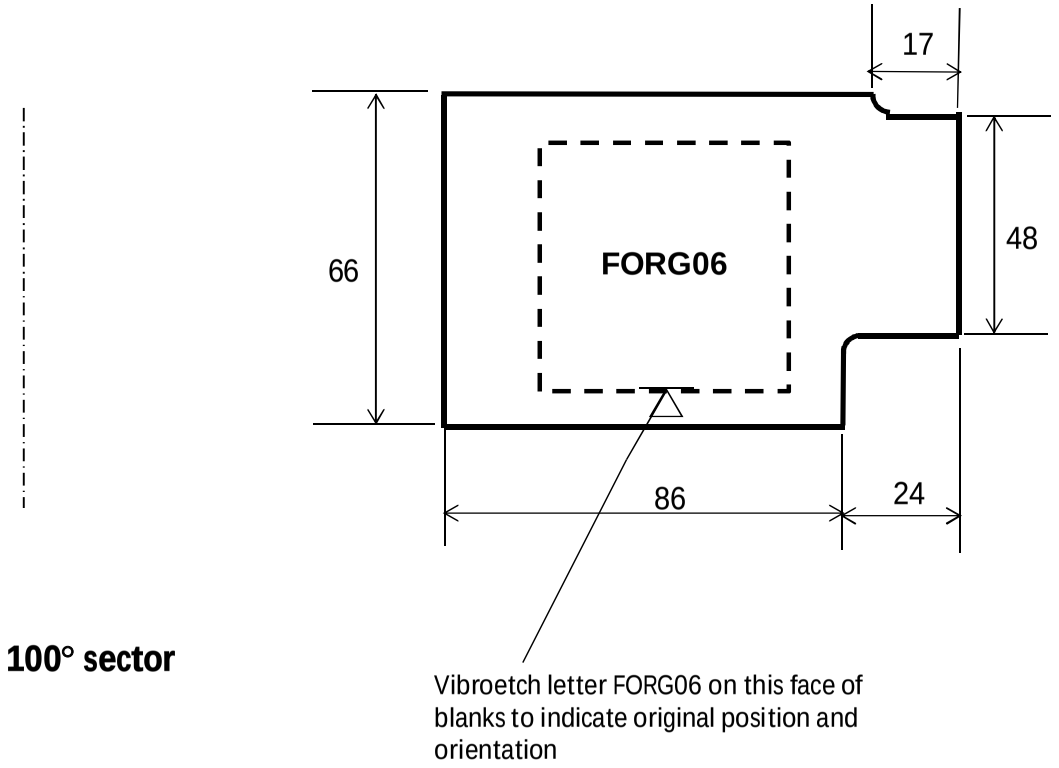

100° sector

N.T.S

Wire cut 50 x 50 x 19mm blank (sheet 2) from positions shown. 2 off type FORG06 in 2 rotational positions.

QC7017 Sheet 11 of 12	Cross-sectional view of forged segments M and N

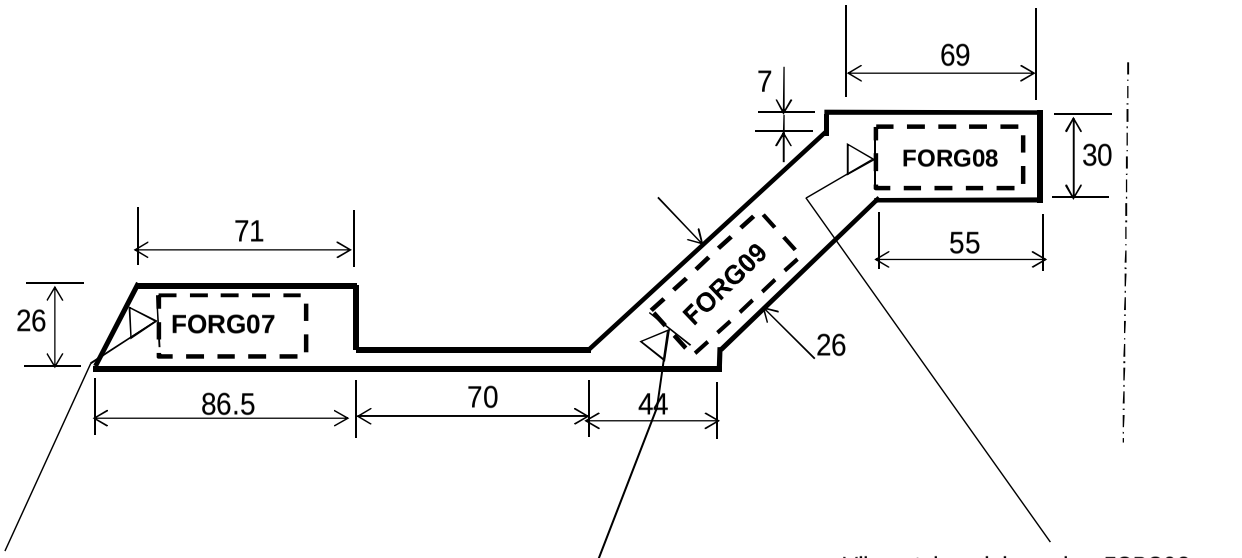

N.T.S

100° sector

Wire cut 50 x 50 x 19mm blank (sheet 2) from positions shown. 3 off types FORG07 and FORG09 in 3 rotational positions. 2 off type FORG08 in 2 rotational positions.

QC7017 Sheet 12 of 12	Cross-section view of forged segments M and N

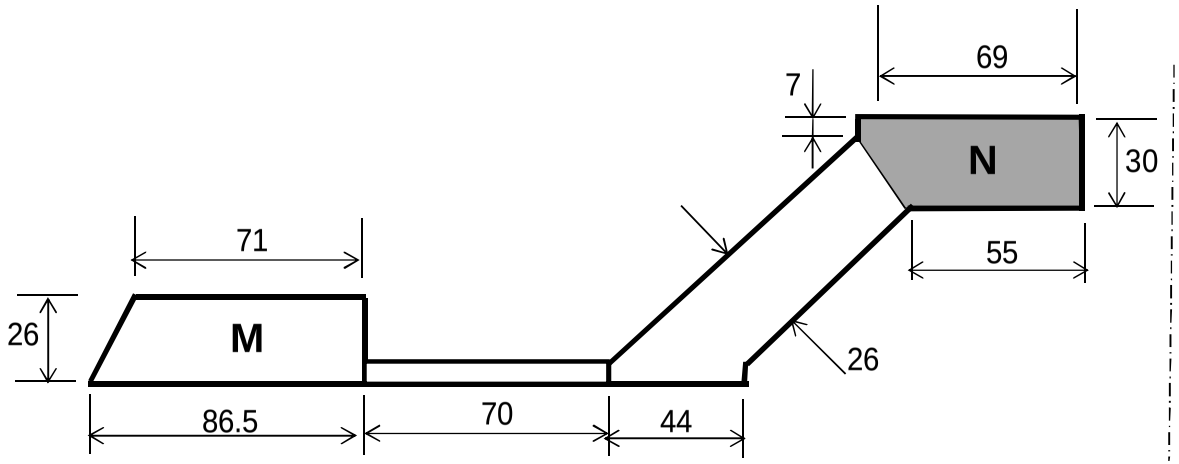

Notes – segment N shown was not cut by subcontractor as requested. Segment N, as returned to Rolls-Royce plc, is highlighted in grey.

N.T.S

Appendix B – Macroetch of Stock Material and Surface Wave Velocity Maps

Figure B 1. Photograph of forged Ti-6Al-4V segment D1, etched to reveal the forging flow lines.

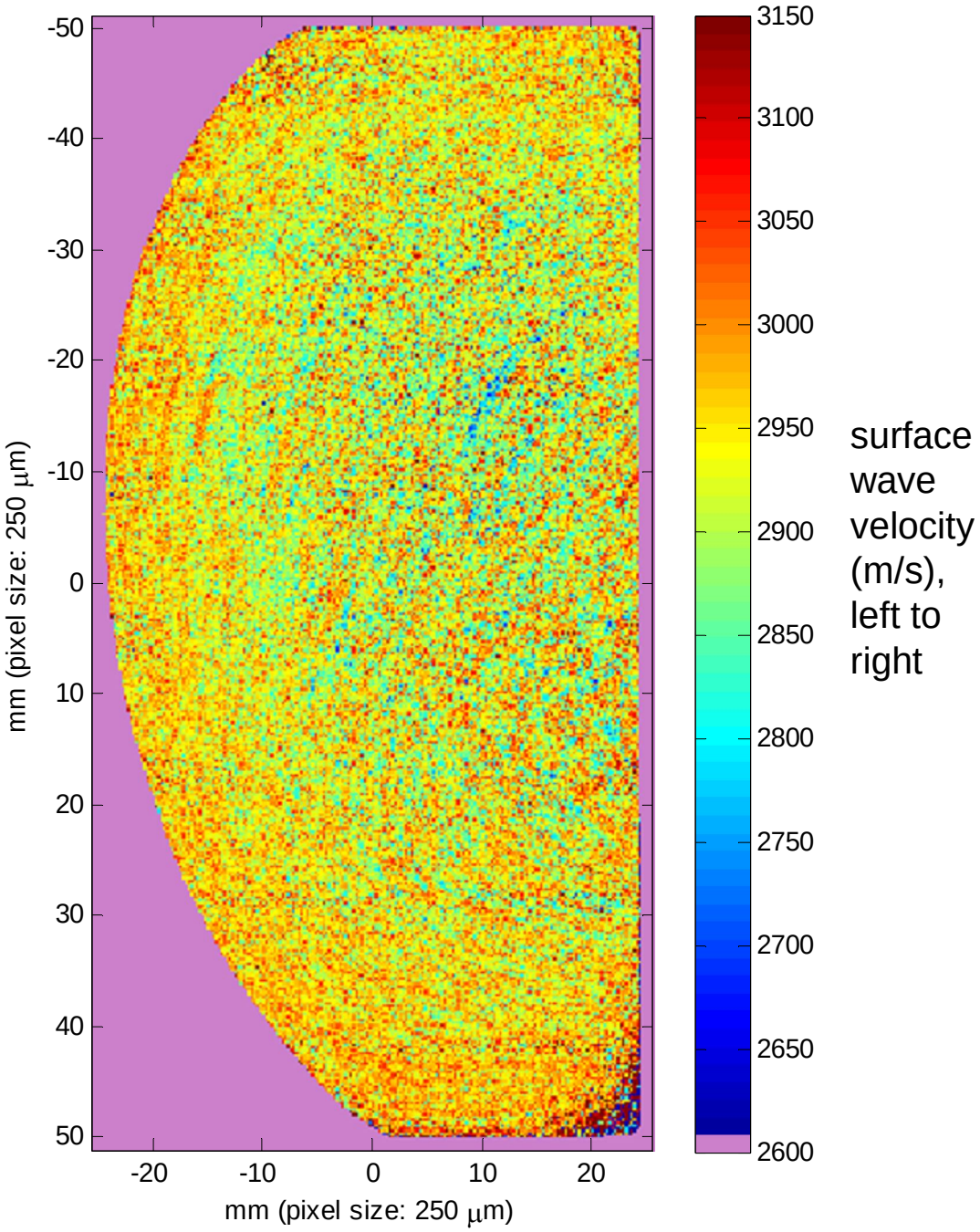

Figure B 2. Surface wave velocity map of slice through forged Ti-6Al-4V segment D1, obtained using optical-scanning acoustic microscope (O-SAM) at University of Nottingham [54]. The surface wave velocity was measured left-to-right over a length of 250μm with a pixel size of 250μm.

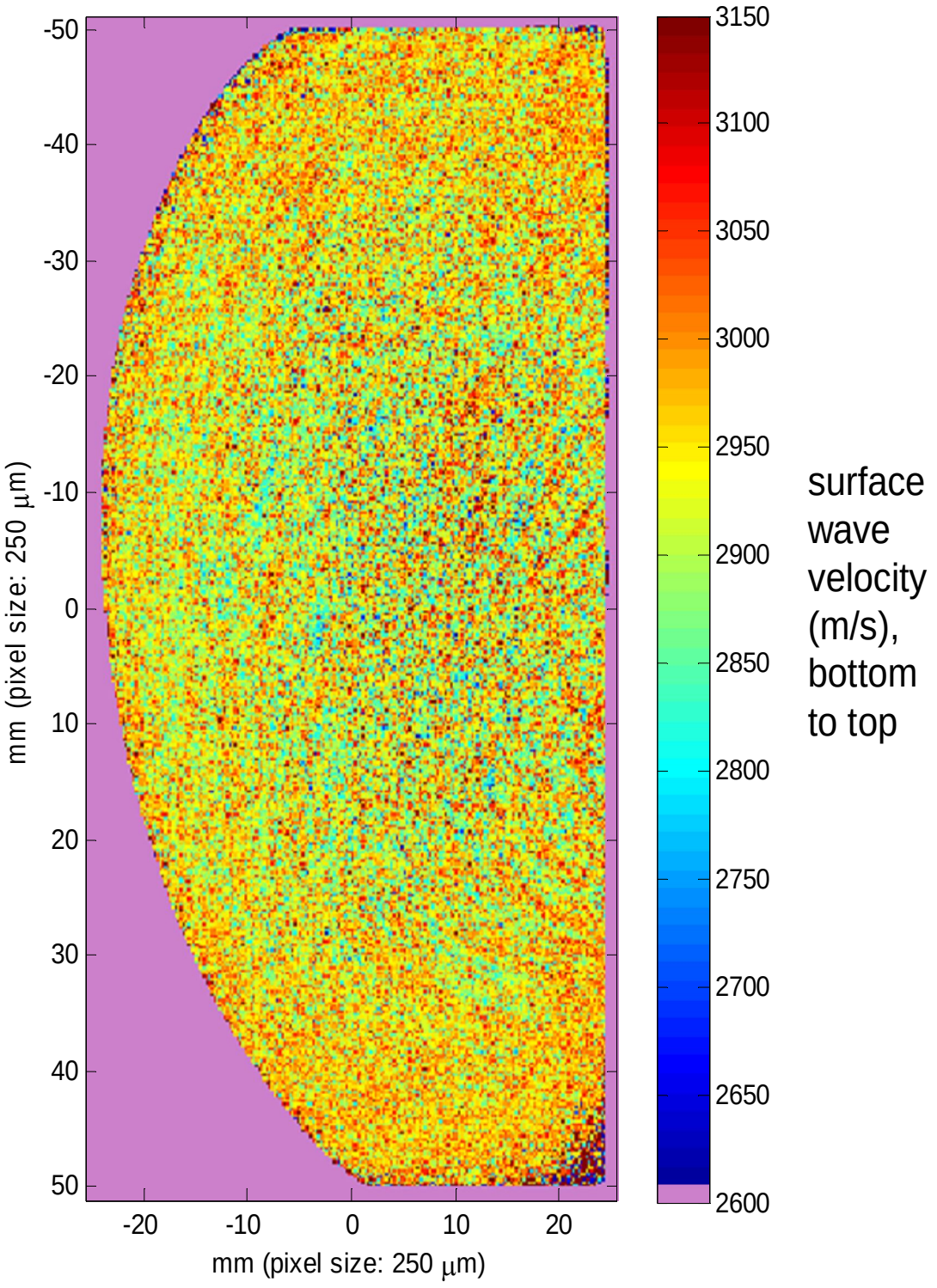

Figure B 3. Surface wave velocity map of slice through forged Ti-6Al-4V segment D1, obtained using optical-scanning acoustic microscope (O-SAM) at University of Nottingham [54]. The surface wave velocity was measured bottom-to-top over a length of 250μm with a pixel size of 250μm.

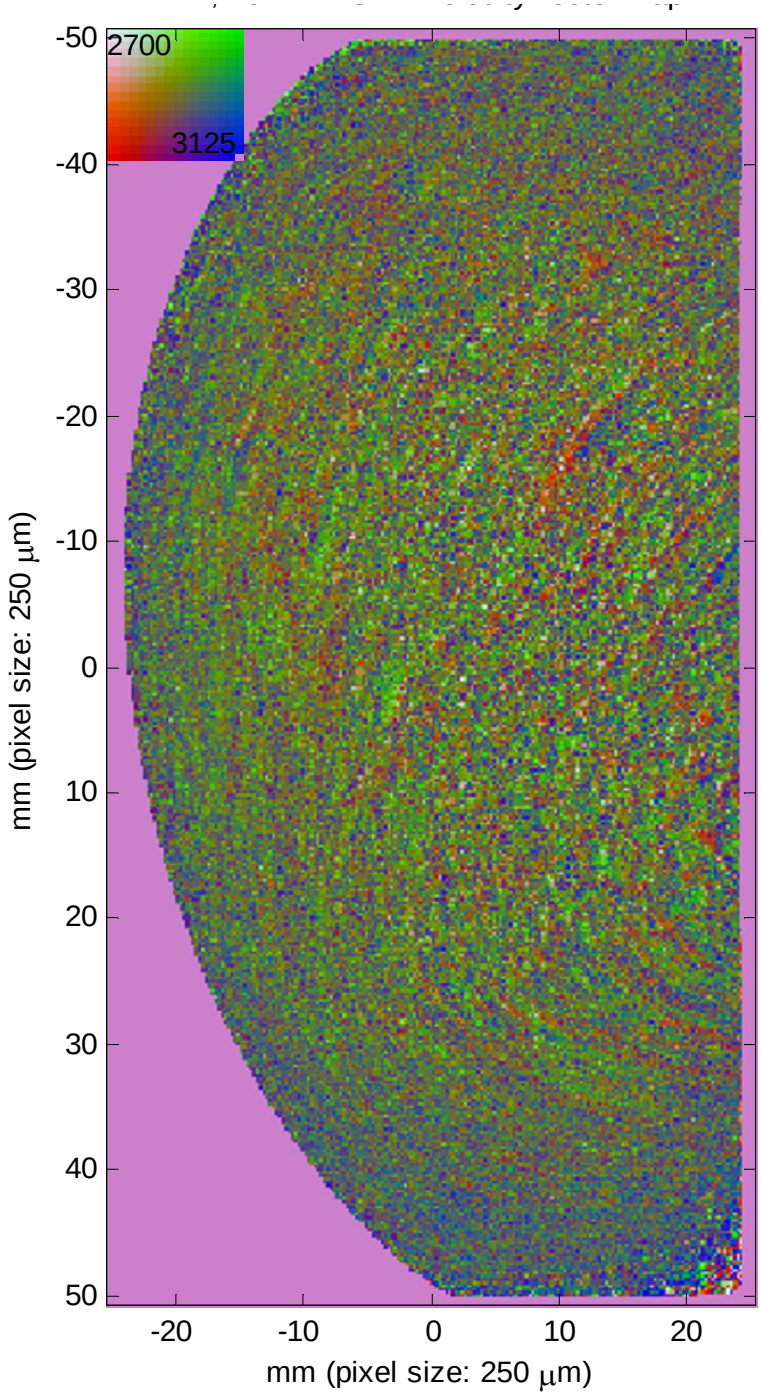

Figure B 4. Surface wave vector velocity map of slice through forged Ti-6Al-4V segment D1, obtained using optical-scanning acoustic microscope (O-SAM) at University of Nottingham [54], made by combining Figure B 2 and Figure B 3. The 2D colour map (top left) shows the surface wave velocity in two directions: left-to-right and top-to-bottom (see Figure 35b). Blue indicates that the velocity is high in both directions.

Figure B 5. Photograph of forged Ti-6Al-4V segment D2, etched to reveal the forging flow lines.

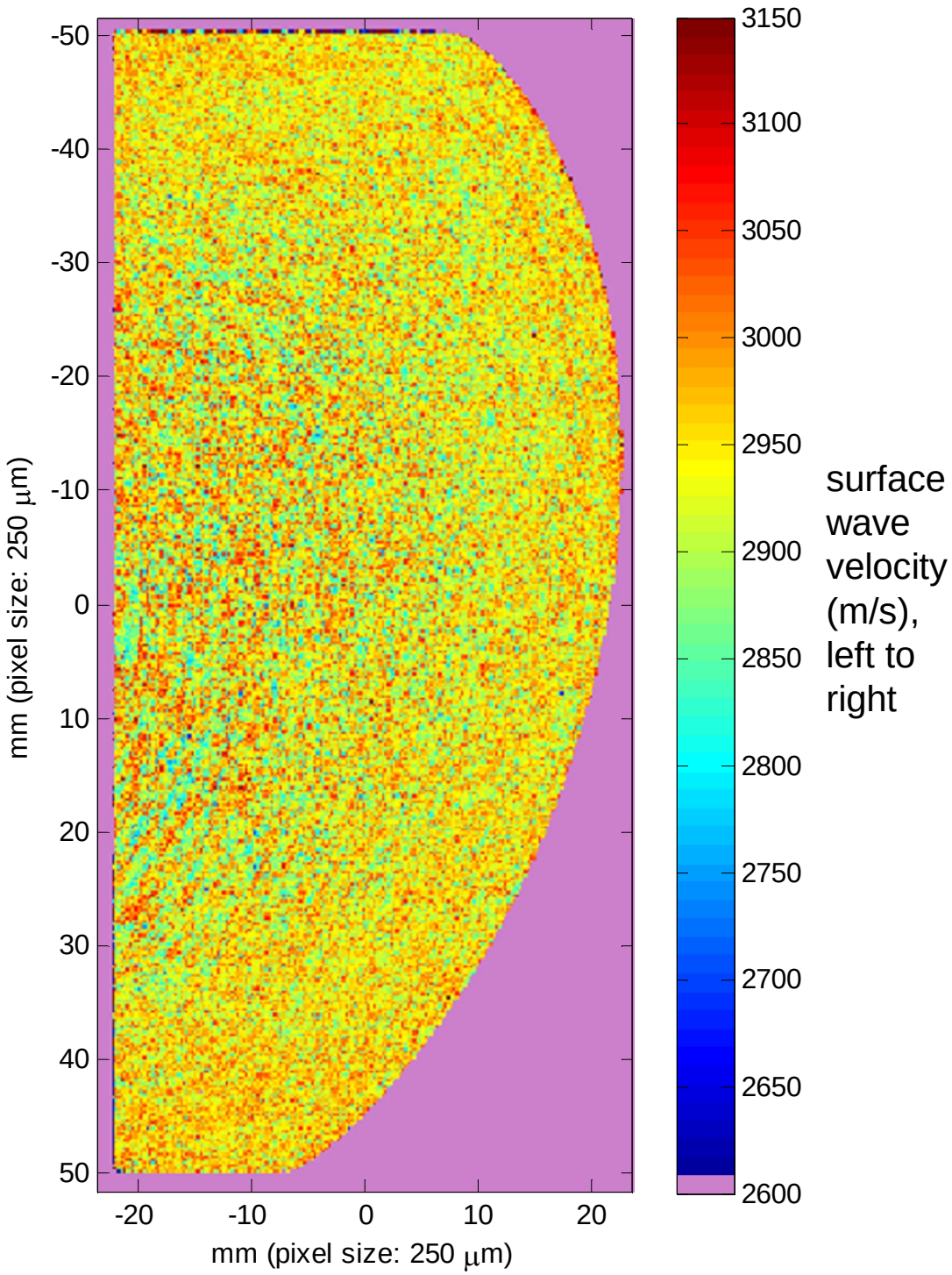

Figure B 6. Surface wave velocity map of slice through forged Ti-6Al-4V segment D2, obtained using optical-scanning acoustic microscope (O-SAM) at University of Nottingham [54]. The surface wave velocity was measured left-to-right over a length of 250μm with a pixel size of 250μm.

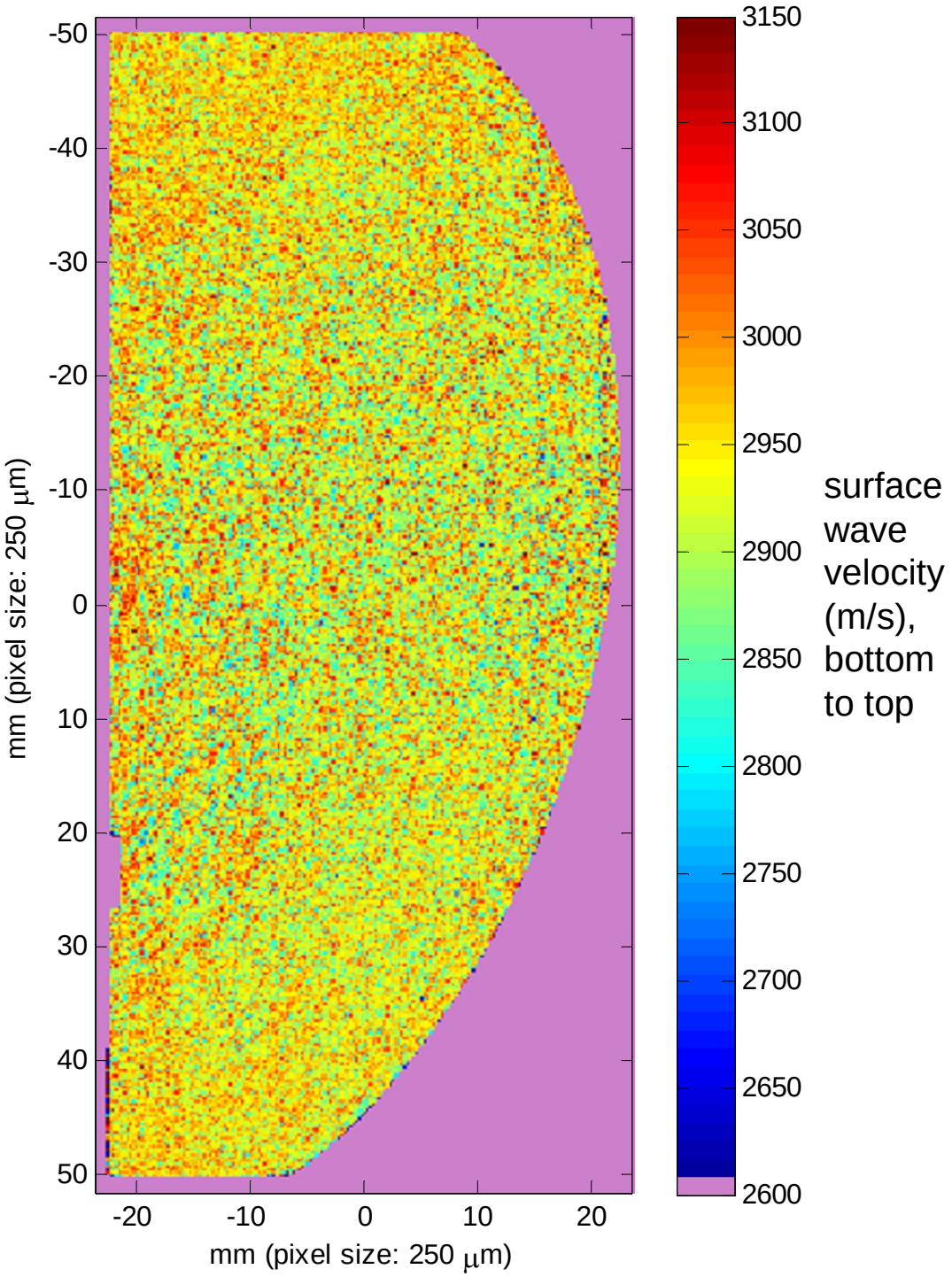

Figure B 7. Surface wave velocity map of slice through forged Ti-6Al-4V segment D2, obtained using optical-scanning acoustic microscope (O-SAM) at University of Nottingham [54]. The surface wave velocity was measured bottom-to-top over a length of 250μm with a pixel size of 250μm.

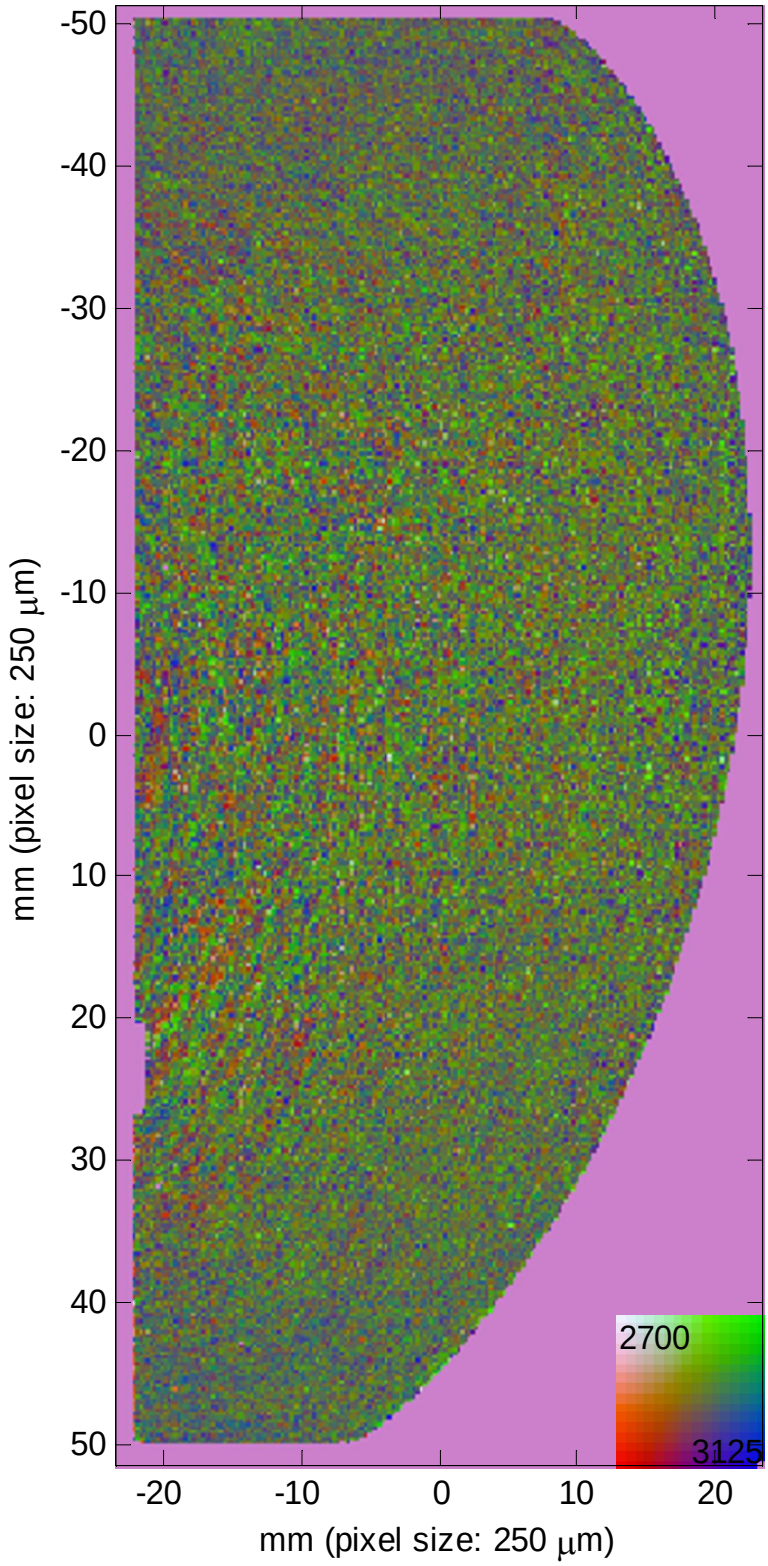

Figure B 8. Surface wave vector velocity map of slice through forged Ti-6Al-4V segment D2, obtained using optical-scanning acoustic microscope (O-SAM) at University of Nottingham [54], made by combining Figure B 6 and Figure B 7. The 2D colour map (top left) shows the surface wave velocity in two directions: left-to-right and top-to-bottom (see Figure 35b). Blue indicates that the velocity is high in both directions.

Figure B 9. Photograph of forged Ti-6Al-4V segment J, etched to reveal the forging flow lines.

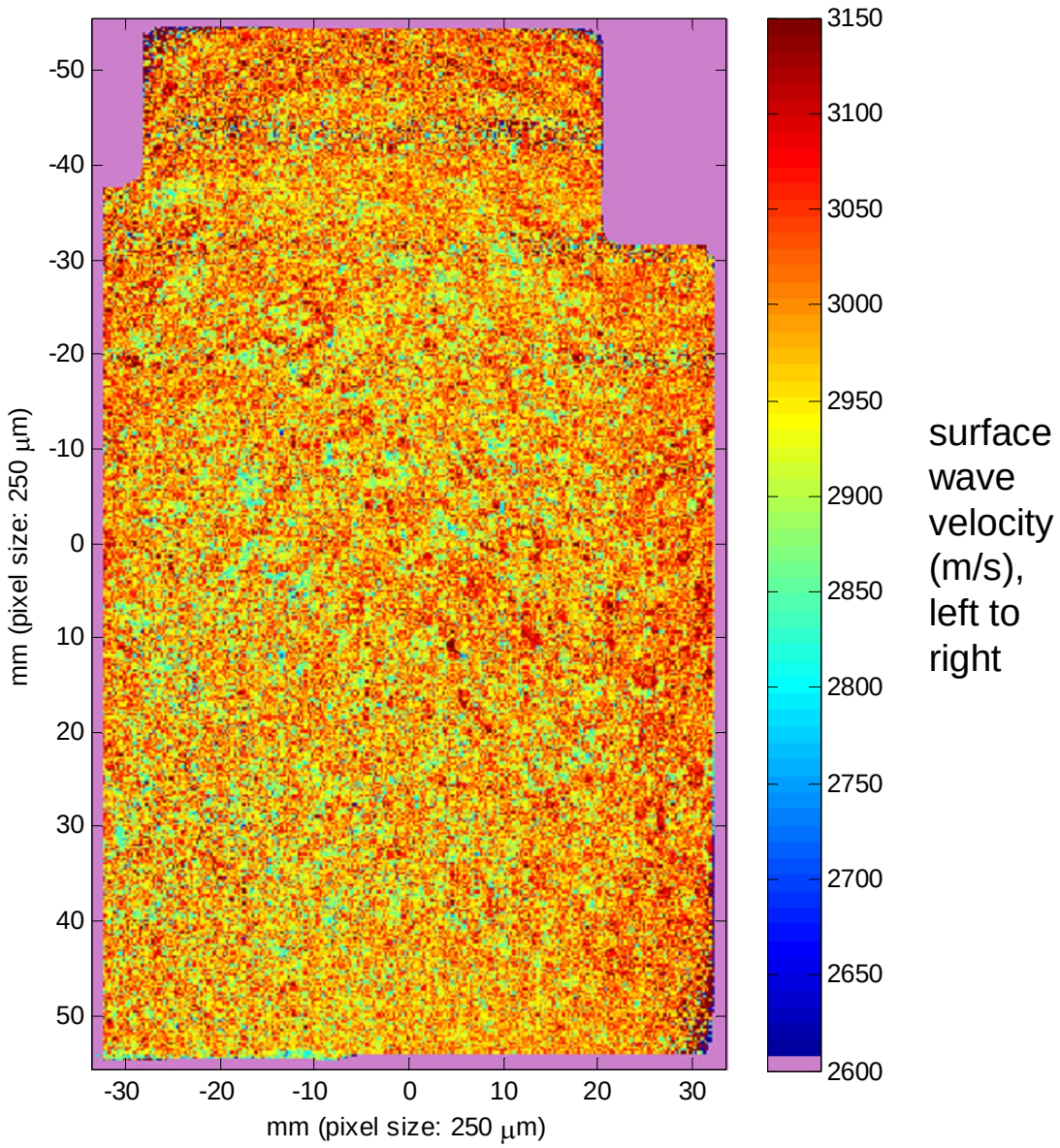

Figure B 10. Surface wave velocity map of slice through forged Ti-6Al-4V segment J, obtained using optical-scanning acoustic microscope (O-SAM) at University of Nottingham [54]. The surface wave velocity was measured left-to-right over a length of 250μm with a pixel size of 250μm.

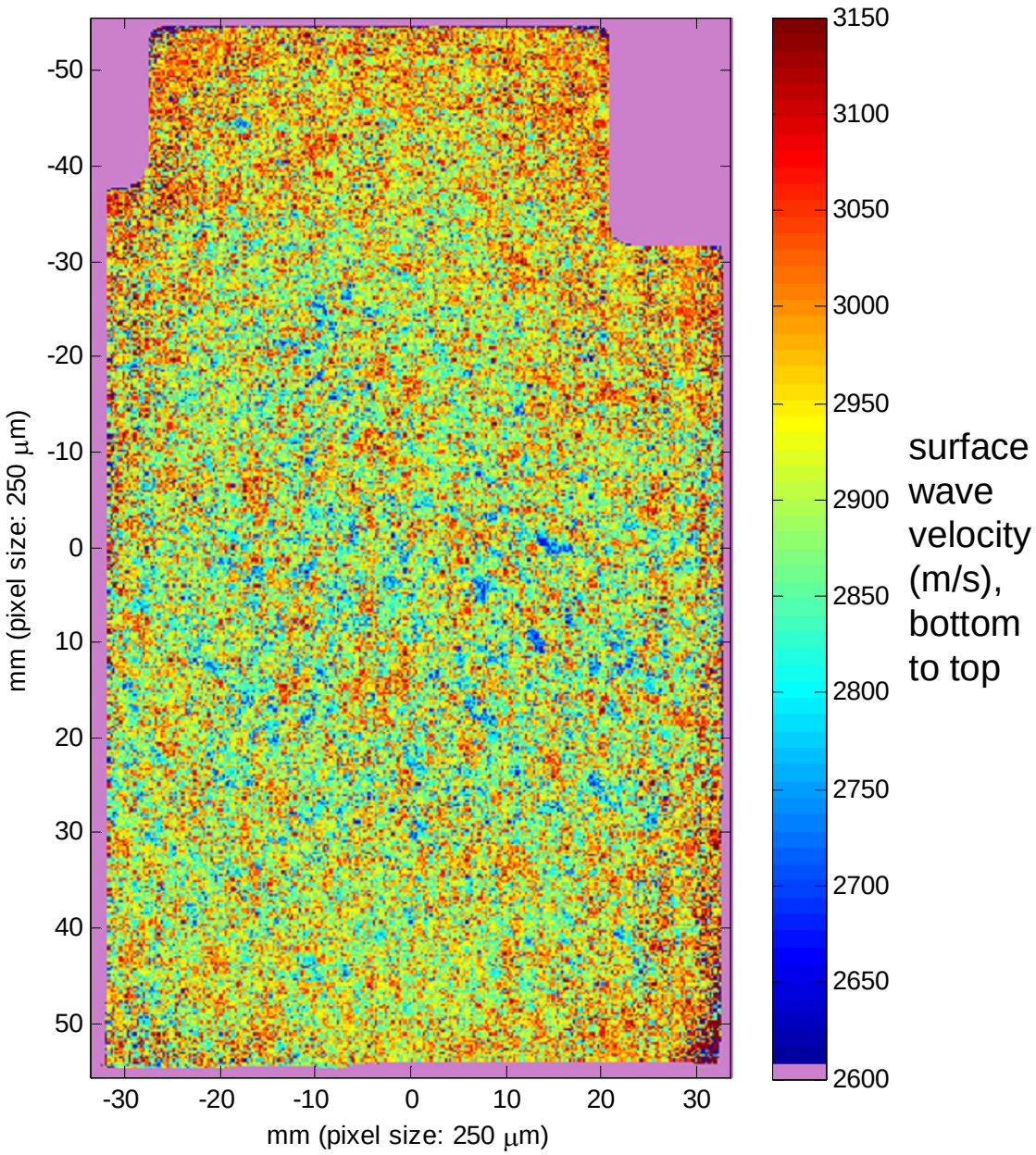

Figure B 11. Surface wave velocity map of slice through forged Ti-6Al-4V segment J, obtained using optical-scanning acoustic microscope (O-SAM) at University of Nottingham [54]. The surface wave velocity was measured bottom-to-top over a length of 250μm with a pixel size of 250μm.

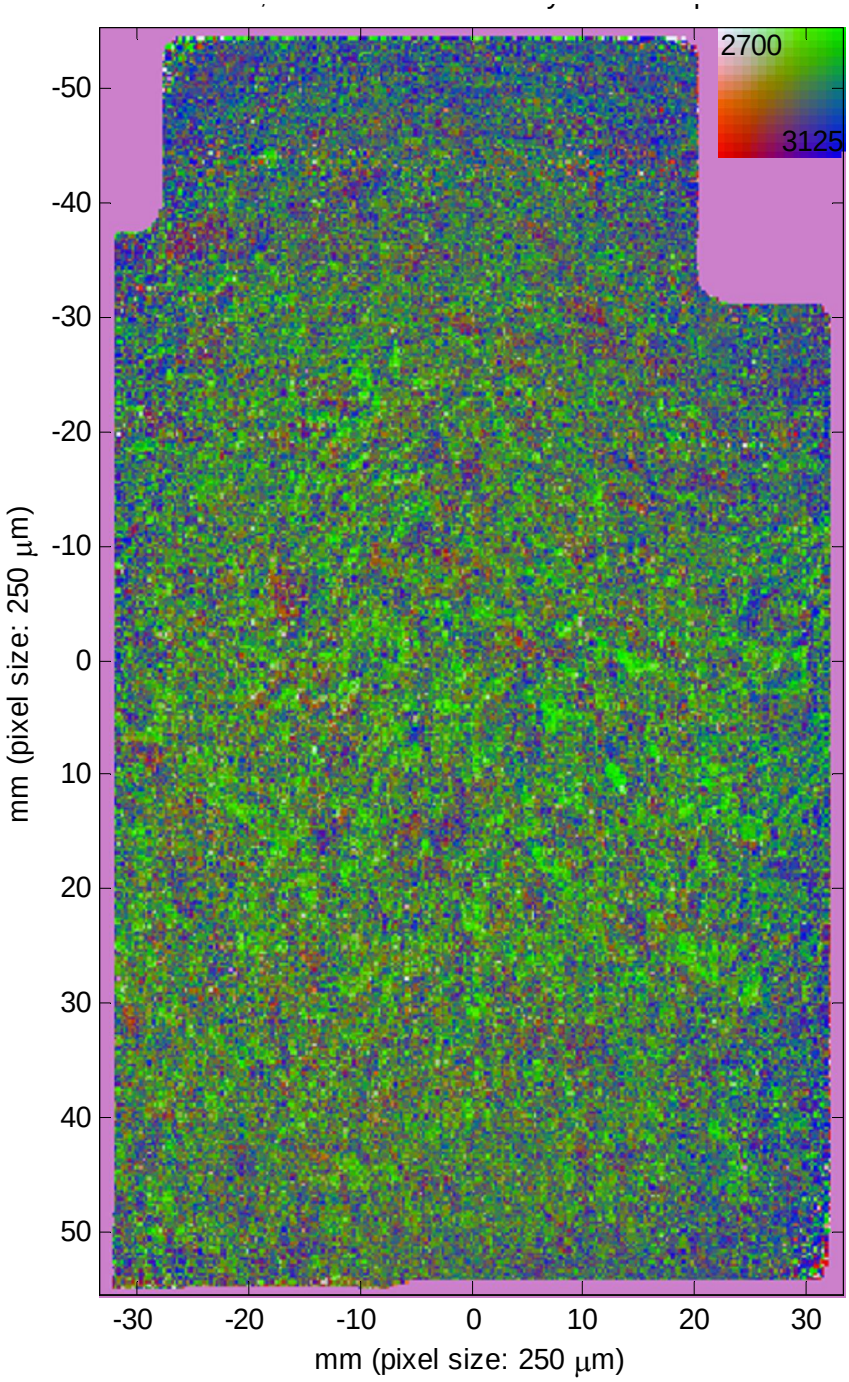

Figure B 12. Surface wave vector velocity map of slice through forged Ti-6Al-4V segment J, obtained using optical-scanning acoustic microscope (O-SAM) at University of Nottingham [54], made by combining Figure B 10 and Figure B 11. The 2D colour map (top left) shows the surface wave velocity in two directions: left-to-right and top-to-bottom (see Figure 35b). Blue indicates that the velocity is high in both directions.

Figure B 13. Photograph of forged Ti-6Al-4V segment M, etched to reveal the forging flow lines.

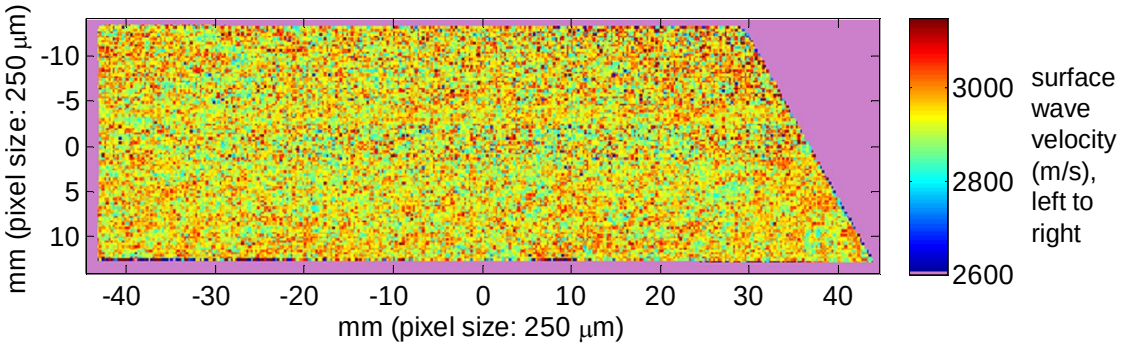

Figure B 14. Surface wave velocity map of slice through forged Ti-6Al-4V segment M, obtained using optical-scanning acoustic microscope (O-SAM) at University of Nottingham [54]. The surface wave velocity was measured left-to-right over a length of 250μm with a pixel size of 250μm.

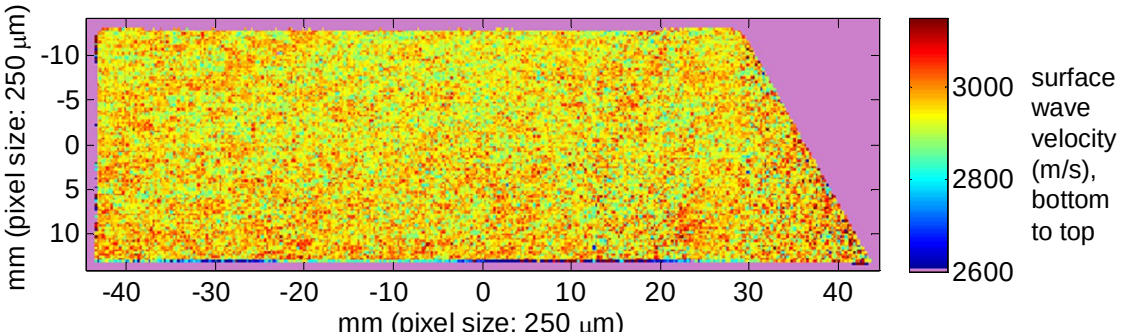

Figure B 15. Surface wave velocity map of slice through forged Ti-6Al-4V segment M, obtained using optical-scanning acoustic microscope (O-SAM) at University of Nottingham [54]. The surface wave velocity was measured bottom-to-top over a length of 250μm with a pixel size of 250μm.

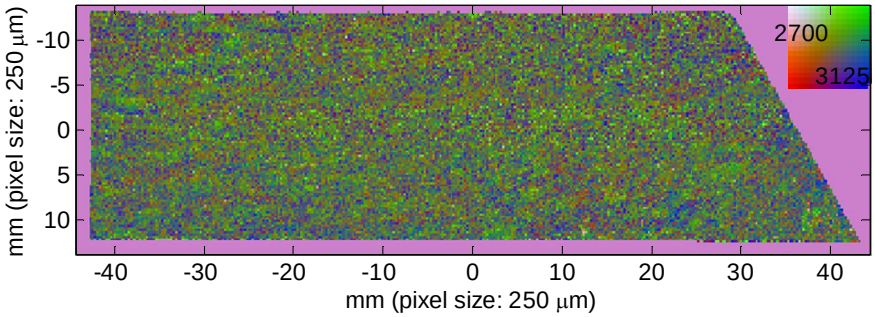

Figure B 16. Surface wave vector velocity map of slice through forged Ti-6Al-4V segment M, obtained using optical-scanning acoustic microscope (O-SAM) at University of Nottingham [54], made by combining Figure B 14 and Figure B 15. The 2D colour map (top left) shows the surface wave velocity in two directions: left-to-right and top-to-bottom (see Figure 35b). Blue indicates that the velocity is high in both directions.

Figure B 17. Photograph of forged Ti-6Al-4V segment N, etched to reveal the forging flow lines.

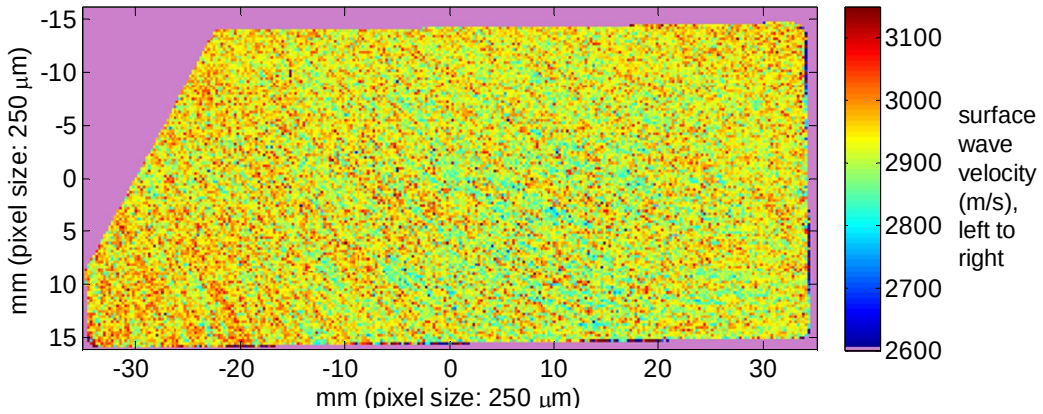

Figure B 18. Surface wave velocity map of slice through forged Ti-6Al-4V segment N, obtained using optical-scanning acoustic microscope (O-SAM) at University of Nottingham [54]. The surface wave velocity was measured left-to-right over a length of 250μm with a pixel size of 250μm.

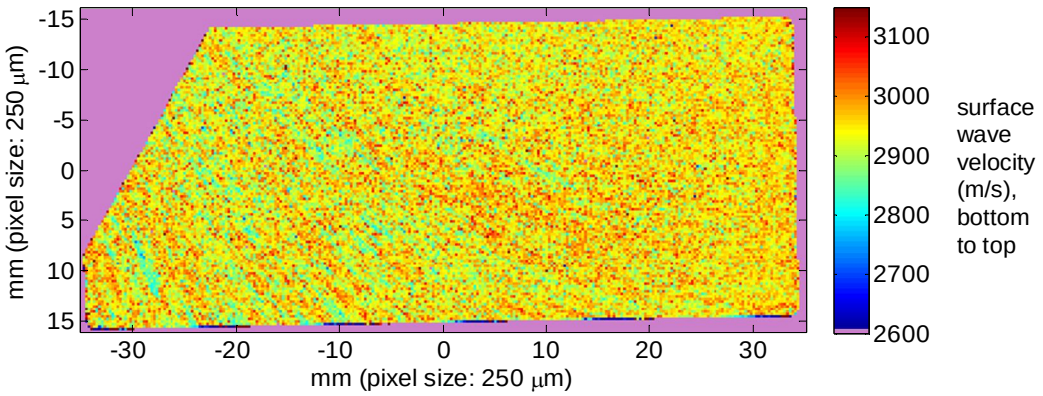

Figure B 19. Surface wave velocity map of slice through forged Ti-6Al-4V segment N, obtained using optical-scanning acoustic microscope (O-SAM) at University of Nottingham [54]. The surface wave velocity was measured bottom-to-top over a length of 250μm with a pixel size of 250μm.

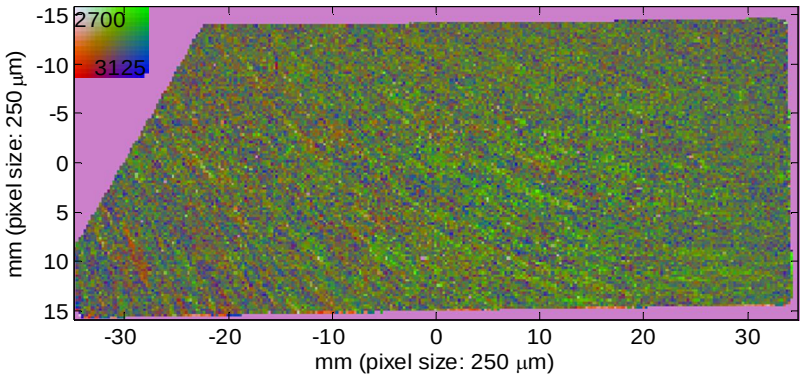

Figure B 20. Surface wave vector velocity map of slice through forged Ti-6Al-4V segment N, obtained using optical-scanning acoustic microscope (O-SAM) at University of Nottingham [54], made by combining Figure B 18 and Figure B 19. The 2D colour map (top left) shows the surface wave velocity in two directions: left-to-right and top-to-bottom (see Figure 35b). Blue indicates that the velocity is high in both directions.

Appendix C - Ultrasonic Probe Characterisation

The samples were ultrasonically scanned in pulse-echo immersion with a nominally 10MHz 8”F 0.75” diameter probe. The actual frequency content and focal length of the probe were determined. The beam diameter at the focal plane was measured. A distance amplitude correction curve was constructed. These measurements are necessary for the ultrasonic inspections described in this report.

C.1. Centre frequency and percentage bandwidth

The centre frequency of the probe was determined by capturing the reflection from the front wall of a glass block. The signal was gated and the frequency for which the ultrasonic amplitude was highest was measured in the frequency domain. The centre frequency was 10.9MHz. The percentage bandwidth was 58%.

C.2. Focal length

The nominal focal length of the probe was 8”. The actual focal length of the probe in water was found using a 0.25mm diameter ball target. The probe was positioned at a distance greater than 8” from the ball target and moved laterally to maximise the reflection. The amplitude of the signal reflected from the ball target was measured against water path. The focal length was taken to be the water path for which the reflected amplitude was highest. It was found to be 6.3”, considerably shorter than the quoted value.

The diffusion bonded samples were inspected with the probe focussed at the bond line depth (Section 4.4). The average longitudinal wave velocity of the titanium reference blocks in the thickness direction is 6214m/s (see Section 4.2.2). To focus at the bond line depth (19mm), a water path of 79mm was used.

C.3. Beam diameter

The ultrasonic beam diameter was measured on a 0.025" diameter flat-bottomed hole in a stainless steel calibration block. The acoustic velocity of titanium is higher than that of stainless steel. For the same water path (79mm), the focal plane in stainless steel will be at a depth of 20.5mm, assuming a velocity of 5770m/s [109]. A standard calibration block containing a 0.8" deep (20.3mm deep) flat-bottomed hole was used. With the transducer normal to the surface of the block and at the chosen water path, the transducer is moved laterally so that amplitude of the flat-bottomed hole reflection is maximised. The transducer is translated first to the right and then to the left until the reflected amplitude decreases by 6dB. The separation of these two points was 1.20mm. The beam diameter at the focal spot is limited by diffraction (Equation 1.2) and is directly proportional to the wavelength. The ratio of wavelength in titanium to stainless steel is given by the ratio of the acoustic velocities (6214m/s divided by 5770m/s). The beam diameter at the focal depth in titanium is expected to be 1.29mm.

C.4. Distance amplitude correction (DAC)

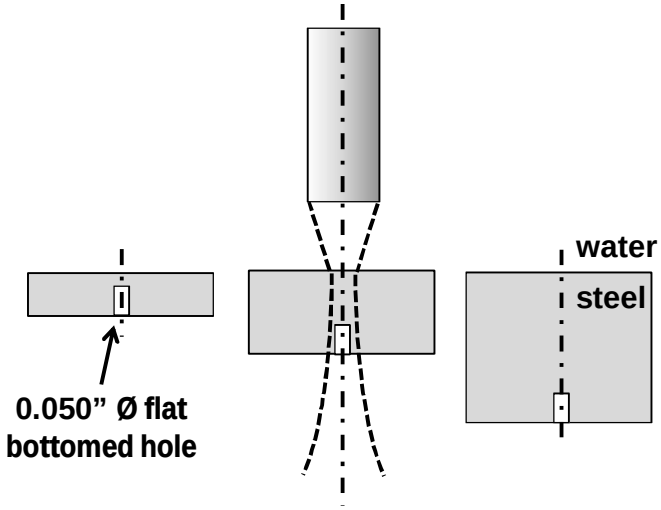

Figure C 1. Distance amplitude curves are constructed by measuring the reflection amplitude from 0.050” flat bottomed holes at different depths in a series of stainless steel calibration blocks. The water path between the probe and the calibration blocks is kept constant.

The amplitude of 0.050” diameter flat-bottomed holes at a range of depths in stainless steel calibration blocks was measured for the chosen inspection probe and water path, as illustrated in Figure C 1. The result is plotted in Figure C 2. This curve can be used to correct the signal amplitude over the same depth range, as described in Section 2.3.

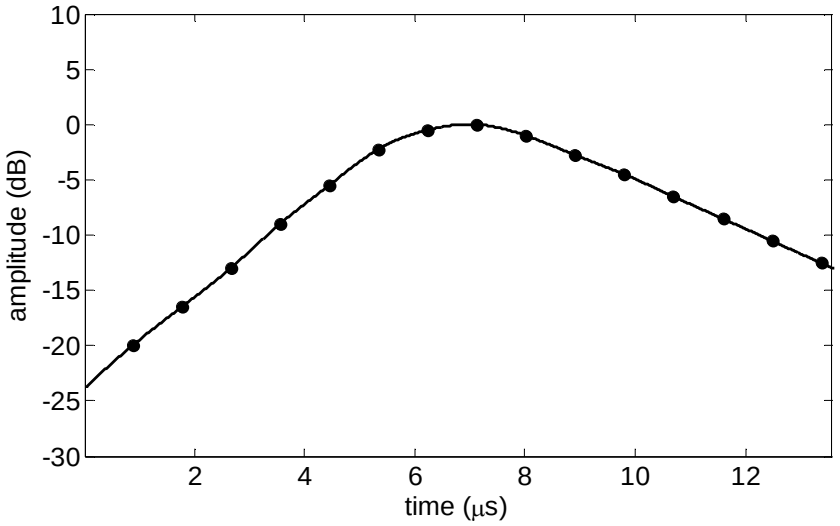

Figure C 2. Distance amplitude curve for 0.050” diameter flat-bottomed holes at a range of time of flight / depth in stainless steel. 0dB is the reflection amplitude for a 20.3mm deep 0.050” diameter flat-bottomed hole.

APPENDIX D – Calculation of Most Probable Chord Length

The partially bonded samples were sectioned as described in Section 4.5. Assume that if the section has cut through the void the distance between the midpoint of the section (chord) and the centre of the circle is somewhere between $y=-r$ and $y=r$. All distances could have occurred with equal probability. r is the radius of the circle.

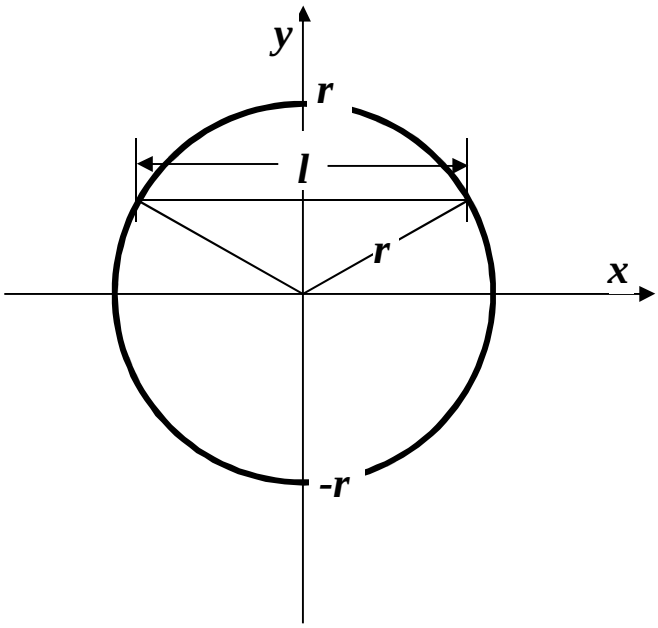

Figure D 1. Relation between most probable chord of length, l, and the diameter, $2r$.

$$\left(\frac{l}{2}\right)^2 = r^2 - y^2$$

$$\langle l \rangle = \frac{1}{2r}\int_{-r}^{r} 2\sqrt{r^2 - y^2}\,dy$$

Subsititue $y=r\sin u$, $dy=r\cos u\,du$:

$$\langle l \rangle = r\int_{-\pi/2}^{\pi/2} \cos^2 u\,du$$

Subst $\cos^2 u = 1/2(1+\cos 2u)$:

$$\langle l \rangle = \frac{r}{2}\int_{-\pi/2}^{\pi/2}(1 + \cos 2u)du$$

$$\langle l \rangle = \frac{\pi r}{2}$$

Appendix E – Ultrasonic Backscatter for Diffusion Bonded Samples

In this appendix, the maximum and root mean square of backscattered ultrasonic noise in the diffusion bonded samples is plotted against time of flight (a function of depth). The ultrasonic scan was carried out with a 10.9MHz 6.3" F 0.75" diameter with the probe focussed at diffusion bond depth. 0dB is the amplitude of the reflection from a 0.050" flat-bottomed hole at a depth of 20.3mm in stainless steel

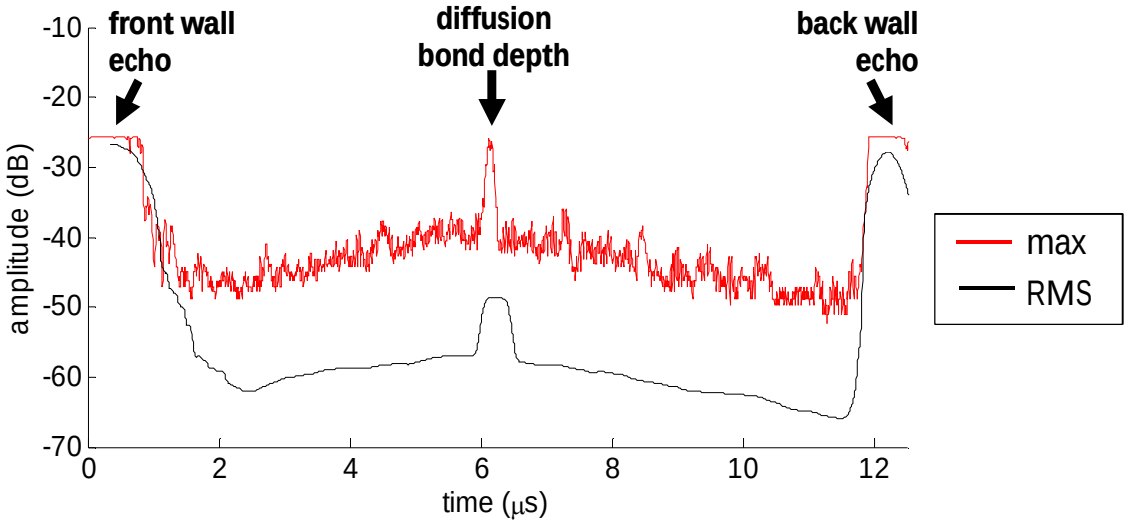

Figure E 1. Sample #1. Maximum and root mean square of backscattered ultrasonic noise vs. time of flight.

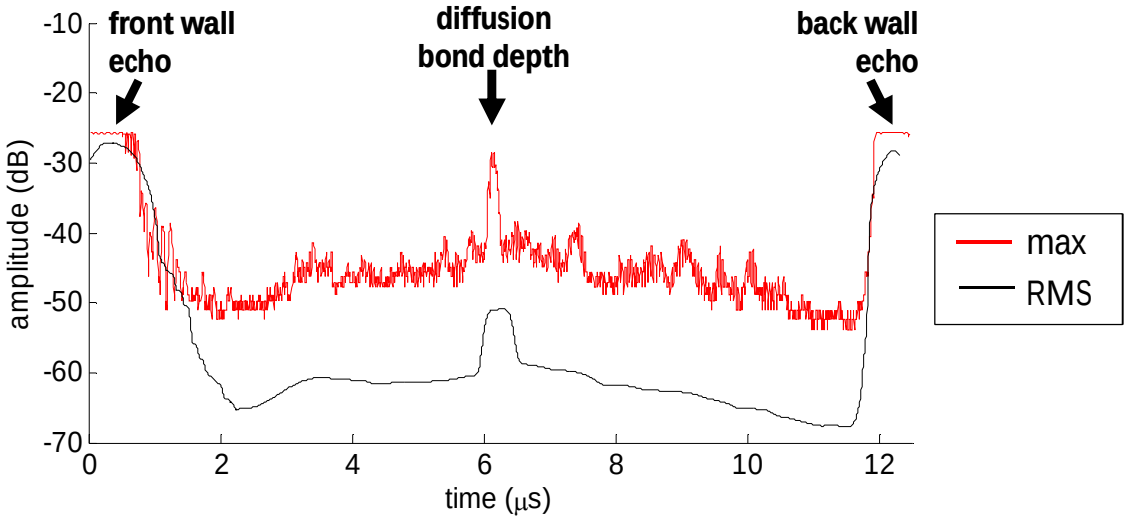

Figure E 2. Sample #2. Maximum and root mean square of backscattered ultrasonic noise vs. time of flight.

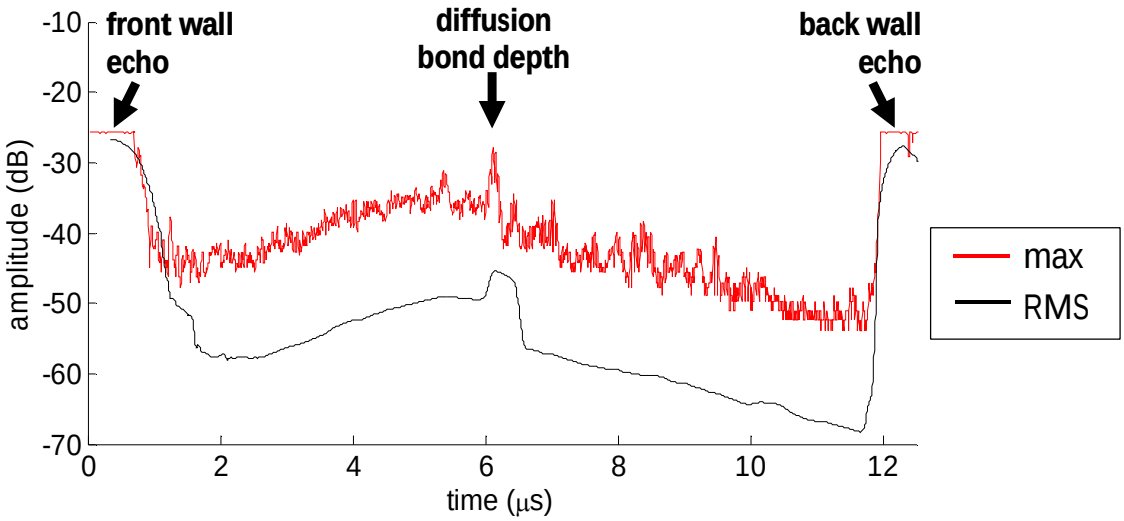

Figure E 3. Sample #3. Maximum and root mean square of backscattered ultrasonic noise vs. time of flight.

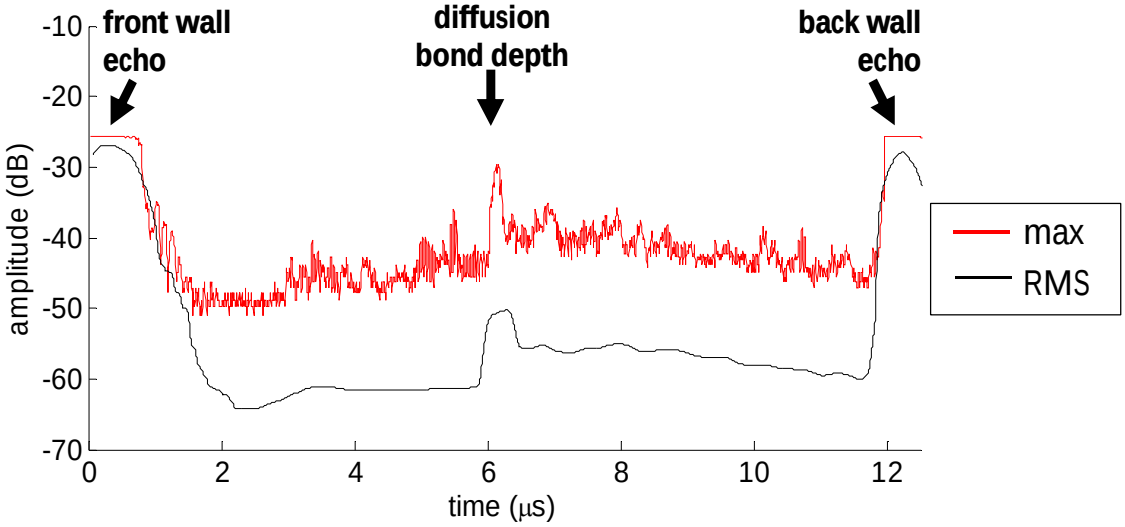

Figure E 4. Sample #4. Maximum and root mean square of backscattered ultrasonic noise vs. time of flight.

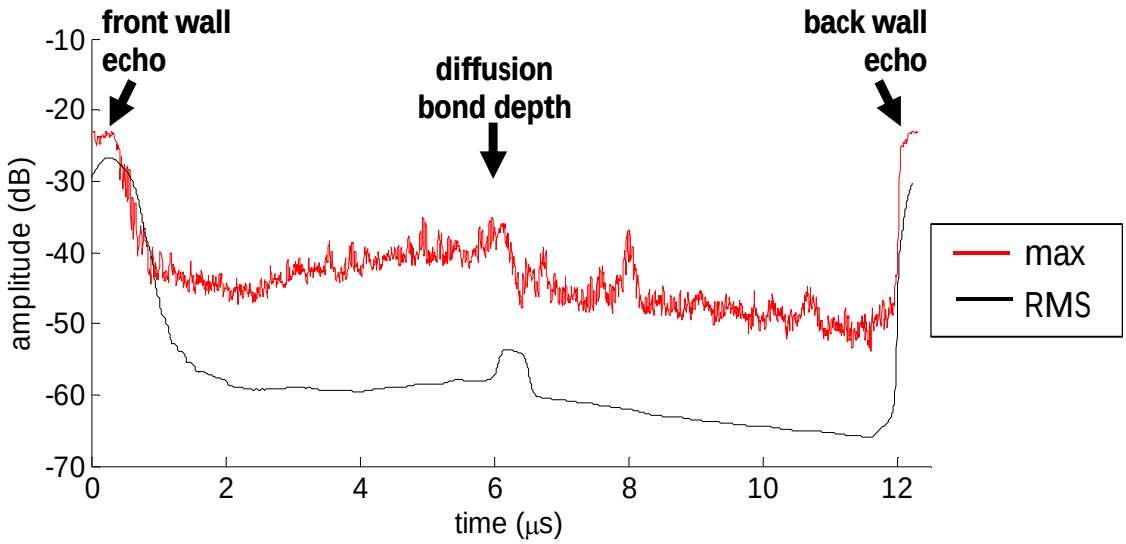

Figure E 5. Sample #5. Maximum and root mean square of backscattered ultrasonic noise vs. time of flight.

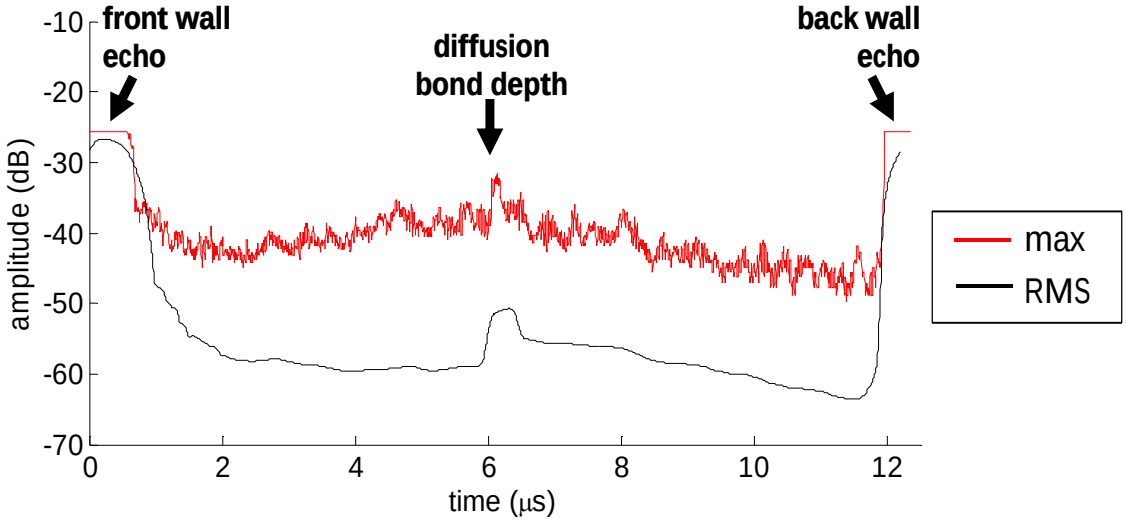

Figure E 6. Sample #6. Maximum and root mean square of backscattered ultrasonic noise vs. time of flight.

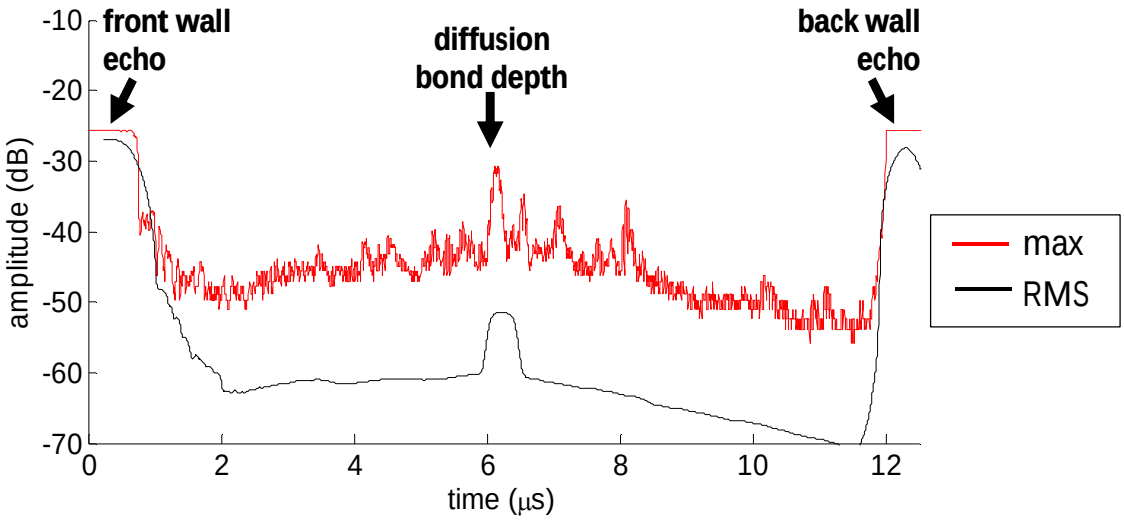

Figure E 7. Sample #7. Maximum and root mean square of backscattered ultrasonic noise vs. time of flight.

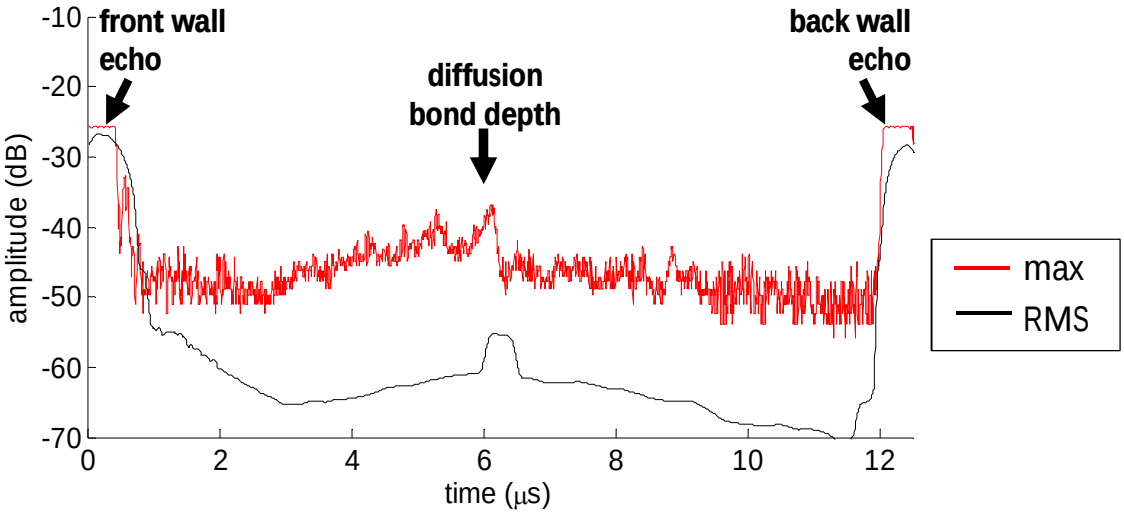

Figure E 8. Sample #8. Maximum and root mean square of backscattered ultrasonic noise vs. time of flight.

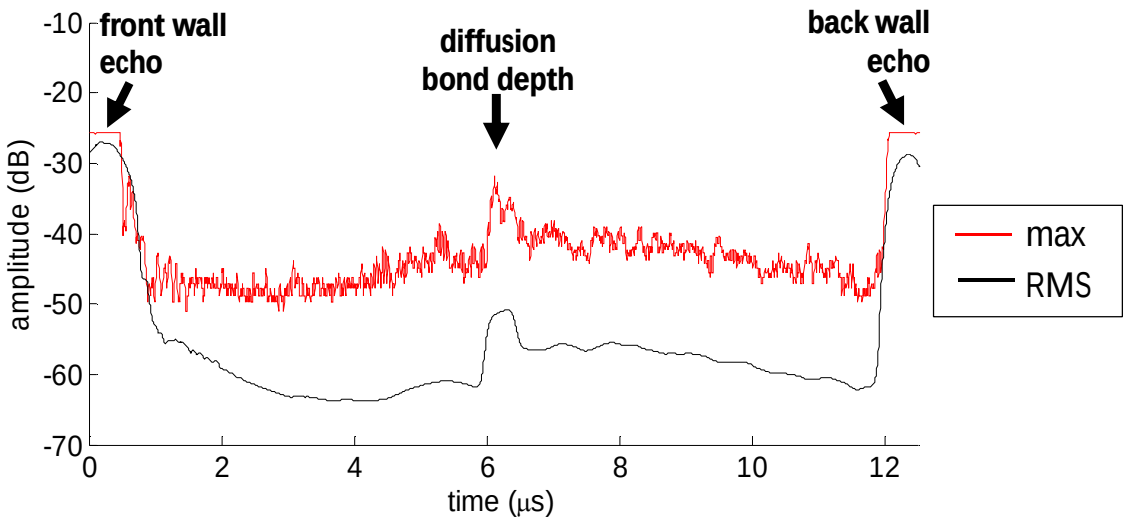

Figure E 9. Sample #9. Maximum and root mean square of backscattered ultrasonic noise vs. time of flight.

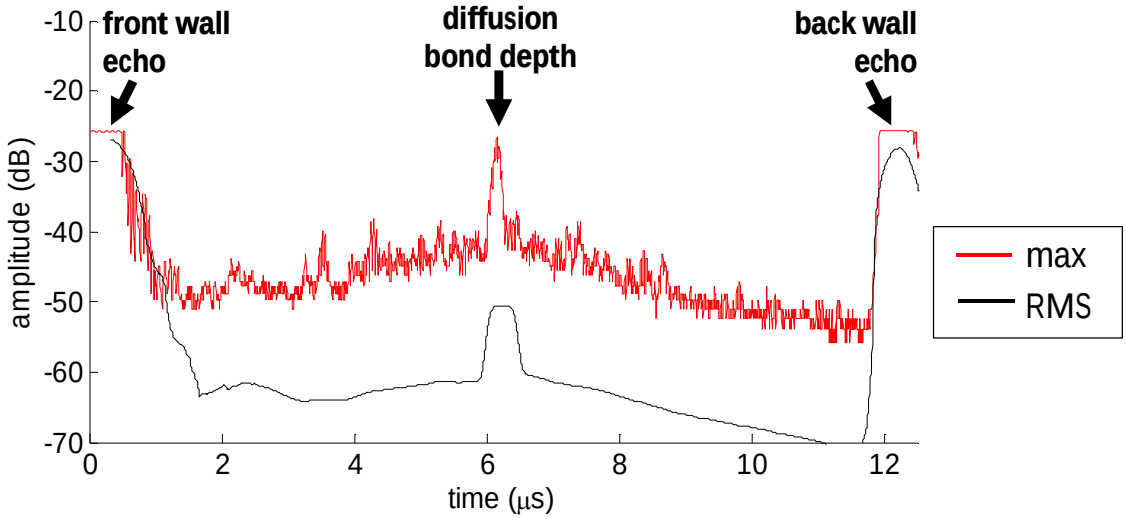

Figure E 10. Sample #10. Maximum and root mean square of backscattered ultrasonic noise vs. time of flight.

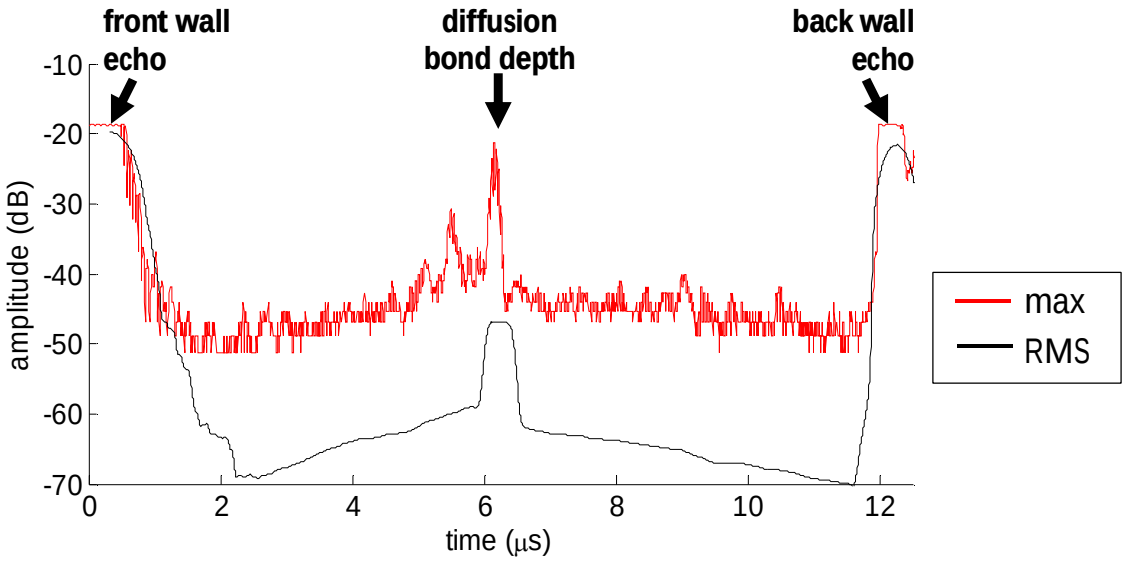

Figure E 11. Sample #11. Maximum and root mean square of backscattered ultrasonic noise vs. time of flight.

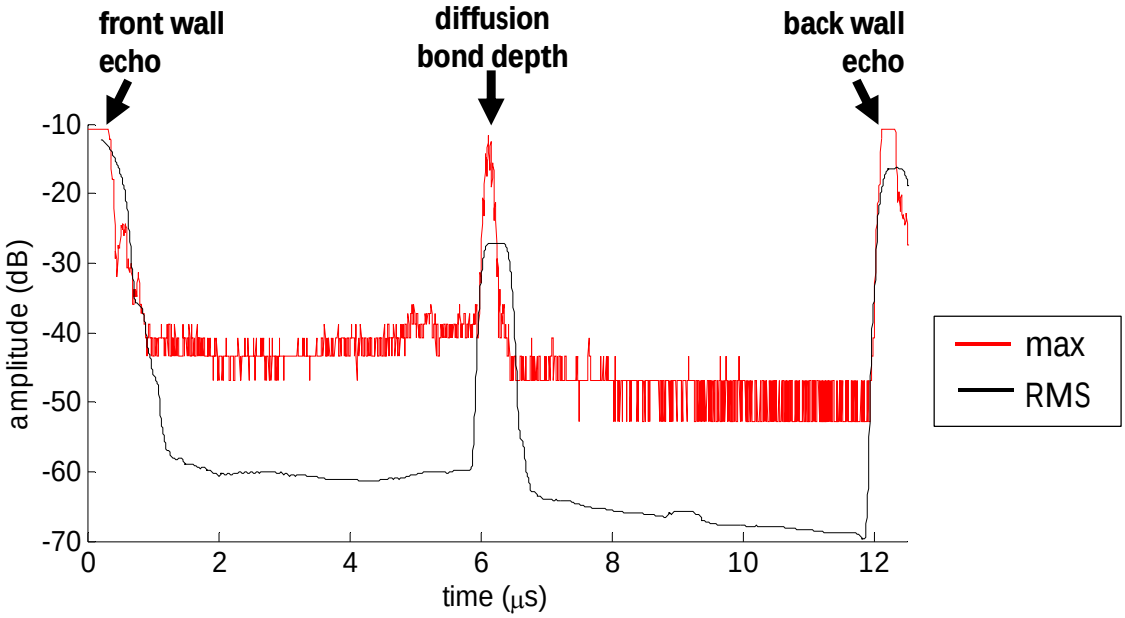

Figure E 12. Sample #12. Maximum and root mean square of backscattered ultrasonic noise vs. time of flight.

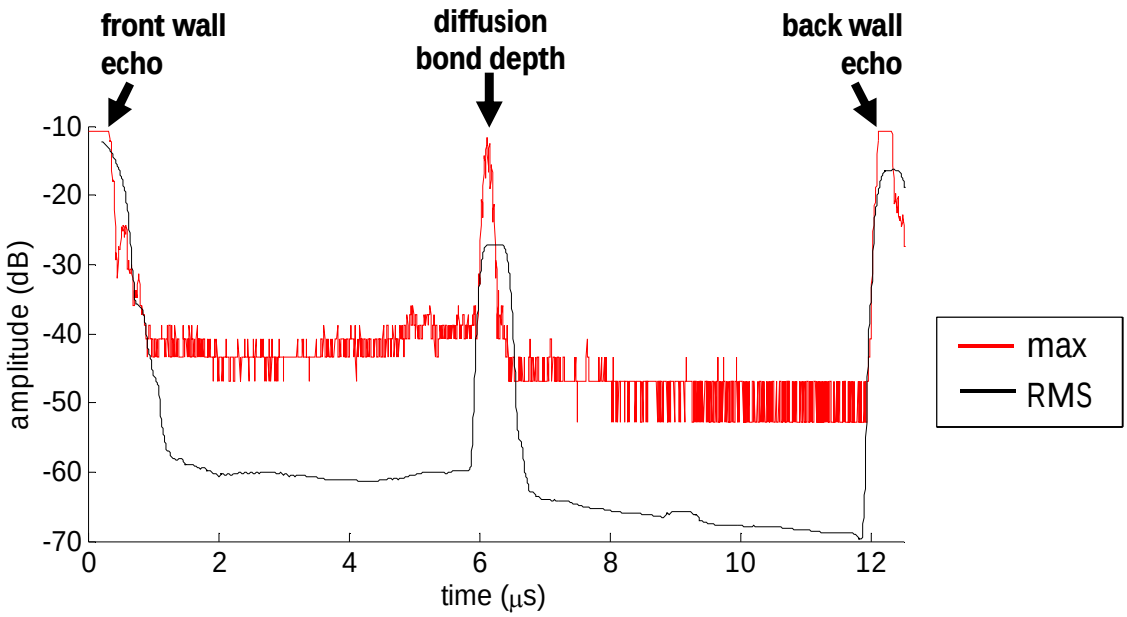

Figure E 13. Sample #13. Maximum and root mean square of backscattered ultrasonic noise vs. time of flight.

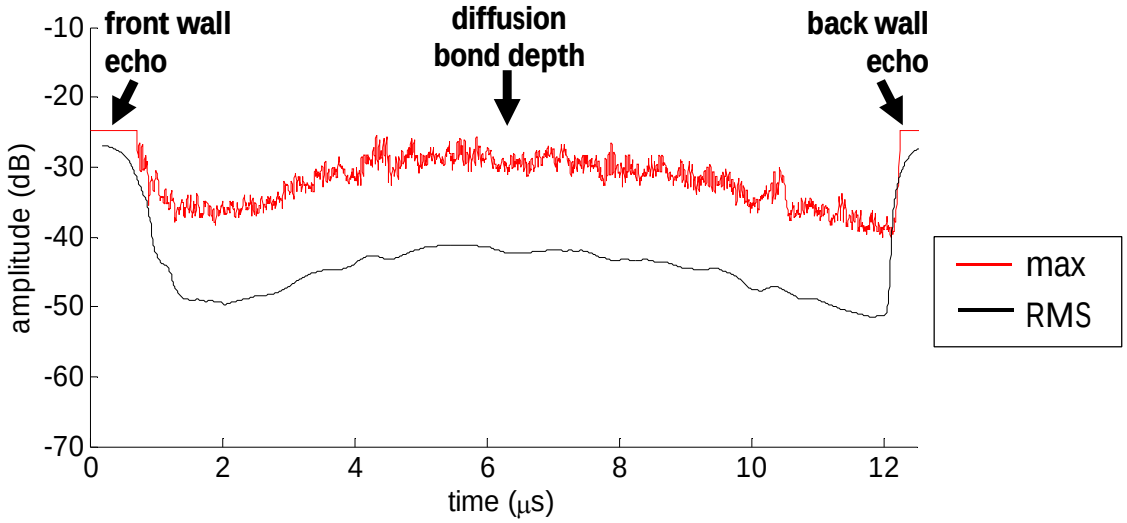

Figure E 14. Sample HUCK02. Maximum and root mean square of backscattered ultrasonic noise vs. time of flight.

Appendix F – Digital Image Correlation

Digital image correlation was used to align the ultrasonic C-scans captured by normal incidence inspection from both sides of the diffusion bond. Two full waveform data cubes had been captured. $A_{12}(t)$ was captured by scanning from the side with the pipe stub. $A_{21}(t)$ was captured by scanning from the opposite side. The maximum absolute amplitude over a 0.48μs gate, centred at the diffusion bond depth, is taken at each position for both data cubes to create two C-scans (images for which each pixel is the amplitude at that position): A_{12} and A_{21}. First, A_{21} is mirrored so that the images appear in the same orientation, as shown in Figure F 1.

Image A_{12} is padded with zeros on all four sides, as shown in Figure F 2, to allow for the situation where the central element of A_{21} is positioned over the corner element of A_{12}. Image A_{21} is shifted incrementally in the x and y directions across padded A_{12}.

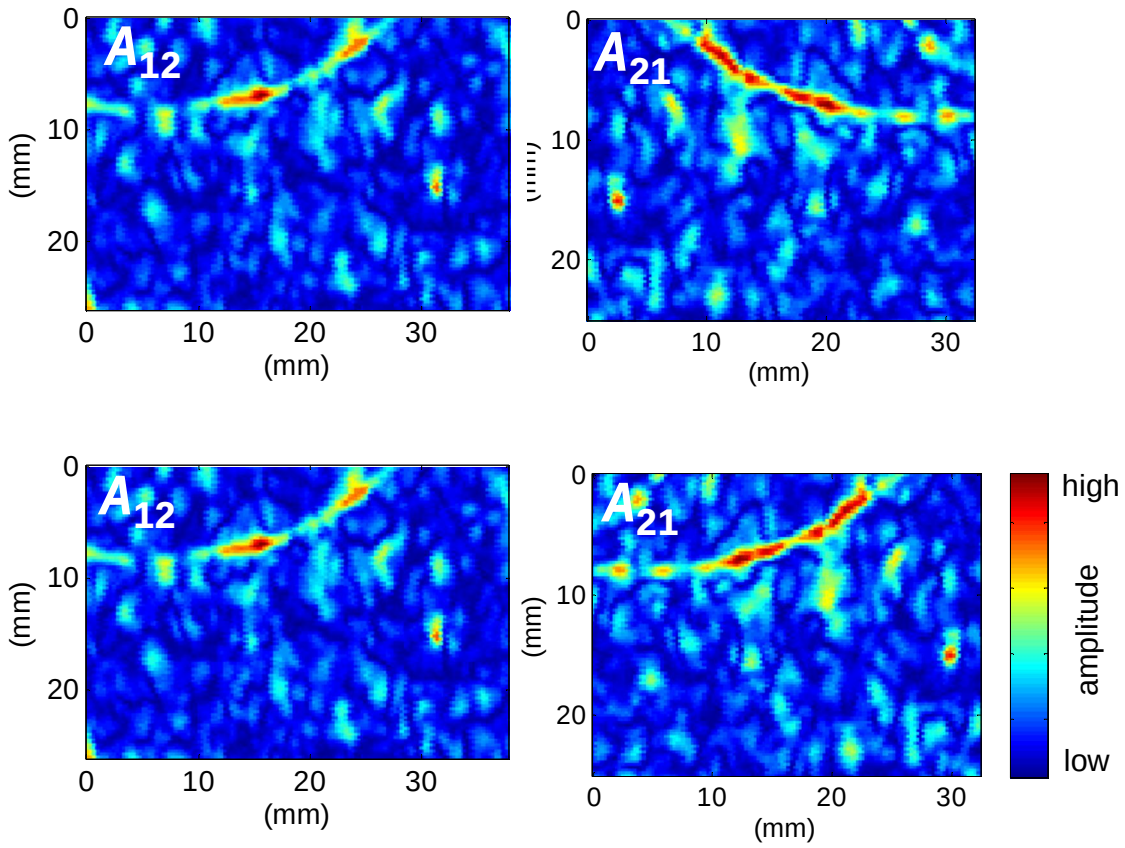

Figure F 1. Ultrasonic C-scans are captured from two directions – A_{12} and A_{21}. A_{21} is mirrored to allow digital image correlation. The colour bar is linear and indicates signal amplitude.

For each position [x,y] of the origin of A_{21} [r=0,s=0] relative to the origin of A_{12} [x=0,y=0], a normalised cross-correlation is calculated using the following equation [110]:

$$\gamma = \frac{\sum_r \sum_s [A_{21}(r,s) - \overline{A_{21}}] \sum_r \sum_s [A_{12}(x+r,y+s) - \overline{A_{12}}(x+r,y+s)]}{\{\sum_r \sum_s [A_{21}(r,s) - \overline{A_{21}}]^2 \sum_r \sum_s [A_{12}(x+r,y+s) - \overline{A_{12}}(x+r,y+s)]^2\}^{\frac{1}{2}}} \quad \text{(F.1)}$$

If the A_{12} and A_{21} are identical over the area of comparison then γ=1. Image A_{21} is then rotated by angle θ and the process is repeated. The position [x,y] and rotation θ for which the correlation coefficient is highest gives the best achievable alignment of the two images. The accuracy of the alignment is limited by the scan pitch (0.25mm) and the increment in rotation θ (0.1° increments were used). Finally, images A_{12} and A_{21} are cropped so that the same areas are present in both.

The alignment is checked by eye. The aligned images A_{12} and A_{21} for sample #10 are shown in Figure F 3.

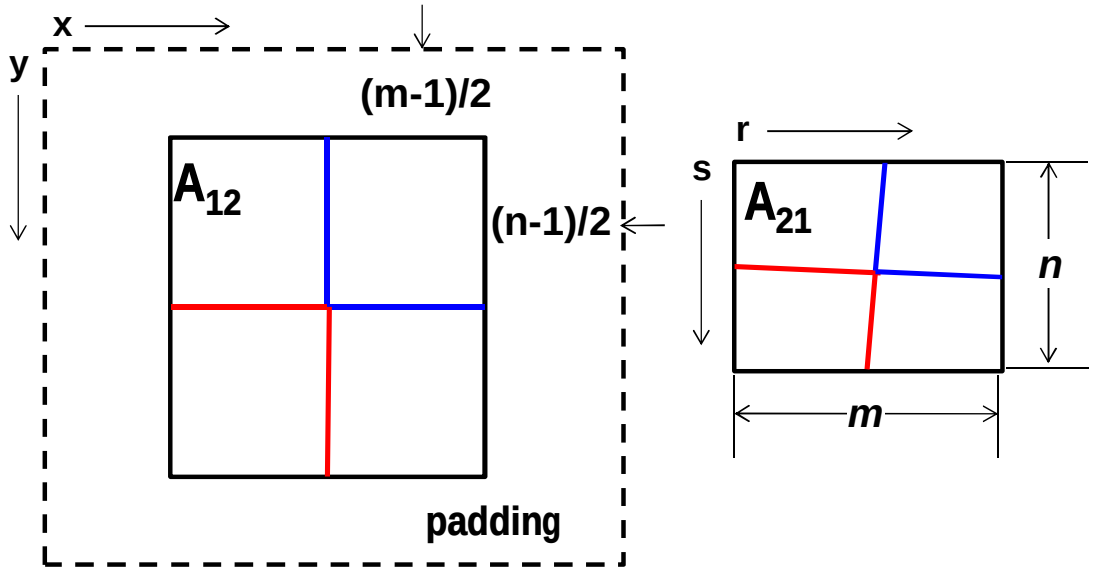

Figure F 2. Image A_{12} is padded so that the central element of A_{21} can be shifted over the origin of A_{12}.

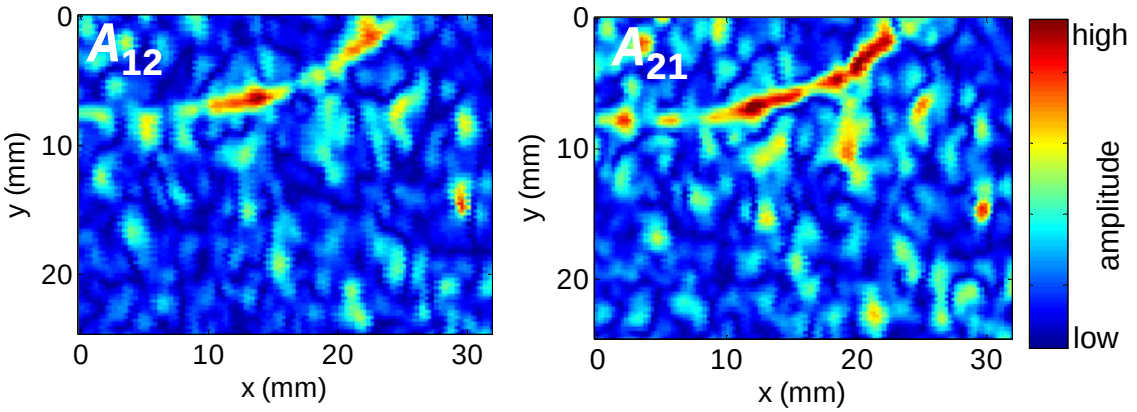

Figure F 3. Aligned C-scans – A_{12} and A_{21}.

For each slice of the full waveform data $A_{21}(t)$, the same lateral shift and rotation is applied. Both full waveform data cubes, $A_{21}(t)$ and $A_{12}(t)$, are cropped. The result is two data cubes for the same area of the diffusion bond, one for inspection from each side.

Appendix G. List of Figures

List of Tables

REFERENCES

1. Ohsumi, M., Kiyotou, S., Sakamoto, M., The application of diffusion welding to aircraft titanium alloys. In *Transactions of the iron and steel institute of Japan*, **25**, pages 513-520, 1985.
2. Doorbar, P., Dixon. M., Chatterjee, A., Aero-engine titanium from alloys to composites. In *Fourth International Light Metals Technology Conference*, Gold Coast, Australia, pages 127-134, 2009.
3. *Rationalised Process Specification 705 - Ultrasonic inspection of disc forms*, Rolls-Royce plc, 1997.
4. Leachman, S., *Material noise levels in titanium forgings compared to flat bottom hole reference standards*, K. Milne, Editor, Rolls-Royce plc, NDE, 2010.
5. Ojard, G.C., Buck, O., Rehbein, D.K., Bond strength evaluation in dissimilar materials. In *Review of Progress in Quantitative NonDestructive Evaluation*, Plenum Press, New York, **10B**, pages 1383-1390, 1991.
6. Nieters, E.J., Gigliotti, M.F.X., Perocchi, L.C., Gilmore, R.S., Ultrasonic evaluation of titanium alloy diffusion bonding. In *Review of Progress in Quantitative NonDestructive Evaluation*, Plenum Press, New York, **15**, pages 1313-1320, 1996.
7. Barnard, D.J., Dace, G.E., Rehbein, D.K., Buck, O., Acoustic harmonic generation at diffusion bonds, *Journal of Nondestructive Evaluation*, **16**(2), 77-89, 1997.
8. Thomas, G.H., Spingarn, J.R., Ultrasonic model for solid state weld evaluation. In *Review of Progress in Quantitative NonDestructive Evaluation*, Plenum Press, New York, **8B**, pages 1941-1948, 1988.
9. Walte, F., On the feasibility of ultrasonic NDE to estimate the bond quality of diffusion-welded joints, *Journal of Nondestructive Evaluation*, **7**(3/4), 175-189, 1988.
10. Thomas, G.H., Spingarn, J.R., Ultrasonic non-destructive evaluation of solid state welds. In *Review of Progress in Quantitative NonDestructive Evaluation*, Plenum Press, New York, **7B**, pages 1319-1325, 1988.
11. Twigg, S., *Private Communication*, Rolls-Royce plc, 2007.
12. Palmer, D.D., Rehbein, D.K., Smith, J.F., Buck, O., Nondestructive characterization of the mechanical strength of diffusion bonds. I. Experimental results, *Journal of Nondestructive Evaluation*, **7**(3/4), 153-166, 1988.

13. Palmer, D.D., Roberts, C.D., Rehbein, D.K., Smith, J.F., Buck, O., Strength and ultrasonic characterization of metallic interfaces. In *Review of Progress in Quantitative NonDestructive Evaluation*, Plenum Press, New York, **7B**, pages 1335-1342, 1988.
14. Margetan, F.J., Thompson, R.B., Rose, J.H., Gray, T.A., The interaction of ultrasound with imperfect interfaces: experimental studies of model structures, *Journal of Nondestructive Evaluation*, **11**(3/4), 109-126, 1992.
15. Yamada, R., Kawashima, K., Murase, M., Application of nonlinear ultrasonic measurement for quality assurance of diffusion bonds of gamma titanium aluminum alloy and steel, *Research in Nondestructive Evaluation*, **17**, 223-239, 2006.
16. Margetan, F.J., Gigliotti, M., Brasche, L., Leach, W., Fundamental studies: inspection properties for engine titanium alloys, DOT/FAA/AR-02/114, FAA, 2002.
17. ASNT, *Nondestructive testing handbook - ultrasonic testing*, Vol. 7, American Society for Metals, 1982.
18. Lutjering, G., Williams, J.C., *Titanium*, Springer-Verlag, Berlin Heidelberg, 2003.
19. Lutjering, G., Influence of processing on microstructure and mechanical properties ($\alpha+\beta$) titanium alloys, *Materials Science and Engineering*, **A243**, 32-45, 1998.
20. Brun, M., Anoshkin., N., Shakhanova, G., Physical processes and regimes of thermomechanical processing controlling development of regulated structure in the $\alpha + \beta$ titanium alloys, *Materials Science and Engineering*, **A243**, 77-81, 1998.
21. Rugg, D., Dixon, M., Dunne, F.P.E., Effective structural unit size in titanium alloys, *Journal of Strain Analysis for Engineering Design*, **42**(4), 269-279, 2007.
22. Germain, L., Gey, N., Humbert, M., Vo, P., Jahazi, M., Texture and microtexture analysis of an IMI 834 alloy after thermo-mechanical processing. In *Ti-2003 Science and Technology*, Hamburg, Wiley-VCH Verlag, **II**, pages 1291-1298, 2003.
23. Germain, L., Gey, N., Humbert, M., Vo, P., Jahazi, M., Bocher, P., Texture heterogeneities induced by subtransus processing of near alpha titanium alloys, *Acta Materialia*, **26**, 4298-4308, 2008.
24. Uta, E., Gey, N., Bocher, P., Humbert, M., Gilgert, J., Texture heterogeneities in α_p/α_S titanium forging analysed by EBSD - Relation to fatigue crack propagation, *Journal of Microscopy*, **233**(3), 451-459, 2009.
25. Stanford, N., Bate, P.S., Crystallographic variant selection in Ti-6Al-4V, *Acta Materialia*, **52**, 5215-5224, 2004.

26. Callister, W.D., *Fundamentals of Material Science and Engineering,* 5th ed, John Wiley & Sons, 2001.
27. Thompson, R.B., Elastic-wave propagation in random polycrystals: fundamentals and application to nondestructive evaluation, in *Imaging of complex media with acoustic and seismic waves*, Edited by Fink, Springer-Verlag, Berlin Heidelberg, 2002.
28. Bhatia, A.B., Scattering of high-frequency sound waves in polycrystalline materials, *J. Acoust. Soc Am.*, **31**(1), 16-23, 1959.
29. Bhatia, A.B., Moore, R.A., Scattering of High Frequency Sound Waves in Polycrystalline Materials II, *J. Acoust. Soc Am.*, **31**, 1140-1141, 1959.
30. Madsen, E.L., Insana, M.F., Zagzebski, J.A., Method of data reduction for accurated determination of acoustic backscatter coefficients, *J. Acoust. Soc Am.*, **76**(3), 913-923, 1984.
31. Papadakis, E.P., Ultrasonic attenuation caused by scattering in polycrystalline metals, *J. Acoust. Soc Am.*, **37**(4), 711-717, 1965.
32. Papadakis, E.P., Revised grain-scattering formulas and tables, *J. Acoust. Soc Am.*, **37**(4), 703-710, 1965.
33. Stanke, F.E., Kino, G.S., A unified theory for elastic wave propagation in polycrystalline materials, *J. Acoust. Soc Am.*, **75**(3), 1984.
34. Rose, J.H., Ultrasonic backscattering from polycrystalline aggregates using time-domain linear response theory. In *Review of Progress in Quantitative Nondestructive Evaluation*, pages 1715, 1991.
35. Rose, J.H., Ultrasonic backscatter from microstructure. In *Review of Progress in Quantitative Nondestructive Evaluation*, **11B**, pages 1677, 1992.
36. Rose, J.H., Theory of ultrasonic backscatter for multiphase polycrystalline solids. In *Review of Progress in Quantitative Nondestructive Evaluation*, **12B**, pages 1719-1726, 1993.
37. Han, K.Y., Thompson, R.B., Ultrasonic backscattering in duplex microstructures: theory and application to titanium alloys, *Metallurgical and materials transactions A*, **28A**, 91-104, 1997.
38. Hirsekorn, S., The scattering of ultrasonic waves by polycrystals, *J. Acoust. Soc Am.*, **72**(3), 1021-1031, 1982.
39. Hirsekorn, S., The scattering of ultrasonic waves by polycrystals. II. Shear waves, *J. Acoust. Soc Am.*, **73**(4), 1160-1163, 1983.
40. Hirsekorn, S., The scattering of ultrasonic waves in polycrystalline materials with texture, *J. Acoust. Soc Am.*, **77**(3), 832-843, 1985.
41. Hirsekorn, S., Directional dependence of ultrasonic propagation in textured polycrystals, *J. Acoust. Soc Am.*, **79**(5), 1269-1279, 1986.
42. Hirsekorn, S., The scattering of ultrasonic waves by multiphase polycrystals, *J. Acoust. Soc Am.*, **83**(4), 1231-1242, 1988.

43. Haldipur, P., Margetan, F.J., Thompson, R.B., Correlation between local ultrasonic properties and grain size within jet-engine nickel alloy billets. In *Review of Progress in Quantitative Nondestructive Evaluation*, **22**, pages 1355-1362, 2003.
44. Han, K.Y., Thompson, R.B., Margetan, F.J., Rose, J., Relationships between ultrasonic noise and macrostructure of titanium alloys. In *Review of Progress in Quantitative Nondestructive Evaluation*, **12**, pages 1743-1750, 1993.
45. Yalda-Mooshabad, I., Margetan, F.J., Thompson, R.B., Monte-Carlo simulation of ultrasonic grain noise. In *Review of Progress in Quantitative Nondestructive Evaluation*, **12**, pages 1727-1734, 1993.
46. Ahmed, S., Thompson, R.B., Panetta, P.D., Ultrasonic attenuation as influenced by elongated grains. In *Review of Progress in Quantitative NonDestructive Evaluation*, **22**, pages 109-116, 2003.
47. Ahmed, S., Thompson, R.B., Influence of columnar microstructure on ultrasonic backscattering. In *Review of Progress in Quantitative Nondestructive Evaluation*, **14B**, pages 1617-1624, 1995.
48. Panetta, P.D., Thompson, R.B., Margetan, F.J., Use of electron backscatter diffraction in understanding texture and mechanisms of backscattered noise generation in titanium alloys. In *Review of Progress in Quantitative Nondestructive Evaluation*, **17**, pages 89-96, 1998.
49. Yalda-Mooshabad, I., Thompson, R.B., Influence of texture and grain morphology on the two-point correlation of elastic constants: theory and implications on ultrasonic attenuation and backscattering, *Review of Progress in Quantitative Nondestructive Evaluation*, **14**, 1939-1946, 1995.
50. Margetan, F.J., Han, K.Y., Yalda-Mooshabad, I., Goettsch, S., Thompson. R.B., The practical application of grain noise models in titanium billets and forgings. In *Review of Progress in Quantitative Nondestructive Evaluation*, **14**, pages 2129-2136, 1995.
51. Panetta, P.D., Thompson, R.B., Ultrasonic attenuation in duplex titanium alloys. In *Review of Progress in Quantitative Nondestructive Evaluation*, **18B**, pages 1717-1724, 1999.
52. Panetta, P.D., Margetan, F.J., Yalda-Mooshabad, I., Thompson, R.B., Ultrasonic attenuation measurements in jet engine titanium alloys. In *Review of Progress in Quantitative Nondestructive Evaluation*, **15B**, pages 1525-1532, 1996.
53. Blodgett, M.P., Eylon, D., The influence of texture and phase distortion on ultrasonic attenuation in Ti-6Al-4V, *Journal of Nondestructive Evaluation*, **20**(1), 1-16, 2001.

54. Sharples, S.D., All-Optical Scanning Acoustic Microscope, PhD, University of Nottingham, 2003.
55. Thompson, R.B., Yu, L., Margetan, F.J., A formal theory for the spatial correlation of backscattered ultrasonic grain noise. In *Review of Progress in Quantitative Nondestructive Evaluation*, **24**, pages 1292-1299, 2005.
56. Yu, L., Thompson, R.B., Margetan, F.J., The spatial correlation of backscattered ultrasonic grain noise: theory and experimental validation, *IEEE Transactions on Ultrasonics, Ferroelectrics, and Frequency Control*, **57**(2), 363-378, 2010.
57. Engler, O., Randle, V., *Introduction to texture analysis: macrotexture, microtexture and orientation mapping,* 2nd ed, Taylor & Francis, 2009.
58. Tattersall, H.G., The ultrasonic pulse-echo technique as applied to adhesion testing, *J. Phys. D: Appl. Phys.*, **6**, 819-832, 1973.
59. *Titanium Ti-6Al-4V (Grade 5), Annealed*, Available from: http://www.matweb.com
60. Nagy, P.B., Ultrasonic classification of imperfect interfaces, *Journal of Nondestructive Evaluation*, **11**(3/4), 127-139, 1992.
61. Nagy, P.B., Ultrasonic detection of kissing bonds at adhesive interfaces, *J. Adhesion Sci. Technol.*, **5**(8), 619-630, 1991.
62. Brotherhood, C.J., Drinkwater, B.W., Guild, F.J., The effect of compressive loading on the ultrasonic detectability of kissing bonds in adhesive joints, *Journal of Nondestructive Evaluation*, **21**(3), 95-104, 2002.
63. Jamieson, E.E., Ultrasonic evaluation of beryllium-copper diffusion bonds, KCP-613-6332, Honeywell, 2000.
64. Rinker, B.A., Jamieson, E.E., Samayoa, J.A., Abeln, T.G., Lerch, T.P., Neal, S.P., Detection of weak interface signals for same material bond/weld inspection. In *Review of Progress in Quantitative NonDestructive Evaluation*, **22**, pages 1080-1087, 2002.
65. Nagy, P.B., Adler, L., Ultrasonic NDE of solid-state bonds: inertia and friction welds, *Journal of Nondestructive Evaluation*, **7**(3/4), 199-215, 1988.
66. Milne, K., Ultrasonic inspection of titanium diffusion bonds: final report, RNE3163, Rolls-Royce plc, 2010.
67. Kawashima, K., Murase, M., Yamada, R., Matsushima, M., Uematsu, M., Fujita, F., Nonlinear ultrasonic imaging of imperfectly bonded interfaces, *Ultrasonics*, **44**, e1329-e1333, 2006.
68. Wang, Z.C., Ridley, N., Lorimer, G.W., Knauss, D., Briggs, G.A.D., Evaluation of diffusion bonds formed between superplastic sheet materials, *Journal of Materials Science*, **31**, 5199-5206, 1996.

69. Derby, B., Briggs, G.A.D., Wallach, E.R., Non-destructive testing and acoustic microscopy of diffusion bonds, *Journal of Materials Science*, **18**, 2345-2353, 1983.
70. Weglein, R.D., Titanium diffusion bond evaluation via acoustic microscopy. In *Ultrasonics Symposium*, IEEE, pages 1988.
71. Baik, J.-M., Thompson, R.B., Ultrasonic scattering from imperfect interfaces: a quasi-static model, *Journal of Nondestructive Evaluation*, **4**(3/4), 1984.
72. Margetan, F.J., Thompson, R.B., Gray, T.A., Interfacial spring model for ultrasonic interactions with imperfect interfaces: theory of oblique incidence and application to diffusion-bonded butt joints, *Journal of Nondestructive Evaluation*, **7**(3/4), 131-152, 1988.
73. Palmer, D.D., Rehbein, D.K., Smith, J.F., Buck, O., Nondestructive characterization of the mechanical strength of diffusion bonds. II. Application of a quasi-static spring model, *Journal of Nondestructive Evaluation*, **7**(3/4), 167-174, 1988.
74. Rose, J.H., Ultrasonic reflectivity of diffusion bonds. In *Review of Progress in Quantitative NonDestructive Evaluation*, Plenum Press, New York, **8B**, pages 1925-1931, 1988.
75. Sotiropoulos, D.A., Achenbach, J.D., Ultrasonic reflection by a planar distribution of cracks, *Journal of Nondestructive Evaluation*, **7**(3/4), 123-129, 1988.
76. Achenbach, J.D., Xu, Y., Reflection by defective diffusion bonds, Ultrasonics Symposium, pages 1107-1111, 1989.
77. Yalda-Mooshabad, I., Margetan, F.J., Gray, T.A., Thompson, R.B., Reflection of ultrasonic waves from imperfect interfaces: a combined boundary element method and independent scattering model approach, *Journal of Nondestructive Evaluation*, **11**(3-4), 141-149, 1992.
78. Drinkwater, B.W., Dwyer-Joyce, R.S., Cawley, P., A study of the transmission of ultrasound across real rough solid-solid interfaces. In *Ultrasonics Symposium*, IEEE, pages 1081-1084, 1994.
79. Lavrentyev, A.I., Beals, J.T., Ultrasonic measurement of the diffusion bond strength, *Ultrasonics*, **38**, 513-516, 2000.
80. Drinkwater, B.W., Dwyer-Joyce, R.S., Cawley, P., A study of the interaction between ultrasound and a partially contacting solid-solid interface. In *Mathematical, Physical and Engineering Sciences*, **452**, pages 2613-2628, 1996.
81. Schoenberg, M., Elastic wave behaviour across linear slip interfaces, *J. Acoust. Soc Am.*, **68**(5), 1516-1521, 1980.

82. Lavrentyev, A., I., Rokhlin, S.I., Ultrasonic spectroscopy of imperfect contact interfaces between a layer and two solids, *J. Acoust. Soc Am.*, **103**(2), 657-664, 1998.
83. Angel, Y.C., Achenbach, J.D., Reflection and transmission of elastic waves by a periodic array of cracks, *Journal of Applied Mechanics*, **52**, 33-41, 1985.
84. Buck, O., Rehbein , D.K, Thompson, R.B., Palmer, D.D., Brasche, L.J.H., Nondestructive characterization and bond strength of solid-solid bonds. In *Review of Progress in Quantitative NonDestructive Evaluation*, Plenum Press, New York, **8B**, pages 1949-1956, 1988.
85. Pilant, W.L., Knopoff, L., Schwab, F., Transmission and reflection of surface waves at a corner 3. Rayleigh Waves (Experimental), *Journal of Geophysical Research*, **69**(2), 291-296, 1964.
86. Instanes, G., Toppe, M., Lakshminarayan, B., Nagy, P.B., Corrosion and Erosion Monitoring of Pipes by an Ultrasonic Guided Wave Method, in *Advanced Ultrasonic Methods for Material and Structure Inspection*, Edited by T. Kundu, ISTE, 2007.
87. Instanes, G., Toppe, M., Nagy, P.B., Corrosion and Erosion Monitoring of Pipes by an Ultrasonic Guided Wave Method. In *International Congress on Ultrasonics*, Vienna, pages 2007.
88. Thomas, G.H., Spingarn, J.R., Ultrasonic evaluation of solid-state welds, *Journal of Nondestructive Evaluation*, **7**(3/4), 227-235, 1988.
89. Thomas, G.H., Spingarn, J.R., Ultrasonic non-destructive evaluation of solid state welds, Plenum Press, New York, **7B**, pages 1319-1325, 1988.
90. Kato, H., Abe, S., Ultrasonic evaluation of the bonding strength of dissimilar metal bonds, *NDT&E International*, **29**(6), 355-361, 1996.
91. Thomas, G.H., Spingarn, J.R., Ultrasonic determination of diffusion bond strength. In *Review of Progress in Quantitative NonDestructive Evaluation*, Plenum Press, New York, **3B**, pages 1243-1250, 1984.
92. Thomas, G.H., Spingarn, J.R., Effects of microstructure and bond quality on the ultrasonic evaluation of dissimilar metal friction welds. In *Review of Progress in Quantitative NonDestructive Evaluation*, Plenum Press, New York, **9**, pages 1331-1337, 1990.
93. Brotherhood, C.J., Drinkwater, B.W, Guild, F.J., A comparison of the detectability of dry contact kissing bonds in adhesive joints using longitudinal, shear and high power ultrasonic techniques. In *Review of Progress in Quantitative NonDestructive Evaluation*, **22**, pages 1033-1044, 2003.

94. Brotherhood, C.J., Drinkwater, B.W, Dixon, S., The detectability of kissing bonds in adhesive joints using ultrasonic techniques, *Ultrasonics*, **41**, 521-529, 2003.
95. Ojard, G.C., Buck, O., Rehbein, D.K., Hughes, M.S., On the differentiation of diffusion bond strength using the total acoustic energy reflected from the bond. In *Review of Progress in Quantitative NonDestructive Evaluation*, Plenum Press, New York, **12**, pages 1453-1458, 1993.
96. Nieters, E.J., Gilmore, R.S., Gigliotti, M.F.X., *Method for ultrasonic evaluation of materials using time of flight measurement*: United States, 1995.
97. Hirose, S., Achenbach, J.D., Higher harmonics in the far field due to dynamic crack-face contacting, *J. Acoust. Soc. Am.*, **91**(1), 142-147, 1993.
98. Zheng, Y., Maev, R.G., Solodov, I.Y., Nonlinear acoustic applications for material characterization: a review, *Can. J. Phys*, **77**, 927-967, 1999.
99. Donskoy, D., Sutin, A., Ekimov, A., Nonlinear acoustic interaction on contact interfaces and its use for non-destructive testing, *NDT&E International*, **34**, 231-238, 2001.
100. Duffour, P., Morbidini, M., Cawley, P., A study of the vibro-acoustic modulation technique for the detection of cracks in metals, *Journal of Acoustical Society of America*, **119**(3), 1463-1475, 2006.
101. Solodov, I.Y., Ultrasonics of non-linear contacts: propagation, reflection and NDE applications, *Ultrasonics*, **36**, 383-390, 1998.
102. Buck, O., Morris, W.L., Richardson, J.M., Acoustic harmonic generation at unbonded interfaces and fatigue cracks, *Appl Physics Letters*, **33**, 371-373, 1978.
103. Kim, J.-Y., Yakovlev, V.A., Rokhlin, I., Parametric modulation mechanism of surface acoustic wave on a partially closed crack, *Applied Physics Letters*, **82**(19), 3203-3205, 2003.
104. Buck, O., Morris, W.L., James, M.R., Remaining fatigue life prediction in the initiation regime using SAW NDE, *Journal of Nondestructive Evaluation*, **1**(1), 3-9, 1980.
105. Morris, W.L., Buck, O., Inman, R.V., Acoustic harmonic generation due to fatigue damage in high-strength aluminium, *J. Appl. Phys*, **50**, 6737-6742, 1979.
106. Wegner, A., Koka, A., Janser, K., Netzelmann, U., Hirsekorn, S., Arnold, W., Assessment of the adhesion quality of fusion-welded silicon wafers with nonlinear ultrasound, *Ultrasonics*, **38**, 316-321, 2000.
107. Ohara, Y., Kawashima, K., Yamada, R., Horio, H., Evaluation of amorphous diffusion bonding by nonlinear ultrasonic method. In *Review of Progress in Quantitative NonDestructive Evaluation*, **23**, pages 944-951, 2004.

108. Margetan, F.J., Nieters, E., Brasche, L., Yu, L., Degtyar, A., Wasan, H., Keller, M., Kinney, A., Fundamental studies of titanium forging materials - engine titanium consortium phase II, DOT/FAA/AR-05/22, 2005.
109. ASNT, *Non-destructive testing handbook - ultrasonic testing*, Vol. 2, American Society for Metals, 1982.
110. Gonzalez, R.C., Woods, R.E., Eddins, S.L., *Digital image processing,* Second ed, Gatesmark, 2009.